

**BULGARIAN ACADEMY OF SCIENCES
INSTITUTE OF ASTRONOMY**

**Stellar and wind parameters of
Galactic OB stars**

**A thesis submitted for the degree of
Doctor of Physical Sciences
presented by Nevena Stefanova Markova**

Sofia, 2009

Contents

1	Introduction	1
1.1	Massive Stars and the Universe	1
1.2	Stellar winds from hot massive stars	4
1.3	Standard wind theory – historical overview	6
1.4	The Castor-Abbott-and-Klein theory	7
1.4.1	The radiative force	7
1.4.2	Predictions from the CAK theory	9
1.5	Wind diagnostics	11
1.5.1	Spectral line diagnostics	11
1.5.2	Stellar continuum diagnostics	13
1.6	Studies underlying the thesis	14
1.6.1	Main topics and goals	14
1.6.2	Approaches and methods used	17
2	“Blanketed” properties of OB stars	21
2.1	Approximate method	21
2.1.1	Sample stars and observational material	21
2.1.2	Input parameters and mass-loss determinations	24
2.1.3	Error analysis.	28
2.1.4	Verifying the approximate approach	29
2.1.5	Enlarging the sample	33
2.1.6	Summary	35
2.2	Complete spectral analysis of B SGs	37
2.2.1	Sample stars and observational material	39
2.2.2	Determination of stellar and wind parameters	41
2.2.3	The T_{eff} scale for B-SGs	48
2.2.4	Metallicity effects	51
2.2.5	Wind momentum - luminosity relationship. Comparison with results from similar studies	53
2.2.6	Summary	55
3	Wind structure and variability in OB stars	57
3.1	Long-term monitoring campaigns of α Cam	58
3.2	Observational material	58
3.2.1	Absorption line-profile variability	58
3.2.2	Wind variability as traced by H_{α}	61
3.2.3	Evidence of a “photospheric connection”	62
3.2.4	Towards a possible interpretation of H_{α} variability	63
3.2.5	Summary	64
3.3	B supergiant HD199478	66
3.3.1	Observational material	66
3.3.2	Photospheric variability	67
3.3.3	Wind variability as traced by H_{α}	71

3.3.4	Summary	73
3.4	Wind structure in late B-SGs	75
3.4.1	Pulsations	75
3.4.2	Magnetic fields	76
3.5	Statistical approach to study wind variability	79
3.5.1	Observational material	79
3.5.2	Methodology and measurements	80
3.5.3	H_α line-profile variability as a function of stellar and wind parameters	86
3.5.4	Empirical properties of the TVS as a function of stellar and wind parameters	88
3.5.5	Simulations of LPV in H_α	91
3.5.6	Spectral variability and the Wind Momentum Luminosity Relationship	101
3.5.7	Summary	102
4	The LBV P Cygni	105
4.1	Introduction	105
4.2	Observational data	106
4.2.1	Photometric and spectroscopic observations	106
4.2.2	H_α equivalent width measurements	107
4.3	Emission line spectrum in the optical	108
4.3.1	Permitted lines	108
4.3.2	Forbidden lines	113
4.4	Photometric and line-profile variability	114
4.4.1	Photometric variability	114
4.4.2	Line-profile variability in the optical	115
4.4.3	Comparison between photometric and spectroscopic variabilities	122
4.5	P Cygni in a short SD phase	124
4.5.1	Photometric evidences	124
4.5.2	Spectroscopic evidences	126
4.5.3	H_α variability due to changes in \dot{M}	127
4.5.4	Possible interpretation	128
4.6	Summary	128
5	Clumping in O-star winds	131
5.1	A combined H_α , IR and radio analysis	133
5.1.1	Variability of the diagnostics used	135
5.1.2	Observations and data processing	136
5.1.3	De-reddening and stellar radii	139
5.1.4	Simulations	141
5.1.5	Two prototypical test cases: ζ Pup and HD 209975	147
5.1.6	Clumping properties of the complete sample	151
5.1.7	Errors in the derived clumping factors	155
5.1.8	Clumping properties as a function of wind density	156
5.1.9	Wind-momentum–luminosity relation	158
5.2	Summary	159
6	Theory and observations	165
6.1	Monte Carlo predictions	165
6.2	The bi-stability jump	167
6.3	The Wind-momentum Luminosity Relationship	169
6.4	Wind efficiency	176
6.5	Wind clumping. Stratification of the clumping factor	177
6.6	Summary	180

Chapter 1

Introduction

The evolution of the Universe, since the time when the first stars were formed, is a central topic of present-day astrophysical research. The main engines of this evolution are stars with masses in excess of $10 M_{\odot}$, referred to as “massive stars”. These stars occupy the upper part of the Hertzsprung-Russell (HR) diagram with luminosities between twenty thousands and one million solar luminosities. On the main sequence, massive stars are spectroscopically identified as types O and early-B with temperatures between ~ 25 and ~ 50 kK while later evolutionary stages can encompass, depending on the initial mass, blue/red supergiants, Wolf-Rayet (WR) stars, Luminous Blue Variables (LBV), and supernovas (SN).

1.1 Massive Stars and the Universe

Observations in the solar neighborhood indicate that in the present cosmos Nature seems to favor the formation of lower mass stars over the formation of the massive stars. However, despite of their rarity, massive stars play very important role in the present, but also in the early Universe. Massive stars are critical agents in galactic evolution. In the present cosmos, they provide most of the metals and energy. In the distant Universe, they dominate the UV light from the young galaxies. The very first generation of these objects, the so-called Population III, might have influenced the formation and evolution of the first building blocks of galaxies. These very massive first stars might have also been responsible for the re-ionization of the early Universe. At the endpoint of their evolution, massive stars suffer a gravitational collapse and explode as a supernova. Eventually, a Gamma-Ray-Burst emerges, the most energetic cosmic flash.

Evolution of the cosmic matter Due to their short lifetime – $\sim 10^7$ years agents one Gyr for stars like our Sun – and powerful stellar winds, massive stars deposit a large amount of momentum and processes material (helium, oxygen and other heavy elements¹) into the InterStellar Medium (ISM) influencing its composition

¹Carbon and nitrogen are mainly produced by low and intermediate-mass stars (Renzini & Voli 1981; Wheeler et al. 1989).



Figure 1.1: What appears to be the hole of an elongated smoke ring in this National Radio Astronomy Observatory image, really is an enormous, nearly empty, bubble blown into the dusty, gas disk of our Milky Way Galaxy. Located at a distance of 30,000 light years from the Earth, this bubble measures 1,100 by 520 light years.

and energetics, and subsequently contributing to the chemical and dynamical evolution of the host galaxies.

Thus, massive stars, and in particular BA supergiants (SGs), can serve as tracers of abundance gradients in galaxies, and in stellar atmospheres. Studies of large samples of hot massive stars (HMS) in different galactic environments can also provide observational constraints on the chemical evolution of the galaxies (see Przybilla et al. 2007 and references therein).

HII regions, Wind bubbles and Star formation HMS emit the bulk of their radiation in the UV. This radiation ionizes and heats a very large volume of the ambient gas which then starts to expand (due to a pressure difference with the cool ISM) leading to the formation of the so-called Stromgren spheres, or S-type H-II regions. Due to the absorption of UV photospheric radiation by thousands of millions of metal lines, continuous mass loss from the stellar surface is also initiated and maintained. Flowing away from the star at supersonic velocities, the gas particles create circumstellar shells and wind-bubbles. Since massive stars are mostly seen grouped in young clusters, wind-blown bubbles frequently interact with each other forming super-bubbles, as the one shown in Fig 1.1. These super-bubbles are presently thought to be places for new stars formation (Oey & Massey 1995). Perhaps, they are also responsible for the phenomenon of galactic energetic outflows in starbursts (Kunth et al. 1998), and in starburst galaxies even at high redshifts (Pettini et al. 1998).

Dark ages and the re-ionization of the Universe One of the most important challenges in modern cosmology is to understand how the cosmic “dark ages” ended. Observations suggest that the Universe was re-ionized at red-shift $z > 5.8$ (Fan et al. 2000) where this process was traditionally attributed to a population

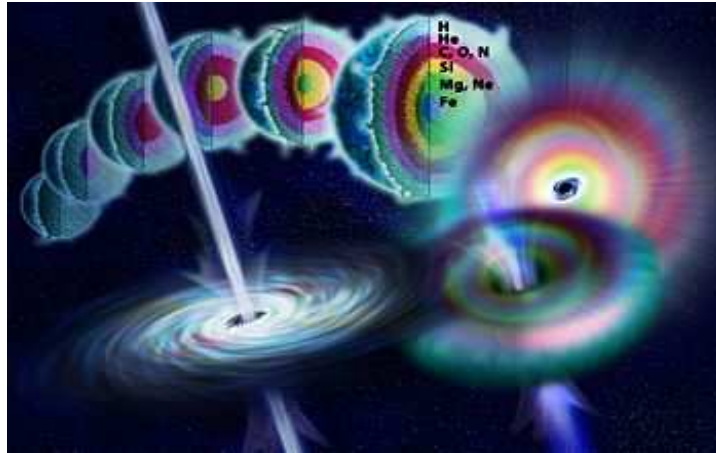


Figure 1.2: Drawing of a massive star collapsing to form a black hole. Energy released as jets along the axis of rotation forms a gamma ray burst. Credit: Nicolle Rager Fuller/NSF

of quasars. However, numerical simulations (e.g., Bromm, Kudritzki, Loeb 2001; Bromm, Coppi, Larson 2002 and references therein) indicate that the primordial mass function might be dominated by very massive ($M_{\star} > 10^2 M_{\odot}$) stars of extremely high temperatures ($T_{\text{eff}} \sim 10^5$ K). Since such stars are very efficient in the ionization of H and He, they might have played a significant role in the re-ionization of the gas, especially at high red-shift ($z \sim 5$) where the known quasars do not seem to be able to maintain the ionization of the intergalactic medium. Thus, an early generation of very massive, zero-metal stars, called Population III, might be responsible for the first light in the “dark ages”. Since no star with metallicity below $10^{-3} Z_{\odot}$ has been so far discovered, this possibility still remains to be observationally proven though. Penetrating deeper into the early Universe, close to the Big Bang, the James Webb Space Telescope (JWST), scheduled for launch in 2013, might help to solve this issue.

γ -ray bursts (GRB) – the most energetic cosmic flashes, second only to the Big Bang – are known for many years, but their origin was discovered only in 1997 when the first afterglow X-ray emission from a GRB (GRB 970508) was detected. Since then, the redshift was measured for more than 100 GRBs. The distribution of the corresponding data shows a peak around $z \sim 1$ with values going up to $z = 6.29$ (Haislip et al. 2006), thus indicating these objects are of extragalactic origin.

Although the nature of GRBs is not still established, there are suggestive evidence to believe this phenomenon is a result of terminal collapses of very massive, low-metallicity, single stars², in particular WR stars of type WO (Hirschi, Meynet, Maeder 2004; Hirschi et al. 2005a). Nice illustration of the collapsar scenario announced by MacFadyen & Woosley (1999) is shown in Figure 1.2 where the core of a very massive, rapidly rotating star collapses into a black hole while its envelope forms a hyper-accreting disc

²An alternative hypothesis that binary stars are the progenitors of GRBs also exists (Izzard et al. 2004; Heger et al. 2005)

around the hole. The infall of material from the disc onto the black hole powers an extremely energetic jet that blasts outwards through the stellar envelope. When the jet reaches the stellar surface, a gamma-ray burst is produced.

The most direct evidence connecting GRBs to massive stars are the observations of the afterglow of GRB 980425 (Galama et al. 1999), GRB 980326 (Bloom et al. 1999), and GRB 970228 (Galama et al. 2000).

First building blocks Observations indicate that the spectral appearance of Lyman break galaxies and $L\alpha$ emitters at high redshifts is dominated by an intrinsic population of hot massive stars (e.g., Shapley et al. 2003). These results imply that the first generation of very massive, low metallicity stars has very likely influenced the formation and evolution of the first building blocks of galaxies (Rhoads & Malhotra 2001; Malhotra & Rhoads 2002).

Extra-galactic distances Another exciting possibility that makes massive stars, in particular blue SGs, very attractive is that they might serve as extra-galactic distance indicators, alternative to Cepheids (Kudritzki et al, 1999, 2003).

1.2 Stellar winds from hot massive stars

It took about 400 years – from the Tycho Brahe observations of the first “nova-like” object in 1572 till the launch of the *Copernicus* satellite in the mid of the 20th century – for astronomers to realize that not only nova-like objects, but nearly all stars undergo continuous mass loss throughout some fraction of their life. The continuous outflow of mass particles from the stellar surface is called “solar/stellar wind” where this term was coined by Eugene Parker (Parker 1958, 1960).

In general, to have a stellar wind an outward directed force, larger than the gravitational force, is required to present in the star. Depending on the physical parameters of the underlying star, various driving mechanisms and thus, various types of stellar winds such as, e.g., line driven winds, coronal winds, sound wave driven winds, Alfvén wave winds etc., have been proposed to explain the results derived by observations³.

In the particular case of hot stars, the driving force is thought to be the radiation force on spectral lines, and the continuum. Indeed, due to their huge luminosities, these stars generate an enormous radiation pressure which at some point in the atmosphere cancels out completely the gravity force leading to

³For a detailed description of wind models based on different driving mechanisms the interested reader is referred to the book of Lamers & Cassinelli (1999).

a continuous mass outflow from the stellar surface. The mass outflow is additionally accelerated by the transfer of photon momentum from the photospheric radiation into the stellar atmosphere through absorption in UV spectral lines. This driving mechanism turns out to be very efficient: velocities up to a factor of 10 higher than the corresponding sound speed can be reached. Due to these reasons, stellar winds from hot stars are known as *supersonic, line-driven* winds. Some aspects of stellar winds from hot stars are summarized below:

- Winds modify the physics of hot massive star atmospheres by dominating the density stratification and the radiative transfer via their transonic velocity fields (Kudritzki 1998). Clear wind signatures can be found both in the emergent spectrum (e.g., blue-shifted absorptions, P Cygni-type profiles and emission lines), and in the spectral energy distribution (e.g., X-ray emission, IR and radio excess emission) of massive stars. In addition, winds modify the temperature structure of the underlying photosphere by scattering back a large part of the continuum photospheric radiation (the so-called “wind-blanketing”, see Sect.1.6.1). All this indicates that the neglect of stellar winds in studies of massive stars can lead to substantial errors in the derived stellar parameters. For example, effective temperatures and surface gravities from optical line diagnostics are heavily influenced by stellar winds.
- Winds play an important role in the evolution of massive stars influencing their evolutionary timescales, surface abundances and luminosities. Due to stellar winds, masses are continuously reduced: a star with initially $60 M_{\odot}$ on the main-sequence is expected to end up its life as a WR star of only $6 M_{\odot}$ (Meynet et al. 1994). This fact has at least two major consequences. First, depending on its final mass, which in turn depends on the amount of mass lost during its entire life, a massive star will end its evolution either as a neutron star, or as a black hole. Second, since the process of mass loss may have a place even during the main-sequence phase, the later evolution of a massive star off the main-sequence into the RED supergiant phase might be strongly influenced. Given the on-going debate on the existence of the Humphreys – Davidson limit (see, e.g., Vink 2000 and references therein), this possibility is especially important.
- As noted in the previous section, winds provide a significant input of mechanical/radiative momentum, energy, and processed material into the ISM thus contributing to the chemical and dynamical evolution of galaxies.
- Stellar winds are a gift of Nature. They provide us with the unique opportunity to investigate distant galaxies by analysing wind features in their integrated spectra (e.g., Pettini et al. 2000; Leitherer et

al. 2001), or by investigating individual spectra of luminous stars hosted in these galaxies (Bresolin et al. 2001, 2002; Urbaneja et al. 2005a).

- Last but not least, spectral observations of wind features from isolated blue-supergiants in spiral and irregular galaxies can in principle provide an alternative tool to determine extra-galactic distances (Kudritzki et al. 1995; Kudritzki 1998; Kudritzki et al. 1999, 2003).

From the outlined in this and in the previous sections two things become apparent: first, our understanding of the Universe as a whole is intimately linked to our knowledge about massive stars and their evolution and second, the overall physics of massive stars is strongly influenced by the processes of stellar winds. As far as these two points have been realized, the development of a quantitative theory to account for the effects of stellar winds in hot stars has become a task of crucial astrophysical importance. Up to now the most promising attempt is *the radiation-driven wind theory*.

1.3 Standard wind theory – historical overview

The starting point of the development of radiation-driven wind theory is rooted in a series of papers by Milne (e.g., Milne 1926 and Milne 1926; see also Johnson 1925) who was the first to realize that radiation could be coupled to ions leading *eventually* to mass outflow from the stellar surface. About thirty years later on, Sobolev (1957) made the next fundamental step developing the basic ideas of radiative transfer in expanding atmosphere.

The idea of Milne was additionally worked out by Lucy & Solomon (1970) who argued that in OB stars line scattering is so efficient that the radiative momentum absorbed by even one strong, resonance line could overcome gravity. Their wind model, however, failed to reproduce the observed mass-loss rates for the contribution of only a few optically thick resonance lines were taken into account.

Soon after that, the situation was significantly improved by Castor, Abbott and Klein (1975) (hereafter CAK) who developed the concept of the “*line-strength distribution function*” to calculate the radiative force caused by a large number of strong and weaker lines (see Sect.1.4.1). Being subject of several drastic approximations, the original CAK approach has been massively improved during the years (Cassinelli, Olson, Stalio 1978; Abbott 1982; Hummer and Rybicki 1985; Pauldrach et al. 1986). Later improvements concern the inclusion of non-LTE effects ⁴ and the effects of photospheric “line blocking” (Pauldrach et al. 1994; Pauldrach et al. 2001), and the announcement of depth dependent line-force parameters (Kudritzki 1998).

⁴Due to the strong radiation field and the low densities in the atmospheres of hot massive stars, non-LTE effects are important

Another more sophisticated approach to calculate the radiative force, known as the “*Monte-Carlo method*”, has been developed by Abbott and Lucy (1985). One of the major advantage of the Monte-Carlo method is that it allows for the process of multi-line scattering which is important for stars with extremely dense winds, e.g., WR stars. The Monte-Carlo method was further developed by Vink et al. (2000, 2001) and by Sim (2004). Due to the improved mass-loss rates for stars with stronger winds, the Monte-Carlo predictions are now superior to those from the modified CAK approach (Vink 2006), and are preferably used to compare with the observations (see Chapter 6, Sect. 6.1).

The original CAK theory as well as its modern-era modifications are know as “standard radiation-driven wind theory”. The basic concept in this theory is the assumption of *a stationary, homogeneous, spherically symmetric* stellar wind.

1.4 The Castor-Abbott-and-Klein theory

Though somewhat simplified (see Sect. 1.6), the *standard* wind theory has a well-established status in the hot-star community, and that is simply because in the framework of this theory the global *mean* wind properties: mass-loss rate, \dot{M} , and velocity field, $V(r)$, are reasonably well-understood for most early-type stars. Indeed, the majority of present-day investigations, including the ones presented in this thesis, still rely on the standard wind models, partly extended to allow for the presence of wind inhomogeneities (clumping) and X-rays.

1.4.1 The radiative force

The core of the radiation-driven wind theory is the determination of the radiative force which comprises the acceleration due to the continuum opacity, and the one due to absorption in spectral lines.

The continuum force, g_{cont} , summarises the contribution of the Thomson scattering by free electrons, and bound-free and free-free absorptions of all considered elements. Since in hot star winds Hydrogen is completely ionized (i.e., a large number of free electrons are available), the continuum radiative force is dominated by the Thomson scattering, and can be expressed as:

$$g_{\text{cont}} = \frac{\sigma_e F_c}{c} = \frac{\sigma_e L_\star}{4\pi r^2 c} \quad (1.1)$$

where F_c marks the flux radiated by the star; σ_e (in cm^2g^{-1}) is the absorption coefficient for the Thomson scattering; L_\star - the total luminosity, and c - the speed of light.

Theoretical considerations (Lucy & Solomon 1970) indicate that in hot star winds the continuum force alone will never overcome gravity, unless the acceleration due to absorption in spectral lines, g_{rad}^{lines} , is not accounted for.

The line force Since hot star winds are driven by absorption of photospheric photons in spectral lines, it is obvious that g_{rad}^{lines} must depend (i) on the available amount of photospheric flux that can be absorbed, F_c ; (ii) on the number of lines being available to absorb significant part of that flux, N_{eff} , and (iii) on their ability to absorb, i.e., on their optical thickness, τ_i . Note that depending on the strength of the transition, two types of lines, optically thick and optically thin⁵, may present in the wind which contribute to the line acceleration in a completely different way (Kudritzki et al. 1989; Puls et al. 2000). Note also that optically thin lines are not solely able to “drive” a stellar wind. This can only be done by optically thick lines.

Within the so-called “Sobolev approximation” (Sobolev 1960), the acceleration generated by a single line at frequency ν , and optical depth $\tau_i = \xi\lambda/(d\nu/dr)$ with ξ the frequency integrated line-opacity, can be approximated as

$$g_{rad,i}^{line} = \frac{L_\nu\nu}{4\pi r^2 c^2} \left(\frac{d\nu}{dr} \right) \frac{1}{\rho} (1 - e^{-\tau_i}) \quad (1.2)$$

where L_ν is the luminosity at the line frequency. Summarizing the individual contribution of all effective lines, the *total* line acceleration can be estimated providing the optical depth (i.e., the oscillator strengths, the statistical weights, and the occupation numbers⁵ of the lower and upper levels) of each line is known. This very difficult job has been done by Abbott (1982), by Pauldrach et al. (1986) and by Shimada et al. (1994).

Fortunately, an elegant way to overcome this difficulty turns out to exist. Investigating of an ensemble of C III lines in Local Thermodynamic Equilibrium (LTE), CAK found that the distribution of these lines on frequency position and line-strength can be approximated by a power law of the form:

$$dN(\nu, k_l) = -N_0 f_\nu(\nu) k_l^{\alpha-2} d\nu dk_l \quad (1.3)$$

where f_ν is the frequency distribution which is rather independent from the distribution of the line strengths; k_l is the line strength; α – a parameter with a value between zero and unity, and N_0 – a normalization constant. The expression given by Eq. 1.3 is known as “*line-strength distribution function*”.

The invention of the *line-strength distribution function* by CAK is a cornerstone in the development of the radiation-driven wind theory. This way the summation over the individual contribution of millions of optically thin and thick lines can be replaced by integration, allowing the *total* line acceleration to be

⁵By definition, an optically thin line with a given frequency cannot absorb all the flux emitted from the core at that frequency while an optically thick line can do this, independent of the number of absorbing particles per unit volume.

easily calculated. Interestingly, and most importantly, this approach has been validated by more recent calculations, which take into account *non-LTE* effects and the contribution of ions from *all* participating elements and ionization stages (see Puls et al. 2000).

Combining Eqs. 1.2 and 1.3, and integrating over frequency and line-strength, CAK have derived the following expression for the *total* line strength:

$$g_{rad}^{lines} = \frac{\sigma_e^{ref} L_{\star}}{4\pi r^2 c} M(t) \quad (1.4)$$

with $\sigma_e^{ref} = 0.325 \text{ cm}^2 \text{ g}^{-1}$ – a reference value for the electron scattering opacity and $M(t)$, the so-called *force multiplier*, given by:

$$M(t) = kt^{-\alpha} \left(\frac{n_e}{W} \right)^{\delta} \quad (1.5)$$

In the last expression, n_e is the electron density in units of 10^{11} cm^{-3} ; W is the geometrical dilution factor, and t is a dimensionless optical depth parameter given by

$$t = \frac{\sigma_e^{ref} v_{th} \rho}{(dr/dv)} \quad (1.6)$$

with v_{th} – the thermal velocity of the protons in the wind.

k , α and δ are known as “*force multiplier parameters (fmeps)*”. k is a measure for the number of the contributing lines, N_{eff} . It can be interpreted as the fraction of the flux that would be blocked already at the photosphere *if* all lines were optically thick. α determines the slope of the line-strength distribution, and also represents the relative contribution of optically thin and thick lines: $\alpha = 0$ corresponds to the optically thin case, $\alpha = 1$ – to the optically thick one. In Eq.1.5, the factor $(n_e/W)^{\delta}$ is added by Abbott (1982) to account for ionization effects in the case when the ionization is *not* frozen in. Thus, δ represents a value for the ionization of the wind.

Here, it is important to realize that the *fmeps* are not free parameter, but their values have to be fixed simultaneously, and in a self-consistent way, from the (NLTE) line opacities and the radiation field (see, e.g., Paudrach et al. 1994). For O-stars and early B-supergiants $\alpha = 2/3$ is predicted by line-statistics (Puls et al. 2000). Typical values of δ for O-stars are $\delta \sim 0.05$ to 0.1 , but exceptions can also present.

1.4.2 Predictions from the CAK theory

To derive the global wind properties: mass-loss rate, \dot{M} and velocity law, $v(r)$, the wind hydrodynamics has to be solved. Within the standard theory (*a stationary, homogeneous and spherically symmetric wind*), the wind hydrodynamics can be described by two equations: *the mass continuity equation* (Eq. 1.7) and *the*

momentum equation (Eq. 1.8):

$$\dot{M} = 4\pi r^2 \rho(r) v(r) \quad (1.7)$$

$$v(r) \frac{dv(r)}{dr} = -\frac{dP_{gas}(r)}{dr} \frac{1}{\rho(r)} - g(r) + g_{rad}(r) \quad (1.8)$$

with $\rho(r)$ – the mass density distribution and r – the radial coordinate. The first term on the right of Eq. 1.8 expresses the contribution of gas pressure, P_{gas} . The second term is related to the gravitational force ($=GM_{\star}/r^2$); the third represents the *radiative acceleration*, g_{rad} , which is the most crucial term in the equation of motion.

Calculating g_{rad} in the way outlined in the previous section, and neglecting the gas pressure term, CAK have solved the equation of motion and derived the following velocity law and scaling relations for \dot{M} and the terminal wind velocity, v_{∞} :

$$v(r) = v_{\infty} \left(1 - \frac{R_{\star}}{r}\right)^{\beta}, \beta = 0.5 \quad (1.9)$$

$$v_{\infty} = C_{\infty} \sqrt{2GM_{eff}/R_{\star}} = C_{\infty} v_{esc}, \quad C_{\infty} = \left(\frac{\alpha}{1-\alpha}\right)^{0.5} \quad (1.10)$$

$$\dot{M} \propto (kL)^{\frac{1}{\alpha'}} M_{eff}^{1-\frac{1}{\alpha'}} \quad (1.11)$$

In the above equations, M_{eff} represents the effective mass, i.e. the mass corrected for the radiative force due to electron scattering ($M_{eff} = M_{\star}(1-\Gamma)$); v_{esc} and G are, respectively, the photospheric escape velocity and the gravitational constant; β describes the slope of the velocity law; v_{∞} is the maximum wind velocity reached at very large distances from the star where the radiative acceleration approaches zero (due to the geometrical dilution of the photospheric radiation field), and $\alpha' = \alpha - \delta$.

From Eqs. 1.9 to 1.11 it is clear that if k , α and δ were *a priori* known, mass loss rates and terminal velocities could be immediately computed as function of effective temperature, luminosity, and stellar mass. Unfortunately, this exciting perspective turned out to be rather optimistic since more recent theoretical investigations have shown that the *fmps* are not unique, but depend on T_{eff} and stellar abundances (Puls et al. 2000), and that the assumption of CAK about depth independent *fmps* is too simplified (Kudritzki et al. 1998a).

Finally in this section, let me point out that though derived by means of a rather simplified approach, Eqs. 1.9 to 1.13 have been proven to be basically correct (with somewhat different values of β and C_{∞} though) by the observations as well as by more elaborate considerations including all details (see Puls, Vink & Najarro 2008 and references therein). This is one of the main achievements of the CAK theory.

1.5 Wind diagnostics

As noted in the previous section, stellar winds are characterized by three parameters: mass-loss rate, \dot{M} , wind terminal velocity, v_∞ , and the velocity exponent β . These parameters can be estimated from the observations, fitting certain observational features, called “wind diagnostics”, with model calculations. However, this task is never straightforward and simple: depending on the degree of sophistication of the underlying model, and on the diagnostics used, the reliability of the obtained results can be vastly different.

1.5.1 Spectral line diagnostics

Technically, one can estimate wind properties either by fitting certain spectral lines in the UV, optical or IR domains with model calculations, or by analysing the IR, Submillimeter or Radio continua. While the first approach provides the opportunity to determine v_∞ and β in parallel with \dot{M} , the second one is generally considered to be more simple and easy for use.

Depending on the mechanism that feeds the upper level of the line transition, two types of lines can be formed in a stellar wind: a P Cygni-type line with a blue-shifted absorption trough and a red-shifted emission peak, and a pure emission line, or an absorption line partly filled in by emission. Both types of lines can be used to derive \dot{M} , v_∞ and β .

Wind diagnostics in the UV are P Cygni profiles of resonance and subordinate lines of highly ionized atoms (e.g., C IV, N V, Si IV, O VI etc): saturated profiles⁶ help to constrain v_∞ and β ; unsaturated profile provide information about \dot{M} . In the optical, the primary wind diagnostic is H_α ; in the IR - members of the Bracket series, but also Helium lines. The theoretical framework for determining wind properties from spectral lines in the UV, optical and IR spectra is in principle identical, but specific features also exist (see below).

UV resonance lines are the most sensitive mass-loss indicators in hot stars. They originate from line scattering, i.e., their optical depth depends linearly on wind density, and therefore sample the entire wind being at the same time less sensitive to wind inhomogeneities and clumpiness. Irrespective of these obvious advantages, the use of UV lines as a wind diagnostic is so far limited because of two reasons: first, UV observations can be obtained only from space and second, to calculate synthetic profiles for these lines, one needs to know the corresponding elemental abundances and ionization/excitation fractions, both being subjects of still open questions (see Kudritzki & Puls 2000 and references therein). Consequently, \dot{M} -estimates derived from UV resonance lines are generally considered less reliable.

⁶Saturated profiles are those which have almost zero intensity for the entire velocity range from zero to v_∞ .

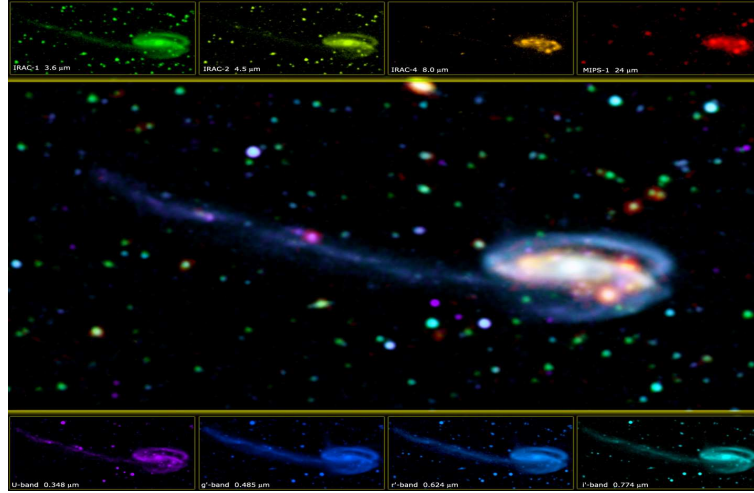


Figure 1.3: Optical-infrared panchromatic view of the Tadpole galaxy (UGC10214). The central image is a composite combination of 8 bands. Maps of the individual bands are shown with side panels (from Jarrett et al. 2006).

On the other hand, UV resonance lines are the outstanding tool to determine v_∞ . The most easy way is to measure the velocity position either of the blue-absorption edge of *saturated* profiles, or of the Discrete Absorption Components (if any). Another widely used approach is the comparison of observed and synthetic profiles, calculated by means of the SEI (Sobolev plus exact integration) method developed by Lamers et al. (1987). Following different methods high-precision (accuracy $\sim 10\%$) v_∞ - estimates of a large number of early-type stars have been derived (e.g., Groenewegen & Lamers 1989; Howarth & Prinja 1989; Haser et al. 1995; Howarth et al. 1997).

Optical lines In hot star winds, the main optical wind diagnostic H_α is mainly a recombination line, i.e., its opacity depends on the square of wind density. This fact has at least three major consequences: firstly, H_α emission can be easily detected even from distant objects. Secondly, H_α can be used to investigate only the inner parts of the envelope, close to the wind base. Finally, since the ionization/excitation of Hydrogen is not an issue, the accuracy of \dot{M} - estimates from H_α is relatively high – $\sim 50\%$ for weaker winds (H_α in absorption) and less than 10% for stronger winds (H_α in emission). For the particular case of stronger winds, an additional advantage is that in parallel to \dot{M} the velocity exponent β can be also fixed with relatively high precision (Puls et al. 1996). All this makes H_α a primary tool to determine wind properties in hot stars. And although problems exist (e.g., the influence of the He II blend, the effects of rotation and clumping), the current consensus is that the results derived from H_α are generally quite reliable.

IR lines Gabler et al. (1989) were the first who pointed out the great potential of IR lines in providing valuable information about the physics of hot star atmospheres and winds. Apart from information about

\dot{M} , these lines can be also used to put constraints on the shape of the velocity field (e.g., Najarro et al. 1997; Hillier et al. 1998). Interestingly and most importantly, due to some non-LTE effects in the line profiles at longer wavelengths (Kudritzki 1979), IR lines can be considered superior to H_α when stars with very weak winds (e.g., Najarro et al. 1998), or luminous stars from regions with large opacity (e.g., Figer et al. 1998; Hanson et al. 2002; Kendall et al. 2003) have to be investigated. Consequently, several tens of massive stars have been discovered in the near-IR spectral window over the last decade. An example illustrating the large potential of the IR observations is given in Figure 1.3.

Due to the fast development of the observational facilities, the IR astronomy has made enormous progress during the last decade. In addition to the large ground-based telescopes, few missions from space (e.g., IRAS, ISO, the Spitzer Space Telescope) have been successfully realized which enlarge the relatively narrow window accessible from the Earth. New missions both from space (e.g., Space Infrared Telescope Facility (SIRFT) and the James Webb Space Telescope) and from the ground (e.g., the LIRIS project for the William Herschel Telescope) are now in progress. In view of the above outlined advantages of the IR observations, these developments should not be a surprise though.

However, the quantitative analysis of IR lines is not an easy task. In particular, modeling hydrogen and helium lines in the *J*, *H*, *K* and *L* spectral windows requires good knowledge of all processes going on in the transition region from the photosphere to the supersonic layers, where most of these lines are formed. And although our present knowledge on this issue is far from complete, the outcomes of the first IR analysis are quite promising (Lenorzer et al. 2004; Repolust et al. 2005).

1.5.2 Stellar continuum diagnostics

It is a well-known fact that all hot stars with moderate and large mass loss show excess radiation at longer wavelengths. Thus, IR, (sub)millimeter, and radio continua of these stars can be used to determine their wind properties. Since the excess radiation originates from relatively simple atomic/ radiation transfer processes (bound-free and free-free transitions), the derived estimates of \dot{M} are usually considered quite reliable.

Radio emission The method to analyze radio emission from OB-stars was developed by Wright & Barlow (1975) and by Panagia & Felli (1975). The basic idea is as follows. Due to the negligible contribution of the photosphere, the *observed* radio flux, S_ν , is essentially determined by three parameters: mass loss rate, wind terminal velocity, and the distance to the star, d , and can be expressed as

$$S_\nu \propto \left(\frac{\dot{M}}{v_\infty} \right)^{4/3} \frac{v^{0.6}}{d^2} \quad (1.12)$$

Following this approach, mass-loss rates of many O and early-B⁷ stars in our Galaxy have been derived using radio data obtained mainly from the Very Large Area (Abbott et al. 1980, 1981; Bieging et al. 1989; Scuderi et al. 1998; Puls et al. 2008), but also from the Australia telescope (Leitherer et al. 1995).

However note that despite of its obvious advantages – knowledge of v_∞ and d is only required to determine \dot{M} from S_ν , – the radio approach has at least two restrictions: (i) due to the $\frac{v^{0.6}}{d^2}$ - dependence of the observed flux, radio emission from extragalactic OB-stars cannot be analyzed, and (ii) *non – thermal* radio emitters must be excluded from the target list. In the later case, since observations at minimum two frequency points are required to estimate the corresponding spectral index, additional Submillimeter observations can be used to extend the frequency base-line (Leitherer & Robert 1991).

IR excess Following the pioneer work of Barlow & Cohen (1977), several groups tried to derive mass-loss rates for OB stars using IR excess in various bands. The agreement between these estimates and those from H_α is generally good, but significant discrepancies are also established (see, e.g., Kudritzki & Puls 2000). A particular problem here is that the continuum radiation in the IR becomes optically thick already below v_∞ , and thus information about the velocity field is required to calculate the corresponding fluxes. Also, the contribution of the photospheric flux has to be taken into account.

To conclude let me point out that in this thesis H_α , but also IR, Submillimeter and Radio continua diagnostics will be used to determine mass-loss rates of OB-stars while terminal velocities will be constrained from the UV resonance lines.

1.6 Studies underlying the thesis

In the very beginning, I have noted that massive stars are not a single group of objects, but comprise various sub-groups in different parts of the HR diagram, and at different evolutionary stages. Luminous OB stars constitute one of the most important sub-groups of massive stars, which represents early stages in the evolution of these objects. In this thesis the main outcomes of a long-term extensive survey of stellar winds from single OB stars in the Milky Way will be presented and largely discussed.

1.6.1 Main topics and goals

By means of my investigations I have aimed to improve our knowledge about the physics of hot luminous stars by addressing three open issues, proven to be of immediate interest to the astronomical community,

⁷Due to their weaker winds, mid and late-B stars have lesser chance to be detected as thermal radio sources.

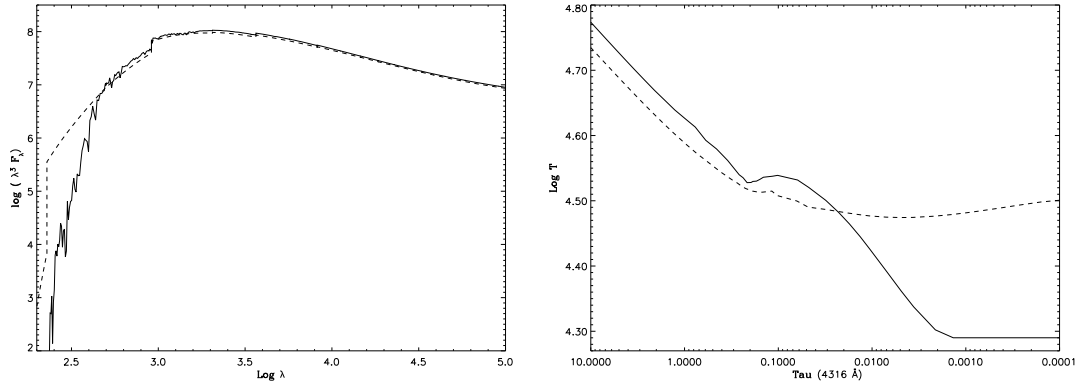


Figure 1.4: Examples illustrating the effects of line blocking and blanketing in a typical O-star model of $T_{\text{eff}} = 40$ kK. Left: Emergent flux, $\log(\lambda^3 F_\lambda)$ as a function of $\log \lambda$; Right: Local kinetic temperature, $\log T$, as a function of monochromatic optical depth at blue wavelength, $\tau_{4316\text{\AA}}$. Dashed lines - metal free models; solid - models accounting for metal line opacity in NLTE. (adopted from Kudritzki & Urbaneja 2006)

namely:

- i) the effects of line-blocking and blanketing
- ii) the wind variability and structure, and
- iii) the validity of the standard wind predictions.

• **Effects of line blocking and blanketing** The most complicating issues to be taken into account when calculating hot star wind models are the departures from LTE, and the presence of multitude of overlapping metal absorption lines in the Extreme UV (EUV). Consequently, only metal free models in LTE were produced and used till recently. The calculations of “blanketed” models, which properly account for NLTE effects and the effects of stellar winds, became possible only few years ago.

As illustrated in Figure 1.4, the inclusion of metal line opacities into the NLTE model calculations is expected to have at least two major consequences: the emerged EUV flux will be significantly blocked (left panel), and the optical and IR fluxes will be slightly amplified due to the so-called back-warming (right panel). Consequently, the ionizing equilibrium of all ions with thresholds in the EUV will change significantly. In particular, the He ionization balance is predicted to move to lower T_{eff} compared to the unblanketed models. In addition, the surface gravities are expected to decrease due to the increase in the radiative acceleration⁸, whilst the stellar radii will stay almost unaffected⁹. Following the decrease in T_{eff} and $\log g$, stellar luminosities and masses will also decrease. Since metal lines are formed both in the photosphere and in the wind, the effects are expected to be stronger in SGs than in DWs, but depend also

⁸Note that in contrast to Helium, Hydrogen is almost unaffected since in this case the two processes, blocking and back-warming, compensate each other.

⁹For stars with known distances R_\star follows from a comparison of absolute magnitudes (independent on the model) with theoretical model fluxes in the V-band, which turned out to be quite similar for both the blanketed and unblanketed models.

on T_{eff} and, of course, on metallicity. (For a detailed discussion on line blanketing, see Puls et al. 2008 and references therein.)

From the above outlined it follows that a revision of the stellar and wind parameters of OB stars derived by means of *unblanketed* model analyses is urgently required. Motivated by this need a project to determine the “blanketed” properties of a large sample of Galactic OB-stars was initiated and accomplished by me in collaboration with other colleagues. The results of these investigations will be outlined in Chapter 2.

- **Wind variability and structure** Though quite successful in explaining the global *mean* wind properties of OB stars, the standard wind models fail to describe a number of observational features, such as, e.g., the X-ray emission, the black troughs in saturated UV lines, the Discrete Absorption Components in UV and optical spectra, the behaviour and complex structure of H_{α} etc. All these features suggest hot stars winds are not smooth and stationary, as assumed in the standard theory, but structured and variable.

This possibility is supported by recent numerical simulations, which have shown that processes, such as, e.g., rotation, magnetic fields, stellar pulsations and radiative wind instability may play significant role in modifying the properties of hot star winds. (For a complete review on this subject, see Kudritzki & Puls 2000.) And although first steps to include these physical ingredients into the standard theory have already been taken (see, e.g., Bjorkman & Cassinelli 1993, for the effects of rotation; Owocki & ud-Doula 2004 and ud-Doula et al. 2008 for the effects of magnetic fields; Owocki & Rybicki 1985 and Owocki, Castor and Rybicki 1988 for the theory of line-force instability and its ongoing refinements by Owocki & Puls 1996, 1999), it still remains to be seen on a broad observational base whether the role of these ingredients is indeed as significant as predicted by theory.

Guided by these perspectives, a long-term project to investigate the nature and the origin of wind structure and variability in hot massive stars was initiated and realized by me (in collaboration with other colleagues mainly from abroad). The main outcomes of this project will be described in Chapters 3, 4 and 5.

- **Verification of theoretical predictions**

The bi-stability jump The standard radiation driven wind theory predicts the terminal flow velocity to be proportional to the escape velocity with a proportionality constant being dependent on the power law exponent of the line-strength distribution functions (see Eq. 1.10). Since the steepness of the line strength distribution function depends on the physical nature of the driving lines, the proportionality constant may also depend on it.

Recent calculations (Vink et al. 1999, 2000) have furthermore shown that at $T_{\text{eff}} \sim 25\,000$ K a drastic change in the ionization stage of the dominant metal species in the wind (from Fe IV to Fe III) should

appear. This would lead to an abrupt decrease in the v_∞/v_{esc} ratio at these temperatures, followed by a dramatic increase in \dot{M} . Due to similar reasons, a second jump is predicted to appear at about 10 000 K.

The predictions of Vink et al. are qualitatively consistent with earlier observations (Lamers et al. 1995) which revealed the presence of a dramatic decrease in the terminal flow velocity from $v_\infty = 2.6v_{\text{esc}}$ for SGs of $T_{\text{eff}} \geq 21$ kK to $v_\infty = 1.3v_{\text{esc}}$ for those cooler than 21 kK. This phenomenon is called a *bi-stability jump* (Pauldrach & Puls 1990). Since the temperature scale of OB stars is expected to change due to the inclusion of metal line opacities into the model calculations, and since new more accurate measurements of v_∞ are available, a re-determination of the parameters of the jump is required. In addition, the temperature behaviour of \dot{M} , have to be examined and compared to the Vink predictions.

Wind momentum Luminosity Relationship The CAK theory predicts the mass loss rate of hot stars to depend strongly on luminosity (Eq. 1.11). Unfortunately, due to the additional dependence of \dot{M} on the effective mass, a stellar parameter that may be highly uncertain for single stars, this relation cannot be directly used as a diagnostic tool. Aiming to overcome this difficulty Kudritzki et al. (1995) have introduced the so-called “modified wind momentum rate”, D_{mom} , by means of which they derived the following expression, known as the “*Wind-momentum Luminosity Relationship*”(WLR):

$$\log D_{\text{mom}} = \log(\dot{M}v_\infty R_\star^{\frac{1}{2}}) = x \log L + D \quad (1.13)$$

where R_\star is expressed in R_\odot , L_\star - in L_\odot , $x = \frac{1}{\alpha} = 2/3$, and the offset D depends on the flux-weighted number of driving lines, N_{eff} .

One of the most important and exciting aspects of the concept of the WLR is that if properly calibrated this relation might serve as a tool to determine luminosities and thus, distances by means of purely spectroscopic diagnostics. First results with respect to this possibility seem very promising, but certain discrepancies between observed and predicted wind momenta of OB-stars have been established which need to be additionally investigated (see, e.g., Puls et al. 1996; Kudritzki et al. 1999).

Motivated by these prospectives, a detailed investigation of the properties of the WLR for Galactic O-stars and B-SGs was performed using original data as well as similar data from other investigations. The empirical results were confronted with the calculations to test the theory and to validate the predictions. The main outcomes of these investigations will be outlined in Chapters 2 and 6.

1.6.2 Approaches and methods used

The line of approach is both theoretical and empirical. The empirical part, which constitutes the major part of this thesis, is concerned with the analysis of a large number of OB stars in our Galaxy. Part of

the used spectral and photometric data were collected at the National Astronomical Observatory (NAO, Bulgaria) while other parts were secured at various observatories all over the world. In particular, spectral observations were obtained at the European South Observatory (ESO), Ritter Observatory (USA), Tartu Astrophysical Observatory (Estonia) and Catania Observatory (Italy). Photometric data were obtained with the two Automatic Photometric Telescopes located in Arizona (USA) and with the 0.4m telescope at the University of Toronto, Canada. Radio data were secured at the Very Large Area (VLA) within the context of a NATO project. IR fluxes were collected at the Crimean Station of the Sternberg Astronomical Institute (Russia) while mm-data were obtained with the SCUBA space observatory. The data were analyzed utilizing state-of-the-art methods of quantitative spectral analysis, model atmosphere analysis, time-series analysis, periodic analysis etc.

The theoretical approach includes: a modification of the approximate method of Puls et al. (1996) to account for the effects of line blocking/blanketing (Sect. 2.1); calculations of NLTE line blanketed wind models to study the properties of Galactic B-supergiants (Sect. 2.2); a modification of the TVS method of Fullerton, Gies & Bolton (1996) to account for the effect of line emission, and a development of a statistical approach to investigate wind variability in O-stars, as traced by H_α (Sect. 3.5); an approximate treatment of wind clumping and its effect on the energy distribution of O-stars (Sect.3.5.5) and etc.

The outline of the thesis is as follows.

In **Chapter 2**, I will focus on the derivation of the “blanketed” stellar and wind parameters of a large sample of OB stars using a modified version of the approximate method of Puls et al. (1996) based on H_α alone (Sect. 2.1), and using the method of complete spectral analysis as implemented in the state-of-the-art model atmosphere code FASTWIND (Sect. 2.2). The new empirical data will be used to investigate and evaluate the effects of line blocking/blanketing on the observed properties of these stars. In addition, the corresponding Wind-momentum Luminosity Relationships will be constructed and used to examine the empirical dependence of hot star wind properties of T_{eff} and $\log g$.

In **Chapters 3**, the outcomes of two long-term, international monitoring campaigns to study wind variability and structures in OB-stars, and their possible relationship to processes in the stellar photosphere, will be outlined and largely discussed (Sections 3.1, 3.3 and 3.4). Also, a statistical approach to detect and quantify variations in line profiles affected by wind emission will be announced and used to study the dependence of wind variability, as traced by H_α , on the stellar and wind parameters of O-stars (Sect. 3.5).

In **Chapter 4**, the main results of a long-term optical (spectroscopic and photometric) survey of the LBV P Cygni will be described with particular emphasis on three general issues: (i) the nature and origin of the emission line spectrum (Sect. 4.3); the large diversity of variability patterns identified in the spectral

and photometric behaviour of the star, and their possible interrelations and interpretations (Sect. 4.4); (iii) the discovery of the short S Dor phase (Sect. 4.5).

In **Chapter 5**, the clumping properties of a large sample of Galactic O stars will be investigated combining our own and archival data for H_α , IR, mm and radio fluxes, and using approximate methods, calibrated to more sophisticated models. Our findings will be compared with theoretical predictions, and the implications will be discussed in detail, by assuming different scenarios regarding the still unknown clumping properties of the outer wind.

In **Chapter 6**, original results about the properties of the bi-stability jump at spectral type B1 (Sect. 6.2), the WLR of O stars and B-SGs (Sect. 6.3), the wind efficiency of OB stars (Sect. 6.4), and the properties of wind clumping in O stars (Sect. 6.5) will be confronted to theoretical predictions to check our standard picture of radiation driven winds.

Finally, in **Concluding remarks and future perspectives**, I will briefly comment on several issues following from our and similar investigations, which have been recognized from the massive star community as ones of the most prominent challenges in the present-day hot star wind research. In addition, I will also provide an overview of the **Main Results and achievements**, and a **List of the publications** underlying the thesis.

Chapter 2

“Blanketed” properties of OB stars

In this chapter I’m going to outline original results about global wind properties of Galactic OB stars derived by means of two diagnostic methods: an approximate method based on the analysis of H α line alone (Sect. 2.1), and a modern-era method of a complete spectral analysis (Sect. 2.2). Both of these methods account for the effects of line blocking and blanketing, and the wind effects.

2.1 Approximate method to determine O-star wind parameters

It is a well-known fact that due to uncertain distances, the error bars in \dot{M} - estimates for individual objects, at least in our Galaxy, are rather large. To diminish the uncertainty, one has to investigate a (very) large sample of stars. The computational effort to analyze the spectra of even *one* star, however, is extremely large, so that the application of the modern-era methods of complete spectral analysis becomes rather problematic.

In order to find a suitable resolution to this problem, we decided to investigate the following question: to what extent can the analysis of the H α profile *alone* provide results consistent with those originating from a complete spectral analysis? In case of reasonable agreement, such an analysis can be used at least in two ways: first, valuable information can be added to complement smaller samples, which have been analyzed in a detailed way by using already available H α spectra (or spectra with missing strategic lines). Second, from such an analysis targets for follow-up observations can be selected, particularly for investigations in the radio and IR band (see Chapter 5).

2.1.1 Sample stars and observational material

Our investigation is based on a sample of 29 stars with spectral classes from O4 to O9.7 including 22 supergiants, one bright giant, 3 normal giants and 3 dwarfs. The stars are listed in Table 2.1 together

with the adopted spectral types and luminosity classes (Column 2), clusters or association membership (Column 3), visual magnitudes and $(B - V)$ colours (Columns 4 and 5), extinction ratio R and distances (Column 6 and 7), and absolute magnitudes, M_V (Column 8).

Spectral types and luminosity classes for the majority of stars are taken from the works of Walborn (1971, 1972, 1973). For HD 24912, however, we adopt a luminosity class I instead of III as assigned by Walborn, in agreement with Herrero et al. (1992). For the two stars without a classification by Walborn, BD+56739 and HD 338926, spectral types and luminosity classes originate from Hiltner (1956) and from Hiltner & Iriarte (1955), respectively.

Cluster and association membership are from Humphreys (1978), from Garmany & Stencel (1992), and from Lennon et al. (1992, HD 30614). For all but two stars, HD 66811 and HD 30614, distances adopted by Humphreys (1978) have been used. In these two exceptional cases, distances are taken from the Galactic O Stars Catalogue (Cruz-Gonzalez et al. 1974). To check the stars for spectroscopic binarity we consulted the list of Gies (1987).

To avoid possible inconsistencies when adopting absolute magnitudes from different sources, we recalculated the M_V of our targets using photometry and colours from *Hipparcos* (columns 4 and 5 of Table 2.1) combined with a mean intrinsic colour $(B - V)_0 = -0.31$ and -0.28 for stars of luminosity classes V/III and I, respectively (Fitzgerald 1970; Wegner 1994), and an extinction law with $R = 3.1$, again, with the distances as mentioned above.

For stars in several associations, individual estimates of the distance and/or R turned out to be available in the literature (Cardelli 1988; Clayton & Cardelli 1988; Cardelli et al. 1989). To address the effects of using different radii on the resulting mass-loss and wind-momentum rates, these data were also taken into account when calculating M_V . Since for the majority of stars the obtained M_V -values agree within ± 0.3 with those published by Howarth & Prinja (1989), this value was adopted as a typical error for our M_V -estimates.

Observational material The study bases on H_α spectra obtained with the Coudé spectrograph of the 2m RCC telescope at the National Astronomical Observatory (NAO), Bulgaria. The project started in 1997 with an ELECTRON CCD with 520 x 580 pixels of 22 x 24 μ as detector. Beginning in the fall of 1998, we used a PHOTOMETRIC CCD with a pixel area of 1024 x 1024 and a pixel size of 24 μ . With the former configuration approximately 115 Å can be observed in one exposure with a resolution of $R = 15\,000$, while with the latter one the spectrum coverage is approximately 200 Å, again with a resolution of 15 000. Few more spectra were taken in April 1998 using a SBIG ST6 Thomson CCD with an area of 375 x 242 pixels and a pixel size of 23 x 27 μ . The resolution of these spectra is 15 000 over a spectral range of 72 Å.

Table 2.1: Spectral types and photometric data of the studied stars. For objects with more than one entry, see footnote below and text.

Star HD	Spec. type	Assoc.	m_V mag	B-V mag	R	d kpc	M_V mag
HD 190 429A	O4If+	CygOB3	6.62	0.148	3.1	2.29	-6.51
HD 66 811	O4I(n)f	Gum Nebula	2.21	-0.269	3.1	0.46	-6.14
HD 66 811 ⁽²⁾		field			3.1		-6.40*
HD 66 811 ⁽⁴⁾		runaway			3.1	0.73	-7.14
HD 16 691	O4If	PerOB1	8.69	0.411	3.1	2.29	-5.25
HD 16 691 ⁽¹⁾		PerOB1			2.8	2.29	-5.04
HD 16 691 ⁽³⁾		runaway			3.1		-6.40*
HD 14 947	O5If+	PerOB1	8.03	0.389	3.1	2.29	-5.84
HD 14 947 ⁽¹⁾		PerOB1			2.8	2.29	-5.64
HD 14 947 ⁽²⁾		field			3.1		-6.90*
HD 210 839	O6I(n)f	CepOB2	5.05	0.192	3.1	0.83	-6.01
HD 210 839 ⁽¹⁾		CepOB2			2.76	0.83	-5.85
HD 210 839 ⁽²⁾		runaway			3.1		-6.60*
HD 42 088	O6.5V	GemOB1	7.55	0.014	3.1	1.51	-4.35
HD 42 088 ⁽⁵⁾		GemOB1			3.1	2.00	-4.96
HD 54 662	O6.5V	CMaOB1	6.23	-0.018	3.1	1.32	-5.28
HD 192 639	O7Ib(f)	CygOB1	7.12	0.279	3.1	1.82	-5.91
HD 193 514	O7Ib(f)	CygOB1	7.42	0.392	3.1	1.82	-5.96
HD 34 656	O7II(f)	AurOB1	6.79	0.00	3.1	1.32	-4.68
HD 34 656 ⁽⁶⁾		AurOB2			3.1	3.02	-6.64
HD 47 839	O7V((f))	MonOB1	4.66	-0.233	3.1	0.71	-4.83
HD 24 912	O7.5I(n)((f))	PerOB2	3.98	0.016	3.1	0.40	-4.95
HD 24 912 ⁽¹⁾		PerOB2	3.98		3.24	0.40	-4.99
HD 24 912 ⁽²⁾		runaway			3.1		-6.70*
HD 36 861	O8III((f))	OriOB1	3.39	-0.160	3.1	0.50	-5.57
HD 36 861 ⁽¹⁾		OriOB1			5.0	0.50	-5.85
HD 210 809	O9Iab	CepOB1	7.56	0.010	3.1	3.47	-6.04
HD 207 198	O9Ib/II	CepOB2	5.94	0.312	3.1	0.83	-5.49
HD 207 198 ⁽¹⁾		CepOB2			2.76	0.83	-5.29
HD 37 043	O9III	OriOB1	2.75	-0.210	3.1	0.50	-6.05
HD 37 043 ⁽¹⁾		OriOB1			5.0	0.50	-6.24
HD 24 431	O9III	CamOB1	6.74	0.349	3.1	1.00	-5.30
HD 24 431 ⁽¹⁾		CamOB1			3.51	1.00	-5.57
HD 16 429	O9.5I/II	CasOB6	7.70	0.530	3.1	2.19	-6.51
HD 30 614	O9.5Ia	NGC1502	4.26	-0.008	3.1	0.95	-6.47
HD 30 614 ⁽²⁾		runaway			3.1		-6.00*
HD 209 975	O9.5Ib	CepOB2	5.07	0.240	3.1	0.83	-6.14
HD 209 975 ⁽¹⁾		CepOB2			2.76	0.83	-5.96
HD 18 409	O9.7Ibe	CasOB6	8.37	0.419	3.1	2.19	-5.50
HD 17 603	O7.5Ib(f)	field	8.49	0.551	3.1		-6.70*
HD 225 160	O8Ib(f)	field	8.19	0.260	3.1		-6.40*
HD 338 926	O8.5Ib(e?)	field	9.52	1.207	3.1		-6.60*
HD 188 209	O9.5Iab	field	5.60	-0.078	3.1		-6.00*
HD 202 124	O9.5Iab	field	7.74	0.209	3.1		-6.00*
HD 218 915	O9.5Iab	runaway	7.23	-0.026	3.1		-6.00*
BD +56 739	O9.5Ib	field	9.95	0.991	3.1		-6.00*
HD 47 432	O9.7Ib	field	6.23	0.086	3.1		-6.00*

* data corresponding to Garmany's spectral type- M_V calibration reproduced by Howarth & Prinja (1989).

- (1) – M_V computed with individual values for R (see text)
(2) – suggested to be a field/runaway star by Gies (1987)
(3) – suggested to be a runaway star by Stone (1979)
(4) – suggested to be a runaway star by Sahu & Blaauw (1993)
(5) – distance (as a member of NGC 2175 in GemOB1) given by Felli et al. (1977)
(6) – distance as a member of AurOB2 (Tovmassian et al. 1994)

2.1.2 Input parameters and mass-loss determinations

As noted in the beginning of this section, the major goal of this study is to check to what extent the analysis of H_α profiles *alone* can provide \dot{M} and β -estimates consistent with those originating from a complete spectral analysis. To this end, we employed the *approximate* method of Puls et al. (1996) which we have modified to account for the effects of line-blocking and blanketing. Since this method considers the wind physics alone requiring additional information from external photospheric diagnostics, in the following, I will describe how those input parameters that are *not* varied throughout the fit have been obtained, and how the effects of line-blocking/blanketing have been accounted for.

Effective temperatures and surface gravities (Columns 2 and 4 of Table 2.2) were determined from spectral types using *own* calibrations based on data obtained by Repolust et al. (2004) via a complete (blanketed) spectral analysis¹. In the particular case of luminosity class V stars, similar data from Martins et al. (2002) were also used to increase the statistics.

Fig 2.1 shows the derived temperature (left panel) and $\log g$ (right panel) calibrations for luminosity classes I (solid line), III (dotted line) and V (dashed line). The scatter of the T_{eff} - data around the regression lines is relatively small ($\sigma = 950, 360$ and 793 K, for lc I, III and V, respectively), while in the case of the spectral type– $\log g$ relations it is somewhat larger ($\sigma = 0.12, 0.17$ and 0.20). The reader may also note that the T_{eff} - calibration for late spectral types (later than O7) remains somewhat uncertain due to the strong influence of the specific wind-density on T_{eff} . The dotted-dashed lines overplotted in each panel represent the empirical calibrations obtained by Vacca et al. (1996) using data derived by means of pure H/He, non-LTE, plane-parallel, hydrostatic model atmospheres.

While the “blanketed” temperatures are found to be systematically lower than the unblanketed ones, our results indicate that the corresponding differences decrease with decreasing T_{eff} , being largest for luminosity class I and smallest for luminosity class V stars due to the additional wind blanketing present in supergiant atmospheres.

Concerning the $\log g$ regressions, for luminosity classes III and V no significant differences between blanketed and unblanketed models were established. For (late) supergiants an increase of less than 0.15 dex is found, in agreement with what might be expected from theory (Puls et al. (1996)).

¹Close binaries (HD 93 129A and HD 303 308, Nelan et al. 2003) and fast rotators (e.g., HD 217 086 and HD 13 268) were excluded due to a possible influence of the secondary on the “observed” temperatures and due to the effects of stellar rotation on the surface temperature distribution (gravity darkening)

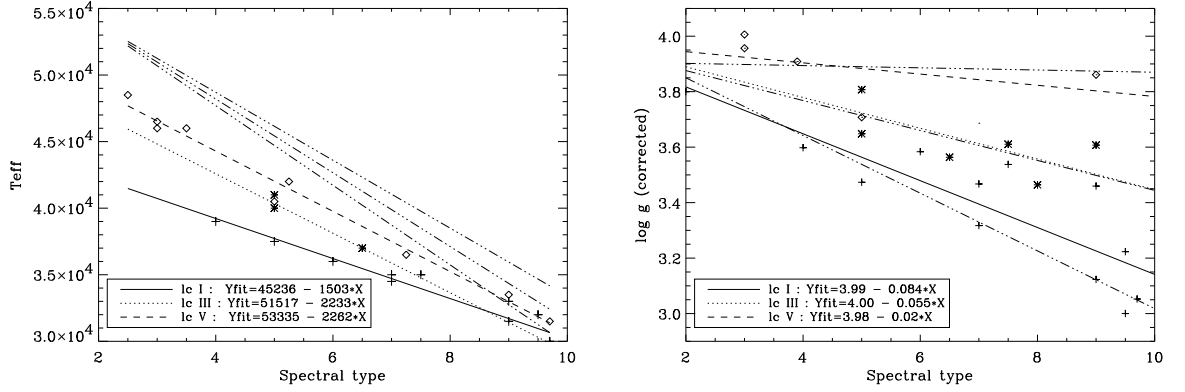


Figure 2.1: Spectral type– T_{eff} (left panel) and spectral type– $\log g$ relations for luminosity class I (bold), III (dotted) and V (dashed) derived and used in the present study. Overplotted are the corresponding data from Repolust et al. (2004) and for lc V objects in the left panel also from Martins et al. (2002): crosses – lc I, asterisks – lc III, diamonds – lc V. The dotted-dashed lines represent the empirical calibrations obtained by Vacca et al. (1996) using data derived by means of pure H/He, non-LTE, plane-parallel, hydrostatic model atmospheres. All gravities have been corrected for the effects of centrifugal forces.

Stellar radii (Column 3 of Table 2.2) have been derived from de-reddened absolute magnitudes, M_V , and the corresponding theoretical fluxes in the V-band, V_{theo} , via

$$5 \log R_{\star} = 29.58 + (V_{\text{theo}} - M_V) \quad (2.1)$$

$$V_{\text{theo}} = -2.5 \log \int_{\text{filter}} 4H_{\lambda} S_{\lambda} d\lambda \quad (2.2)$$

where H_{λ} is the theoretical Eddington flux from the calculated models ($H_{\lambda} \approx B_{\lambda}(T_{\text{rad}}) \propto T_{\text{eff}}$), and S_{λ} is the spectral response of the photospheric system (for more information see Kudritzki 1980). The theoretical fluxes have been approximated using a radiation temperature of $T_{\text{rad}} \approx 0.9 T_{\text{eff}}$ (V-band!), where this approximation results from an analysis of line-blanketed O-star model atmospheres. The typical accuracy of this approximation (which translates almost linearly into the derived radii) is of the order of 5% in the O-star domain.

Helium abundance. For those stars in common with the sample by Repolust et al., we have adopted their helium abundance. For the rest, a “normal” abundance of $Y_{\text{He}} = \text{N}(\text{He})/\text{N}(\text{H}) = 0.1$ was used as a first guess. Subsequently, this value was increased, if necessary, to obtain a better fit (with respect to the He II blend). Therefore, these values can be considered only as rough estimates.

Radial and rotational velocities For stars hotter than 35 500 K, radial velocities (not listed in Table 2.2) and projected rotational velocities $v \sin i$ (Column 6 of Table 2.2) are taken from the General Catalogue of Mean Radial Velocity (GCMRV, Barbier-Brossat & Figon 2000) and from Penny (1996), respectively.

For the rest, we obtained our own estimates for V_{sys} and $v \sin i$ fitting the He I $\lambda 6678$ absorption line with model calculations. The reliability of these estimates was checked by comparison with data from other investigations. In particular, our set of $v \sin i$ - estimates conforms quite well (within $\pm 10 \text{ km s}^{-1}$) with those from Penny (1996) for 9 out of 11 objects in common. Good agreement was also found between our set of V_{sys} - data and that of Conti et al. (1977) (within $\pm 20 \text{ km s}^{-1}$) for 13 stars in common.

Wind terminal velocities (Column 8 of Table 2.2) have been derived either by fitting UV metal lines, available from the *ines* IUE archive (<http://ines.hia.nrc.ca/ines>), with model calculations, or by interpolating various estimates available in the literature (Haser 1995; Howarth et al. 1997; Lamers et al. 1995; Groenewegen et al. 1989). For several stars v_{∞} - data derived by means of the spectral type – v_{∞} calibrations of Kudritzki & Puls (2000) were also used.

Radiation temperatures at H_{α} and photospheric profiles. To account for the effects of line blanketing, we have used a value of $T_{\text{rad}} = 0.91 T_{\text{eff}}$ for luminosity class I objects, and $T_{\text{rad}} = 0.86 T_{\text{eff}}$ for the other luminosity classes, where these values originate from a calibration of a large grid of (line-blanketed) model fluxes. (For unblanketed model atmospheres this value is of the order of $0.77 T_{\text{eff}}$ (cf. Puls et al. 1996).)

In principle, the *photospheric input profiles* have to be recalculated as well. Because of the insensitivity of the Balmer lines to changes in T_{eff} in the *O-star domain*, however, we employed the same (unblanketed) grid of photospheric profiles as described in Puls et al. (1996), evaluated at the “new” effective temperatures, of course.

Wind minimum velocity, v_{min} , and the electron temperature, T_e Following Puls et al., we adopt $v_{\text{min}} = 1 \text{ km s}^{-1}$ and $T_e = 0.75 T_{\text{eff}}$. These values are consistent with the parameterized run of the H/He departure coefficients, which remains roughly unaffected by blanketing effects, at least if the values of T_{rad} as cited above were used.

Determination of global wind parameters In our approach mass-loss rates, \dot{M} (Column 9 of Table 2.2), are derived from the best fit of the observed H_{α} profiles with model calculations. For stars with H_{α} in emission, also the velocity exponent β can be estimated from the line-profile fit in parallel with \dot{M} (Puls et al. 1996). In these cases (β given as italic numbers in Table 2.2), an average value of $\beta = 1.02 \pm 0.09$ was derived. For objects with H_{α} in absorption, on the other hand, $\beta = 0.8$ (as expected from theory for thin winds) was adopted as a starting value and subsequently improved, where possible.

In several cases a perfect fit to the observed H_{α} profile was not possible to be derived using the Puls et al. “standard” parameterization of the He II and H_{α} departure coefficients. In these particular cases, to improve

Table 2.2: Blanketed stellar and wind parameters of the O-star sample, as derived in the present study. Stars with more than one entry correspond to the entries in Table 2.1 and differ mainly in the adopted stellar radius and in the dependent quantities.

Bold face numbers for $\log L$ and D_{mom} indicate the preferred solution that is used in our final analysis of the WLR (“case C”, cf. Sect. 2.1.4) while italics for β mark values *derived* from emission type profiles. Modifications of departure coefficients for He II are given as *multipliers* $r_{4,6}$ to standard values from Puls et al. (1996). Modifications of departure coefficients for hydrogen are given by absolute numbers, $b_2^{\text{in}}/b_3^{\text{in}}$. “pt” indicates whether H_α is in absorption or emission.

T_{eff} in kK, L in L_\odot , $v \sin i$ and v_∞ in km s^{-1} , \dot{M} in $10^{-6} M_\odot/\text{yr}$, D_{mom} in cgs and Q in units of M_\odot/yr .

Object	T_{eff}	R_\star	$\log g$	Y_{He}	$v \sin i$	$\log L$	v_∞	\dot{M}	β	$r_4^{\text{in}}/r_6^{\text{in}}$	$b_2^{\text{in}}/b_3^{\text{in}}$	$\log D_{\text{m}}$	$\log Q$	pt
HD 190429A	39.2	20.8	3.65	0.14	135	5.97	2400	14.2	<i>0.95</i>	1.05/		29.99	-6.82	e
HD 66811	39.2	17.5	3.65	0.20	203	5.82	2300	6.4	<i>0.92</i>		/1.05	29.59	-7.06	e
HD 66811 ⁽²⁾		19.8				5.92		7.6			/1.05	29.69	-7.06	
HD 66811 ⁽⁴⁾		27.8				6.22		12.8			/1.05	29.99	-7.06	
HD 16691	39.2	11.6	3.65	0.10	140	5.46	2300	5.6	<i>0.96</i>			29.46	-6.85	e
HD 16691 ⁽¹⁾		10.6				5.38		4.9				29.38	-6.85	
HD 16691 ⁽³⁾		19.8				5.92		12.5				29.92	-6.85	
HD 14947	37.7	15.7	3.56	0.20	133	5.65	2300	7.7	<i>0.98</i>	1.15/	/1.45	29.65	-6.91	e
HD 14947 ⁽¹⁾		14.3				5.57		6.67		1.15/	/1.45	29.56	-6.91	
HD 14947 ⁽²⁾		25.6				6.08		16.0		1.15/	/1.45	30.07	-6.91	
HD 210839	36.2	17.5	3.48	0.10	214	5.68	2200	5.1	<i>1.00</i>	1.05/	2./	29.47	-7.16	e
HD 210839 ⁽¹⁾		16.3				5.62		4.6		1.05/	2./	29.41	-7.16	
HD 210839 ⁽²⁾		23.0				5.91		7.7		1.05/	2./	29.71	-7.16	
HD 42088	38.6	7.7	3.85	0.12	62	5.08	2200	0.38	0.85	1.3/		28.17	-7.75	a
HD 42088 ⁽⁵⁾		10.7				5.36		0.62		1.3/		28.45	-7.75	
HD 54662	38.6	11.9	3.85	0.12	85	5.45	2450	0.6	0.80			28.50	-7.84	a
HD 192639	34.7	17.2	3.39	0.20	110	5.59	2150	5.3	<i>1.09</i>	1.25/80		29.47	-7.13	e
HD 193514	34.7	17.6	3.39	0.10	95	5.61	2200	2.7	0.80		/1.48	29.20	-7.44	a
HD 34656	34.7	9.8	3.50	0.12	85	5.10	2150	0.62	1.09	1.5/		28.42	-7.69	a
HD 34656 ⁽⁶⁾		24.1				5.88		2.40		1.5/		29.20	-7.69	
HD 47839	37.5	9.9	3.84	0.10	62	5.24	2200	1.2	0.75			28.72	-7.41	a
HD 24912	34.0	11.2	3.35	0.15	204	5.18	2400	1.19	0.78	1.3/85		28.78	-7.50	a
HD 24912 ⁽¹⁾		11.5				5.20		1.23		1.3/85		28.80	-7.50	
HD 24912 ⁽²⁾		25.2				5.88		4.0		1.3/85		29.48	-7.50	
HD 36861	33.6	15.1	3.56	0.10	66	5.42	2400	0.8	0.80			28.67	-7.87	a
HD 36861 ⁽¹⁾		17.2				5.53		0.97				28.78	-7.87	
HD 210809	31.7	19.6	3.23	0.14	100	5.54	2100	4.5	<i>0.91</i>	1.1/		29.42	-7.29	e
HD 207198	31.7	15.2	3.23	0.12	85	5.32	2100	0.9	0.97	1.3/		28.67	-7.82	a
HD 207198 ⁽¹⁾		13.9				5.25		0.79		1.3/		28.59	-7.82	
HD 37043	31.4	19.8	3.50	0.12	120	5.54	2300	1.2	0.85	1.6/		28.89	-7.87	a
HD 37043 ⁽¹⁾		21.6				5.61		1.37		1.6/		28.97	-7.86	
HD 24431	31.4	14.0	3.50	0.12	90	5.24	2150	0.3	0.95	1.3/		28.18	-8.24	a
HD 24431 ⁽¹⁾		15.9				5.35		0.36		1.3/		28.29	-8.25	
HD 16429	31.0	24.8	3.19	0.10	80	5.71	1600	1.4	0.85	1.3/9		28.85	-7.95	a
HD 30614	31.0	24.9	3.19	0.10	100	5.71	1550	4.2	<i>1.05</i>	1.3/		29.31	-7.47	e
HD 30614 ⁽²⁾		19.6				5.51		2.9		1.3/		29.10	-7.48	
HD 209975	31.0	20.9	3.19	0.10	90	5.56	2050	1.8	0.80	1.3/	/1.42	29.03	-7.72	a
HD 209975 ⁽¹⁾		19.2				5.49		1.58		1.3/	/1.42	28.95	-7.73	
HD 18409	30.6	15.7	3.17	0.14	110	5.29	1750	1.5	0.70			28.82	-7.62	a
HD 17603	34.0	25.2	3.35	0.12	110	5.88	1900	5.90	<i>1.05</i>	1.1/		29.55	-7.33	e
HD 225160	33.0	22.4	3.31	0.12	125	5.73	1600	5.3	<i>0.85</i>	1.5/9		29.40	-7.30	e
HD 338926	32.5	22.7	3.27	0.12	80	5.72	2000	5.7	<i>1.00</i>			29.53	-7.28	e
HD 188209	31.0	19.6	3.19	0.12	87	5.51	1650	1.6	0.90	1.4/	/1.47	28.87	-7.73	a
HD 202124	31.0	19.6	3.19	0.12	140	5.51	1700	3.2	<i>1.25</i>	1.4/7		29.18	-7.43	e
HD 218915	31.0	19.6	3.19	0.12	80	5.51	2000	1.7	0.95	1.2/	/1.54	28.98	-7.71	a
BD+56 739	31.0	19.6	3.19	0.12	80	5.51	2000	2.3	0.85	1.35/	/1.33	29.02	-7.61	a
HD 47432	30.5	18.9	3.17	0.12	95	5.45	1600	1.9	<i>1.03</i>	1.4/8	/1.07	28.92	-7.64	e

the fit we were forced to “play” with the departure coefficients. The finally adopted values are listed in Columns 11 and 12 of Table 2.2. However, note that all these modifications are more or less “cosmetic”, i.e., they improve the quality of the fit, but do not affect the values of \dot{M} and β derived throughout the fitting procedure. (For more detailed information see Markova et al. 2004).

Having T_{eff} , R_{\star} , v_{∞} and \dot{M} determined as outlined above, stellar luminosities $\log L/L_{\odot}$ ($= 4\pi R_{\star}^2 \sigma T_{\text{eff}}^4$) and modified wind momentum rates D_{mom} ($= \dot{M} v_{\infty} R_{\star} / R_{\odot}^{0.5}$) were calculated and used to construct the corresponding WLR.

2.1.3 Error analysis.

In this section I will briefly describe the error analysis, an issue that is particularly important when deriving the wind-momentum luminosity relationship (see Sect. 2.1.4).

To estimate the errors in the derived stellar and wind parameters, we followed the philosophy outlined in detail by Repolust et al. (2004) with one exception though. Since in our approach T_{eff} and $\log g$ are derived from empirical calibrations, the error in these quantities is not determined by the quality of the line profile fits, but instead reflects the uncertainties in our calibrations and in the underlying data-base.

Concerning stellar radius, from Eq. 2.1 it follows that the error in this parameter can be calculated as:

$$\Delta \log R_{\star} \approx 0.2 \sqrt{(\Delta M_V)^2 + (2.5 \Delta \log T_{\text{eff}})^2} \quad (2.3)$$

$$\Delta \log T_{\text{eff}} = \log \left(1 + \frac{\Delta T_{\text{eff}}}{T_{\text{eff}}} \right) \quad (2.4)$$

With $\Delta M_V = \pm 0.3$ and $\Delta T_{\text{eff}} = \pm 1500$ K, the corresponding error in R_{\star} of our sample stars is dominated by the uncertainty in M_V , and is of the order of $\Delta \log R_{\star} \approx \pm 0.06$, i.e., roughly 15 %.

Specified in this way, the error in luminosity is given by

$$\Delta \log L \approx \sqrt{(4 \Delta \log T_{\text{eff}})^2 + (2 \Delta \log R_{\star})^2} \quad (2.5)$$

and results in $\Delta \log L \approx \pm 0.15$.

To assess the errors in \dot{M} , it is important to realize that any line-fit to H_{α} does not specify \dot{M} itself, but only the quantity $Q = \frac{\dot{M}}{R_{\star}^{1.5}}$ introduced by Puls et al. (1996). The error in this quantity is determined by:

$$\Delta \log Q = \log \left(1 + \frac{\Delta \dot{M}}{\dot{M}} \right)_{R_{\star}=\text{const}} \quad (2.6)$$

For emission profiles, where also β can be constrained from the fit, we estimated the precision of the

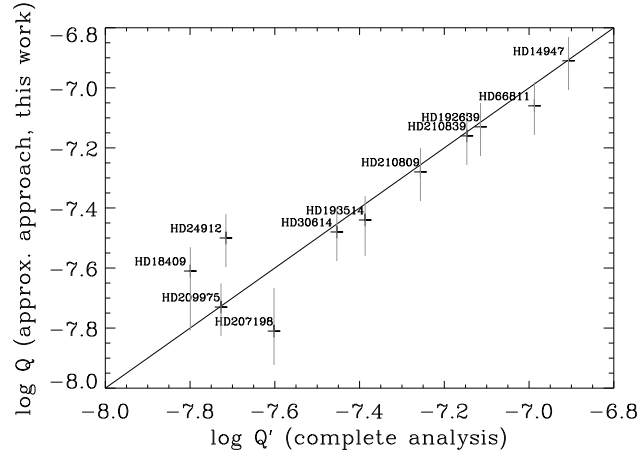


Figure 2.2: Comparison of derived Q -values from our analysis with corresponding data from Repolust et al. (2004), for eleven stars in common. The Q -values of the complete analysis have been corrected for differences in T_{eff} . Overplotted are the individual error bars calculated according to Sect. 2.1.3

derived Q as $\pm 20\%$ (from the fit quality). For absorption profiles, we have varied β typically by ± 0.1 (or more, if necessary), and obtained the corresponding upper and lower boundaries of \dot{M} (actually, of Q) from additional fits to the observed profiles. When these error estimates were smaller than the adopted error from above (i.e., $\pm 20\%$), the latter value was chosen as a conservative minimum. Note that the maximum errors in Q can reach factors of almost two for absorption profiles (the so-called β - *problem*).

From the error in Q , the uncertainty in the derived wind-momentum rate, D_{mom} , can be calculated via

$$\Delta \log D_{\text{mom}} \approx \sqrt{(\Delta \log Q)^2 + (2 \Delta \log R_{\star})^2 + (\Delta \log v_{\infty})^2}. \quad (2.7)$$

With a typical error of about $\pm 150 \text{ km s}^{-1}$ in v_{∞} , the error in $\log D_{\text{mom}}$ was estimated of the order of ± 0.15 , i.e., similar to the error in $\log L$.

2.1.4 Verifying the approximate approach

The basic outcome of our approximate analysis are the Q - and $\log D_{\text{mom}}$ - values. Now, in accordance with our primary goal, we have to convince ourselves that our estimates for these quantities are consistent with the results of the complete analysis. That way, we will particularly verify our modifications concerning the effects of line-blocking/blanketing.

Comparisons in terms of Q -values

There are 11 stars in common between our O-star sample and the one of Repolust et al. (2004) analyzed by means of the complete NLTE spectral analysis. In the following, I will use these stars as a reference to justify the validity of our approximate approach to provide reliable estimates of Q .

In their work Puls et al. (1996) have noted that any Q -value derived from H_α profiles should be almost independent of stellar parameters *if* in the underlying models the same terminal velocities were used, and *if* the influence of different effective temperatures were considered by applying a temperature correction (their Eqs. 48 and 49). For each of the eleven stars in common with Repolust et al., identical values of v_∞ have been used in the both analyses, whilst the corresponding temperatures are somewhat different. Following the procedure outlined by Puls et al. (1996), the temperatures of these stars were unified, and the two sets of $\log Q$ - values were subsequently compared.

The results of the comparison are shown in Fig. 2.2. Whilst at higher values of $\log Q$ (denser winds), the agreement is excellent (within 0.06 dex), at lower values the differences can become significant. Insofar, the above mentioned β -problem might be the source of this discrepancy, and a closer inspection of the corresponding errors (see Table 3 of Markova et al. 2004) revealed that this actually is the major source of disagreement. In many cases real variability in the strength of the studied winds seems also contribute.

Comparisons in terms of WLR

“Fine-tuning” effects Since the derived wind momenta are strongly dependent on the used redding law and the adopted distances, in our analysis we are forced to deal with more than one entry for many of our sample objects. Using these data, we can now study the consequences of “fine tuning” direct and indirect parameters entering the Wind-momentum Luminosity Relation (see Sections 1.6 and 6.3).

Let me first comment on the influence of using different values for the total to selective extinction, R . The larger R , the brighter the star is in the visual, and the larger the stellar radius. Since we are fitting for Q , the mass-loss and the wind-momentum rate also increase, as well as the (bolometric) luminosity. Even in cases of an “extreme” extinction ratio of 5.0, however, the resulting differences in R_\star and \dot{M} are small, roughly 10 to 14% of the values derived with $R = 3.1$. (Hereafter all data obtained using $R = 3.1$ will be referred to as “standard” values). The corresponding variations in $\log L$ and D_{mom} are also small, (much) smaller than the individual uncertainties for these quantities. Moreover, the corresponding shifts are found to be almost in parallel to any expected wind-momentum luminosity relationship (see Fig. 5 of Markova et al. 2004). These findings indicate that any uncertainty in R should be of minor influence on the results concerning the WLR.

To account for the total effect of the “fine tuning” on the derived WLR, various combinations of input data have been considered:

- i) Case A includes those entries without any superscript (standard, i.e., (almost) all distances from Humphreys (1978) and $R = 3.1$) plus the specific values adopted for the four “peculiar objects” (HD 16 691, HD 4 912, HD 34 656 and HD 42 088)².
- ii) Case B refers to entries with superscript 1 (individual reddening) plus “peculiar objects” plus data without superscript for the rest of the stars.
- iii) Case C combines data with superscript 2 plus “peculiar objects” plus data with superscript 1 (if no entry with superscript 2 available) plus standard values for the rest.
- iv) Case D comprises case C plus field stars.

In Fig. 2.3 the WLR based on the data-set corresponding to case D is shown. Numbers correspond to luminosity classes. Linear regressions, obtained by means of χ^2 minimization accounting for the individual errors in *both* directions, are shown as solid (l.c. I/II) and dotted (l.c. III/V) lines. We have used the conventional formulation given by Eq. 1.13, namely

$$\log D_{\text{mom}} = x \log(L/L_{\odot}) + D_0 \quad (2.8)$$

with exponent x being the inverse of α' , which corresponds to the slope of the line-strength distribution function corrected for ionization effects (Puls et al. 2000; Kudritzki & Puls 2000).

To our knowledge, this investigation together with that of Repolust et al. (2004) are the first to account for errors in both directions. We consider this type of regression as essential since the errors in $\log L$ are of the same order as those in $\log D_{\text{mom}}$, and they *are* furthermore correlated. Indeed, if we assume that the momentum rate is lower because of a smaller radius, we also have to assume that the luminosity is smaller (and vice versa), a fact not accounted for in the standard type of regression. Actually, by comparing with results from a conventional least square fit (even accounting for the specific errors in $\log D_{\text{mom}}$), we sometimes find significant differences in the regression coefficients. Only when the errors in $\log L$ are small, both methods yield similar results.

What is immediately apparent from Fig. 2.3 is that *normal giants and dwarfs show lower wind momenta (roughly by 0.3...0.5 dex) than supergiants at the same bolometric luminosity*, and that they are in good agreement with the theoretical predictions (dashed line) by Vink et al. (2000). However, note that due to the

²From a detailed investigation of the derived stellar and wind parameters of these stars we concluded that the corresponding estimates seem somewhat dubious.

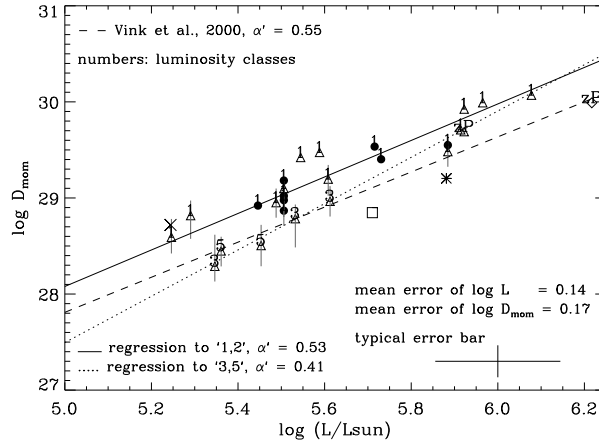


Figure 2.3: WLR for our sample of Galactic O-type stars, case D. Error bars with respect to $\Delta \log D_{\text{mom}}$ are displayed for all stars with H_{α} in absorption. The errors for the remaining objects with H_{α} in emission and the errors for $\Delta \log L$ roughly agree with the typical error bars displayed in the figures. Regressions accounting for individual errors in both co-ordinates are also shown.

Numbers 1, 3 and 5 correspond to luminosity classes I, III and V, respectively. Special symbols: “zP” corresponds to ζ Pup; the “x” denotes HD 47 839 (15 Mon, 1c V), the open square - HD 16 429 (1c I) and the asterisk - HD 34 656; circles denote the field stars.

short interval in $\log L$ covered by giants and dwarfs, the regression for luminosity III/V objects cannot be regarded as significant. Consequently, in Table 2.3 only the regression coefficients for the luminosity class I objects obtained for the different samples (A, B, C and D) are listed. Similar data from other investigations (Kudritzki & Puls 2000; Herrero et al. 2002; Repolust et al. 2004), and such predicted by theory for stars with $T_{\text{eff}} > 30\,000$ K (Vink et al. 2000), are also included for comparison.

Close inspection of the data in Table 2.3 indicates that moving from Case A to Case D the regression somewhat improves, i.e., the errors of the parameters decrease (and move towards those predicted by theory). Accounting for the fact that the positions of the field stars (case D) remain somewhat uncertain since they strongly depend on the accuracy of the empirical M_V -calibration, I will concentrate now on sample C, which appears to be the most relevant, in terms of both statistics and underlying physical assumptions.

Comparison to results from complete spectral analyses A comparison between our results (Case C) to such from other investigations shows that except for the data from Kudritzki & Puls (2000), the remaining “observational” results are rather similar. Given that the values quoted by Kudritzki & Puls (2000) have been derived by means of *unblocked* model atmospheres, and that the other three investigations either use, or rely on the same (line-blanketed) model atmosphere code, FASTWIND, these findings should not be a surprise though. On the other hand, however, the fairly good agreement between our results (case D) and those from the complete spectral analysis (Repolust et al. 2004) indicates that *the approximate approach*

Table 2.3: Coefficients of the WLR obtained for the supergiants of our sample cases A, B, C and D in comparison to results from other investigations. The values of the minimized χ^2 (not displayed here) indicate an acceptable fit in all four cases. Regression accounting for errors in both co-ordinates for case A to D and the analysis by Repolust et al.; standard least square fit for remaining entries.

Sample	$\log D_o$	x	α'
Case A	16.88±2.53	2.21±0.45	0.45±0.09
Case B	17.53±2.18	2.10±0.38	0.48±0.09
Case C	19.00±1.37	1.83±0.24	0.55±0.08
Case D	18.58±1.25	1.90±0.22	0.53±0.06
Herrero et al.	19.27±1.37	1.74±0.24	0.58±0.08
Repolust et al.	18.30±2.12	1.97±0.38	0.51±0.10
Kudritzki & Puls	20.69±1.04	1.51±0.18	0.66±0.08
Vink et al.	18.68±0.26	1.83±0.044	0.55±0.013

followed by us actually can provide compatible results in terms of both Q - values (respectively, \dot{M}) and WLR, not only qualitatively, but also quantitatively.

2.1.5 Enlarging the sample

The latter conclusion allows us to proceed in the spirit as outlined in the introduction, namely to combine our data with the data-sets from Repolust et al. (2004) for stars not in common and Herrero et al. (2002), in order to improve the statistics, and to study the WLR of Galactic O stars by means of the largest sample of stars used so far. In total, this sample comprises 19 supergiants and 15 lc III/V objects entering the regression. Again, we have accounted for the errors in both directions, with errors taken from the respective investigations. Note that the errors in the sample from Repolust et al. are dominated by the uncertainty in radius, similar to the objects from our sample. In contrast, the errors in the sample from Herrero et al. are somewhat lower, since these authors have investigated objects from *one* association only, i.e. Cyg OB2, which reduces the scatter.

The WLR for the unified O-star sample is illustrated in Fig. 2.4. Theoretical wind momenta as predicted by Vink et al. (2000) (see Sect. 6.1, Eq. 6.3) are also shown (solid line) for comparison. Obviously, *the WLR for luminosity class III/V objects strictly follows the theoretical predictions while the relation for the supergiants shows a vertical offset, corresponding now to an average factor of roughly 0.25 dex.* Note that with respect to lc III/V objects, the “unified” sample covers a much larger range in $\log L$. Thus, a more precise determination of the corresponding regression coefficients than before is possible. Note in addition that even those stars with only upper limits for D_{mom} (those with an arrow), which have *not* been included into the regression, follow the continuation of lc III/V objects - a finding that has already been discussed by Repolust et al. (2004).

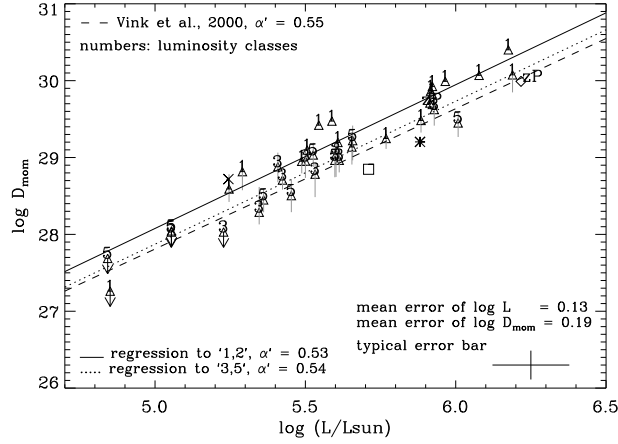


Figure 2.4: WLR for Galactic O-type stars. Sample includes our sample case C, the sample by repo04 for objects *not* in common and the sample by Herrero et al. (2002). Regression accounting for errors in both directions and appropriate correlations; errors corresponding to respective publications. All symbols as in Fig. 2.3; arrows indicate upper limits for objects with almost purely photospheric profiles which have been discarded from the regression.

Table 2.4: Coefficients of the WLR obtained for Galactic O-stars, by combining our sample case C with the results from Herrero et al. (2002) and Repolust et al. (2004) for objects not in common. Regression accounting for errors in both co-ordinates. $\chi^2/(N - 2)$ gives the “average” value of the minimized χ^2 per degree of freedom, when N is the number of objects included in the sample. “lc” denotes regression as function of luminosity class. Asterisks mark corresponding data from Repolust et al.

Sample	$\log D_0$	x	α'	$\chi^2/(N - 2)$
lc I	18.73 ± 1.13	1.87 ± 0.20	0.53 ± 0.06	0.77
lc I*	18.24 ± 1.76	1.96 ± 0.30	0.51 ± 0.08	
lc III/V	18.57 ± 1.98	1.86 ± 0.36	0.54 ± 0.10	0.66
lc III/V*	18.64 ± 1.29	1.85 ± 0.23	0.54 ± 0.07	

The results of the regression analysis for our “unified” sample, and for the “unified” sample of Repolust et al. (2004), are summarized in Table 2.4. Note in particular that the coefficients for lc I objects derived by us are closer to the values predicted by theory and affected by smaller errors (due to the improved statistics) than those obtained by Repolust et al. (2004). Note also that because of the inclusion of giants and dwarfs from our investigation, the “unified” lc III/V sample now shows a better coverage along the $\log L$ axis (with no gaps in between). The corresponding regression coefficients, however, deviate stronger from the values predicted by theory and have a somewhat larger error than those derived by Repolust et al. (2004). This finding (for weak winds) again points to the β problem discussed in Sect. 2.1.4, and may also indicate a higher sensitivity of the results on the approximations used by our method.

2.1.6 Summary

In this section I have outlined main results about wind properties of Galactic O-stars derived by mean of an approximate approach using H_α alone. One of the main objectives was to investigate the potential of this approach to provide mass-loss and wind-momentum rates, compatible to those from a complete spectral analysis. This goal has been attained in two ways: (i) by comparing the derived mass-loss rates (actually, the corresponding Q -values) to those determined by Repolust et al. (2004) via a complete NLTE spectral analysis for stars in common, and (ii) by comparing the Wind-momentum Luminosity Relationship for our sample stars to those derived by other investigators (Kudritzki & Puls 2000; Herrero et al. 2002; Repolust et al. 2004) Additionally, we studied the consequences of “fine tuning” direct and indirect parameters entering the WLR, e.g., by taking different values for stellar reddening and distance into account.

The main outcomes of this study can be summarized as follows:

- To determine \dot{M} and the velocity field exponent β , we applied the approximate method developed by Puls et al. (1996), which has been modified by us to account for the effects of metal line-blocking/blanketing. The major modification concerns the change of radiation temperature in the neighboring continuum.
- To estimate the “blanketed” T_{eff} , and $\log g$ -values of the sample stars, needed to perform the H_α profile fitting, we derived own calibrations for luminosity classes I, III and V using data from recent spectroscopic analyses of individual Galactic stars derived via NLTE atmospheric models with mass-loss, sphericity and metal line blocking/blanketing (Repolust et al. 2004; Martins et al. 2002).
- A comparison of our Q -values with those from Repolust et al. (2004) for 11 stars in common indicates that both methods give excellent agreement in those cases where the wind-emission is significant, whereas for (very) low wind-densities discrepancies may arise, which are mostly related to the problem of uncertain velocity exponents, β . Our analysis furthermore showed that not only the Q -values, but also the WLR derived by means of our approximate approach, are in good agreement to the results originating from a complete spectral analysis. Therefore, this method can be used to solve the statistical problem mentioned in the introduction when studying wind properties of Galactic O-stars.
- Based on the complete set of stellar and wind parameters, we investigated the influence of using different combinations of stellar reddening and distances (available in the literature) on the properties of the empirical WLR. In particular, this analysis indicates that using individual instead of mean values for stellar reddening causes variations in $\log L$ and D_{mom} , which are (much) smaller than the individual uncertainties for these quantities.
- Based on our original data and incorporating similar data from other investigations (Repolust et al. 2004;

Herrero et al. 2002), we studied the properties of the WLR of Galactic O stars by means of the largest sample of stars used so far. Consequently, a clear separation between the WLRs for luminosity class I objects, and those of luminosity class III/V, was established. This finding is in agreement with Repolust et al. (2004), but disagrees with results from theoretical simulations of line-driven winds (Vink et al. 2000; Puls et al. 2003), which do not find such a separation, but predict a unique relation instead. In Sect. 5 I will return to this point again.

2.2 Complete spectral analysis of B supergiants with FASTWIND

While the number of Galactic O and early B stars with reliably determined stellar and wind parameters has progressively increased during the last few years (e.g., Herrero et al. 2002; Repolust et al. 2004; Markova et al. 2004; Garcia & Bianchi 2004; Bouret et al. 2005; Martins et al. 2005; Crowther et al. 2006), mid- and late-B supergiants (SGs) are under-represented in the sample of stars investigated so far. Indeed, due to the larger variety of atomic species being visible – the most important among which is Silicon, the main temperature indicator in the optical domain – the reproduction of B-star spectra is a real challenge for state-of-the-art model atmosphere codes since it requires a good knowledge of the physics of these objects combined with accurate atomic data. On the other hand, B-SGs represent an important phase in the evolutionary sequence of massive stars, and it is therefore particularly important to increase and improve our knowledge of these objects.

In this section, I will outline the main outcomes of a project to study the physical properties of Galactic B-SGs employing modern-era methods of complete spectral analysis. One of the main goals of the project is to test and to apply the potential of the NLTE atmosphere code FASTWIND to provide reliable estimates of stellar and wind parameters of stars with T_{eff} from 30 to 11 kK. By means of these data and incorporating additional datasets from alternative studies, several important, but still open issues, such as, e.g., the effects of line-blocking/blanketing, the WLR for B SGs etc, will be addressed and investigated in detail.

Before discussing the main topic, let me first consider two other issues that might be of interest to the reader: the status-quo of the present-day quantitative spectroscopy of hot massive stars, and the FASTWIND code.

Modern-era quantitative spectroscopy of hot stars Quantitative spectroscopy is the most powerful tool to get observational constraints on the physics of various types of stars. The ultimate goal of the quantitative spectral analysis is by means of appropriate “model atmosphere”³ to reproduce the observed spectral energy distribution of a given star and to determine its fundamental stellar and wind properties.

However, to produce reliable quantitative predictions, model atmospheres have to include a realistic description of the physics involved. In this respect, modeling the atmosphere of hot massive stars is a tremendous challenge for the present day astrophysics. Indeed, due to their huge luminosities, the physics of hot star atmosphere is dominated by radiative processes, i.e. *non-LTE* effects in the entire atmosphere

³What astrophysicists understand when saying “model atmosphere” is a complete description of the behaviour of certain depth-dependent variables (e.g., temperature, pressure, density of ions and electrons, velocity fields and chemical composition) by means of which a given star, and its spectrum, can be characterized.

are important, and therefore have to be taken into account. In addition, the effects of stellar winds on the structure of the atmosphere have to be also accounted for.

While the first attempts to obtain quantitative information from the spectrum of a hot star dates back to Unsold in his *LTE* analysis of τ Scorpii, the first successful explanation of the optical spectrum of hot massive stars by means of *model atmosphere* dates to the work of Auer & Mihalas (1972), where *non-LTE* effects in a plane-parallel and hydrostatic atmosphere have been taken into account.

Since this milestone, the quantitative spectroscopy of hot massive stars has made a dramatic progress. Thanks to the enormous advancement of model atmosphere, atomic physics and radiative transfer techniques, and thanks to the exponential growth of the computational power, a new generation of model atmosphere codes have been developed, which properly account for *non-LTE* effects and the effects of stellar wind, including *metal line blocking/blanketing* and *wind clumping* (see Sect.1.6.1). These are: *CMFGEN* (Hillier & Miller 1998; Hillier et al. 2003), the *PoWR* code developed by W.R. Hamann and collaborators, the multi-purpose model atmosphere code “*PHOENIX*” (Hauschildt & Baron 1999), *WM – Basic* (Pauldrach et al. 2001), and *FASTWIND* (Santolaya-Rey et al. 1997; Puls et al. 2005). For the particular case of late-B and A-SGs, a hybrid non-LTE technique to determine their stellar and wind parameters was developed and used by Przybilla et al. (2006).

Here, it is important to realize that the calculation of *a realistic* hot star model atmosphere is a very complicate task, which requires clever numerical techniques to be developed and used. And although the problem is tractable from the mathematical point of view, none of the codes cited above is able to solve consistently, and simultaneously, the complete physics in a reasonable amount of time. Consequently, various simplifying assumptions and approximations have been introduced by the modellers to decrease the complexity of the system, and thus to reduce the computational time required.

Apart from the assumptions and approximations applied, the codes can also differ in the methods used to calculate the models. (For a brief comparison of the available codes see Puls 2008.) Presently, three such methods exist and are largely used, these are:

- i) *self-consistent* methods in which the wind structure is determined by a radiative force, calculated by means of self-consistent NLTE occupation numbers, and the corresponding radiation field. To determine the atmospheric structure and to produce the synthetic spectrum, these methods require four input parameters: T_{eff} , $\log g$, R_{\star} and chemical abundances (plus eventually clumping factors and a description of the X-rays/UV emission).
- ii) *consistent* methods where the main wind properties, \dot{M} and v_{∞} , can be adapted to fit the wind-lines by varying the force-multiplier parameters. The corresponding input parameters are T_{eff} , $\log g$,

R_\star , stellar abundances, and the force-multiplier parameters k , α and δ (plus clumping factors and description of X-ray/EUV emission (if necessary)).

- iii) *unified model atmosphere* methods where the wind structure is analytically described via a β velocity law, and a smooth transition between the wind and the quasi-hydrostatic photosphere. The input parameters here are T_{eff} , $\log g$, R_\star , chemical abundances, \dot{M} , v_∞ , β , and eventually clumping factors and description of X-ray/EUV emission. (For more detailed comments on this issue the interested reader is referred to Puls, Vink & Najarro (2008).)

The FASTWIND code Most of the results presented in this thesis have been obtained by means of the FASTWIND code (Fast Analysis of Stellar atmospheres with WIND), which calculates NLTE line blanketing model atmosphere for hot stars with winds. The method implemented in this code belongs to those described in the last item above, i.e. the code comprises the concept of *unified model atmospheres* (Gabler et al. 1989) where the photosphere is assumed to be in hydrostatic equilibrium with a velocity law following from the equation of continuity (Eq. 1.7), while near the sonic point⁴ a smooth transition to a β type velocity law of the form

$$v(r) = v_\infty \left(1 - \frac{bR_\star}{r}\right)^\beta \quad b = 1 - \left(\frac{v(R_\star)}{v_\infty}\right)^{1/\beta} \quad (2.9)$$

is made for the supersonic part of the wind. Consequently, the code can deal with extreme emission lines produced by very strong winds as well as with an entire absorption spectrum for extremely weak winds. This point is particularly important when optical (but also IR) spectra of OB stars have to be analyzed.

One of the main advantages of FASTWIND is that it is extremely fast enabling a vast amount of models to be calculated. In particular, it needs about 30 min, against several hours for *CMFGEN* or *WM-Basic*, to produce a single model. This high efficiency is obtained by applying appropriate physical approximations to certain processes where high precision is not required. A detailed and complete description of the code can be found in Puls et al. (2005).

2.2.1 Sample stars and observational material

Sample stars. Table 2.5 lists our sample stars, together with their corresponding spectral and photometric characteristics, association/cluster membership and distances. For hotter and intermediate temperature stars, spectral types and luminosity classes (Column 2) were taken from the compilation by Howarth et al. (1997), while for the remainder, data from *SIMBAD* have been used.

Since *HIPPARCOS* based distances are no longer reliable in the distance range considered here (e.g.,

⁴This is the point where the velocity equals the sound speed.

Table 2.5: Galactic B-SGs studied in this work, together with adopted photometric data. For multiple entries, see text.

Object (HD#)	spectral type	member-ship	d	V	$B - V$	$(B - V)_0$	M_V
185 859	B0.5 Ia						-7.0*
190 603	B1.5 Ia+		1.57 ^c	5.62	0.760	-0.16	-8.21
				5.62	0.54±0.02		-7.53
206 165	B2 Ib	Cep OB2	0.83 ^a	4.76	0.246	-0.19	-6.19
198 478	B2.5 Ia	Cyg OB7	0.83 ^a	4.81	0.571	-0.12	-6.93
				4.84	0.40±0.01		-6.37
191 243	B5 Ib	Cyg OB3	2.29 ^a	6.12	0.117	-0.12	-6.41
			1.73 ^b				-5.80
199 478	B8 Iae	NGC 6991	1.84 ^d	5.68	0.408	-0.03	-7.00
202 850	B9 Iab	Cyg OB4	1.00 ^a	4.22	0.098	-0.03	-6.18
212 593	B9 Iab						-6.5*

^a Humphreys (1978); ^b Garmany & Stencel (1992); ^c Barlow & Cohen (1977);

^d Denizman & Hack (1988)

* from calibrations (Humphreys & McElroy 1984)

de Zeeuw et al. 1999; Schröder et al. 2004), photometric distances collected from various sources in the literature have been adopted (Column 4). In particular, for stars members of OB associations, we drew mainly from Humphreys (1978), but also consulted the lists published by Garmany & Stencel (1992), and by Barlow & Cohen (1977). In most cases, good agreement between the three datasets was found, and only for Cyg OB3 did the distance modulus provided by Humphreys turned out to be significantly larger than that provided by Garmany & Stencel. In this latter case, two entries for d are given in Table 2.5.

Apart from those stars belonging to the OB associations, there are two objects in our sample which have been recognised as cluster members: HD 190 603 and HD 199 478. The former was previously assigned as a member of Vul OB2 (e.g., Lennon et al. 1992), but this assignment has been questioned by McErlean et al. (1999) who in turn adopted a somewhat arbitrary distance of 1.5 kpc. This value is very close to the estimate of 1.57 kpc derived by Barlow & Cohen (1977), and it is this latter value which we will use in the present study. For the second cluster member, HD 199 478, a distance modulus to its host cluster as used by Denizman & Hack (1988) was adopted.

Visual magnitudes, V , and $B - V$ colours (Column 5 and 6) have been taken from the *HIPPARCOS Main Catalogue (I/239)*. While for the majority of sample stars the *HIPPARCOS* photometric data agree quite well with those provided by *SIMBAD*, for two of them (HD 190 603 and HD 198 478) significant $B - V$ differences were found. In these latter cases two entries for $B - V$ are given, where the second one represents the mean value averaged over all measurements listed in *SIMBAD*.

Absolute magnitudes, M_V (Column 8), were calculated using the standard extinction law with $R = 3.1$ combined with intrinsic colours, $(B - V)_0$, from Fitzpatrick & Garmany (1990) (Column 7), and distances,

V and $B - V$ magnitudes as described above. For two stars which do not belong to any cluster/association (HD 185 859 and HD 212 593), absolute magnitudes according to the calibration by Humphreys & McElroy (1984) have been adopted.

For the majority of cases, the absolute magnitudes we derived, agree within ± 0.3 mag with those provided by the Humphreys-McElroy calibration. Thus, we adopted this value as a measure for the uncertainty in M_V for cluster members (HD 199 478) and members of spatially more concentrated OB associations (HD 198 478 in Cyg OB7, see Crowther et al. 2006). For other stars with known membership, a somewhat larger error of ± 0.4 mag was adopted to account for a possible spread in distance within the host association. Finally, for HD 190 603 and those two stars with calibrated M_V , we assumed a typical uncertainty of $\Delta M_V = \pm 0.5$ mag, representative for the spread in M_V of OB stars within a given spectral type (Crowther 2004).⁵

Observations and data reduction. High-quality ($R = 15\,000$ and $S/N \sim 200$ to 300) optical spectra for the sample stars were collected using the Coudé spectrograph of the NAO 2-m telescope of the Institute of Astronomy, Bulgarian Academy of Sciences. Since our spectra sample about 200 \AA , five settings were used to cover the ranges of interest, from $4\,100$ to $4\,900 \text{ \AA}$, plus H_α . To minimise the effects of temporal spectral variability (if any), all spectra referring to a given star were taken one after the other, with a time interval between consecutive exposures of about half an hour. Thus, we expect our results to be only sensitive to temporal variability of less than 2 hours. The spectra were reduced following standard procedures, and using the corresponding IRAF⁶ routines.

2.2.2 Determination of stellar and wind parameters

To allow for an initial assessment of the stellar and wind parameters, a coarse grid of FASTWIND models (appropriate for the considered targets) was used. The grid involves 270 models covering the temperature range between 12 and 30 kK (with increments of 2 kK), and including $\log g$ values from 1.6 to 3.4 (with increments of 0.2 dex). An extended range of wind-densities, as combined in the optical depth invariant Q ($= \dot{M} / (v_\infty R_\star)^{1.5}$, cf. Puls et al. 1996) has been accounted for as well, to allow for both thin and thick winds.

All models have been calculated assuming solar Helium ($Y_{\text{He}} = 0.10$, with $Y_{\text{He}} = N(\text{He})/N(\text{H})$) and Silicon abundance ($\log(\text{Si}/\text{H}) = -4.45$ by number⁷, cf. Grevesse & Sauval 1998 and references therein), and a micro-turbulent velocity, v_{mic} , of 15 km s^{-1} for hotter, and 10 km s^{-1} for cooler subtypes, with a

⁵For a hypergiant such as HD 190 603 this value might be even higher.

⁶The IRAF package is distributed by the National Optical Astronomy Observatories, which is operated by the Association of Universities for Research in Astronomy, Inc., under contract with the National Sciences Foundation.

⁷According to latest results (Asplund et al. 2005), the actual solar value is slightly lower, $\log(\text{Si}/\text{H}) = -4.49$, but such a small difference has no effect on the quality of the line-profile fits.

Table 2.6: Radial velocities (from Si), projected rotational velocities, macro- and micro-turbulent velocities (all in km s^{-1}) and Si abundances, given as $\log [N(\text{Si})/N(\text{H}) + 12]$, of the sample stars as determined in the present study. The number in brackets refers to the number of lines used to derive $v \sin i$ and v_{mac} .

Object	Sp	V_r	$v \sin i$	v_{mac}	v_{mic}	Si abnd
HD 185 859	B0.5 Ia	12	62(5)	58(3)	18	7.51
HD 190 603	B1.5 Ia+	50	47(8)	60(3)	15	7.46
HD 206 165	B2 Ib	0	45(7)	57(3)	8	7.58
HD 198 478	B2.5 Ia	8	39(9)	53(3)	8	7.58
HD 191 243	B5 Ib	25	38(4)	37(3)	8	7.48
HD 199 478	B8 Iae	-12	41(4)	40(3)	8	7.55
HD 212 593	B9 Iab	-13	28(3)	25(3)	7	7.65
HD 202 850	B9 Iab	13	33(3)	33(3)	7	7.99

border line at 20 kK.

By means of this model grid, initial estimates on T_{eff} , $\log g$ and \dot{M} were obtained for each sample star. These estimates were subsequently used to construct a smaller subgrid, specific for each target, to derive the final, more exact values of the stellar and wind parameters (including Y_{He} , $\log (\text{Si}/\text{H})$ and v_{mic}).

Radial velocities. To compare observed with synthetic profiles, radial velocities and rotational speeds of all targets have to be known. Radial velocities from the General Catalogue of Mean Radial Velocities (III/213, Barbier-Brossat & Figon 2000) were used as a first step. These values were then modified (if necessary) to obtain better fits to the analyzed metal lines. (Helium or Hydrogen lines were discarded since they might be influenced by (asymmetrical) wind absorption/emission.) The finally adopted V_r -values are listed in Column 3 of Table 2.6. The accuracy of these estimates is typically $\pm 2 \text{ km s}^{-1}$.

Projected rotational velocities and macro-turbulence. As a first guess, $v \sin i$ -values obtained by means of the Spectral type – $v \sin i$ calibration for Galactic B-type SGs (Abt et al. 2002) were used. However, during the fitting procedure we found that these values provide poor agreement between observed and synthetic profiles, and that to improve the fits an additional line-broadening must be introduced and used. These findings are consistent with similar results from earlier investigations claiming that absorption line spectra of O stars and B SGs exhibit a significant amount of broadening in excess to the rotational broadening (Rosenhald 1970; Conti & Ebbets 1977; Lennon et al. 1993; Howarth et al. 1997). And although the physical mechanism responsible for this additional line-broadening is still not understood, I will follow Ryans et al. (2002) and will refer to it as “macro-turbulence”.

Since the influence of macro-turbulence, v_{mac} , is similar to those caused by axial rotation, and since stellar rotation is a key parameter for stellar evolution calculation (e.g., Meynet & Maeder 2000; Hirschi et al. 2005b), it is particularly important to distinguish between the individual contributions of these two

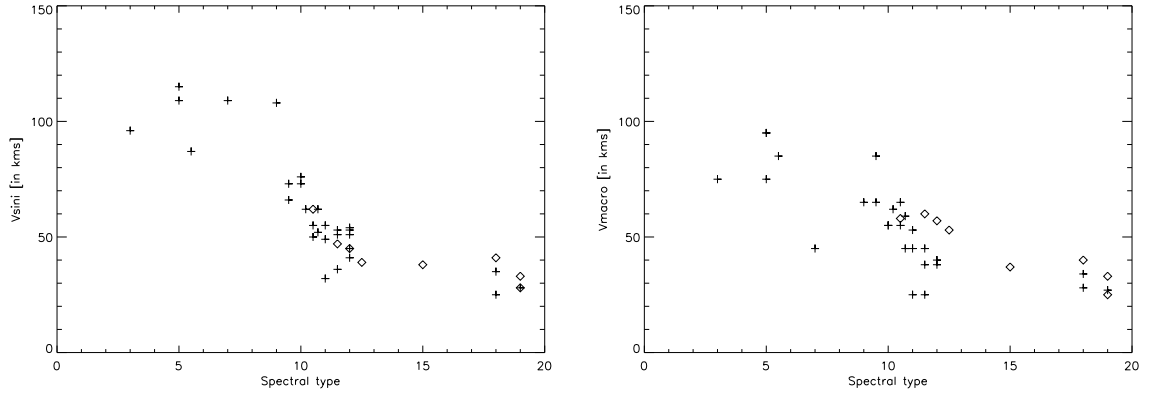


Figure 2.5: Projected rotational (left panel) and macro-turbulent (right panel) velocities of OB-SGs (spectral types refer to O-stars, i.e., 10 corresponds to B0 and 20 to A0). Our determinations are marked with diamonds while crosses refer to published data (Dufton et al. 2006; Simon-Diaz & Herrero 2007).

processes. To this end, we used the implementation of the FT technique as developed by Simon-Diaz & Herrero (2007) (based on the original method proposed by Gray 1973, 1975), and applied it to a number of preselected absorption lines. The obtained pairs of $(v \sin i, v_{\text{mac}})$, averaged over the measured lines, were then used as input parameters for the fitting procedure, and subsequently modified to improve the fits. The finally adopted values of $v \sin i$ and v_{mac} are listed in Columns 4 and 5 of Table 2.6, respectively. Numbers in brackets refer to the number of lines used for this analysis. The uncertainty of these estimates is typically less than $\pm 10 \text{ km s}^{-1}$, being largest for those stars with a relatively low rotational speed, due to the limitations given by the resolution of our spectra ($\sim 35 \text{ km s}^{-1}$).

Although the sample size is small, the $v \sin i$ - and v_{mac} - data listed in Table 2.6 indicate that:

- in none of the sample stars is rotation alone able to reproduce the observed line profiles (width and shape).
- both $v \sin i$ and v_{mac} decrease towards later subtypes (lower T_{eff}), being about a factor of two lower at B9 than at B0.5.
- independent of spectral subtype, the size of the macro-turbulent velocity is similar to the size of the projected rotational velocity.
- also in all cases, v_{mac} is well beyond the speed of sound.

Compared to similar data from other investigations for stars in common (e.g. Rosenhald 1970; Howarth et al. 1997), our $v \sin i$ - estimates are always smaller, by up to 40%, which is understandable since these earlier estimates refer to an interpretation in terms of rotational broadening alone.

On the other hand, and within a given spectral subtype, our estimates of $v \sin i$ and v_{mac} are consistent with those derived by Dufton et al. (2006) and Simon-Diaz & Herrero (2007) (see Figure 2.5). From these data, it is obvious that both $v \sin i$ and v_{mac} appear to decrease (almost monotonically) in concert, when

proceeding from early-O to late-B types.

Basic stellar parameters

Effective temperatures, T_{eff} . To estimate effective temperature we exploited the Silicon ionization balance involving the Si II features at $\lambda\lambda 4129, 4131$, the Si III features at $\lambda\lambda 4553, 4568, 4575$ and at $\lambda\lambda 4813, 4819, 4828$, with a preference on the first triplet (for more details see Markova & Puls 2008), and the Si IV feature at $\lambda 4116$.

For stars of spectral type B2 and earlier, Helium can also be used as an additional check on T_{eff} . Thus, He I transitions at $\lambda\lambda 4471, 4713, 4387, 4922$, and He II transitions at $\lambda\lambda 4200, 4541, 4686$, were also analysed.

Column 2 of Table 2.7 lists all effective temperatures as derived in the present study. These estimates are influenced by several processes and estimates of other quantities, among which are micro- and macro-turbulence, He and Si abundances, surface gravity and mass-loss rate (see below). Nevertheless, we are quite confident that, to a large extent, we have consistently and partly independently (regarding v_{mic} , v_{mac} and Si abundances) accounted for these influences. Thus, the error in our T_{eff} - estimates should be dominated by uncertainties in the fitting procedure, amounting to about ± 500 K. Of course, these are differential errors assuming that physics complies with all our assumptions, data and approximations used within our atmosphere code.

Micro-turbulent velocities and Si abundances. Recent studies have shown that the introduction of a non-vanishing velocity, called “micro-turbulence”, can significantly improve the agreement between synthetic profiles and observations (McErlean et al. 1998; Smith & Howarth 1998). However, some stellar properties, such as, e.g., abundances, T_{eff} and $\log g$ might also be significantly modified by micro-turbulence. For O-stars, these effects were proven to be relatively small (see Villamariz & Herrero 2000). For B-type stars, however, this issue has been investigated for several individual objects only.

Motivated by the above outlined, we decided to investigate the influence of micro-turbulence on the derived effective temperatures for the complete range of B-type SGs. To this end, we calculated a sub-grid of FASTWIND models with v_{mic} ranging from 4 to 18 km s⁻¹ (with increments of 4 km s⁻¹), and $\log Q$ values corresponding to the case of relatively weak winds. This sub-grid was then used to study the behaviour of the SiIV4116/SiIII4553 and SiIII4128/SiIII4553 line ratios, which are the main temperature indicators in the B-star domain.

The obtained results, illustrated in Fig. 2.6, show that within the temperature ranges of interest ($18 \leq T_{\text{eff}} \leq 28$ kK for SiIV/SiIII and $12 \leq T_{\text{eff}} \leq 18$ kK for SiII/SiIII), the differences caused by vari-

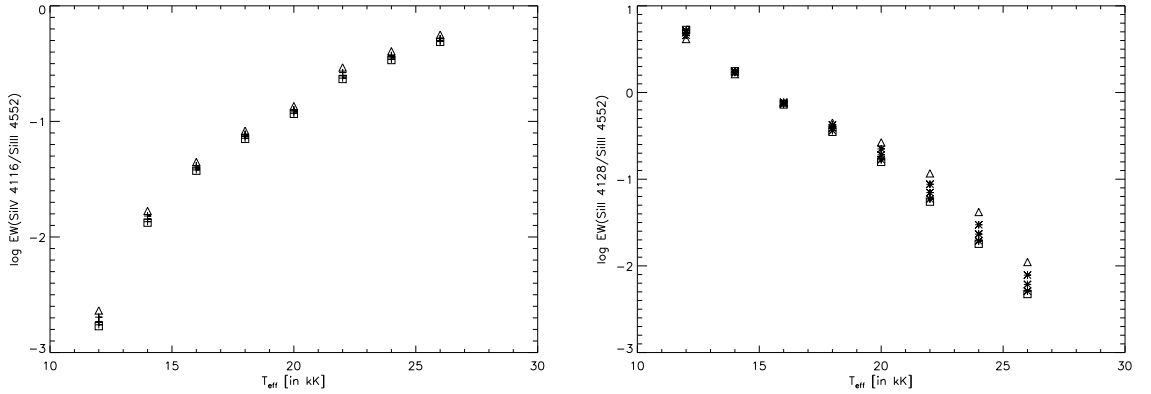


Figure 2.6: Effects of micro-turbulence on the strength of Si IV 4116/Si III 4553 (left panel) and Si II 4128/Si III 4553 (right panel) equivalent width ratios for B-type SGs. Triangles refer to the lowest value of $v_{\text{mic}} = 4 \text{ km s}^{-1}$, squares to the highest one - 18 km s^{-1} (see text).

ous v_{mic} are relatively small, resulting in temperature differences lower than 1 000 K, i.e., within the limits of the adopted uncertainties (see below).

Based on these results, we relied on the following strategy to determine T_{eff} , v_{mic} and Si abundances. As a first step, we used the FASTWIND model grid, as described previously, to put initial constraints on the stellar and wind parameters of the sample stars. Then, by varying T_{eff} (but also $\log g$, \dot{M} and the velocity exponent β) within the derived limits, and by changing v_{mic} within $\pm 5 \text{ km s}^{-1}$ to obtain a satisfactory fit to most of the strategic Silicon lines, we fixed $T_{\text{eff}}/\log g$ and derived rough estimates of v_{mic} . Final v_{mic} - values and Si abundances then follow from the following procedure: for each sample star a grid of FASTWIND models was calculated, combining four abundances and five values of micro-turbulence (ranging from 10 to 20 km s^{-1} , or from 4 to 12 km s^{-1} , to cover hot and cool stars, respectively). By means of this grid, then we determined those abundance ranges which reproduce the observed individual EWs (within the corresponding errors) of several previously selected Si lines from different ionization stages. Subsequently, we sorted out the value of v_{mic} which provides the best overlap between these ranges,

In Column 6 and 7 of Table 2.6, our final values for v_{mic} and Si abundance are given. The error of these estimates depends on the accuracy of the measured equivalent widths (about 10%) and is typically about $\pm 2 \text{ km s}^{-1}$ and $\pm 0.15 \text{ dex}$ for v_{mic} and the logarithmic Si abundance, respectively. A closer inspection of these data indicates that v_{mic} of B-type SGs might be closely related to spectral type (see also McErlean et al. 1999), being highest at earlier (18 km s^{-1} at B0.5) and lowest at later B subtypes (7 km s^{-1} at B9). Interestingly, the latter value is just a bit larger than the typical values reported for A-SGs (3 to 8 km s^{-1} , e.g., Venn 1995), thus implying a possible decline in micro-turbulence towards even later spectral types.

Table 2.7: Final results for our sample of Galactic B-SGs derived using FASTWIND. T_{eff} in kK, R_{\star} in R_{\odot} , M_{\star} in M_{\odot} , v_{∞} in km s^{-1} , \dot{M} in $10^{-6}M_{\odot}/\text{yr}$. D_{mom} (in cgs-units) denotes the modified wind-momentum rate. High precision β -values are given bold-faced. For non-tabulated errors, see text.

Star	T_{eff}	$\log g$	$\log g_{\text{true}}$	R_{\star}	Y_{He}	$\log L/L_{\odot}$	M_{\star}	v_{∞}	β	$\log \dot{M}$	$\log D_{\text{mom}}$
HD 185 859	26.3	2.95	2.96	35	0.10	5.72	41^{+27}_{-16}	1 830	1.1 ± 0.1 ^{a)}	-5.82 ± 0.13	29.01 ± 0.20
HD 190 603	19.5	2.35	2.36	80	0.20	5.92	53^{+41}_{-23}	485	2.9 ± 0.2	-5.70 ± 0.16	28.73 ± 0.22
			2.36	58		5.65	28^{+21}_{-12}			-5.91 ± 0.16	28.45 ± 0.22
HD 206 165	19.3	2.50	2.51	32	0.10-0.20	5.11	12^{+7}_{-4}	640	$1.5^{+0.2}_{-0.1}$ ^{a)}	-6.57 ± 0.13	27.79 ± 0.17
HD198 478*	17.5	2.10	2.12	49	0.10-0.20	5.31	11^{+5}_{-3}	—	1.3 ± 0.1	$-6.93..-6.39$	$26.97..27.48$
			2.12	38		5.08	7^{+3}_{-2}			$-7.00..-6.46$	$26.84..27.36$
HD 191 243	14.8	2.60	2.61	34	0.09	4.70	17^{+9}_{-6}	470	0.8...1.5	$-7.52^{+0.26}_{-0.20}$	$26.71^{+0.27}_{-0.23}$
			2.60	46		4.96	31^{+17}_{-11}			$-7.30^{+0.25}_{-0.17}$	$27.00^{+0.25}_{-0.21}$
HD 199 478	13.0	1.70	1.73	68	0.10	5.08	9^{+5}_{-3}	230	0.8...1.5	$-6.73..-6.18$	$27.33..27.88$
HD 212 593	11.8	2.18	2.19	59	0.06-0.10	4.79	19^{+13}_{-8}	350	0.8...1.5	$-7.04^{+0.25}_{-0.19}$	$27.18^{+0.28}_{-0.24}$
HD 202 850	11.0	1.85	1.87	54	0.09	4.59	8^{+4}_{-3}	240	0.8...1.8	$-7.22^{+0.25}_{-0.17}$	$26.82^{+0.25}_{-0.20}$

* - for this star v_{∞} is highly uncertain ranging from 200 to 470 km s^{-1}

^{a)} H_{α} (though in absorption) indicates $\beta > 1$.

Surface gravity. Classically, the Balmer lines wings are used to determine the surface gravity, $\log g$, where only higher members (H_{γ} and H_{δ} when available) have been considered to prevent a bias because of potential wind-emission effects in H_{α} and H_{β} . Note that due to stellar rotation, the $\log g$ values derived from such diagnostics are only *effective* values. To derive the *true* gravities, $\log g_{\text{true}}$, required to calculate masses, one has to apply a centrifugal correction (approximated by $v \sin i^2/R_{\star}$). For all our sample stars this correction was found to be typically less than 0.03 dex. Corresponding values for effective and corrected surface gravities are listed in Columns 3 and 4 of Table 2.7. The error of these estimates was consistently adopted as ± 0.1 dex due to the rather good quality of the fits and spectra.

Helium abundance. For all sample stars a “normal” helium abundance, $Y_{\text{He}} = 0.10$, was adopted as a first guess. Subsequently, this value has been adjusted (if necessary) to improve the Helium line fits. For the two hottest stars with well reproduced Helium lines (and two ionization stages being present!), an error of only ± 0.02 seems to be appropriate because of the excellent fit quality. Among those, an overabundance in Helium ($Y_{\text{He}} = 0.2$) was found for the hypergiant HD 190 603, which might also be expected according to its evolutionary stage.

In mid and late-B types, on the other hand, the determination of Y_{He} was more complicated, due to fitting problems (for more informations see Markova & Puls 2008). Particularly for stars where the discrepancies between synthetic and observed triplet and singlet lines were opposite to each other (HD 206 165 and HD 198 478), no unique solution could be obtained by varying the Helium abundance, and thus for these stars only upper and lower limits were derived. For HD 212 593, on the other hand (where all available singlet and triplet lines turned out to be over-predicted), a Helium depletion by 30 to 40% would be required

to reconcile theory with observations.

All derived values are summarized in Column 6 of Table 2.7, but note that alternative fits of similar quality are possible for those cases where an overabundance/depletion in He has been indicated, namely by using a solar Helium content and v_{mic} being a factor of two larger/lower than inferred from Silicon: Due to the well known dichotomy between abundance and micro-turbulence (if only one ionization stage is present), a unique solution is simply not possible, accounting for the capacity of the diagnostic tools used here.

Stellar radii, luminosities and masses. The input radii used to calculate our model grid have been drawn from evolutionary models. Of course, these radii are somewhat different from the finally adopted ones (listed in Column 5 of Table 2.7), derived following the procedure outlined in Sec. 2.1.3. With typical uncertainties of ± 500 K in our T_{eff} and of ± 0.3 to 0.5 mag in M_V , the error in the stellar radius (see Eq. 2.4) is dominated by the uncertainty in M_V , and is of the order of $\Delta \log R_{\star} = \pm 0.06 \dots 0.10$, i.e., less than 26% in R_{\star} .

Luminosities have been calculated from T_{eff} and R_{\star} , while masses were inferred from $\log g_{\text{true}}$. These estimates are given in Columns 7 and 8 of Table 2.7, respectively. The corresponding errors are less than ± 0.21 dex in $\log L/L_{\odot}$ and ± 0.16 to 0.25 dex in $\log M_{\star}$.

Compared to the evolutionary masses (Meynet & Maeder 2000), and apart from two cases, our estimates of M_{\star} are generally lower. While for some stars, the discrepancies are less than, or comparable to the corresponding errors, they are significant for some others (mainly at lower luminosities), and might indicate a “mass discrepancy”, in common with previous findings (Crowther et al. 2006; Trundle & Lennon 2005).

Wind parameters

Terminal velocities. For the four hotter stars in our sample, we adopted the v_{∞} -estimates of Howarth et al. (1997). Interestingly, the initially adopted value of 470 km s^{-1} for v_{∞} of HD 198 478 did not provide a satisfactory fit to H_{α} , which in turn required a value of about 200 km s^{-1} . The later value, however, is rather close to the corresponding photospheric escape velocity, v_{esc} . Thus, for this object we considered a rather large uncertainty, accounting for possible variations in v_{∞} .

For the four cooler stars, on the other hand, no literature data were found and v_{∞} -data from appropriate calibrations (Kudritzki & Puls 2000) were used instead. In all but one of these objects (HD 191 243, first entry), the calibrated v_{∞} -values were lower than the corresponding escape velocities, and we adopted $v_{\infty} = v_{\text{esc}}$ to avoid this problem.

The used v_{∞} -values are listed in Column 9 of Table 2.7. The error of these data is typically less than

100 km s⁻¹ (Prinja et al. 1990), except for the last four objects where an asymmetric error of -25/+50% was assumed instead, allowing for a rather large insecurity towards higher values.

Velocity exponent β . For stars with H α in emission, β was fixed from the H α profile shape. For stars with H α in absorption, since the determination of β from optical spectroscopy alone is (almost) impossible, a typical value of $\beta = 1$ was consistently adopted, but lower and larger values have been additionally used to constrain the errors. (In Sect. 2.1.3 I have referred to this issue as to a β - problem.)

Mass-loss rates, \dot{M} , have been derived from fitting the observed H α profiles with model calculations. The obtained estimates are listed in column 11 of Table 2.7. Corresponding errors, accumulated from the uncertainties in Q , R_* and v_∞ (see Sect. 2.1.3), are typically less than ± 0.16 dex for the three hotter stars in our sample and less than ± 0.26 dex for the rest, due to more insecure values of v_∞ and Q . Since we assume an unclumped wind, the *actual* mass-loss rates of our sample stars might, of course, be lower (see Chapter 5).

A comparison of present results with such from previous studies (Crowther et al. 2006; Barlow & Cohen 1977) for three stars in common indicates that the parameters derived by Crowther et al. for HD 190 603 and HD 198 478 are similar to ours (accounting for the fact that higher T_{eff} and M_V result in larger $\log g$ and \dot{M} , respectively, and vice versa).

2.2.3 The T_{eff} scale for B-SGs

Comparison to similar studies. Besides the present study, two other investigations have determined the effective temperatures of *Galactic* B-type SGs by methods similar to ours. Crowther et al. (2006) have used the non-LTE line blanketed code CMFGEN to determine T_{eff} of 24 supergiants (luminosity classes Ia, Ib, Iab, Ia+) of spectral type B0-B3 with an accuracy of $\pm 1\,000$ K; Urbaneja (2004) employed FASTWIND and determined effective temperatures of five early B (B2 and earlier) stars of luminosity classes Ia/Ib with an (internal) accuracy of ± 500 K. In addition, Przybilla et al. (2006) have recently published very precise temperatures (typical error of ± 200 K) of four BA SGs (among which one B8 and two A0 stars), again derived by means of a line-blanketed non-LTE code, in this case in plane-parallel geometry neglecting wind effects.

In Fig. 2.7 the effective temperatures, originating from these four investigations, are plotted as a function of spectral type. Overplotted (dashed line) is a 3rd order polynomial regression to these data, with a grey-shaded area denoting the corresponding standard deviation.

Obviously, the correspondence between the different datasets is (more than) satisfactory: for a given

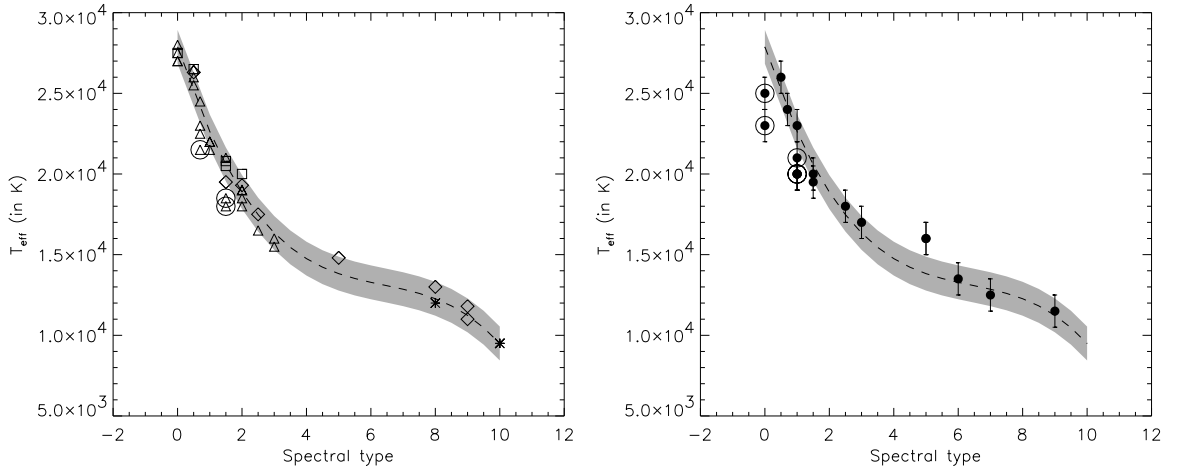


Figure 2.7: *Left:* Comparison of our T_{eff} - determinations with data from similar investigations. Diamonds - our data; triangles - data from Crowther et al. (2006); squares - Urbaneja (2004); asterisks - Przybilla et al. (2006). Large circles mark the three objects with strongest winds (all from the sample by Crowther et al.). The regression to the data (dashed line) and its standard deviation (grey-shaded area) are also shown. Spectral types refer to B-stars (i.e., “-1” corresponds to O9, and “10” to A0).

Right: T_{eff} - estimates for the Lefever et al. GROUP I stars are compared to the regression from the left. The error bars correspond to ± 1000 K. Large circles mark data points which deviate significantly from this regression (see text).

spectral sub-type, the dispersion of the data does not exceed ± 1000 K. There are only three stars (marked with large circles) that make an exception showing significantly lower temperatures: HD 190 603, HD 152 236 and HD 2 905. Given their strong P Cygni profiles seen in H_{α} and their high luminosities, this result should not be a surprise though (higher luminosity \rightarrow denser wind \rightarrow stronger wind blanketing \rightarrow lower T_{eff}).

Very recently, one more study on B-SGs has been published (Lefever et al. 2007) where stellar and wind parameters have been determined by means of FASTWIND. However, due to the lack of appropriate data, the authors were not able to exploit the Silicon ionization balance to determine T_{eff} , but instead had to rely on the analysis of one ionization stage alone, *either* Si II *or* Si III, plus two more He I lines ($\lambda 4471$ and $\lambda 6678$). Consequently, the results derived through this investigation might be prone to larger error bars than those obtained by methods where *all* strategic lines could be included.

To test this possibility, in Fig. 2.7 (right panel) T_{eff} - estimates for stars from the so-called GROUP I of the Lefever et al. sample are piloted together with the regression from the left panel. The error bars correspond to ± 1000 K quoted by the authors as a nominal error. While most of the data are consistent (within their errors) with our regression, there are also objects (marked again with large circles) which deviate significantly.

Among these are two stars of B5-type, with same T_{eff} , which lie above the regression. For one of them,

HD 108 659, the derived $\log g$ -value seems to be somewhat large for a SG, appropriate for a bright giant. Interestingly, the surface gravity of “our” B5 star, HD 191 243, appears also to be larger than what is typical for a supergiant of B5 sub-type. Thus, these two stars seem to be misclassified. This possibility, however, cannot be applied to the other B5 target from the Lefever sample, which $\log g$ (and M_V) is consistent with its classification as a supergiant.

Concerning the outliers situated below the regression, given their strong emission components in H_α we suggest that wind effects might be the reason of their “underestimated” temperatures (see next section).

Effects of line-blocking/blanketing and the wind effects. To improve the statistics and thus to diminish the corresponding errors, the five datasets discussed above have been combined into one sample, which was subsequently used to evaluate the effects of line-blocking and the wind effects in the B SG domain.

Figure 2.8, left panel, displays the differences between “unblanketed” and “blanketed” effective temperatures for this combined sample, as a function of spectral type. The “unblanketed” temperatures have been estimated using the T_{eff} – spectral type calibration provided by McErlean et al. (1999). Objects enclosed by large circles are the same as in Fig. 2.7, i.e., three from the analysis by Crowther et al., and seven from the sample by Lefever et al.⁸. As to be expected, the “blanketed” temperatures of Galactic B-SGs are systematically lower than the “unblanketed” ones. The differences range from about zero to roughly 6 000 K, with a tendency to decrease towards later sub-types (see below for further discussion).

The most remarkable feature in Figure 2.8 is the large dispersion in ΔT_{eff} for stars of early B0-B3 sub-types. Since the largest differences are seen for stars showing P Cygni profiles with a relatively strong emission component in H_α , we suggest that most of this dispersion is related to wind effects.

To investigate this possibility, we have plotted the distribution of the ΔT_{eff} -values of the B0-B3 object as a function of the distant-invariant optical depth parameter $\log Q$. Since the H_α emission strength does not depend on Q alone, but also on T_{eff} - for same Q -values cooler objects have more emission due to lower ionization - stars with individual sub-classes were studied separately to diminish this effect. The right-hand panel of Fig. 2.8 illustrates our results, where the size of the circles corresponds to the strength of the emission peak of the line. Filled symbols mark data from CMFGEN; open ones – data from FASTWIND. Inspection of these data indicates that objects with stronger H_α emission tend to show larger $\log Q$ -values and subsequently higher ΔT_{eff} – a finding that is model independent. This tendency is particularly evident in the case of B1 and B2 objects.

On the other hand, there are at least three objects that appear to deviate from this rule, but this might still be due to the fact that the temperature dependence of Q has not been completely removed (of course,

⁸Four B1 stars from the Lefever et al. sample have the same T_{eff} and thus appear as one data point in Figs 8 (right) and 9.

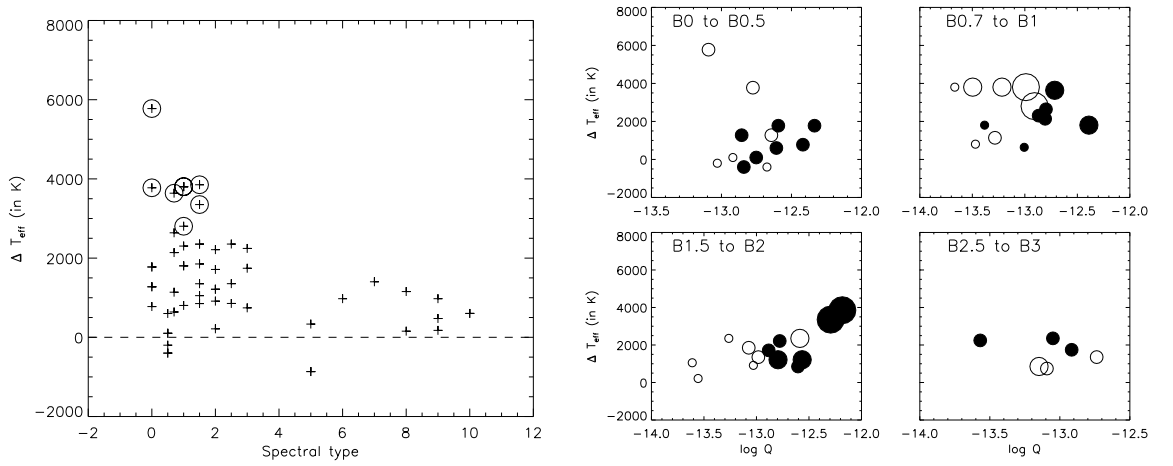


Figure 2.8: Differences between “unblanketed” and “blanketed” effective temperatures for the combined sample (this work, Urbaneja 2004, Crowther et al. 2006, Przybilla et al. 2006 and GROUP I objects from Lefever et al. 2007), as a function of spectral type (left panel) and as a function of $\log Q$ for individual subtypes, B0 to B3 (right panel). Unblanketed T_{eff} are from McErlean et al. (1999).

Left: Large circles denote the same objects as in Fig. 2.7. The data point indicating a significant *negative* temperature difference corresponds to the *two* B5 stars (at same temperature) from the Lefever et al. sample. *Right:* The size of the symbols corresponds to the size of the peak emission seen in H_{α} . Filled circles mark data from CMFGEN, open circles those from FASTWIND.

uncertainties in β , T_{eff} and $\log g$ can also contribute). All three stars (HD 89 767, HD 94 909 (both B0) and HD 154 043 (B1)) are from the Lefever et al. sample and do not exhibit strong H_{α} emission, but nevertheless the highest ΔT_{eff} among the individual sub-classes.

In summary, we suggest that the dispersion in the derived effective temperature scale of early B-SGs is physically real and originates from *wind effects*. Moreover, there are three stars from the Lefever et al. GROUP I sample (spectral types B0 to B1) whose temperatures seem to be significantly underestimated, probably due to insufficient diagnostics. In our follow-up analysis with respect to wind-properties, we will discard these “problematic” objects to remain on the “conservative” side.

2.2.4 Metallicity effects

Wanted to obtain an impression of the influence of metallicity on the temperature scale for B-type SGs, by comparing Galactic with SMC data. To this end, we derived a T_{eff} – spectral type calibration for Galactic B-SGs on basis of the five datasets discussed above, discarding only those (seven) objects from the Lefever et al. sample where the temperatures might be particularly affected by strong winds, or other uncertainties (marked by large circles in Fig. 2.7, right). Accounting for the errors in T_{eff} , we obtain the following

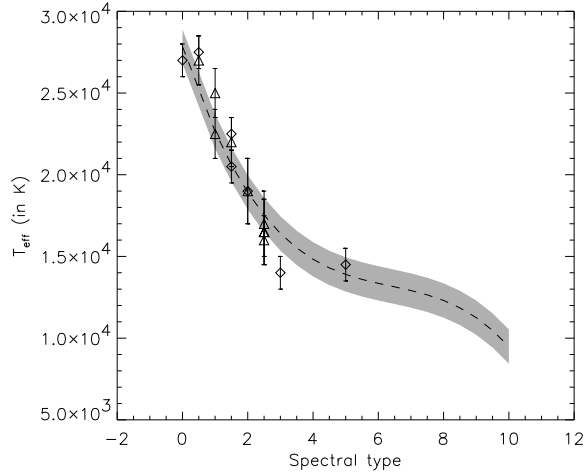


Figure 2.9: Temperature scale for Galactic B-SG as derived in the present study (dashed, see text), compared to T_{eff} estimates for similar stars in the SMC (from Trundle et al. 2004 (diamonds) and Trundle & Lennon 2005 (triangles)). The grey area denotes the standard deviation of the regression for Galactic objects. Spectral types account for metallicity effects (from Lennon 1997), see text.

regression (for a precision of three significant digits)

$$T_{\text{eff}} = 27\,800 - 6\,000\text{ SP} + 878\text{ SP}^2 - 45.9\text{ SP}^3, \quad (2.10)$$

where “SP” (0-9) gives the spectral type (from B0 to B9), and the standard deviation is ± 1040 K. This regression was then compared to T_{eff} - estimates obtained by Trundle et al. (2004) and Trundle & Lennon (2005) for B-SGs in the SMC.

We decided to compare with these two studies *only*, because Trundle et al. have used a similar (2004), or identical (2005) version of FASTWIND as we did here, i.e., systematic, model dependent differences between different datasets can be excluded, and because the metallicity of the SMC is significantly lower than in the Galaxy, so that metallicity dependent effects should be maximized.

The outcome of our comparison is illustrated in Fig. 2.9: In contrast to the O-star case (cf. Massey et al. 2004, 2005; Mokiem et al. 2006), the data for the SMC stars are, within their errors, consistent with the temperature scale for their Galactic counterparts. This result might be interpreted as an indication of small, or even negligible, metallicity effects (both directly, via line-blanketing, and indirectly, via weaker winds) in the temperature regime of B-SGs, at least for metallicities in between solar and SMC (about 0.2 solar) values. Such an interpretation would somewhat contradict our findings about the strong influence of line-blanketing in the Galactic case (given that these effects should be lower in the SMC), but might be misleading since Trundle et al. (2004, 2005) have used the spectral classification from Lennon (1997), which already accounts for the lower metallicity in the SMC.

To check the influence of this re-classification, we recovered the original (MK) spectral types of the SMC targets using data provided by Lennon (1997, Table 2), and subsequently compared them to our results for Galactic B-SGs. Unexpectedly, SMC objects still do not show any systematic deviation from the Galactic scale, but are, instead, distributed quite randomly around the Galactic mean.

Most plausibly, this outcome results from the large uncertainty in spectral types as determined by Azopardi & Vigneanu (1975)⁹, such that metallicity effects cannot become apparent for the SMC objects considered here. Nevertheless, we can also conclude that the classification by Lennon (1997) has been done in a perfect way, namely that Galactic and SMC stars of similar spectral type also have similar physical parameters, as expected.

2.2.5 Wind momentum - luminosity relationship. Comparison with results from similar studies

Using the stellar and wind parameters, the modified wind momenta can be calculated (column 12, Table 2.7), and the wind momentum - luminosity diagram constructed. The results for the combined sample (to improve the statistics, but without the “problematic” stars from the Lefever et al. GROUP I sample) are shown in Figure 2.10. Data from different sources are indicated by different symbols. For HD 190 603 and HD 198 478, both alternative entries (from Table 2.6) are indicated and connected by a dashed line. Before considering the global behaviour, I will first comment on few particular objects.

- The position of HD 190 603 corresponding to $B - V = 0.540$ (lower luminosity) appears to be more consistent with the distribution of the other data points than the alternative position with $B - V = 0.760$. In the following, we give more weight to the former solution.
- The positions of the two B5 stars suggested as being misclassified (HD 191 243 and HD 108 659, large diamonds) fit well the global trend of the data, implying that these bright giants do not behave differently from supergiants.
- The minimum values for the wind momentum of HD 198 478 (with $v_{\infty} = 200 \text{ km s}^{-1}$) deviate strongly from the global trend, whereas the maximum ones ($v_{\infty} = 470 \text{ km s}^{-1}$) are roughly consistent with this trend. For our follow-up analysis, we discard this object because of the very unclear situation.
- HD 152 236 (from the sample of Crowther et al., marked with a large circle) is a hypergiant with a very dense wind, for which the authors adopted $R_{\star} = 112 R_{\odot}$, which makes this object the brightest one in the sample.

⁹using low quality objective prism spectra in combination with MK classification criteria, both of which contribute to the uncertainty.

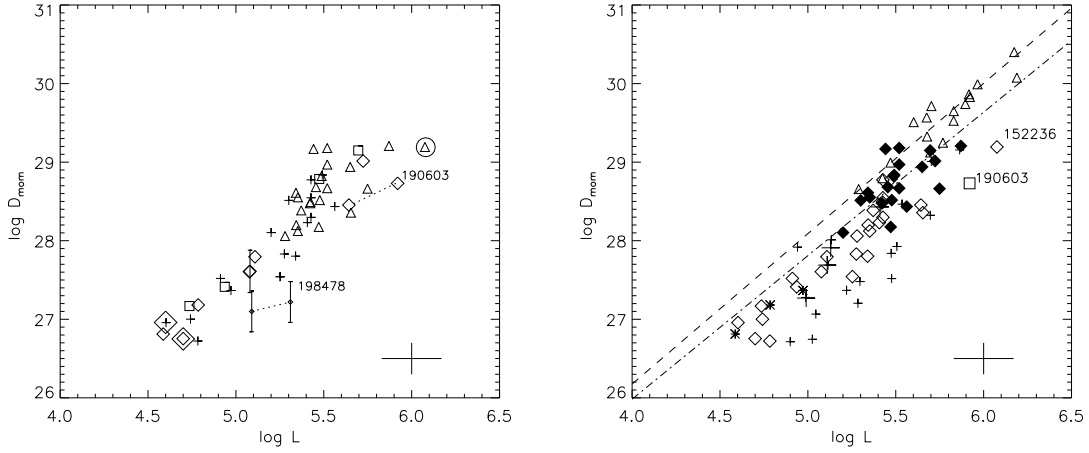


Figure 2.10: *Left*: Empirical WLR for Galactic B-SGs: diamonds - our data; triangles - data from Crowther et al. (2006); squares - data from Urbaneja (2004) and plus signs - data from Lefever et al. (2007). The two pairs of symbols connected with dashed lines correspond to the two entries for HD 190 603 and HD 198 478 as listed in Table 2.6. For the latter object and for HD 199 478, error bars indicating the rather large uncertainty in their wind-momenta are also provided.

Right: Empirical WLR for Galactic O-stars (triangles) and B-SGs (diamonds and asterisks). Filled diamonds, asterisks and open diamonds separate B-type objects with $T_{\text{eff}} \geq 21\,000$ K, $T_{\text{eff}} \leq 12\,500$ K and $12\,500 \leq T_{\text{eff}} \leq 21\,000$ K, respectively. Overplotted are the early/mid B- (small plus-signs) and A-SGs (large plus-signs) data derived by Kudritzki et al. (1999) and the theoretical predictions from Vink et al. (2000) for Galactic SGs with $27\,500 \leq T_{\text{eff}} \leq 50\,000$ (dashed-dotted) and with $12\,500 \leq T_{\text{eff}} \leq 22\,500$ (dashed). Error bars provided in the lower-right corner of each panel represent the typical errors in $\log L/L_{\odot}$ and $\log D_{\text{mom}}$ for data from our sample. Maximum errors in $\log D_{\text{mom}}$ are about 50% larger.

Global features. From the left panel of Figure 2.10, one can see that the lower luminosity B-SGs seem to follow a systematically lower WLR than their higher luminosity counterparts, with a steep transition between both regimes located in between $\log L/L_{\odot} = 5.3$ and $\log L/L_{\odot} = 5.6$. (Admittedly, most of the early type (high L) objects are Ia’s, whereas the later types concentrate around Iab’s with few Ia/Ib’s.) This finding becomes even more apparent when the WLR is extended towards higher luminosities by including Galactic O supergiants (from Repolust et al. 2004; Markova et al. 2004; Herrero et al. 2002), as done on the right of the same figure.

Kudritzki et al. (1999) were the first to point out that the offsets in the corresponding WLR of OBA-supergiants may depend on spectral type, being strongest for O-SGs, decreasing from B0-B1 to B1.5-B3, and *increasing* again towards A supergiants. While some of these results have been confirmed by recent studies, others have not (Crowther et al. 2006; Lefever et al. 2007).

To investigate this issue in more detail and based on the large sample available now, we have highlighted the early objects (B0–B1.5, $21\,000 \leq T_{\text{eff}} \leq 27\,500$ K) in the right-hand panel of Figure 2.10 using filled diamonds. (Very) Late objects with $T_{\text{eff}} \leq 12\,500$ K have been indicated by asterisks, and intermediate temperature objects by open diamonds. Triangles denote O-SGs. Additionally, the theoretical predictions

by Vink et al. (2000) are provided via dashed-dotted and dashed lines, corresponding to the temperature regimes of O and B-supergiants, respectively (from here on referred to as “higher” and “lower” temperature predictions). Indeed,

- O-SGs show the strongest wind momenta, determining a different relationship than the majority of B-SGs (see below).
- the wind momenta of B0–B1.5 sub-types are larger than those of B1.5–3, and both follow a different relationship. However, a direct comparison with Kudritzki et al. reveals a large discrepancy for mid B1.5–B3 sub-types ($\Delta \log D_{\text{mom}}$ about 0.5 dex), while for B0–B1.5 subtypes their results are consistent with those from our combined dataset.
- Late B4–B9 stars follow the same relationship as mid subtypes.

Thus, the only apparent disagreement with earlier findings relates to the Kudritzki et al. mid-B types, previously pointed out by Crowther et al. (2006), and suggested to be a result of line blocking/blanketing effects not accounted for in the Kudritzki et al. analysis¹⁰. After a detailed investigation of this issue for one proto-typical object from the Kudritzki et al. sample (HD 42 087), we are convinced that the neglect of line blocking/blanketing cannot solely account for such lower wind momenta. Other effects must also contribute, e.g., overestimated β -values, though at least the latter effect still leaves a considerable discrepancy.

Another feature of particular importance is that the wind momenta of the Kudritzki et al. A-SGs (marked with large plus-signs on the right of Fig. 2.10) seem quite similar to those of mid- and late-B sub-types. Further investigations based on better statistics are required to clarify this issue.

On the other hand, from the right panel of Figure 2.10 it is obvious that the observed wind momenta of Galactic OB-stars do not follow the theoretical predictions by Vink et al. (2000). Instead, the majority of O-SGs (triangles – actually those with H_{α} in emission) follow the low-temperature predictions (dashed line), while most of the early B0–B1.5 sub-types (filled diamonds) are consistent with the high-temperature predictions (dashed-dotted), and later subtypes (from B2 on, open diamonds) lie below (!), by about 0.3 dex. Only few early B-types are located in between both predictions, or close to the low-temperature one. In Chapter 6 I will return to this point again.

2.2.6 Summary

In this section, I have presented a detailed investigation of the optical spectra of a small sample of Galactic B-SGs, from B0 to B9. Stellar and wind parameters have been obtained by employing the NLTE unified model atmosphere code FASTWIND (Puls et al. 2005) assuming unclumped winds. The major findings of this analysis can be summarized as follows.

¹⁰These authors have employed the *unblanketed* version of FASTWIND (Santolaya-Rey et al. 1997) to determine wind parameters/gravities while effective temperatures were adopted using the unblanketed, plane-parallel temperature scale of McErlean et al. (1999).

- We confirmed recent results (Ryans et al. 2002; Dufton et al. 2006; Simon-Diaz & Herrero 2007) of the presence of a (symmetric) line-broadening mechanism in addition to stellar rotation, denoted as “macro-turbulence”. The derived values of v_{mac} are highly supersonic, decreasing from $\sim 60 \text{ km s}^{-1}$ at B0 to $\sim 30 \text{ km s}^{-1}$ at B9. How can we explain such an effect within our present-day atmospheric models of hot massive stars is still not clear.
- We determined the Si abundances of our sample stars in parallel with their corresponding micro-turbulent velocities.
 - (i) For all but one star, the estimated Si abundances were consistent with the corresponding solar value (within ± 0.1 dex), in agreement with similar studies (Gies & Lambert 1992; Rolleston et al. 2000; Urbaneja 2004; Przybilla et al. 2006). For HD 202 850, on the other hand, an overabundance of about 0.4 dex has been derived, suggesting that this late-B supergiant might be a silicon star.
 - (ii) The micro-turbulent velocities tend to decrease towards later B subtypes, from 15 to 20 km s^{-1} at B0 (similar to the situation in O-supergiants) to 7 km s^{-1} at B9, which is also a typical value for A-SGs.
 - (iii) The effect of micro-turbulence on the derived effective temperature was found to be negligible as long as Si lines from the two major ions are used to determine it.
- Based on original T_{eff} - estimates and incorporating data from similar investigations (Crowther et al. 2006; Urbaneja 2004; Przybilla et al. 2006; Lefever et al. 2007), we confirmed previous results (e.g., Crowther et al. 2006) on a 10% downwards revision of the effective temperature scale of early B-SGs, required after incorporating the effects of line blocking/blanketing. Furthermore, we suggest a similar correction for mid and late sub-types. When strong winds are present, this reduction can become a factor of two larger, similar to the situation encountered in O-SGs.
- To our surprise, a comparison with data from similar SMC objects (Trundle et al. 2004; Trundle & Lennon 2005) did not reveal any systematic difference between the two temperature scales. This result is interpreted as an indication that the re-classification scheme as developed by Lennon (1997) to account for lower metal line strengths in SMC B-SGs also removes the effects of different degrees of line blanketing.
- We found that the empirical WLR for Galactic B-SGs does not follow the theoretical predictions by Vink et al. (2000). In particular, the observed wind momenta of most of the early B0–B1.5 sub-types are consistent with the predictions for O-stars, while later B sub-types (from B2 on) lie even below (by about 0.3 dex) it. In Sect. 6.3 this issue will be investigated in more detail.

Chapter 3

Wind structure and variability in OB stars

As noted in Chapter 1, the standard (i.e., *stationary, homogeneous and spherically symmetric*) wind models are generally quite successful in describing the overall wind properties of OB stars. Nonetheless, there are theoretical considerations, supported by numerous observational evidences, which indicate that hot stars winds are very far from being *smooth* and *stationary*.

In particular, spectroscopic time-series in the satellite UV (with IUE), and in ground-based wavelength ranges, have shown that time variability is a general characteristic of the winds of early type stars. The most prominent signatures of this variability are optical depth enhancements, migrating from red to blue within the absorption troughs of P Cygni profiles, called Discrete Absorption Components (DAC) (e.g., Kaper et al. 1999; Prinja et al. 2002; Markova 1986b). Observations indicate that at least in some cases, stellar rotation plays a dominant role in setting the recurrence timescale of the DACs variability (Prinja 1988; Kaper et al. 1999). Large-scale structures rooted in the photosphere have been suggested to explain this phenomenon.

On the other hand, absorption line-profile variability (LPV) seems to be commonplace among hot stars (Fullerton, Gies & Bolton 1996 and references therein). Stellar pulsation and magnetic fields might equally be responsible for this phenomenon. The coexistence of photospheric and wind variability, and the rough similarity of their timescales, suggest that these two phenomena might be related in some way. Attempts to detect a direct coupling between deep photospheric variability and time-dependent wind variability have become known as the search for “*a photospheric connection*” (Abbott et al. 1986).

The most frequently used approach to investigate the wind variability and to look for a possible “*photospheric connection*”, is to monitor the properties of spectral lines, formed in different regions of the atmosphere, in order to determine relevant time-scales and variability patterns, which are then confronted to obtain deeper insight into the nature and the physical origin of the variations. Surveys of this kind, how-

ever, are observationally very demanding: long sets of high quality and high temporal resolution spectra are required. As a result only a limited numbers of OB-stars have been so far analyzed.

In this chapter, I am going to present main results derived throughout two long-term international monitoring campaigns to study wind structure and variability in OB-stars.

3.1 Long-term monitoring campaigns of α Cam

The late-O supergiant α Cam has been known to be spectroscopically variable for a relatively long time. Changes in H_α have been observed by Ebbets (1982) and by Kaper et al. (1997). Lamers et al. (1988) argued that the UV resonance lines are also variable, but this result has been questioned by more recent observations (Kaper et al. 1996). On the other hand, absorption line-profile variability seems also to present (Zeinalov & Musaev 1986; Fullerton, Gies & Bolton 1996). All this makes α Cam a promising target for the search of the “*photospheric connection*”.

Motivated by these perspectives, I have organized a long-term international spectroscopic monitoring campaign α Cam to investigate the nature of its variability, and to search for evidence of a “*photospheric connection*”. The project was developed in collaboration with colleagues from the Catania Observatory, Italy, and the University College London, Great Britain.

3.2 Observational material

The observational material includes spectroscopic data from 1998, 1999, 2002 and 2004. During the 1998-1999 campaigns, 65 H_α coude spectra were obtained at the NAO 2m telescope of the Institute of Astronomy, Bulgarian Academy of Sciences.

The 2002-2004 observational data-sets, on the other hand, includes time-series of primarily He I $\lambda 5875.67$ obtained during January, February and March 2002, and time-series of H_α , He I $\lambda 6678$ and He I $\lambda 5876$ obtained during November 2004. The majority of these observations were secured at the NAO 2m telescope, but complementary spectra obtained at the 0.9-m telescope of the Catania Observatory (Italy) were also used. A summary log of all data, together with some characteristics, such as, e.g., Heliocentric Julian Date, spectral resolution, $R=\lambda/\delta\lambda$, the wavelength span recorded, $\Delta\lambda$ and the S/N ratio, can be found in Markova (2002) and Prinja et al. (2006).

3.2.1 Absorption line-profile variability

All data have been analyzed in terms of LPV. In particular, to detect and quantify the level of significant variability in the absorption lines as a function of velocity bin, the Temporal Variance Spectrum (TVS)

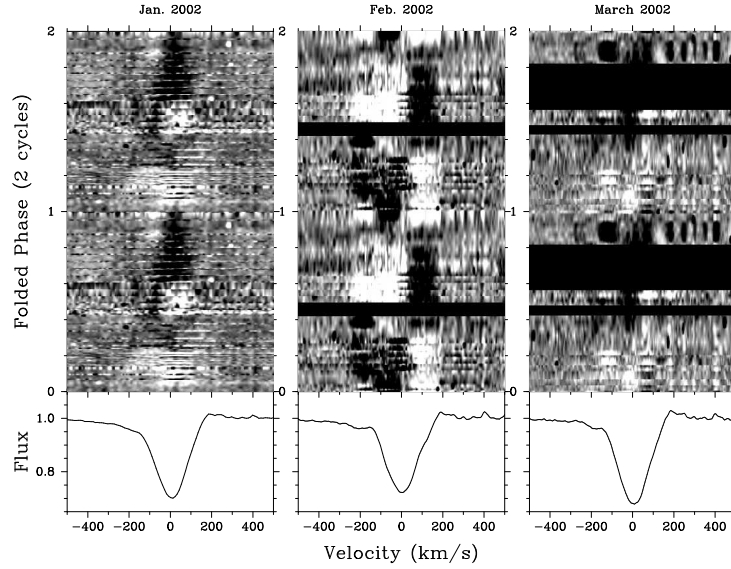


Figure 3.1: Grey-scale representations of variability in He I $\lambda 5876$ for individual spectra phased on 0.36-d period for the January (left), February (middle) and March (right) runs in 2002.

analysis as developed by Fullerton, Gies & Bolton (1996) was applied.

The He I $\lambda 6678$ absorption line. The calculated TVS of He I $\lambda 6678$ revealed the presence of significant LPV within a velocity range of $\sim 400 \text{ km s}^{-1}$. This interval is a factor of 2 to 3 larger than the expected width of a photospheric line with no other broadening than stellar rotation ($2 v \sin i = 160 \text{ km s}^{-1}$), thus indicating that at least part of the observed variations originate from the wind. The double-peaked morphology of the TVS suggests time-dependent alterations in the position the line core. This possibility was confirmed by our measurements which revealed systematic changes in radial velocity with an amplitude of $\sim 20 \text{ km s}^{-1}$ on a timescale of 3 to 4 days.

The He I $\lambda 5876$ absorption line was intensively observed at the NAO and the CO between 21 to 27 January, 2002. The obtained data-set includes 114 spectra and is thus well-suited to perform a periodic analysis.

Due to its larger opacity, He I $\lambda 5876$ is expected to form in layers above the formation region of He I $\lambda 6678$, and its behaviour might be therefore influenced by processes in the wind. However, since the wind changes occur over time-scales of days, it seems still possible to pursue the effects of shorter time-scale photospheric variability in this line, e.g., by normalizing the individual line profiles to the corresponding nightly mean profile, and subsequently performing time-series analyses on the residual spectra.

This approach turned out to be very successful. The obtained periodogram, based on the 2-d Discrete

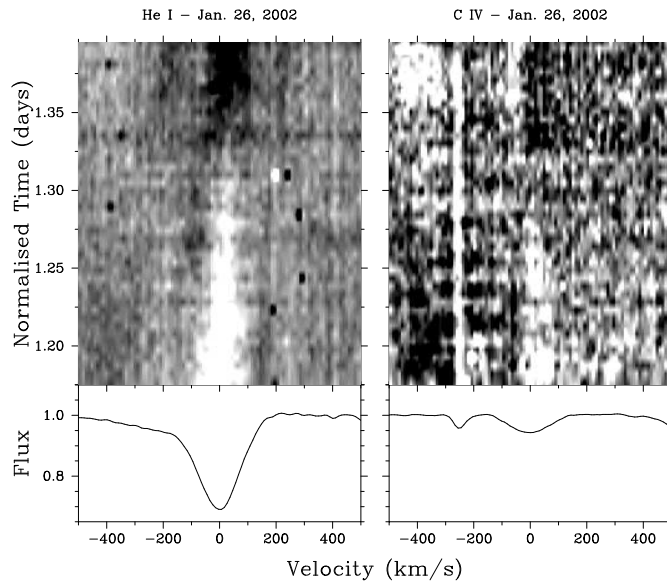


Figure 3.2: Grey-scale representations of variability in He I $\lambda 5876$ (left) and the C IV doublet (right) for individual spectra phased on 0.36-d period for the January 2002 runs.

Fourier Transform and the iterative CLEAN algorithm (Roberts et al. 1987), clearly indicated a (dominant) primary frequency, corresponding to a period of 0.36 ± 0.01 days. We are very confident that this period is not directly connected to the sampling window of each night since the length of the nightly runs in 2002 is between ~ 0.12 to 0.27 days.

Grey-scale images of the phase versus velocity behaviour of the individual residual He I $\lambda 5876$ spectra on the 0.36-d period are shown in Figure 3.1. The left-hand panel illustrates the coherent behaviour during our main (January 2002) time-series. The two nights of data secured in February 2002 and March 2002 are not suitable for a reliable Fourier analysis, but they do provide some indication that the 0.36-d period persists over at least several weeks.

In addition, the January data-set reveals some indication for progressive changes across the absorption profile, though the acceleration of the pseudo-absorption (emission) feature is not substantial. There is evidence for characteristic “blue-to-red” motion, accommodated within the projected rotation velocity (115 km s^{-1}). We estimated a prograde feature traveling across the line center with $(dV/d\phi) \sim 80 \text{ km s}^{-1}/\text{cycle}$. This behaviour would be consistent with a low-order, sectorial non-radial pulsation mode. Unfortunately, these time-series of α Cam are not extensive enough, nor sufficiently high signal-to-noise, to attempt more detailed modelling to determine pulsational parameters.

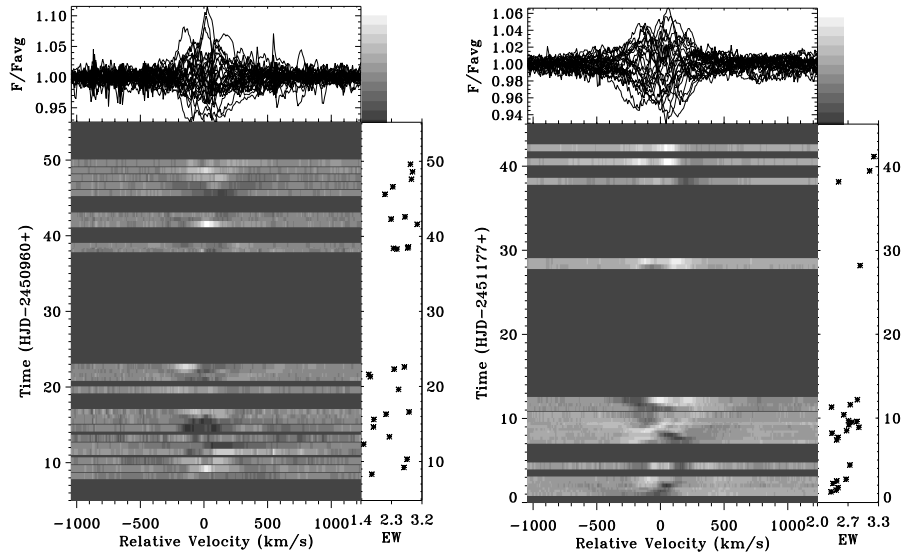


Figure 3.3: Dynamic quotient spectra of $H\alpha$ in June – July, 1998 (left panel) and in December – February, 1999 (right panel). The zero-point in velocity is set to the laboratory wavelength of the line. The top panels show an overplot of all profiles from the relevant time series. The gray-scale bar on the right of each plot shows the intensity scaling. The panel on the right-hand side of each image shows the equivalent width of the line (in \AA) as a function of time.

The C IV $\lambda\lambda 5801, 5812$ absorption lines. The wavelength range of the NAO spectra of January, 2002 includes the very weak photospheric metal lines of C IV $\lambda\lambda 5801, 5812$. Unfortunately, the intensity of these lines is rather small, but we are confident that they are also temporally active. The results of the period analysis illustrated in Fig. 3.2 shows that the subtle prograde traveling pattern identified in He I $\lambda 5876$ (left) is tentatively mimicked in C IV (right). This finding supports an interpretation in terms of photospheric velocity fields, though confirmation of this result clearly requires much higher S/N time-series data.

3.2.2 Wind variability as traced by $H\alpha$

The two longest $H\alpha$ time-series, from June – July, 1998 and December, 1998 – February 1999 are shown in Figure 3.3 in the form of the so-called “*dynamic quotient spectrum*”. Within this representation, regions and times of excess emission with respect to the mean appear brighter, while darker regions indicate intervals, when the local flux is smaller than its mean value. The plots on the right-hand side of the images show the $H\alpha$ equivalent width, W_λ . The internal precision of individual W_λ determinations equals $\sim 0.29\text{\AA}$ and $\sim 0.15\text{\AA}$ for data obtained before October 1998 and afterwards.

Figure 3.3 indicates that the $H\alpha$ variability is rather systematic than erratic. In June and July (left panel), for example, episodes of enhanced emission alternate with those of reduced emission. The period analysis of these data revealed a dominant frequency of $0.143 \pm 0.020 \text{ d}^{-1}$ corresponding to $P = 6.99$ days. Parallel

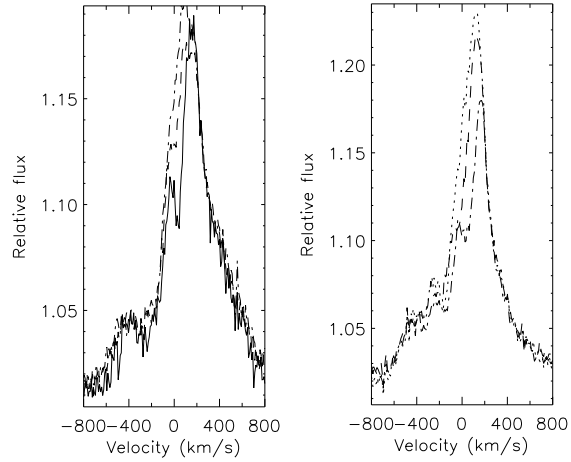


Figure 3.4: Examples of short-term LPV of $H\alpha$. Profiles obtained within one night are overplotted to enhance the significance of the observed variations. From left to right the corresponding dates of observations are: December 31, 1989 and January 6, 1999.

variations in W_λ are also seen. Notice the sudden appearance of the blue-shifted enhanced emission at $\sim -150 \text{ km s}^{-1}$ on $T = 22$ days.

On the other hand, the December – February quotient spectrum (right panel) indicates another variability pattern: two waves, one of enhanced emission and another of reduced emission/enhanced absorption, run from “red” to “blue” and back to “red” within the profile (between $\pm 300 \text{ km s}^{-1}$). In addition to the wave-like variability, an episode of enhanced blue-shifted absorption is clearly noticed ($T = 11$ to $T = 12$ days). The absorption moves blueward with a mean acceleration of $\sim 0.0017 \text{ km s}^{-1}$. This event has been accompanied by strong increase in emission: W_λ reaches its maximum values.

Although scanty, the February data (right panel, $T = \geq 38$ days) clearly indicate that the wave-like phenomenon observed in December – January is no longer at work, and that the star has likely returned to the kind of behaviour demonstrated in June and July which seems to be its “normal” state.

Generally, the $H\alpha$ profile of α Cam is not substantially variable on *hourly* time-scales. However, exceptions do present. Few examples are shown in Figure 3.4 where localized *systematic* changes are clearly evident over ~ 10 hours. Such a behaviour was observed during the November, 2004 run as well.

3.2.3 Evidence of a “photospheric connection”

In Figure 3.5 the LPV of the wind formed line H_α over the December – January run is compared to that of He I $\lambda 6678.15$ and He II $\lambda 6683.2$ absorption lines. The dynamic quotient spectrum of the He I+He II complex (right panel) gives clear evidence for systematic line-flux variations in the He I $\lambda 6678$ profile (within $\pm 4\%$ in continuum units). No indication for such variations in the He II $\lambda 6683$ line, located at $+227 \text{ km s}^{-1}$ respect to He I $\lambda 6678$, is noticed.

At the same time, the He I $\lambda 6678$ variations are almost symmetric with respect to the line center. The pattern of variability is reminiscent of that of $H\alpha$, but some differences are still noted. For example, the

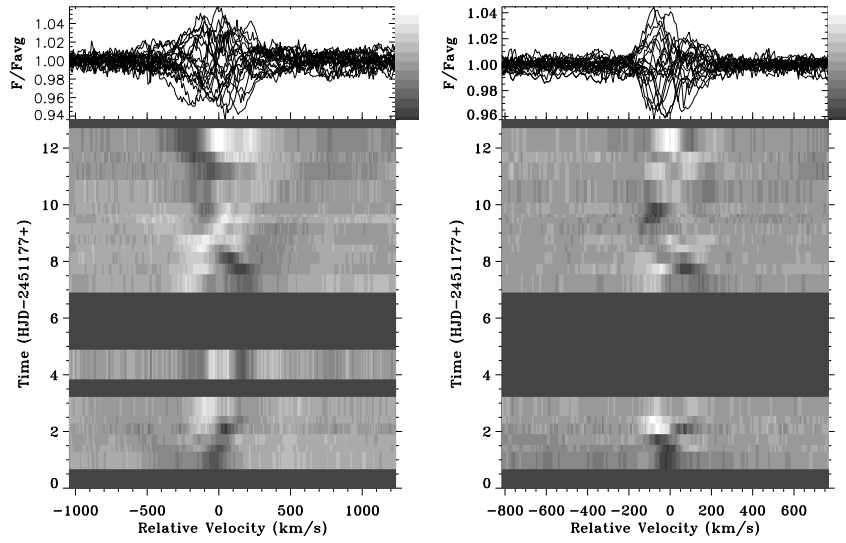


Figure 3.5: Dynamic quotient spectra of $H\alpha$ (left panel) and the He I $\lambda 6678$ and He II $\lambda 6683$ lines (right panel) in December, 1998 – January, 1999. The zero-point in velocity is set at the laboratory wavelength of $H\alpha$ and He I $\lambda 6678$. 15. Darker shadings denote regions and times where the profile has a lower intensity than its time-averaged value. Panels on the top show an overplot of all profiles (in difference flux) from the relevant time series. The gray-scale bar on the right of each plot shows the intensity scaling.

variations extend to lower velocities, $\sim \pm 200 \text{ km s}^{-1}$. Also, the episode of enhanced blue-shifted absorption seen in $H\alpha$ during the last few days of the run is not observed. No clear evidence for a time lag between the variations in the two lines is seen.

These findings suggest that (i) the He II $\lambda 6683$ line is more likely of “pure” photospheric origin; (ii) the He I $\lambda 6678$ absorption line is partially formed in the wind, as suggested by the analysis of the TVS plot; (iii) the spectacular spiral-like event seen in $H\alpha$ affects the deepest layers of the wind close to its base.

3.2.4 Towards a possible interpretation of $H\alpha$ variability

The observed behaviour of $H\alpha$ suggests the inner part of the wind of α Cam is not smooth and stationary, but temporary variable and structured.

In particular, the properties of the LPV in June–July, 1998 and in February, 1999 appear to be widely consistent, at least qualitatively, with the idea of a short-term perturbation in wind density caused by changes in the mass-loss rate. The perturbations should be large and should have significant azimuthal extents so as to be able to significantly modify the profile shape over an extended velocity range simultaneously. The limitation of the corresponding LPV in the central part of the profile as well as its recurrent character both argue in favor of consecutive spherically symmetric shells. However note that some evidence about deviation from spherical symmetry (such as, e.g., the blue- and red-shifted enhanced/reduced emissions)

seems also to present.

On the other hand, the properties of variability of H_α in the December, 1998 – January, 1999 run is completely different and requires different interpretation. In particular, the spiral-like event we have observed is surprisingly similar to that derived by Harries (2000) via 3-D line-profile simulations involving a corotating (one-armed) spiral density structure. This finding suggest that this event might be due to rotational modulation of a perturbed stellar wind. At least the timescale of this phenomenon is consistent, i.e. falls between, the lower (=4.9 days) and upper (=18.3 days) limits for the rotational period of α Cam, as determined from its $v \sin i$, and the adopted stellar parameters (Table 1 of Markova 2002).

Concerning the physical cause of the wind perturbation, stellar pulsations seem to be the most plausible candidate. Indeed, according to our results α Cam seems to experience non-radial pulsations, though on a limited time-periods. Also, its $(L/L_\odot)/(M/M_\odot)$ ratio is a factor of two larger than the lower limit required for “strange-mode” instability to occur (Glatzel 1999) in the star.

3.2.5 Summary

α Cam is an example of a massive star that demands substantial observational and theoretical effort to understand its time-variable conditions. In this section I have outlined main results derived via a long-term spectroscopic survey of this star with particular emphasis on LPV of lines formed in different part of its atmosphere. Our findings show that the optical line spectrum of this star is subject of at least three different forms of variability patterns:

- i) systematic changes in the photosphere with some evidence that the behaviour may be linked to surface velocity fields due to non-radial pulsations;
- ii) short time-scale (\sim hourly) perturbations operating in the transition zone of the atmosphere, which potentially give rise to localized changes in H_α , and
- iii) a variable stellar wind with a complicated origin.

Concerning the deep-sited wind variability (iii), our results suggest that in most cases this variability is widely consistent with the idea of short-term, low-amplitude variations in \dot{M} , which cause the formation of large-scale wind density perturbations. The morphology of these perturbations cannot be specified with confidence. Some of our results argue in favor of consecutive spherically symmetric shells whilst others support interpretation in terms of spatially localized, density enhancements like, e.g., blobs.

Interestingly, a wind model including outward accelerating shells/blobs, caused by variations in \dot{M} , was also suggested by de Jager et al. (1979) and Lamers et al. (1988) to explain the daily changes in the

high-velocity part of the UV line profiles of α Cam. The possibility that the wind of α Cam is not smooth but structured (clumped) has got additional support by recent results derived by Fullerton et al. (2006) and Puls et al. (2006).

Another result of particular interest is that we found clear evidence of time-dependent, large-scale asymmetries in the wind which seem to be rotationally modulated. The presence of large-scale, time-dependent structures in the wind of α Cam was suggested by Kaper et al. (1999) based on observations in H_α . Unfortunately, no further details were provided. Thus, and at least at present, the character of the spectacular S-like event observed by us is unclear: it may be either accidental, or may reoccur on some (still unknown) timescale. Nevertheless, the detection of this event is particularly important since it is among the first empirical evidence for the presence of rotationally modulated structure in O-star winds as predicted by 2D hydrodynamical simulations (Cranmer & Owocki 1996).

3.3 Long-term monitoring campaign of HD 199 478

A close inspection of literature data shows that most of the time-dependent observational campaigns refer to O-stars and early B supergiants (SGs), while mid- and late-B candidates are currently under-represented in the sample of stars investigated to date.

Indeed, theoretical predictions supported by observational results (Markova & Puls 2008) indicate that while winds in late-B SGs are significantly weaker than those in O SGs, there is no currently established reason to believe that weaker winds might be less structured than stronger ones.

The first extended spectroscopic monitoring campaigns of line-profile variability (*LPV*) in late-B SGs have been performed by Kaufer et al. (1996a,b), who showed that stellar winds at the cooler temperature edge of the B-star domain can also be highly variable. Interestingly, in all 3 cases studied by these authors the variability patterns, as traced by $H\alpha$, were quite similar consisting of (i) blue- and red-shifted emission with V/R variations similar to those in Be-stars, and (ii) sudden appearance of deep and highly blue-shifted absorptions, called high-velocity absorptions (HVAs).

Though the kinematic properties of the HVAs in $H\alpha$ were found to be completely different from those of DACs in the UV spectra of O and early-B stars (e.g. HVAs do not propagate outwards but instead extend to zero velocity indicating even mass infall) similar scenarios consisting of large-scale wind structures rooted in the photosphere were suggested to interpret their appearance and development in time.

Motivated by the intriguing time-variable properties reported above, I organized and conducted an international long-term photometric and spectroscopic monitoring of HD 199 478 to study time-dependent phenomena in the stellar wind of this late-B SG, and their possible connection to processes in stellar interior. The project was worked out in collaboration with colleagues from the University College London, Great Britain; the University of Toronto, Canada; the Tartu Observatory, Estonia; the Ritter Observatory, Ohio and the Citadel's Physics Department, SC, USA. The results of this investigation are published in Markova & Valchev (2000), Markova et al. (2008), Percy et al. (2008), Markova & Markov (2008) and Austin et al. (2008).

3.3.1 Observational material

Photometric data. About 400 observations in the Stromgren *uvby* system were obtained with the Automatic Photometric Telescope (APT) operated by the Four-College Consortium. Additional 168 *UBV* observations were collected with the other APT operated by the APT Service. Both APTs are located in Arizona. Few more *UBV* observations were derived by the 0.4m telescope at the University of Toronto, Canada. Summary of the photometric observations is given in Table 3.1

Table 3.1: Summary of photometric observations. N denotes the number of observations

Author	N	Accuracy <i>in</i> $V, B - V$	Reference
Percy	300	not reported	Percy et al. 1988
Zsoldos	10	not reported	private communication
CAMC	124	0.05; --	Carlsberg 1985 – 1994
APT	220	0.006; 0.010	Genet et al. 1987

Table 3.2: Summary of the spectral data sets.

Region	Observational dates	HJD 2450950	N_{spec}	S/N
H_{α}	1998 June, 3 – July, 14	18.4 – 59.6	16	200
$H_{\alpha} + \text{CII}$	1998 Dec., 30 – May, 2	228.2 – 351.6	19	240
$H_{\alpha} + \text{CII}$	1999 Sept., 17 – Dec., 2	489.4 – 565.2	15	423
$H_{\alpha} + \text{CII}$	2000 March, 28 – June, 23	682.6 – 769.4	10	275
$H_{\alpha} + \text{CII}$	2000 Sept, 5 – Dec., 8	842.7 – 937.2	32	320
He I $\lambda 5876$	1999 March, 2 – April, 24	290.6 – 343.5	4	240
He I $\lambda 5876$	1999 Sept, 17 – Dec., 2	489.4 – 565.2	15	423
He I $\lambda 5876$	2000 March, 28 – June, 23	682.6 – 769.4	10	275
He I $\lambda 5876$	2000 Sept., 14 – Dec., 8	852.3 – 937.2	17	320

Spectroscopic data, consisting of 92 spectra centred on H_{α} and 46 on He I $\lambda 5876$, have been predominantly obtained with the coudé spectrograph of the 2m telescope of the National Astronomical Observatory, Bulgaria. Individual H_{α} observations were also secured at the Tartu Observatory, Estonia, using a 1.5-m reflector equipped with a Cassegrain spectrograph, and at Ritter Observatory, USA, with a 1-m telescope, fiber-fed échelle spectrograph. The resolution of these data ranges between 15 000 and 30 000 with a signal to noise ratio of 300 to 500.

The total time coverage of the spectra is from March, 1998 to December, 2000 with large gaps in the summer and the winter each year. The time sampling was typically 3 to 6 spectra per month, with a time-interval between successful exposures of 1 to 2 days, except for the fall of 2000 when HD 199 478 was monitored more intensively. The distribution of the data on time and spectral regions are given in Table 3.2. More information about the reduction strategy and the methods used can be found elsewhere (Markova & Valchev 2000; Markova et al. 2008).

3.3.2 Photospheric variability

Photometric evidence. The analysis of the collected photometric data indicates that the photometric

behaviour of HD 199478 is characterized by continuous irregular/multi-periodic variations with an amplitude of about 0.15 mag on a time-scale of 20 to 50 days. In some observational runs colour variations of up to 0.05 mag, in phase with the light curve, have been also observed while in others no colour variations were detected above the corresponding error. In these properties HD 199478 is similar to other OB SGs which also show small amplitude micro-variations in the visual, with little colour variations, on a time scale from days to months (see, e.g., Aerts et al. 1999; van Genderen 2001; Mathias et al. 2001). (For more detailed information about our photometric analysis see Percy et al. 2008.)

Spectroscopic evidence. The absorption lines due to C II $\lambda\lambda 6578.03, 6582.85$, He I $\lambda 6678$ and He I $\lambda 5876$ were used to probe the deep-seated variability, and photospheric structure in HD 199478 during the period covered by our observations.

To improve the internal consistency of the wavelength scale in the extracted spectra from different observatories, which is of crucial importance for the purposes of the time-series analysis, the C II and He I $\lambda 6678$ line profiles were realigned using the diffuse interstellar band at $\lambda 6613.6$ as a fiducial. Similarly, the interstellar line of Na I D $\lambda 5889.95$ was aligned for our study of profile changes in He I $\lambda 5876$. Following these adjustments, we estimate that the velocity scale local to each line profile is stable to $1-2 \text{ km s}^{-1}$. We are also confident that the C II lines are not severely affected by large fluctuations in the outer red wing of H_α , and for the photospheric analyses the C II lines were normalized to a local continuum assigned (using a low-order polynomial) between $\lambda\lambda 6570$ to 6590 \AA .

The shape of the TVS of C II and He I $\lambda 6678$ lines is double-peaked, suggesting existence of radial velocity variability (Fullerton, Gies & Bolton 1996). This possibility was confirmed by direct radial-velocity measurements which revealed changes in V_r with a peak-to-peak amplitude of 10 to 20 km s^{-1} . Parallel variations of $\sim 15\%$ in the total equivalent widths of the lines were also established. There is a tighter correlation between the strength and velocity changes seen in C II and He I $\lambda 6678$, than between either of these lines and He I $\lambda 5876$. The simultaneous appearance of radial-velocity and line-strength variations implies that the variability is more likely connected to changes in velocity and temperature structures of the stellar photosphere.

Periodic analysis. To search for periodicity in the behaviour of the analyzed absorption lines, we applied the CLEAN method (Roberts et al. 1987) to the measured radial velocities. The obtained power spectra did not reveal any strictly periodic signal that remains coherent between 1998 to 2000. There is instead some indication that the absorption lines are semi-modulated in their central velocities over time-scales of \sim weeks to months. The only signal in the 2000 power spectrum that is consistent between C II and He

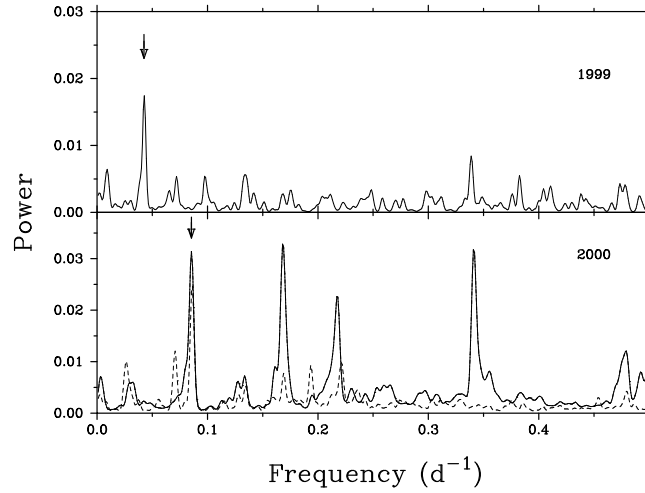


Figure 3.6: Power spectrum (in arbitrary units) for the C II (solid line) and He I $\lambda 6678$ photospheric absorption lines. The arrow marks the ‘stable’ peaks at ~ 11.7 days and 23.4 days.

I $\lambda 6678$ is at a frequency of $\sim 0.085 \text{ days}^{-1}$, i.e. a period of ~ 11.7 days (Figure 3.6). Interestingly, while in 1998 this modulation is essentially absent, in 1999 the strongest peak in the C II dataset at 0.0478 days^{-1} corresponds to precisely twice the 11.7 days period. No evidence for a 11.7 days or 23.4 days modulation was found in He I $\lambda 5876$, but this might still be due to the bad data-sampling.

Despite the high signal-to-noise and spectral resolution of our data, there is also no evidence for sub-features traveling blue-to-red (prograde) in the absorption troughs of the lines, that might for example be identified in terms of the presence of low-order non-radial pulsations.

Comparison between spectral and photometric variability. The 2000 photometry (differential *uvby* and *UBV*) of HD 199478, though not strictly simultaneous, covers the same time period as the corresponding spectroscopic data. The Fourier and self-correlation analyses of these data indicate the presence of a periodic variation of 18 ± 4 (*UBV*) to 21 ± 4 (*uvby*) days with an amplitude of about 0.15 mag. The colour curve of this micro variation is blue in the maxima and red in the minima of the light curve, thus resembling α Cyg variations in BA-SGs.

The estimated photometric period is somewhat larger, but still consistent (within 3σ) with the 11.7 day period variation in radial velocity of C II and He I $\lambda 6678$ photospheric lines. This finding strongly suggests that same physical mechanism (based in the stellar photosphere) is more likely responsible for the two phenomena observed, which might be identified as signatures of pulsations.

However, note that the interpretation of the photospheric variability of HD 199478 is not straightforward

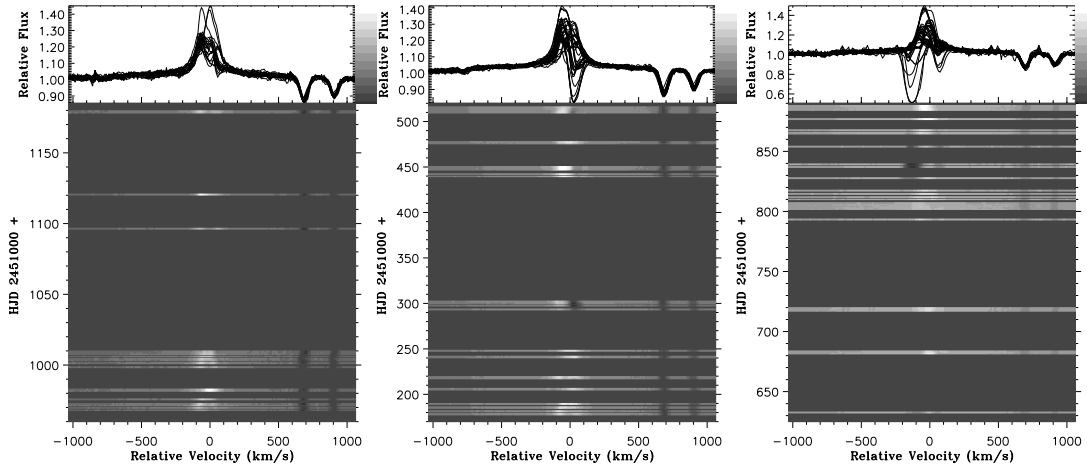


Figure 3.7: The 1998 (left), 1999 (middle) and 2000 (right) time-series of H_{α} shown as one-dimensional plots (top) and two-dimensional grey scale images (bottom). All spectra have been corrected for $V_{\text{sys}} = -12 \text{ km s}^{-1}$. Velocity scale given with respect to the rest wavelength of H_{α} .

in terms of pulsation. On the one hand, radial pulsations are not likely since the period is not stable between the observing runs carried out in different years, and since with only one exception, the estimated periods are longer than the radial fundamental pulsational period, $P_{\text{r}rad, \text{fund}} \sim 8$ days.

On the other hand, the irregular character of this variability is quite similar to that observed in other late B-SGs and A-type stars (Kaufer et al. 1997). One possible origin for these variations, at least for stars with M_{\star} lower than $40 M_{\odot}$, is the action of non-radial oscillation modes excited by the opacity mechanism.

In this respect, we note that:

- i) a period of about 20 days, as derived from photometric and spectroscopic data of HD 199 478, is fully consistent with the value inferred via the period-luminosity relation for B-type variables with excited g -mode oscillations (Fig. 2 in Waelkens et al. 1998);
- ii) on the HR diagram, and with parameters as derived with FASTWIND, HD 199 478 elegantly joins the group of B-type SGs studied by Burki (1978) for which g -mode instability is suggested to explain their variability (Fig. 3 of Waelkens et al. 1998.)

Therefore, non-radial g -mode oscillations might explain the photospheric variability of HD 199 478. But note again, the lack of evidence in our data for traveling blue-to-red (prograde) features within the absorption troughs of the lines, which normally betray non-radial pulsational behaviour.

Clearly, very extended time-series datasets are requisite for extracting reliable long period signals from the irregular absorption lines changes which characterize B SGs. These targets lend themselves obviously to modest-sized robotic telescopes equipped with high-resolution spectrographs.

3.3.3 Wind variability as traced by H_α

In Figure 3.7 the H_α time-series for 1998, 1999 and 2000 are shown in the form of two-dimensional gray-scale images. Above each of the velocity-time frames, the corresponding one-dimensional spectra are plotted to allow for an easy assessment of the size of the fluctuations at each velocity bin. Gaps between observations, if equal or larger than 1.0 day, are represented by black bands. All spectra have been corrected for systemic velocity, $V_{\text{sys}} = -12 \text{ km s}^{-1}$. The zero point in velocity corresponds to the rest wavelength of H_α .

From Figure 3.7 it is obvious that the H_α profile of HD 199 478 is strongly variable, exhibiting a large diversity of profile shapes and behaviour patterns. In particular, in June-July, 1998 as well as during the first two months of 1999, the profile has appeared fully in emission evolving from a double-peak morphology with a blue component, being somewhat stronger than the red one, to a single-peaked feature centred almost at the rest frame. Some hints about further development of this feature to the red seem also to be present. Three such cycles have been identified: the first - between HJD 2450 968-982; the second - between HJD 2450 998-1009, and the third - between HJD 2451 178-189. One more cycle taking place between HJD 2451 217-247 can be easily recognized in March, 1999. This finding implies that the variability pattern described above is relatively stable (over at least 9 months) with a characteristic time-scale of about 15 days, and a possible re-appearance after one month, or longer.

Another variability pattern, where H_α appears not only in emission, but also in absorption (partly or completely), can be identified during the 1999 and 2000 observations. In particular, on HJD 2451 293 (April 24, 1999) in addition to the blue-shifted emission ($V_r = -75 \text{ km s}^{-1}$) a slightly red-shifted absorption feature ($V_r = +40 \text{ km s}^{-1}$) has appeared giving rise to a reverse P Cygni profile. The latter persisted for at least 8 days, growing slightly stronger in intensity.

High-velocity absorptions. The 2000 observations (right panel of Figure 3.7) have revealed the presence of another unusual event during which H_α changes suddenly and drastically from pure emission to pure absorption, and back to pure emission. By chance, the distribution of the available observations in time was quite good allowing the development of this spectacular event to be followed in more detail.

In particular, from Figure 3.8 it is apparent that before the onset of the high-velocity absorption (HVA) event H_α has occurred fully in emission, developing from a double-peaked to a single-peaked morphology, and strengthening slightly with time (HJD 2451 792-816). On HJD 2451 827, in addition to the emission, a localized blue-shifted ($V_r = -150 \text{ km s}^{-1}$) absorption extending from -68 to -250 km s^{-1} appears making the profile appear P Cygni-like. Over the next 9 days, the P Cygni feature evolves into double absorption with central emission, where the blue component is significantly stronger and wider than the red one. Two weeks

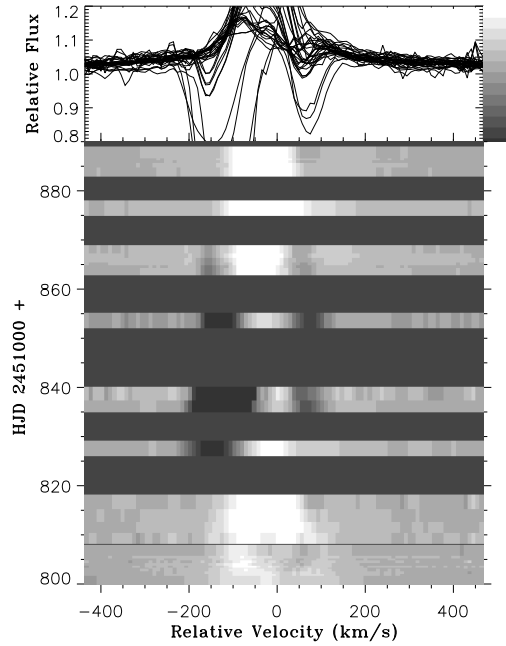


Figure 3.8: HVA event observed in the H_α data of HD 199478 in 2000.

later (HJD 2 451 863), the morphology of the profile is still the same though the blue component is weaker and narrower while the red one has apparently strengthened becoming somewhat wider. Subsequently, the two absorptions are fading in parallel and disappear completely on HJD 2 451 877.

Interestingly, our observations suggest that the absorption event seen in the H_α time-series of HD 199478 between HJD 2451 827 – 876 may not be unique. Indeed, readers should note that on HJD 2451 632 (see right panel of Figure 3.7) H_α has also appeared as a double absorption feature. Unfortunately, due to poor temporal coverage, the time development of this feature cannot be followed, but given the similarity in the morphology of this profile, and the one taken, e.g., on HJD 2451 853, we are tempted to speculate that about 6 months earlier an absorption phenomena similar to the one recorded in September - October 2000 may have occurred in this star.

A comparison of our Figure 3.8 with similar results from Kaufer et al. (1996a,b) shows that the spectacular absorption event seen in H_α of HD 199 478 is qualitatively similar to those observed in HD 34 085 (B8 Ia, β Ori), in HD 91 619 (B7 Ia) and in HD 96 919 (B9 Ia), with one exception though: in our data-set the blue and the red-shifted absorption components do not merge to form an extended blue-to-red absorption, as is the case of the objects of Kaufer et al., but instead occur parallel to each other (though we accept the caveat that a more intensive and extended dataset is required ideally).

The fact that such a spectacular phenomenon as HVAs in H_α has been so far observed in 4 late-B SGs with peculiar emission in H_α is quite interesting and deserves special attention since it might point out to

Table 3.3: Properties of HVAs in H_α observed in 3 late-B SGs. Data for HD 34 085 and HD 96 919 are taken from Kaufer et al. (1996b). All velocities, measured with respect to the stellar rest frame, are given in units of the corresponding wind terminal velocities

	HD 34 085	HD 96 919	HD 199 478
Signature	1994	1995	2000
MJD of max. blue depth	2449493	2449792	2451836
Max depth in % of cont	20	70	49
Vel. of max. depth	0.40...0.60	0.29...0.43	0.37...0.76
Blue-edge velocity	0.79...1.20	0.43...0.64	0.68...1.39
Red-edge velocity	0.34...0.52	0.32...0.48	0.41...0.84
Rise time of W_λ [d]	11	21	22
Decay time of W_λ [d]	20	46	33
Duration of event [d]	40	90	55

some fundamental property of the winds of these stars. With this in mind we followed Kaufer et al. (1996b) and measured the main properties of the 2000 HVA in H_α of HD 199 478 at the time of its maximum intensity.

The derived estimates are listed in Table 3.3 together with similar data for HD 34 085 and HD 96 919 (from Kaufer et al. 1996b). The comparison of these data shows that the HVA in HD 199 478 is of intermediate duration and strength. Its development in time is roughly consistent with results from Kaufer et al., which show rising times that are smaller than the time of decay.¹

The data listed in Table 3.3 suggest that the duration of a HVA event likely depends on its maximum strength (stronger maximum absorption – longer duration), while its development in time (rising time vs time of decay) appears to be independent of this parameter. In addition, the blue-edge velocity and the velocity of maximum depth of a HVA event may anti-correlate with its strength, i.e., stronger features tend to reach maximum depth at lower velocities being less extended in velocity space than weaker ones. Furthermore, and as also noted by Israelian et al. (1997), the maximum positive velocity of a HVA is always lower than the corresponding maximum negative velocity. However note that due to the limited number of stars, these results can only be regarded as suggestive and they have to be confirmed with improved statistics.

3.3.4 Summary

Based on optical spectroscopic and photometric data-sets secured between 1999 and 2000, a quantitative analysis of time-variable phenomena in the photospheric, near-photospheric, and wind regions of the late-B supergiant (SG) HD 199 478 was performed. The primary objective was to provide new perspectives on the nature of outflows in late-B SGs, and on the influence of large-scale structures rooted at the stellar

¹This result has to be considered with caution since the exact time of maximum depth absorption in HD 199 478 is not known with confidence due to limited time-series coverage.

surface. The results derived throughout this project are presented in Markova & Valchev (2000), Markova et al. (2008), Austin et al. (2008), Percy et al. (2008) and Markova & Markov (2008). The main outcomes show that the temporal behaviour of HD 199 478 is characterized by two key empirical properties:

- (i) *photospheric variability* which manifests itself as irregular/multi-periodic changes in the stellar brightness whose properties resemble those of α Cyg variations in BA-SGs, and as systematic low-amplitude variations in line-strengths and core velocity of photospheric absorption lines. Non-radial g -mode oscillations excited by the opacity mechanism seems to be the most plausible mechanism to explain the photospheric variability of HD 199 478.
- (ii) *continuous deep-seated wind variability* which gives rise to peculiarly strong blue- and red-shifted emission with cyclic V/R variations similar to those in Be-stars. Variations of this type suggest presence of large-scale asymmetries in the wind of the star (see next section).
- iii) *occasional episodes of strong wind absorption* indicating simultaneous mass *infall* and *outflows*. In these properties HD 199 478 resembles few other late-B SGs, namely HD 91 619, HD 34 085, HD 96919. In the next section I will consider and largely discussed various possibilities to interpret the peculiar behaviour of these stars.

3.4 Wind structure in late B-SGs

Extensive monitoring campaigns of several late-B SGs, namely HD 199 478 (Markova & Valchev 2000; Markova et al. 2008) and HD 91 619, HD 34 085 and HD 96 919 (Kaufer et al. 1996a,b, 1997; Israelian et al. 1997), indicate that their H_α profiles exhibit quite similar peculiarities consisting of a double-peaked emission with V/R variations, and occasional episodes of strong absorption indicating *simultaneous mass infall and outflows*.

The investigation of these stars by means of a complete spectral analysis performed with FASTWIND (Markova et al. 2008) has shown that such line signatures cannot be reproduced in terms of the standard (i.e. *non-rotating, spherically symmetric, smooth*) wind models, which instead predict profiles in absorption partly filled in by emission at this temperature regime. Consequently, axially symmetric, disc-like envelopes (Kaufer et al. 1996a; Markova & Valchev 2000); episodic, azimuthally extended, density enhancements in the form of co-rotating spirals rooted in the photosphere (Kaufer et al. 1996b), or closed magnetic loops similar to those in our Sun (Israelian et al. 1997) have been suggested to account for the peculiar behavior of H_α in these stars.

3.4.1 Pulsations

Results of 2D hydrodynamical simulations (Cranmer & Owocki 1996) showed that “bright/dark” spots on the stellar surface can effectively enhance/reduce the radiative driving, leading to the formation of high/low-density, low/high-speed streams. Consequently, a specific wind structure, called Corotating Interaction Region (CIR) structure, forms where fast material collides with slow material giving rise to traveling features in various line diagnostics (e.g., Discrete Absorption Components in UV resonance lines of O stars, cf. Kaper et al. 1996). The CIR scenario for the case of a “bright” surface spot in a rotating O-star is schematically illustrated in Figure 3.9.

It is generally mooted that non-radial pulsations (NRPs) and surface magnetic spots may equally be responsible for creating large-scale inhomogeneities in hot star winds (Fullerton, Gies & Bolton 1996).

For the four late-B SGs discussed here, non-radial pulsations due to g -modes oscillations have been suggested to explain absorption LPV in their spectra (Kaufer et al. 1997; Markova & Valchev 2000). This explanation is supported by more recent results which indicate that on the HR diagram, and for parameters derived with FASTWIND, these stars fall exactly in the region occupied by known variable B-SGs, for which g -modes instability was suggested (Markova et al. 2008). In addition, and at least in HD 199 478, the photometric variability seems to be consistent with a possible origin in terms of g -mode oscillations (Percy et al. 2008). Thus, it seems likely that these late-B SGs are non-radial pulsators. Extensive, high-quality

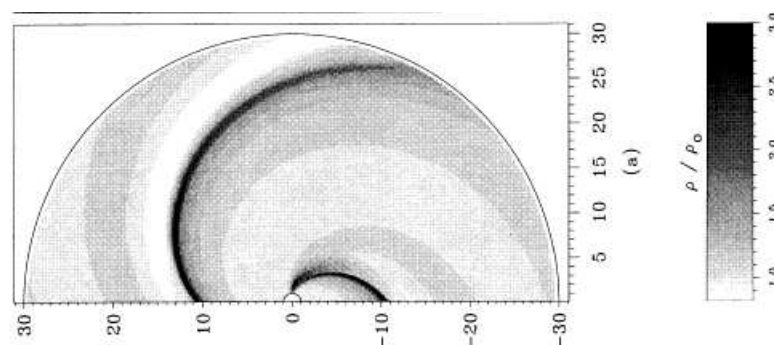


Figure 3.9: CIR structure created by a “bright” spot on the surface of a rotating O star. (adopted from Cranmer & Owocki (1996))

data-sets are needed to investigate this possibility further. However note that for any of these objects no clear evidence of any causality between photospheric and wind variability (as traced by H_α) has been so far derived. Note also that the variability patterns observed in H_α do not give any evidence of migrating red-to-blue features, as those expected to originate from a CIR structure.

3.4.2 Magnetic fields

An alternate possibility exists that magnetic fields can be responsible for the appearance of large-scale structures and wind asymmetries in hot stars. In particular, magneto-hydrodynamical (MHD) simulations for rotating O and early-B stars (plus a magnetic dipole aligned to the stellar rotation) showed that depending on the magnetic spin-up, an equatorial compression, dominated by radial *infall* and/or *outflows* can be created, with no apparent tendency to form a steady, Keplerian disc (Owocki & ud-Doula 2003; ud-Doula et al. 2008).

Indeed, due to the lack of strong convection zones associated with hydrogen recombination, normal (i.e. without any chemical peculiarities) hot stars are not generally thought to be magnetically active. However, theoretical considerations (e.g., Cassinelli & Macgregor 2000) supported by more recent observations (Bychkov 2003; Hurbig et al 2005, 2007) indicate that this may not necessarily be true and that relatively strong, stable, large-scale dipole magnetic fields are present in different groups of B stars (e.g., SPB, Be, β Cep itself etc.)

Thus, it seems likely that in, at least some, hot stars magnetic fields can be an alternative source of wind perturbations and asymmetries. And although the four late-B SGs discussed here have not been recognized so far as magnetically active stars (except for HD 34 085, see below), the potential role of magnetic fields in these stars remains intriguing, especially because it might provide a clue to understand the puzzling problem of the simultaneous presence of red- and blue-shifted absorptions/emissions in their H_α profiles.

Table 3.4: Magnetic field strength, B (in G), required to get an equatorial confinement with simultaneous mass infall and outflows around each of our targets. The Keplerian, R_K , the Alfven, R_A , and the escape, R_E , radii (in units of R_\star above the photosphere) are calculated following Owocki & ud-Doula (2003). The HD 34 085 estimates correspond to the 2nd entry in

Parameters	91 619	199 478	34 085	96 919
R_K	0.37	0.45	0.38	0.42
R_A	0.83..3.73	0.77..4.59	0.83..3.79	1.0..4.13
R_E	3.77	4.58	3.81	4.18
B ($R_K < R_A < R_E$)	5..100	5..180	5..105	5..85

To investigate this possibility further, I have employed the scaling relations of Owocki & ud-Doula (2003) and calculated the Alfven, R_A , the Keplerian, R_K , and the “escape”, R_E , radii of the four stars, using data for their stellar and wind parameters as derived by Markova et al. (2008), and fixing the magnetic field strength at the values required to create an equatorial confinement. Interestingly, the results listed in Table 3.4, show that in all four cases a very weak dipole magnetic field is required to effectively channel the wind outflows, leading to the formation of an equatorial compression with simultaneous radial mass infall and outflow.

Guided by these prospectives, MHD simulations for the case of our targets have been recently initiated. The preliminary results derived for HD 199 478 (see Fig. 3.10) are quite promising showing in particular that a pure dipole magnetic field of only a few tens of Gauss can effectively structure the wind of this star leading to the formation of *cool* equatorial compression with mass infall and outflow.

Thus, it appears that very weak dipole magnetic fields can be responsible for creating wind structures in the envelopes of late-B SGs. An obvious advantage of this hypothesis is that it has the potential to account for, at least qualitatively, some of the puzzling properties of H_α of our targets. In particular, the sudden appearance of red and blue-shifted absorptions might be explained if one assumes that during this event the plasma in the infalling/outflowing zones of the compression can become optically thick in the *Lyman* continuum and L_α thus forcing H_α to behave as a resonance line, i.e., to absorb and emit line photons. The kinematic properties of the resulting absorption features² are difficult to predict from simple qualitative considerations, but it is clear that these properties cannot be dominated by stellar rotation, but instead will be controlled by the physical conditions inside the compression.

Concerning the interpretation of the peculiar H_α emission, the situation is more complicated since such emission can originate from different parts of the envelope under quite different physical conditions. For example, one can expect that the cool, less dense plasma outside the compression will only emit line photons (via recombinations), producing pure emission feature(s) in H_α . Also, the cool equatorial compression

²(Depending on the size of the H_α forming region emission may not appear in the spectrum.)

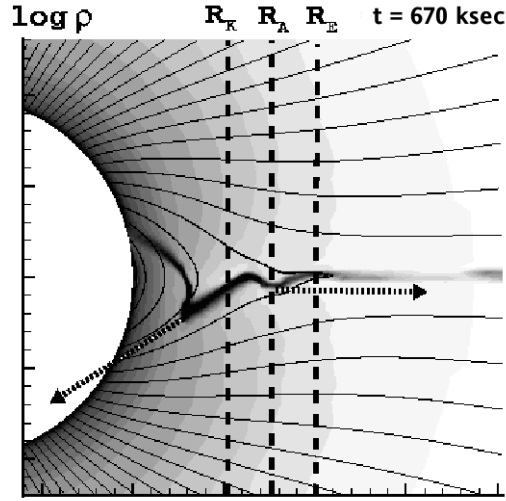


Figure 3.10: Density stratification for a model with stellar and wind parameters typical for O stars 670 ksec after the initial introduction of a dipole magnetic field. The arrows illustrate the upward and downward flow direction of dense material above and below the Keplerian radius (from ud-Doula and Owocki Owocki & ud-Doula (2003)). The results for late-B SGs models are qualitatively similar.

might contribute to the H_α emission providing the plasma inside the compression can occasionally become optically thin in this line. However, note that even a plasma that is optically thick in $L\alpha$ and the Lyman continuum can, under specific conditions, produce *pure* emission profiles in H_α (e.g., *if* collisions dominate the H_α formation, or *if* due to some reasons the 2nd and 3rd levels of Hydrogen go into LTE (Petrenz and Puls 1996)).

Additional observations to prove/disprove the presence of weak magnetic fields can help to clarify the picture. Of course, due to the low strength of the magnetic fields required, one cannot expect to detect these fields directly, but indirect evidence such as e.g., the detection of X-ray emission, abundance anomalies, specific periodic variations in UV resonance lines, interferometric observations (for more information see Henrichs 2001), might also be considered. Here, we feel it important to note that a weak longitudinal magnetic field of about 130 ± 20 G, was actually detected in HD 34 085 (β Ori) (Severny 1970).

Finally, let me point out that at the cooler edge of the B-star temperature regime pure emission profiles in H_α can be accounted for if one assumes the winds are *clumped*. Indeed, a spherically symmetric, clumped wind will mimic wind densities higher than the actual ones, thus giving rise to strong line emission, similar to that in O stars. Such winds may also give rise to wind absorption, providing some of the clumps are optically thick in H_α . Detailed numerical simulations and line formation calculations are required to discriminate between the different possibilities. (More detailed discussion about HVA phenomena in late B-SGs can be found in Markova et al. 2008 and Markova & Markov 2008.)

3.5 Statistical approach to study wind variability

Wind structures and temporal variability are among the most important physical processes that may significantly modify the mass-loss rates derived from observations. Since accurate mass-loss rates are crucial for evolutionary studies (e.g., Meynet et al. 1994), and for extra-galactic distance determinations (via the Wind Momentum Luminosity Relationship (WLR), cf. Kudritzki & Puls 2000), it is particularly important to know to what extent the outcomes of these studies might be influenced by uncertainties in \dot{M} due to the effects of wind structures and variability. Indeed, Kudritzki (1999) has noted that wind variability is not expected to affect the concept of the WLR significantly. However, this suggestion is based on results obtained via a detailed investigation of *one* object only, while similar data for a large number of stars of different spectral types and luminosity classes are needed to resolve the problem adequately.

Following the outlined reasoning, a project to study wind variability in a large sample of Galactic O-type stars has been initiated and worked out by me, in collaboration with colleagues from the University Observatory Munich, Germany, and the Catania Observatory, Italy. As a result, a statistical approach to detect and quantify variations in spectral lines affected by wind emission was developed, and subsequently used to address the important questions (i) of the dependence (if any) of O-star wind variability on fundamental stellar and wind parameters, and (ii) of the impact of this variability on the estimated mass-loss and wind-momentum rates. In this section, main results derived throughout this investigation will be described and commented. Complete information about the project and its outcome can be found in Markova et al. (2005).

3.5.1 Observational material

The sample consists of 15 Galactic supergiants with spectral classes from O4 to O9.7, all drawn from the list of stars analyzed by Markova et al. (2004) in terms of their mass-loss and wind momentum rates. Table 3.5 lists the objects along with some of their stellar and wind parameters, as used in the present study.

A total of 82 high-quality H_α spectra ($R = 15\,000$) of the sample stars were collected between 1997 and 1999. The observations were obtained at the Coudé focus of the 2m RCC telescope at the National Astronomical Observatory (Bulgaria) using an ELECTRON CCD ($520 \times 580, 22 \times 24 \mu$) and a PHOTOMETRIC CCD ($1024 \times 1024, 24 \mu$).³ For all stars but one, the S/N ratio, averaged within each spectral time series, lies between 150 to 250, while in the case of HD 190429 it is ~ 100 .

The temporal sampling of the data for each target is not systematic but random, with typical values of the

³The use of different detectors is not expected to bias the homogeneity of our sample because the noise characteristics of these two devices are practically the same. The root-mean-square (*rms*) read-out noise of the ELECTRON CCD is 3 electrons per pixel (i.e. 1.5 ADU with 2 electrons per ADU) while the *rms* read-out noise of the PHOTOMETRIC CCD is 3.3 electrons per pixel (2.7 ADU with 1.21 electrons per ADU).

Table 3.5: Stellar and wind parameters of the sample stars used in the present study. All data are taken from Markova et al. (2004).

Object	Sp	V_{sys}	T_{eff}	R_{\star}	$\log g$	Y_{He}	$\log L$	$v \sin i$	v_{∞}	β
HD 190 429A	O4If+	-36	39 200	20.8	3.65	0.14	5.97	135	2 400	0.95
HD 16 691	O4If	-51	39 200	19.8	3.65	0.10	5.92	140	2 300	0.96
HD 14 947	O5If	-56	37 700	25.6	3.56	0.20	6.08	133	2 300	0.98
HD 210 839	O6If	-71	36 200	23.0	3.48	0.10	5.91	214	2 200	1.00
HD 192 639	O7Ib(f)	-7	34 700	17.2	3.39	0.20	5.59	110	2 150	1.09
HD 17 603	O7.5Ib(f)	-40	34 000	25.2	3.35	0.12	5.88	110	1 900	1.05
HD 24 912	O7.5I(f)	59	34 000	25.2	3.35	0.15	5.88	204	2 400	0.78
HD 225 160	O8Ib(f)	-40	33 000	22.4	3.31	0.12	5.73	125	1 600	0.85
HD 338 926	O8.5Ib	-9	32 500	22.7	3.27	0.12	5.72	80	2 000	1.00
HD 210 809	O9Iab	-90	31 700	19.6	3.23	0.14	5.54	100	2 100	0.91
HD 188 209	O9.5Iab	-16	31 000	19.6	3.19	0.12	5.51	87	1 650	0.90
BD+56 739	O9.5Ib	-5	31 000	19.6	3.19	0.12	5.51	80	2 000	0.85
HD 209 975	O9.5Ib	-18	31 000	19.2	3.19	0.10	5.49	90	2 050	0.80
HD 218 915	O9.5Iab	-84	31 000	19.6	3.19	0.12	5.51	80	2 000	0.95
HD 18 409	O9.7Ib	-51	30 600	15.7	3.17	0.14	5.29	110	1 750	0.70

minimum and maximum time intervals between successive spectra of 1 to 2 and 7 to 8 months, respectively. In several cases, observations with a time-resolution of 1 to 5 days are also available, but in none of these cases these observations dominate the corresponding time series. Thus, we expect the results of our survey to be sensitive to variations that occur on a time-scale significantly larger than the corresponding wind flow time (of the order of a couple of hours).

3.5.2 Methodology and measurements

Since we were going to study a large number of objects, and since in many cases our observations were not systematic, but with large temporal gaps in between, from the onset of this investigation we recognized that our ability to characterize the wind variability of individual targets would be restricted, e.g., we would not be able to determine time-scales and variability patterns. Moreover, to work effectively, we would need to employ some simple and fast method both to detect and quantify line profile variability (LPV) and to constrain the properties of this variability as a function of fundamental stellar and wind parameters of the sample stars.

In the previous sections of this chapter, the TVS analysis (Fullerton, Gies & Bolton 1996) was widely used to *detect* and *follow* LPV in various lines of α Cam and HD 199 478. However, note that this technique was initially designed to handle LPV in *pure absorption* lines. Thus, its implication for the objectives of a *comparative* analysis of lines influenced to a different extent by wind emission may not be completely justified.

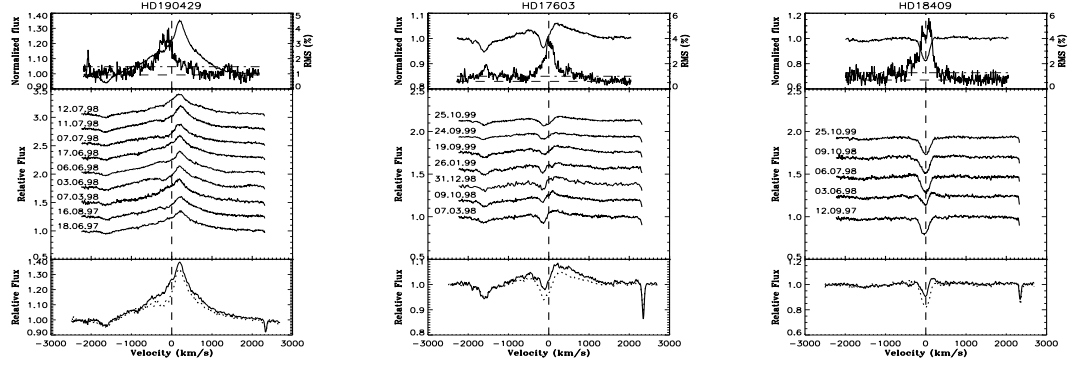


Figure 3.11: Results for two typical objects in our sample. *Upper part of each panel:* Mean H_α profiles (thick line) and RMS deviations as a function of velocity across the line. *Middle part of each panel:* Time-series of observed H_α profiles. *Lower part of each panel:* H_α profiles with maximum and minimum wind emission in the time series. Velocity scale centered at the corresponding systemic velocity.

Guided by these perspectives we decided to modify the main philosophy of the TVS analysis in order to take into account the effect of wind emission.

Calculating the TVS. To compute the TVS of H_α as a function of velocity across the line, and to determine the velocity width over which *significant* variability occurs, ΔV , we followed the original approach of Fullerton, Gies & Bolton (1996), but assumed that the noise is dominated by photon noise.⁴ In this case, the TVS for the pixels in column j (i.e., at wavelength/velocity j) is calculated from

$$TVS_j = \sum_i^N \frac{w(i)(S_{ij} - \overline{S}_j)^2}{S_{ij}(N-1)} \quad (3.1)$$

where \overline{S}_j is the weighted mean spectrum for the j -th pixel, averaged over a time series of N spectra, and given by

$$\overline{S}_j = \frac{\sum_i^N S_{ij} w_i}{N}. \quad (3.2)$$

In the above expressions w_i are the weighting factors given by

$$w_i = \left(\frac{\sigma_0}{\sigma_{ic}} \right)^2 \quad (3.3)$$

with

$$\sigma_0 = \left(\frac{1}{N} \sum_i^N \sigma_{ic}^{-2} \right)^{-1} \quad (3.4)$$

and σ_{ic} , the value of the noise in the i -th spectrum, averaged over a certain number of continuum pixels (40 in our case).

⁴This assumption seems to be justified because we rely on Coudé spectra of relatively high quality.

The *RMS* deviations ($RMS = TVS^{0.5}$) as a function of velocity across H_α for the time series of 3 representative targets (HD 190 603, O4If; HD 17 603, O7.5Ib and HD18409, O9.7Ib) are shown in the top panels of Figures 3.11. The level of deviations in the continuum, σ_0 , is represented by a dashed line; the threshold of *significant* LPV, fixed at the corresponding 99% confidence level, is marked with a dashed-dotted line. I want to stress here that although our implementation is in terms of $TVS^{0.5}$, hereafter we shall continue to refer to the “TVS” and the “TVS analysis”, respectively.⁵

“Blue” and “red” velocity limits, v_b and v_r . To localize LPV in velocity space we used the “blue” and “red” velocity limits of *significant* variability introduced by Fullerton, Gies & Bolton (1996). These quantities were measured interactively by fixing the positions of the two points where the TVS crosses the horizontal line representing the threshold of *significant* LPV. The accuracy of our measurements depends on the quality of the used data, and on the strength of LPV. For example, in the limiting case of a strong LPV (i.e., a TVS with large amplitudes and steep spectral gradients), the accuracy of the individual measurements might be as good as $\pm 20 \text{ km s}^{-1}$.

Alternatively, in the case of a weak LPV (e.g., with amplitudes just above the threshold of *significant* variability), the determination of the velocity limits might become so uncertain that different positions of almost similar probability may exist for each limit. In these latter cases, and in order to assess the effects of such uncertainties on the outcomes of our analysis, we provide two couples of estimates for v_b and v_r . These two sets of values, expressed in km s^{-1} , are listed in Column 6 of Table 3.6 as a first and a second entry. We consider the first entry as the more reliable one, and will refer to it as the “conservative case”.

Total velocity width, ΔV . As a by-product of the measurement of v_b and v_r , we obtain the total velocity width over which *significant* variability in H_α occurs, $\Delta V = (v_r - v_b)$. In order to find some constraints on the distribution of the LPV in *physical* space, we furthermore determined the radial distance r_{\max} , where $v(r = r_{\max}) = v_b$, assuming the wind velocity obeys a standard law of the form

$$v(r) = v_\infty \left(1 - b \frac{R_\star}{r}\right)^\beta, \quad (3.5)$$

$$b = 1 - \left(\frac{v_{\min}}{v_\infty}\right)^{1/\beta}, \quad (3.6)$$

with β and v_∞ from Table 3.5 and $v_{\min} = 1.0 \text{ km s}^{-1}$. The obtained estimates of r_{\max} , expressed in units of R_\star , are given in Column 7 of Table 3.6. We are aware of the fact that emission variability is difficult to localize, and could in principle be due to the net effect of fluctuations that occur in different locations under

⁵Root mean square deviations have been used instead of the TVS itself since the former quantity scales linearly with the size of the deviations. Thus, it is more appropriate for a direct comparison of the strength of LPV in various stars (see also Fullerton et al.).

different conditions, and therefore consider these estimates as upper limits only.

Mean and fractional amplitude of deviations. To quantify and compare LPV, Fullerton, Gies & Bolton (1996) have introduced two parameters, called mean and fractional amplitude of deviations. (In the following we will refer to these quantities as to A_F and a_F with ‘‘F’’ referring to Fullerton). The first parameter is expressed in units of the normalized continuum flux, while the second one is a dimensionless quantity. The authors define these quantities as follows:

$$A_F = \frac{1}{\Delta V} \int_{v_b}^{v_r} TVS_j^{0.5} dv \quad (3.7)$$

$$a_F = \frac{100 \int_{v_b}^{v_r} (TVS_j - \sigma_0^2)^{0.5} dv}{\int_{v_b}^{v_r} |\bar{S}_j - 1| dv} \quad (3.8)$$

From the above expressions it is clear that while, A_F is *independent* of profile type and can therefore be used for deciding the statistical significance of LPV both in absorption and in emission profiles, a_F depends (via the denominator) on the strength of the underlying spectral feature without making any difference between profiles in absorption and in emission. Thus, a_F is *inappropriate* for investigating profiles, which are influenced by wind emission of different extent.

Fractional amplitude, a_N . In order to optimize the fractional amplitude to account for the systematic difference in the strength of H_α as a function of wind strength, we normalized the integral over the TVS to a quantity which we called ‘‘Fractional Emission Equivalent Width’’ (FEEW). With this new definition of the fractional amplitude, now denoted by a_N to distinguish it from Fullerton’s parameter a_F , this quantity is a measure of the *observed degree of variability per unit fractional wind emission*. ‘‘Fractional’’ refers here to the observed range of significant variability, $[v_b, v_r]$. Formally, a_N is given by⁶

$$a_N = \frac{100 \int_{v_b}^{v_r} (TVS_j - \sigma_0^2)^{0.5} dv}{\int_{v_b}^{v_r} (\bar{S}_j - 1) dv - \int_{v_b}^{v_r} (S_j^{\text{phot}} - 1) dv} \quad (3.9)$$

The first term in the denominator of Eq.3.9 represents the fractional equivalent width of the observed profile (positive for emission and negative for absorption), while the second one gives the fractional equivalent width of the photospheric component of H_α (always negative). In total, the denominator thus gives the fractional *wind* emission (always positive).

⁶In this expression only the uncertainty caused by the photon noise is taken into account, while the error due to small differences in the continuum level of individual spectra in a given time series is neglected.

Mean amplitude, A_N . The mean amplitude, as defined by Eq. 3.7 does not seem to pose any problem concerning an assesment of the statistical significance of variability across H_α . In their original study, Fullerton et al. have noted that this quantity *cannot* serve as a comparative tool because it does not account for differences in the strength of the underlying absorption feature. In contrast, in the case of H_α from O-type SGs the mean amplitude *might depend* on the wind strength⁷, and might therefore become of interest as well, in order to examine and compare the wind variability in stars of various spectral types.

Motivated by this possibility, we re-defined the mean amplitude to account (partially) for differences in the overall quality (i.e., in S/N) of the time series of the sample stars, by subtracting σ_0^2 from the TVS,

$$A_N = \frac{100}{\Delta V} \int_{\nu_b}^{\nu_r} (TVS_j - \sigma_0^2)^{0.5} d\nu. \quad (3.10)$$

The *photospheric profiles* of H_α required to derive the values of a_N have been selected from a grid of plane-parallel models in dependence of the particular stellar parameters (Table 1, see also Markova et al. (2004)). Note that the (relative) uncertainty of the denominator becomes rather large in those cases where the wind-emission is only marginal, since in this case the errors introduced by uncertainties in the stellar parameters (affecting the actual choice of the photospheric profiles) become significant.

Accuracy of the mean amplitude determinations, $\sigma(a_N)$. To estimate the uncertainty in a_N , we followed Fullerton, Gies & Bolton (1996), but used a re-formulation (derived by A. Fullerton, priv. com.) of Eq. 16. Additionally, we assumed that the errors in both σ_0 and FEEW are negligible, and that the accuracy of the deviations for each pixel j within H_α is identical and equals σ_0 .⁸ Under these circumstances, standard error propagation gives:

$$\begin{aligned} \sigma(a_N) &= \frac{100 \sigma_0^2 \Delta v}{FEEW} \left[\frac{1}{2(N-1)} \right]^{0.5} \times \\ &\times \left[\sum_j^n \frac{1}{TVS_j - \sigma_0^2} \right]^{0.5} \end{aligned} \quad (3.11)$$

where j runs over all the pixels between ν_b and ν_r , while N and Δv denote the number of spectra in the time series and the discretized integration step, respectively. In our case $\Delta v \sim 9 \text{ km s}^{-1}$ (To not be confused with the total velocity width ΔV !).

The factor of 100 appearing in Eqs. 3.8 to 3.11 converts the corresponding quantities to a percentage. The estimates of σ_0 , A_N and $a_N \pm \sigma(a_N)$ for each sample star are listed in Table 3.6, Columns 5, 13 and 14,

⁷E.g., the numerator in Eq. 3.7 is expected to react on wind density (the higher the density the larger the emitting volume).

⁸The latter assumption is justified since we rely on Coudé spectra of relatively high signal to noise ratio.

respectively.

Net H_α emission. To assess the contribution of changes in H_α line strength to the LPV detected by the TVS analysis, we estimated the mean value of the net wind emission, $\overline{W_{em}}$, by subtracting the equivalent width (EW) of the photospheric profile, W_{phot} , from the EW of the time-averaged observed profiles.

The observed equivalent widths were measured integrating the line flux between limits which were set interactively, judging by eye the extension of the emission/absorption wings. These limits did not change for a given star, but they could for different stars. The internal precision of individual EW measurements, estimated in the way described in Markova & Valchev (2000), is better than 10%. The EW of the photospheric component was calculated by integrating over the appropriate synthetic profiles. The $\overline{W_{em}}$ estimates and their (standard) error are given in Column 8 of Table 3.6, together with the EW of the photospheric components.

Contribution of absorption LPV. Since in O-type SGs H_α originates from processes taking place in the wind *and* in the photosphere, contributions from *absorption* LPV to the observed LPV might be expected (via the photospheric components of H_α and He I $\lambda 5876$). To investigate this possibility, we consulted the literature concerning the presence of absorption LPV in our sample. In addition, and as a secondary criterion, we used the TVS of the He I $\lambda 6678$ absorption line located in close proximity to H_α . In those cases where the results of our TVS analysis of He I $\lambda 6678$ did not agree with the results from the literature, the latter were adopted.⁹ The results of this analysis are listed in column 3 of Table 3.6.

Mass-loss rate variability. To obtain constraints on the variability of mass-loss rate, for each star we determined lower and upper limits for \dot{M} . This has been done by fitting the H_α profiles with the smallest and the largest wind emission present in the time-series, by means of synthetic profiles. These have been calculated using stellar and wind parameters from Table 3.5, and employing the approximate method described and used in Chapter 2, Sect. 2.1. The accuracy of the \dot{M} determinations equals $\pm 20\%$ for stars with H_α in emission, and $\pm 30\%$ for stars with H_α in absorption (Markova et al. 2004). The estimates of \dot{M}_{min} and \dot{M}_{max} as well as the amplitude of the \dot{M} variability (given in percent of \dot{M}_{min}) are listed in Columns 9 to 11 of Table 3.6.

⁹Such inconsistencies may occur because the time sampling of our observations is not well-suited for studying LPV on short time scales (e.g., hours) which seem to be typical for absorption LPV in O-type stars (Fullerton, Gies & Bolton 1996).

Table 3.6: H_α line profile and variability parameters. Objects ordered as in Table 3.5. N denotes the number of used spectra. v_e is the velocity of the emission peak while v_b , v_r are the “blue” and “red” velocity limits of significant variability. All velocities (in km s^{-1}) are measured with respect to the stellar rest frame. σ_0 is the standardized dispersion of the corresponding time-series multiplied by 100. r_{max} (in R_\star) denotes the upper limit in physical space where significant variations in H_α are present. $\overline{W_{\text{em}}}$ is the mean equivalent width of net wind emission and its standard deviation, both given in \AA . W_{phot} is the equivalent width of the photospheric component. \dot{M}_{min} and \dot{M}_{max} (in $10^{-6} M_\odot/\text{yr}$) denote the corresponding limits if the observed variability is attributed to variations in \dot{M} alone, while $\Delta\dot{M}$ is the amplitude of this variability expressed in percents of \dot{M}_{min} . $\langle \rho \rangle$ is the mean wind density (Eq. 3.12), and A_N and a_N are the mean and the fractional amplitudes, respectively.

#	N	lpv	v_e	σ_0	$[v_b, v_r]$	r_{max}	$\overline{W_{\text{em}}}/W_{\text{phot}}$	\dot{M}_{min}	\dot{M}_{max}	$\Delta\dot{M}$	$\log \langle \rho \rangle$	A_N	a_N
1	9	no	210	0.93	[-491, 234] [-491, 363]	1.23	10.99±0.63/3.2	13.0	14.0	8%	13.16	2.24	6.07±0.03 2.09 5.73±0.03
2	3	no	223	0.51	[-448, 266]	1.22	10.87±0.81/3.2	12.0	13.0	8%	13.13	2.89	7.17±0.02
3	4	no	82	0.50	[-704, 747]	1.43	9.35±0.90/3.2	14.5	16.0	10%	13.27	1.90	7.84±0.02
4	11	yes	220	0.67	[-633, 478] [-838, 665]	1.40	4.74±0.55/3.0	6.8	9.8	44%	13.42	1.92	11.63±0.03 1.73 12.95±0.04
5	7	no	140	0.67	[-393, 460]	1.27	6.15±0.52/3.0	4.7	5.4	16%	13.38	3.36	13.77±0.03
6	7	yes	210	0.60	[-373, 619]	1.27	4.04±0.49/2.8	5.5	7.2	31%	13.56	1.87	12.49±0.05
7	5	yes	-50	0.40	[-419, 309]	1.12	1.36±0.14/2.8	4.5	5.2	16%	13.77	1.09	15.32±0.14
8	4	no	140	0.46	[-491, 384]	1.33	4.51±1.04/2.6	5.1	5.7	12%	13.45	3.21	15.61±0.02
9	3	yes	140	0.44	[-352, 362]	1.21	4.54±0.38/2.6	4.5	5.4	20%	13.59	2.48	11.78±0.03
10	5	no	10	0.63	[-336, 909]	1.15	3.63±0.63/2.6	3.2	4.5	41%	13.60	2.77	24.11±0.05
11	6	yes	-6	0.72	[-176, 144]	1.09	1.56±0.19/2.2	1.5	1.8	17%	13.87	2.67	16.37±0.08
12	3	no	13	0.69	[-295, 96]	1.12	1.78±0.31/2.2	2.1	2.5	19%	13.80	2.84	24.66±0.72
13	4	no	26	0.48	[-277, 220]	1.09	1.36±0.29/2.2	1.5	1.9	27%	13.92	1.90	20.85±0.10
14	6	no	-8	0.70	[-149, 206]	1.07	1.81±0.24/2.2	1.6	2.0	25%	13.91	2.51	17.14±0.10
15	5	no	3	0.70	[-274, 268]	1.08	1.40±0.47/2.2	1.5	2.2	47%	13.64	3.39	47.18±0.11

Mean wind density, $\langle \rho \rangle$. To quantify the wind strength, we finally calculated the “mean wind density” using data given in Table 3.5 and Table 3.6 (Column 12), by means of

$$\langle \rho \rangle = \frac{\dot{M}}{4\pi(1.4R_\star)^2 v_\infty}, \quad (3.12)$$

i.e., we considered the density at a typical location of $1.4 R_\star$.

3.5.3 H_α line-profile variability as a function of stellar and wind parameters

In order to obtain further clues concerning the origin of wind variability (as traced by $H\alpha$) in O SGs, we examined various correlations between line profile parameters and parameters of the TVS of $H\alpha$, on one hand, and fundamental stellar and wind parameters of the sample stars, on the other. To search for such correlations, we used the Spearman rank-order correlation test (see e.g. Press et al. 1992) which apart from the linear correlation coefficient of ranks, also calculates the two-sided significance of its deviation from zero, without any assumption concerning the distribution of uncertainties in the individual quantities.

H $_{\alpha}$ profile shape as a function of spectral type. An inspection of the *mean* H $_{\alpha}$ profiles of the sample stars (all supergiants!) shows that these profiles evolve as a function of spectral type from a slightly asymmetric emission with a peak value red-shifted with respect to V_{sys} , via an emission feature with a P Cygni-like core, to a feature in absorption (with or without central emission reversal). In stars of early and intermediate spectral type extended emission wings can be seen, while in stars of late spectral type the presence of such wings is rare.

There are two stars that deviate from this behaviour, HD 24912 and HD 210809. The former one exhibits a pure absorption profile instead of a P Cygni-like profile. Consequently, its H $_{\alpha}$ line resembles much more those profiles from luminosity class III than from luminosity class I objects of the same spectral type. This finding implies that the (re-)assignment in luminosity class done by (Herrero et al. 1992) is likely erroneous - that would be not a surprise due to the uncertain distance - and that the original value assigned by Walborn (1973), luminosity class III, is more appropriate.

The second outlier, HD 210809, shows a P Cygni-like profile instead of an absorption profile partly filled in by wind emission. The “peculiar” shape of the mean H $_{\alpha}$ profile might be explained if a strong deviation from spherical symmetry is present in the wind, a possibility that is also suggested by the observations. Hereafter, we will refer to HD 24912 and HD 210809 as to “peculiar” stars.

The observed evolution of H $_{\alpha}$ in O-SGs with spectral type (actually with T_{eff}) is in fair agreement with results from theoretical line-profile computations performed in terms of NLTE, spherically symmetric, smooth stellar wind models. The main drivers of this evolution are: decreasing line emission caused by decreasing wind density (since \dot{M} decreases with decreasing T_{eff} and $\log L/L_{\odot}$, see Vink et al. 2000), and decreasing contribution of the HeII $\lambda 6560$ blend¹⁰. Outliers, such as HD 210809 and HD 24912, can occur either as a result of strong deviations from spherical symmetry and homogeneity in the wind (due to, e.g., fast rotation, CIRs, clumps), or as a result of an erroneous spectral type/luminosity class classification or uncertain/wrong parameters.

Red-shifted emission-peaks. Our observations suggest that the position of the emission peak of the H $_{\alpha}$ profiles of O SGs depends on the strength of the wind: for stars of weaker winds (H $_{\alpha}$ in absorption with/without central reversal) this peak is centered almost at the rest wavelength, while for stars of stronger winds (H $_{\alpha}$ in emission) it is red-shifted instead. This observation is supported by results of the correlation analysis, which shows that the velocity of the emission peak, v_e correlates significantly with $\langle \rho \rangle$, (0.79/0.0007) and in addition with T_{eff} (0.82/0.0003)¹¹.

¹⁰In contrast, purely photospheric H $_{\alpha}$ profiles of a given luminosity class do not change significantly as a function of T_{eff} , because in this temperature regime the photospheric ionization fraction of neutral hydrogen remains fairly constant.

¹¹In this particular case and because of the reasons outlined above, the “peculiar” stars HD 210809 and HD 24912 have been discarded from the correlation analysis.

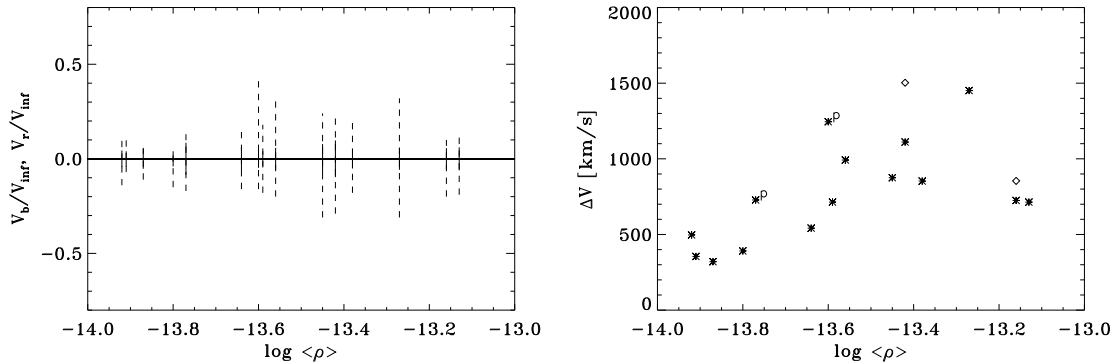


Figure 3.12: Blue and red velocity limits (left panel) and velocity width (right panel) of *significant* LPV in $H\alpha$, as a function of mean wind density of the sample stars. Thick vertical lines denote the corresponding projected rotational velocity, $\pm v \sin i$. Asterisks refer to the conservative estimates for ΔV , while diamonds mark the non-conservative ones.

Hereafter, numbers in brackets denote the Spearman rank correlation coefficient and the two-sided significance of its deviations from zero. Since the latter quantity measures the probability to derive a given correlation coefficient from uncorrelated data, smaller values mean higher significance of the correlation.

Red-shifted emission peaks have been observed in UV resonance lines of O-type stars, where this finding can be explained in terms of “micro-turbulence” effects, with v_{micro} of the order of $0.1 v_{\infty}$ (e.g., Hamann 1980 and references therein, Groenewegen & Lamers 1989). On a first glance, the phenomenon seen in $H\alpha$ seems to be somewhat similar. In contrast to the situation for UV resonance lines, however, our $H\alpha$ profile simulations meet no problem in reproducing the red-shifted peak, even if the shift is large, *without any inclusion of micro-turbulence*. This can be seen clearly by comparing theoretical profiles with observations, e.g., Markova et al. (2004); Repolust et al. (2004). A closer inspection of the profile formation process reveals that the apparent shift of the emission peak results (at least in our simulations) from the interaction between the red-side of the Stark-broadened photospheric profile and the wind emission. Let me note that we do not exclude the presence of micro-turbulence, but simply we do not need it to reproduce the observed amount of v_e .

3.5.4 Empirical properties of the TVS as a function of stellar and wind parameters

Before investigating the properties of the $H\alpha$ TVS for our sample stars, let me point out that all results outlined below refer to the “conservative case” (see Sect. 3.5.2). Although the “non-conservative” data have not been analyzed in detail, they are included in the corresponding plots and I will comment on their influence on the final outcome.

Distribution of H_α line-profile variability in velocity space

In Figure 3.12 we show the blue and red velocity limits (left panel, dashed) and the velocity width ΔV (absolute value, right panel) of H_α LPV as a function of the mean wind density. In combination with the results described in Sect. 3.5.3, these plots indicate that:

- i) for all stars the H_α LPV extends beyond the limits determined by stellar rotation and therefore must be linked to the wind;
- ii) in most of the stars in the sample, the variations extend either symmetrically (within the error) with respect to the rest wavelength, or with a weak blue-to-red asymmetry. In addition, in two objects, HD 17 603 and HD 210 809, TVS with a noticeable red-to-blue asymmetry have been observed, while in other two stars, HD 190 429A and HD 16 691, the variations are stronger and more extended bluewards of the rest wavelength.
- iii) the velocity width for *significant* variability in H_α is larger in stronger winds than in weaker ones. There are two stars that deviate from this rule: HD 190 429A and HD 16 691 which exhibit variations over a velocity interval that is considerably smaller than expected from the strength of their winds.

Further analysis of the velocity data shows that in all sample stars *significant* LPV in H_α occurs below $0.3 v_\infty$ (i.e., $\leq 1.5R_\star$). Additionally, we found a significant correlation between r_{\max} and $\log \langle \rho \rangle$, (0.87/0.00001). This result as well as the possible dependence between ΔV and $\log \langle \rho \rangle$ (0.62 \pm 0.01) are readily understood in terms of an increasing wind volume which contributes to the H_α emission, as a function of wind density.

We are aware of the fact that due to observational selection effects, and other uncertainties affecting the determination of the velocity limits, the results described above might be questioned. However, a more detailed investigation of this issue indicates that the velocity limits determined here do not seem to be strongly biased by either observational selection, or uncertainties in the measured quantities. (But see also the next sub-section.)

Mean and fractional amplitudes of deviations as a function of stellar and wind parameters

Our TVS analysis shows that the mean amplitude of deviations always exceeds the corresponding threshold for *significant* variability, indicating genuine variability in H_α . The actual values of A_N range between 1 and 4 percent of the continuum flux, without any clear evidence for dependence on stellar and wind parameters.

This independence of A_N on $\log \langle \rho \rangle$ can have a twofold interpretation: First, *if* the mean amplitude is a reasonable measure for wind variability, then the wind variability is actually more or less independent

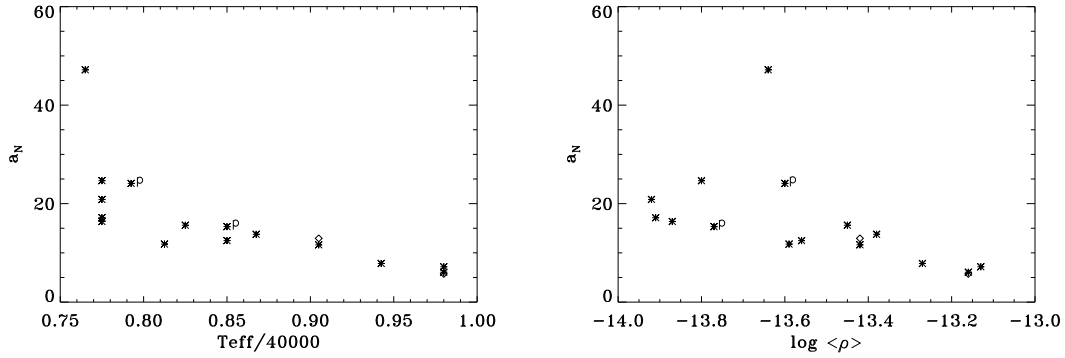


Figure 3.13: Examples of significant correlations between the fractional amplitude of deviations, a_N , and stellar and wind parameters of the sample stars. Asterisks refer to the conservative estimates, while diamonds mark the non-conservative ones. Positions of the two “peculiar” stars are denoted by ‘P’.

on wind-strength. Second, the mean amplitude is not the relevant quantity to compare to the strength of H_α LPV in our sample stars.

Leaving aside these two possibilities, let first consider the following problem. If we assume that the sources of observable variability are distributed over a certain volume, which increases as a function of mean wind density (as it is suggested from the increase of r_{max} with $\log \langle \rho \rangle$), then one should expect that also A_N should increase with mean density: the numerator of this quantity (the integral over $(TVS - \sigma_0^2)^{0.5}$) increases as a function of the emitting *volume*, whereas the denominator corresponds to an (increasing) 1-D quantity only. The fact that the *observed* mean amplitude is actually independent on $\log \langle \rho \rangle$ shows that such a simple model is not sufficient to explain the observations. I will come back to this point again in Sect. 3.5.5.

In contrast to the established independence of the mean amplitude on wind density, our analysis shows the presence of a *negative* correlation between the *fractional* amplitude of deviations, a_N , and a number of stellar/wind parameters. Scatter plots for the strongest correlations, with T_{eff} (0.92/0.000001) and with $\log \langle \rho \rangle$ (0.80/0.0003), are illustrated in Fig. 3.13. In particular, the decrease of a_N with increasing $\log \langle \rho \rangle$ suggests that *the observed variability per unit fractional net emission is smaller in denser winds than in thinner ones*.

The reliability of the derived values of the mean and fractional amplitudes has been checked in two ways: *first*, we examined the stability of the results against effects caused by observational selection and other uncertainties in the measured quantities; *second*, we checked the validity of the assumptions underlying our definitions of A_N and a_N . The obtained results show that the established independence of A_N on stellar and wind parameters as well as the negative correlations between these parameters and a_N *cannot* be explained in terms of either observational selection or uncertainties in the measured quantities.

3.5.5 Simulations of LPV in H_α

In order to obtain clues concerning the systematic difference in the strength of H_α as a function of spectral type/mean wind density, in Sect. 3.5.2 the fractional amplitude has been optimized by normalizing the integral over the TVS to a quantity called fractional emission equivalent width, FEEW (see Eq. 3.9).

The parameter a_N defined in this way has been used in the previous section to investigate the dependence of the observed variability on wind density. The obtained results might be interpreted as an indication that *denser winds are less active than thinner winds*, a finding which would give firm constraints on present hydrodynamical simulations.

Note, however, that (i) our definition of a_N implicitly assumes that the TVS amplitude is proportional to the corresponding amount of wind-emission and that (ii) this assumption has NOT been checked so far. In particular, if this assumption was justified, the derived values of a_N would provide a robust measure for the “observed” degree of wind-variability, as it is true for the photospheric LPV’s described in terms of a_F .

1D model simulations

Thus, a test of our hypothesis is urgently required. Ideally, such a test would make use of at least 2-D models of instable winds, since the assumption of 1-D shells would most probably overestimate the actual degree of variability. However, given that 2-D simulations involving a consistent physical description are just at their beginning (Dessart & Owocki 2003), we have proceeded in the following way.

Model grids In complete analogy to our stationary models (Markova et al. 2004), we have constructed a large number of very simple wind-models with variable H_α wind emission. The resulting profiles (10 per model) have been analyzed in the same way as the observed ones, i.e., by means of the TVS-analysis as described in Sect. 3.5.2. To allow for a direct comparison with results from our observations, we have added artificial Gaussian noise to the synthesized profiles ($S/N = 200$, which is a typical value), and have re-sampled the synthetic output onto constant wavelength bins corresponding to an average resolution of 15 000.

In order to account for the effects of wind disturbances of different size and density contrast in different geometries, we calculated various series of models: three consisting of spherical shells (series SS) and four consisting of broken shells (i.e., clumps, series BS1 and BS2). A summary of the various models and their designation is given in Table 3.7.

All simulations are based on our (quiet) model for HD 188 209 with $\dot{M} = 1.6 \cdot 10^{-6} M_\odot/\text{yr}$ (cf. Markova et al. 2004). In order to investigate the reaction of the TVS of the underlying profile as function of wind-strength, for each model series we calculated 9 different models with $\Delta \log \dot{M} \approx 0.1$, particularly

Table 3.7: Summary of simple 1-D simulations. Models denoted by “SS” refer to spherical shells, models denoted by “BS” to broken shells, respectively.

Series	properties	$\max(\delta\rho/\rho_0)$
SS1	$\delta v = 0.5v_{\text{th}}(\text{H})$	± 0.7
SS2	$\delta v = 1.0v_{\text{th}}(\text{H})$	± 0.7
BS11	$\delta m = \text{const}, \Delta p(\text{core}) = 0.1 R_\star$	± 0.35
BS12	$\delta m = \text{const}, \Delta p(\text{core}) = 0.1 R_\star$	± 0.7
BS21	$\delta m = \text{const}, \Delta p(\text{core}) = R_\star$	± 0.35
BS22	$\delta m = \text{const}, \Delta p(\text{core}) = R_\star$	± 0.7
SS3	$\delta m = \text{const}$	± 0.35

at 0.8, 1.25, 1.6, 2.0, 2.5, 3.2, 4.0, 5.0 and $10.0 \cdot 10^{-6} M_\odot/\text{yr}$. In this way, profile shapes going from pure absorption over P Cygni type to pure emission have been obtained covering all “observed” mean wind densities.

In all these models, only the density was allowed to be variable, whereas the velocity field and thus the NLTE departure coefficients (as a function of velocity) have been kept at their original value.

In a first step (series SS1/SS2), we used the most simplistic approach of disturbing the density, namely we varied this quantity in a random way as a function of radius only, i.e., we assumed spherical shells. This step, although rather unrealistic, has been performed particularly to check the stability of results from somewhat more “sophisticated” models (series BS1/BS2), which are described below.

In order to preserve the mean profile, the variations are defined in such a way as to allow for both positive and negative disturbances around the “quiet” model. We divided the wind into shells of equidistant velocity range, δv_{shell} , where

$$\delta v_{\text{shell}} = c \cdot v_{\text{th}}(\text{H}), \quad c = 0.5, 1 \quad (3.13)$$

with $v_{\text{th}}(\text{H})$ the thermal velocity of hydrogen. The two values of c define two different series, SS1 and SS2. Inside each of the shells, the density has been perturbed by a maximum amplitude of $\pm 70\%$,

$$\rho = \rho_0(1 + \delta\rho/\rho_0), \quad \delta\rho/\rho_0 = -0.7 + 1.4 \cdot \text{RAN}, \quad (3.14)$$

with ρ_0 the stationary density and RAN a random number uniformly drawn from the interval $[0,1]$. The specific maximum amplitudes (for series SS, but also for series BS, see below) have been chosen in such a way that the resulting TVS-integrals and FEEWs are (roughly) consistent with the observed values. Lower maximum amplitudes would result in a too low degree of variability, and higher ones in too large values.

Note that the density contrast has been assumed to be constant within each of the shells, i.e., the number of drawn variables is given by the total number of shells, which is of the order of 80 for $v_\infty = 1650 \text{ km/s}$

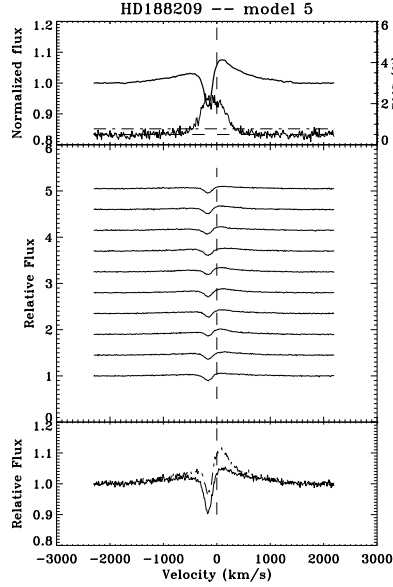


Figure 3.14: As Fig. 3.11, but for *synthetic* profiles corresponding to model BS11 (broken shells, low amplitude) of HD 188 209, at $\dot{M} = 2.5 \cdot 10^{-6} M_{\odot}/\text{yr}$ (see text).

and $c = 1$. Note also that only the wind has been allowed to be variable, i.e., we considered perturbations only outside the sonic point, located roughly at 20 km s^{-1} .

In this way then, different and random amplitudes within the maximum range $\delta\rho/\rho_0 \in [-0.7, 0.7]$ are created, however, once more, at one unique value per shell. To allow for a temporal variability of the resulting profiles at “random” observation times, for each model we performed 10 simulations with different initialization of RAN and different locations of the contributing shells. The resulting 10 different profiles have been analyzed subsequently by means of the TVS method (an example is given in Fig. 3.14).

Model series SS suffers from (at least) two major problems. At first, the assumption of *spherical shells* might amplify the LPV at all frequencies, since, especially in the wind lobes, there is only a weak chance that fluctuations will cancel out due to statistical effects. Second, our simulations define equal amplitudes of disturbance inside shells of equidistant range in *velocity* space. Accounting for the rather steep increase in velocity inside and the flat velocity field outside, this means that the contributing volume per shell is strongly increasing with radius, which might give too much weight to disturbances in the outer wind.

To “cure” both problems, we have calculated four additional model series, which should be more realistic than the above ones. At first, the spherical symmetry is broken by the following modification.¹² For the core-rays, we assume *coherent* shells (blobs), either of a relatively small lateral extent, $\Delta p \approx R_{\star}/10$ (series BS1), or of a larger extent, $\Delta p = R_{\star}$ (series BS2). For each of the non-core rays (distributed roughly logarithmically), on the other hand, we assume different locations of the density variations *per ray*, to simulate the presence of *broken shells*. The latter modification results in a lower TVS particularly in the red part of

¹²Remember that the radiative transfer is performed in the usual $p - z$ geometry, with impact parameter p and height over equator z . The so-called *core rays* are defined by $p \leq R_{\star}$, and the *non-core* rays passing *both* hemispheres of the wind lobes by $p > R_{\star}$.

the profiles, due to cancellation effects. Note that we have convinced ourselves that different distributions of non-core rays gave very similar results.

In order to avoid the volume effect, instead of assuming $\delta\rho/\rho_0$ as random, however constant per shell of thickness $\delta v = \text{const}$, we now require that the random perturbations should occur in shells of *equal mass*,

$$\delta m_{\text{shell}} = 4\pi r^2 \rho dr, \quad (3.15)$$

with roughly 50 (broken) shells per model. Inside each broken δm shell, the density fluctuations are evaluated as above. For each of our simulations BS1 and BS2, we have used two different values for the maximum amplitude, $\max(\delta\rho/\rho_0) = \pm 0.35$ and ± 0.7 (BS11/BS21 and BS12/BS22, respectively), which gives a fair consistency with the range of observed variability.

Obtained results Before I discuss the results in detail, let me already point out here the major outcome. Although the assumptions inherent to the various model series (SS vs. BS) are rather different, the results with respect to interesting quantities are not. The real difference concerns “only” the distribution of the variability over the profile. For the spherical shells models, we find significant variability on the red side, whereas for the broken shell model the variability extends to larger blue velocities, due to the increased influence of the shells in front of the disk (cancellation effects in the lobes, see Fig. 3.14).

In Fig. 3.15, the numerator entering a_N (lower set of curves) and the fractional emission equivalent width (FEEW, denominator of a_N , upper set of curves) are compared as a function of mean wind density $\langle \rho \rangle$. Obviously, series SS and BS give similar results. In particular, the results of models SS1 and models BS11 (lower dotted and fully drawn curves) are almost identical, which shows that a large number (~ 160) of spherical shells (model SS1) can simulate the outcome of a model with a lower number (~ 50) of broken shells and a lower density contrast. Moreover, it seems that the “volume effect” discussed above is insignificant, simply because H_α forms in the lower wind region. This similarity in the results points to a rather large probability that our results are robust and independent of the specific assumptions.

Interestingly, both the observations (except for the two objects with highest wind-density and *more localized TVS*, HD 190429A and HD 16691) and all simulations roughly follow a power-law for both quantities,

$$\log(TVS_{\text{integral}}) \approx a + b \log \langle \rho \rangle \quad (3.16)$$

$$\log(\text{FEEW}) \approx c + d \log \langle \rho \rangle \quad (3.17)$$

which immediately shows that our hypothesis of both quantities being proportional to each other fails.

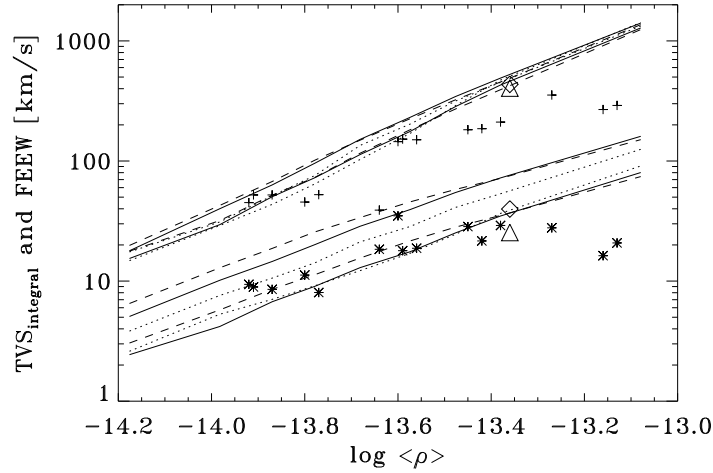


Figure 3.15: “Observed” values of the numerator entering a_N (asterisks) and of the fractional emission equivalent width (denominator of a_N , crosses), compared with simulated quantities, as a function of mean wind density $\log \langle \rho \rangle$. The dotted curves correspond to simulations with spherical shells and constant δv spacing; fully drawn and dashed – to simulations with broken shells and constant δm . Note that inside each series of simulations the maximum amplitude of density-fluctuations, $\delta\rho/\rho_0$, is identical, i.e., independent on wind density.

The special symbols correspond to results from our TVS-analysis of the 3-D models presented by Harries (2000), cf. Sect. 3.5.5 (diamonds: spiral structure; triangles: clumpy structure).

The established logarithmic dependence of the FEEW on $\log \langle \rho \rangle$ can be readily understood if one remembers that the *total* emission equivalent width of H_α scales as a power-law of mean wind-density (cf. Puls et al. 1996), and that the integration range $[v_b, v_r]$, entering the fractional equivalent width, is only weakly increasing with $\langle \rho \rangle$, if scaled to v_∞ and evaluated on a logarithmic scale (see Fig. 3.12). Given that the TVS and its integral are both related to the mean wind-density¹³, the power-law dependence of this quantity on $\langle \rho \rangle$ can also be understood. Concerning the somewhat lower slope, it can be attributed, at least in our simulation, to optical depth effects and the cancellation of fluctuations in the emission lobes.

From Eqs. 3.9, 3.16 and 3.17 then it follows that a_N is a decreasing function of $\log \langle \rho \rangle$,

$$\log a_N \approx (a - c) + (b - d) \log \langle \rho \rangle, \quad b < d, \quad (3.18)$$

and since all our model series predict the same dependency, it is rather likely that this effect should be present also in more realistic simulations. In conclusion, we predict that a_N becomes a decreasing function of mean wind density, *even if the disturbances* (more precisely, their relative amplitudes) *are independent of* $\langle \rho \rangle$. The vertical off-set of this relation, on the other hand, depends strongly on the density contrast, i.e., on $\max(\delta\rho/\rho_0)$. All this simulations, of course, refer to the case of fluctuations which are “globally”

¹³at least if the disturbances do not totally decouple from this quantity

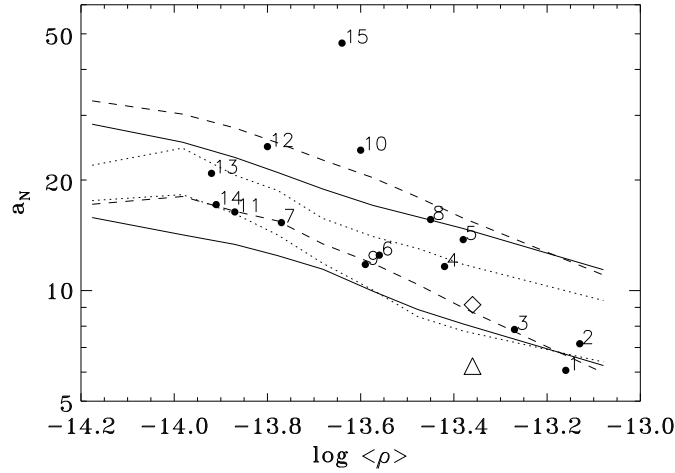


Figure 3.16: Comparison of “Observed” and simulated values of the fractional amplitude a_N (in %). The object numbers correspond to the entries given in Table 3.6. All symbols as in Figure 3.15.

present, and will not explain effects from localized macro-structures such as CIRs.

Fractional amplitudes, a_N The actual and predicted behaviour of a_N is shown in Fig. 3.16. For lower wind densities, the slopes of the relations for numerator and denominator are rather similar (optically thin winds, wind emission dominated by core-rays), so that the predicted amplitude a_N remains roughly constant or is even increasing, whereas from $\log \langle \rho \rangle \approx -14.0$ the predicted decrease is obvious. By comparison with observations, we find that almost all stars lie in the range suggested by BS11/BS12 and BS21/BS22, i.e., correspond to differences in (relative) amplitude within a factor of two. There are only two outliers, HD 210 809 (#10) and particularly HD 18 409 (#15, at $a_N \approx 50$). While the former star has been designated as a “peculiar” object, the strong deviation of the last is more likely due to uncertainties in wind parameters (Repolust et al. 2004)¹⁴.

Even for the two objects with the largest wind densities, which have been found not to follow the individual relations for the TVS-integral and the FEEW, the results for a_N are consistent with the predictions. In our interpretation, this would mean that both stars have the same degree of activity as the other stars, only in different and more localized regions.

In summary, there are no indications of a dependence of wind activity on wind density, at least on basis of our present simulations; in our interpretation, the decrease of a_N is an artefact of the normalization, which (unfortunately) does not follow the same slope as the TVS-integral.

Furthermore, from our simulations, we may also conclude that the underlying disturbances (at given

¹⁴The large value of a_N is *not* due to a large TVS-integral, but due to a rather small value of its FEEW (located at $\log \langle \rho \rangle \approx -13.64$ and FEEW = 39 km/s in the left panel).

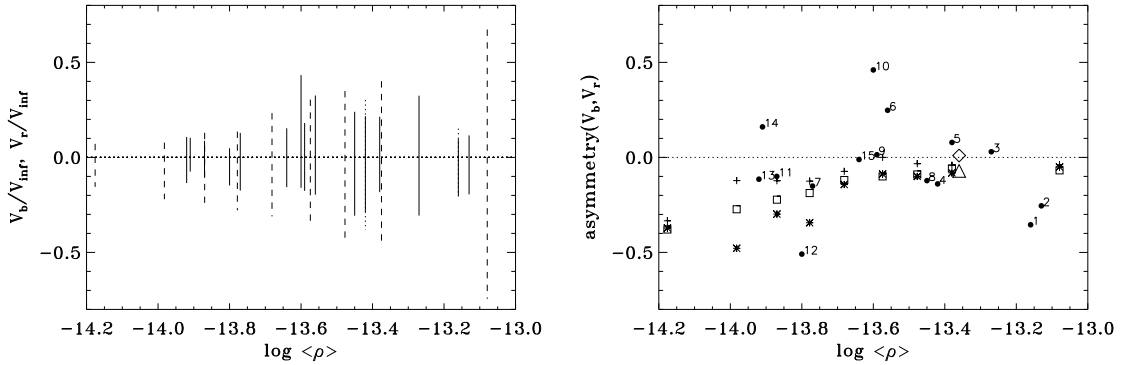


Figure 3.17: *Left*: Observed blue and red velocity limits, v_b, v_r (conservative and non-conservative values) in units of v_{∞} , as a function of mean wind-density, compared with results from simulation BS21 (dashed). *Right*: Observed asymmetry, $(v_r - |v_b|)/(v_r + |v_b|)$ (conservative values, black dots), compared with simulations (asterisks: BS21, squares: BS11, crosses: SS3). The object numbers correspond to the entries given in Table 3.6. The diamond and triangle refer to the data resulting from our TVS-analysis of the 3-D spiral and clumpy model presented by Harries (2000), cf. Sect. 3.5.5.

wind density) may introduce a scatter up to a factor of two in the maximum amplitude. Of course, more realistic simulations are needed before a final statement concerning this problem can be made.

Velocity limits and distribution of LPV. Further insight into the origin of the variability might be found from a comparison of observed vs. predicted velocity limits, v_b, v_r and particularly of their asymmetry. In the left panel of Fig. 3.17, we compare these velocity limits (normalized to v_{∞} , to obtain a unique scale) with our predictions from BS21 (broken shells, low amplitude). Obviously, for stars with low and intermediate wind strength ($[\log \langle \rho \rangle] < -13.2$) and except for HD 210 809 (at $\log \langle \rho \rangle = -13.6$, with strongly asymmetric velocity limits), our models do fairly reproduce the observed amount of increase of ΔV as a function of $\langle \rho \rangle$. Since at largest wind densities we have only two objects in our sample, it is not clear at present whether their discrepant behaviour is peculiar or not. Thus, except for the outliers, it might be concluded that the observed variability results from effects which are present *everywhere in the wind*, in accordance with our models. This conclusion seems to be also supported by the fact that HD 210 809 deviates from our predictions: for this star our observations have suggested the presence of large-scale wind disturbances which are localized rather than uniformly distributed over the wind volume.

The right panel of Fig. 3.17, however, shows the shortcomings of our models. Plotted is the asymmetry of v_b, v_r by means of the expression $(v_r - |v_b|)/(v_r + |v_b|)$ (negative values correspond to blue-to-red, positive values to red-to-blue asymmetries, respectively). Let me firstly discuss the “theoretical” predictions. We have plotted the results for model series BS21 (asterisks), BS11 (squares) and for a model that has been constructed additionally for this comparison, namely a model with *spherical* shells and $\delta m = \text{const}$ (SS3,

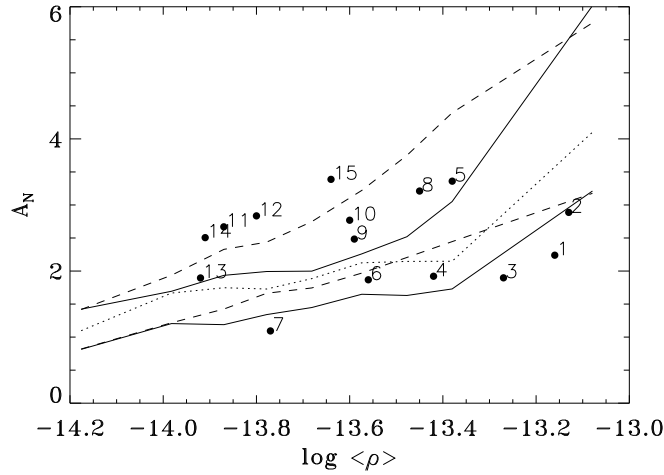


Figure 3.18: “Observed” values of the mean amplitude of deviations, A_N (conservative values) compared with simulated quantities, as a function of mean wind density $\log \langle \rho \rangle$. The bold curves correspond to series BS11/BS12, the dashed curves to series BS21/BS22 and the dotted curve to series SS3 (spherical shells, low amplitude), respectively. Each series shows a positive correlation with mean wind density. The object numbers correspond to the entries given in Table 3.6.

crosses). All three models have the same maximum amplitude, $\max(\delta\rho/\rho_0) = \pm 0.35$. Not surprisingly, the last model shows the least asymmetry, whereas model BS21 shows the largest one (due to the large lateral extent of the assumed broken shells in front of the stellar disk). Note that most models show a blue-to-red asymmetry, even those with spherical shells, whereas *in no case a redwards asymmetry is found*. This prediction, of course, results from cancellation effects in the lobes, compared to the situation for core-rays. For large wind-densities, all models converge to small, or even negligible asymmetry, because of the increasing influence of the lobes. For model SS3 (spherical shells), symmetry is reached earliest, roughly at $\log \langle \rho \rangle = -13.5$.

With respect to the observations, the situation is as follows. At low and intermediate wind densities, only four objects display a *significant* asymmetry, mostly to the red. The majority of stars, however, show either a small degree of asymmetry (to the blue *and* to the red), or behave symmetrically. The predictions of series SS3 are closest to this behaviour. For the two stars with larger wind densities, the predictions definitely deviate from what has been observed.

Mean amplitude, A_N In Sect. 3.5.4 I have noted that the mean amplitude of deviations seems to be uncorrelated with mean wind density, at least for our sample. Also I speculated that if the sources of wind variability were (uniformly) distributed over the contributing wind volume, one should see a positive correlation. By means of our simple models, this conjecture can be now checked and additional constraints

on the origin of wind variability may be found.

Fig. 3.18 shows the behaviour of the simulated mean amplitude as a function of mean wind density for series BS11/BS12, BS21/BS22 and SS3. Actually, A_N is strongly correlated with $\langle \rho \rangle$ where the vertical offset is a function of (relative) amplitude $\delta\rho/\rho_0$. On a first glance, we might conclude that the observed values are again (i.e., as we have found for a_N) consistent with the models, if we allow for a variation in amplitude of roughly a factor of two.

A closer inspection, on the other hand, reveals that at least for two low density objects (HD 188 209, #11 and HD 218 915, #14) there is the following problem. The mean amplitudes of these objects are consistent with our simulations with larger $\delta\rho/\rho_0$ (BS22). Concerning the fractional amplitudes, a_N , however, they are consistent with our simulations for lower $\delta\rho/\rho_0$ (BS21, cf. Fig. 3.15), which in turn produce a much too large bluewards asymmetry in the TVS (Fig. 3.17). Remarkably, one of these objects (HD 218 915, #14) even suffers from an observed red-to-blue asymmetry.

Thus, from the comparison of mean amplitudes and asymmetry in the velocity limits we find a number of indications that at least two (from 3) low and the high density objects *cannot* be explained by our simple models consisting of *density fluctuations distributed everywhere in the wind*. If we return to our original TVS analysis, the primary sources for these inconsistency can be clearly identified: (i) the strong variability of a central reversal at zero rest velocity, which gives rise to a rather large TVS within a narrow, symmetric velocity range for stars of weaker winds and (ii) the rather small extent of the observed variability, preferentially bluewards of the emission peak for stars of stronger winds.

3D model simulations

Recently, Harries (2000) has published results for 3-D line-profile simulations of H_α for ζ Pup, performed by means of his Monte Carlo stellar wind radiative transfer code. Two distinct models for the wind morphology have been considered: one with a co-rotating (one-armed) spiral structure and another one consisting of a clumpy wind. In the first case the author examined the effect of one spiral streamline of enhanced density on H_α , while in the latter one he considered random blobs propagating throughout the wind.

In order to obtain an impression to what extent the outcome of our model analysis might be influenced by the fact that we consider 1-D instead of more realistic 3-D models, we analyzed the two different sets of synthetic profiles derived by Harries (kindly made available to us by the author), in the same way as for the time-series of our sample stars and for our own simulations. The corresponding results are shown in Fig. 3.19. Apart from the impressive sequence of synthetic profiles which allows to easily follow any evolution of wind structure in time a number of interesting features are noticeable.

In the first place, the distributions of amplitudes for the two models are rather different: in the one-armed

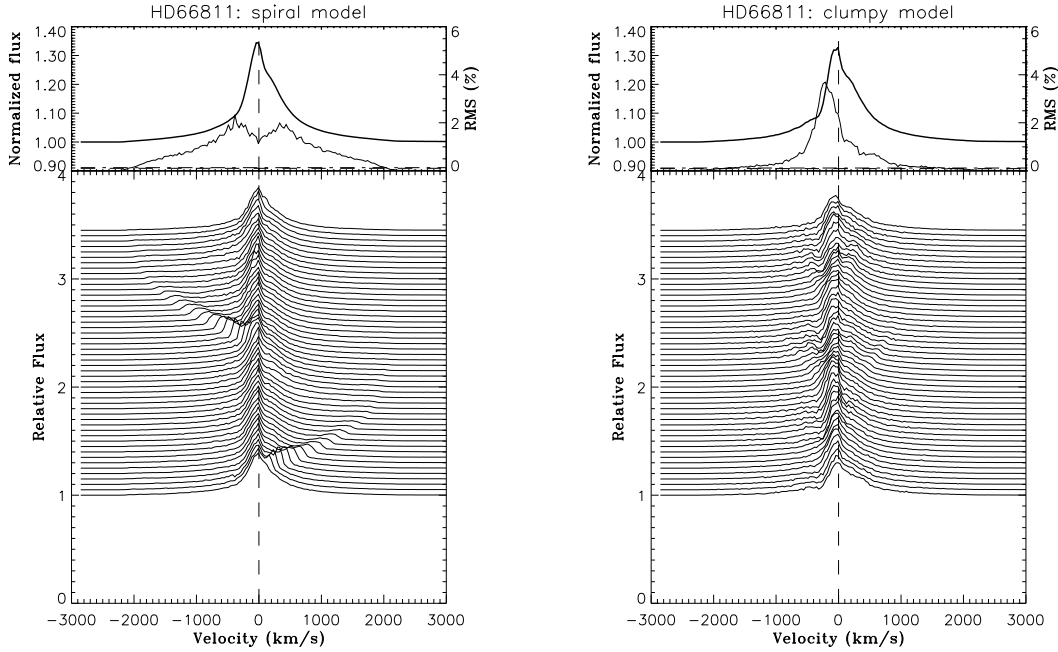


Figure 3.19: As Fig. 3.11, however for the time-series of synthetic H_α profiles from ζ Pup as calculated by Harries (2000), using two different 3-D models for the wind morphology. *Left*: wind with co-rotating, one-armed spiral density enhancement; *Right*: clumped wind. Note the different distributions of the corresponding TVS.

spiral model, the derived TVS is double-peaked and *symmetric with respect to the stellar rest frame*, while in the clumped model it is single peaked with maximum amplitudes concentrated on the blue. In addition, for the clumped model the velocity range of *significant* variability shows a clear blue-to-red asymmetry ($v_b=-1670$, $v_r=1440$ km s $^{-1}$) while for the spiral model it is almost symmetrical with respect to the rest wavelength ($v_b=-2010$, $v_r=2050$ km s $^{-1}$).

Interestingly, also the parameters derived from the TVS analysis of the spectra for the 3-D clumped model are quite similar to the ones we have derived in terms of our 1-D broken shell (i.e., clumpy) models (see Figures 3.15 and 3.17), whereas the small differences might be explained by the fact that the spectra from the 3-D simulations are free of noise, in contrast to the spectra from our 1-D models.

These findings suggest that at least in the case of a clumpy wind the TVS signatures do not, or little, depend on the specific model, and that the results of our simple 1-D simulations are comparable to those from more realistic simulations. A final conclusion concerning this point can be drawn only, of course, when a larger set of 3-D simulations for a variety of wind parameters, will be performed.

From the point of view of the observations, on the other hand, the above finding means also that the probability to obtain a symmetric TVS of H_α will be very low if the wind is clumpy, even if using snapshot

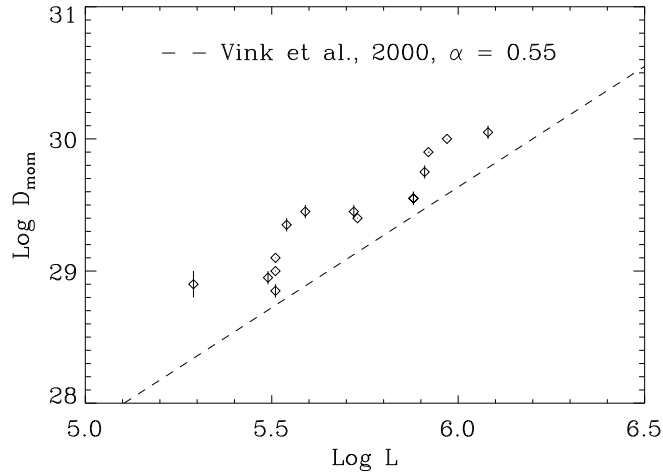


Figure 3.20: WLR for our sample of Galactic O-type stars. Error bars display the influence of H_α LPV (interpreted in terms of \dot{M}) on the modified wind-momenta.

observations.

In our models, a large variation at rest wavelength cannot be reproduced, at least if we allow for fluctuations of both positive and negative amplitude. Such a behaviour might be explained by radially extended, coherent structures in front of the disk, which would mimic a certain global increase of mass-loss by bringing the innermost part of H_α into emission. That our models can never reproduce a (strongly) localized variability has been discussed already above.

3.5.6 Spectral variability and the Wind Momentum Luminosity Relationship

The most extreme case of snapshot observations occurs when performing a spectral analysis, since usually only one spectrum (or two consecutive ones) is/are available. Because of the spectral variability inherent to the objects under discussion, these individual data might be not very representative. In the following, I will discuss on this point with respect to derived mass-loss rates, with special emphasis on the question in how far the Wind Momentum Luminosity Relationship (WLR) of Galactic O-type stars is influenced.

Firstly, let me assume that the observed variability of H_α is only due to processes in the wind (i.e., the contribution of absorption LPV is neglected), and that this variability is interpreted in terms of a variable mass-loss rate. Note that the latter assumption is inherent to a typical spectrum analysis, since due to the scarcity of the available data-set(s) a particular mass-loss rate is derived, which of course might be not representative.

Following this philosophy, we derived upper and lower limits of the mass-loss rate for all our sample stars, from the two most extreme spectra present in the time-series, and calculated the corresponding limits

for the modified wind-momentum rate. Due to the adopted simplifications (standard model, no clumping) the obtained values of \dot{M} might be overestimated.

The mass-loss rate estimates listed in Table 3.6 show that the observed variations in \dot{M} range from $\pm 4\%$ of the mean value, for stars with stronger winds, to $\pm 16\%$ for stars with weaker winds. Since the accuracy of our determinations also depends on the strength of the wind – $\pm 20\%$, for stars with H_α in emission, and $\pm 30\%$, for stars with pure absorption profiles (Markova et al. 2004) – we conclude that *the observed variability of \dot{M} does not exceed the errors of individual determinations and thus is not significant*. This result seems somewhat astonishing, especially in those cases when drastic changes in the H_α profile shape have been observed. Note, however, that for wind densities not too low small changes in \dot{M} give rise to large changes both in the profile shape and the EW (Puls et al. 1996).

The derived amplitudes of the \dot{M} variability have been used to cast constraints on the variability of the corresponding wind momentum rates. The results indicate that wind variability affects the momentum rates by less than 0.16 dex, which is smaller than the error of individual estimates (0.30 dex, Markova et al. 2004) and thus is insignificant again. In addition, and as it can be seen from Figure 3.20, the uncertainty caused by wind variability does not provide any clue to resolve the problem concerning the WLR of Galactic O-type stars being a function of luminosity class (Puls et al. 2003; Repolust et al. 2004; Markova et al. 2004).

Finally, I would like to note that the assumption of a homogeneous and spherically symmetric wind (underlying our analysis) is in some obvious contrast with the presence of large-scale perturbations in the winds of some of our targets, which have been suggested by different investigators on various occasions. Consequently, problems may occur when trying to fit the H_α profiles with model calculations. Exemplary is the case of HD 210839, where we failed to obtain a good fit for a number of profiles of the time series.

3.5.7 Summary

Although line-profile variability of H_α in O-type supergiants has been known for a relatively long time (e.g., Rosendhal 1973; Conti & Frost 1977), our survey is the *first* where this variability is detected and quantified in an *objective* and *statistically rigorous* manner for a large sample of stars.

The main results can be summarized as follows:

- To study the wind variability in O supergiants, as traced by H_α , we employed the TVS analysis, originally developed by Fullerton, Gies & Bolton (1996), however modified in such a way as to account for the effects of wind emission of various strength on the observed profiles.
- Our results show that all sample stars experience *significant* line-profile variations in H_α with *mean* amplitudes A_N between 1 and 4% of the continuum strength. Since absorption LPV seems to be common among O-type stars (Fullerton, Gies & Bolton 1996), these amplitudes can in principle be due to a combination of

variations generated in the photosphere and in the wind. However, our analysis indicate that even at lower wind densities ($\log \langle \rho \rangle \approx -14$) contributions from wind effects have to be accounted for, and that for a number of stars wind variability is actually the dominating source.

- By means of the newly introduced quantity a_N , we found that the observed variability of H_α per unit wind emission is a slight decreasing function of mean wind density. This result might be interpreted as an indication that *stronger winds are less active than weaker ones*. However, at least on the basis of our present, simplistic line-profile simulations, this hypothesis cannot be supported.
- For the case of density perturbations uniformly distributed in the wind, our simulations predict that the mean amplitude of deviations, A_N , should increase with increasing mean wind density. Interestingly, this prediction is *not* supported by our observations which gave no evidence of any correlation between mean amplitude and density. Moreover, it turned out that a comparison of observed a_N and A_N with corresponding simulated quantities would give different information. In so far, both quantities deserve their own right and have to be reproduced simultaneously by future models which claim to explain the observed variability.
- By means of a series of models with different wind morphology, we showed that the properties of the TVS of H_α can provide some insight into the structure of the inner wind where this line forms. In particular, and for not too large wind density, it was found that models with spherically symmetric shells produce a TVS with a blue-to-red asymmetry similar to that originating from models with blobs, providing the both kinds of disturbances are distributed uniformly over the contributing volume. The only difference is the actual degree of asymmetry: at the same mean density, shell models produce less asymmetry than those with broken shells (i.e., blobs). Moreover, this result does not seem to depend on whether snapshots or systematic simulations have been used. Note, however, that an asymmetric large-scale, long-lived co-rotating structure will always produce a symmetric TVS *if* the whole period of rotation is covered by observations.
- Allowing for a scatter within a factor of two for the maximum amplitude of the disturbances at given wind density, a good correspondence between the predicted and the empirically derived parameters of the TVS of H_α can be derived for stars of intermediate wind density. For stars of lower and higher wind densities, on the other hand, the established disagreement might simply point to the presence of wind effects that are not accounted for in our simulations. In particular, to reproduce the variations observed in H_α at lower wind densities, one might suggest the presence of a radially extended, coherent structure in front of the disk which can mimic variations in the global mass-loss rate. Concerning the (two!) stars with stronger winds, this corresponding discrepancy might be interpreted in terms of a rather confined region of variability close to the star.
- Our analysis shows that *significant* variations in H_α occur below $0.3 v_\infty$. Converted to units of physical space, this limit corresponds to 1.4 to $1.5 R_\star$, in good agreement with results from theoretical calculations

with respect to the outer limits of H_α line-formation in O supergiant winds.

- Interpreted in terms of variable mass-loss rates, the observed variations in the H_α wind emission indicate variations in \dot{M} of $\pm 4\%$ of the mean value for stars with stronger winds, and of $\pm 16\%$ for stars with weaker winds. The ratio of maximum to minimum mass-loss averaged over the whole sample is 1.22, in good agreement with the value provided by Prinja & Howarth (1986). The distribution of this ratio over wind density suggests that weaker winds seem to be more variable than stronger ones.
- The influence of wind variability on the derived wind momenta is found to be small, smaller than 0.16 dex and hence not significant. This result agrees well with an investigation by Kudritzki (1999) who reported 0.15 dex as the error in the wind momentum rate of one(!) A-supergiant, HD 92 207, introduced by wind variability. Thus, part of the scatter in the WLR of Galactic O-type stars might be caused by spectral variability.

Finally, it may be worth noting that the H_α profiles of the sample stars derived throughout our observations are quite similar, both in shape and strength, to those obtained by other investigators in various epochs (e.g., Rosendhal 1973; Conti & Frost 1977; Scuderi et al. 1992; Ebbets 1982; Underhill 1995; Kaper et al. 1997). This finding suggests that the atmospheres of our targets are not subject to long-term variability. On the other hand, no information about previous H_α observations concerning the stars BD+56 739 and HD 338 926 was found in the literature.

Chapter 4

Wind structure and variability in P Cygni

4.1 Introduction

P Cygni is an early B-type supergiant classified variously as B1eq, B0-B1, B1p or B1Ia⁺ (Lamers et al. 1983). Because of its spectral characteristics, the star is considered the prototype of the P Cygni-type stars (PCT), defined by Lamers (1986) as “luminous supergiants of spectral type O, B and A, which in their visual spectrum show or have shown P Cygni profiles of not only the strongest Balmer and He I lines, but also of other lines, such as lines of higher Balmer members and/or lines of other ions”. In comparison with normal supergiants, the PCT stars have an effective gravity a factor of 3 to 10 lower, a mass-loss rate a factor of 3 to 10 higher, and a terminal wind velocity a factor of 10 lower, which results in a wind density a factor of 30 higher. So, the PCT stars are an extreme case among the hot massive stars with mass loss.

Together with η Carina and S Dor, P Cygni is also considered as one of the prototypes of the Luminous Blue Variables (LBVs). LBVs form a rather heterogeneous class of very massive unstable stars located close to the Humphreys-Davidson limit on the HR diagram. The term “*LBVs*” was coined by Peter Conti in 1984 and comprises the galactic P Cygni type stars, the S Doradus variables and the Hubble-Sandage variables in M31 and M33. All these stars are characterized by high mass-loss rates, episodes of shell ejection and large eruptions. The evolutionary status of the LBVs is a subject of ongoing debates. In some stellar models, the LBV phase occurs during (or shortly after) the main-sequence phase, produces an enormous mass loss, and prevents evolution to the red (Schaller et al. 1992; Meynet et al. 1994; Langer et al. 1994); in others, the LBVs are post-red-supergiant objects in a late blue phase of dynamical instability (Stothers & Chin 1996, 2000). Some believe that two types of LBVs appear to exist: “*classical*” LBVs with M_{bol} brighter than -9.5 mag and “*low – luminous*” LBVs with M_{bol} weaker than -9.5 mag, both of which share the main characteristics of the class, but may be in different evolutionary state (e.g. Humphreys & Davidson 1994).

The observational history of P Cygni has begun more than 400 years ago, when it was discovered by Williem Blaeu as a nova-like object. Since then, the star has been many times investigated both photometrically and spectroscopically, but despite of these continuing efforts no clear understanding of its physics has been achieved to date. (For a detailed review see Israelian & de Groot 1999, and the proceedings of the workshop on “*P Cygni 2000. 400 years of progress.*”, ASPCS, Vol 233.)

Guided by the prospects to shed additional light on this issue, I have initiated and leaded a long-term international project to study wind variability and structure in the LBV P Cygni. The survey was performed in collaboration with colleagues from: the Catania Obs., Italy; the Tartu Obs., Estonia; the Armagh Obs., N. Ireland; the Ritter Obs., USA; the Canaries Astrophysical Institute, Spain; the Paris Astrophysical Institute and the Marseille Astrophysical Laboratory, France. In this chapter, main outcomes of this project will be outlined and briefly discussed. More detailed information can be found elsewhere (Markova & Kolka 1984, 1985, 1988; Markova 1986a,b, 1993a,b, 1994; Markova 2000; Markova 2001; Markova & Zamanov 1995; Markova & de Groot 1997; Markova & Tomov 1998; Markova et al. 2000, 2001a,b; Muratorio et al 2002; Friedjung et al. 2001).

4.2 Observational data

The observational part of the project includes long-term photometric and spectral monitoring campaigns of P Cygni performed from different sites all over the world, with various instruments, equipments and detectors.

4.2.1 Photometric and spectroscopic observations

Photometry In addition to our own UBV data derived with the NAO 0.6m telescope, photometric data from various literature sources have been collected and used. The total time-coverage of these data ranges from March 1985 to October 1998 with some gaps between due to inclement weather in addition to the seasonal gaps. The distribution of the data by means of their origin is given in Table 4.1. Information about the number of observations from a given source, $N_{\text{obs.}}$, the accuracy in V and $B - V$, and the corresponding reference is also provided.

Spectroscopy The majority of the original data have been collected with the coudé spectrograph of the NAO 2-m RCC telescope using either photographic plates or CCD detectors (after 1993). Additional CCD observations were secured at the Ritter Observatory (USA) using a fiber-fed échelle spectrograph attached to the 1-m telescope, and at the Tartu Astrophysical Observatory (Estonia) using a Cassegrain spectro-

Table 4.1: Photometric observations of P Cygni

Source	N _{obs}	Accuracy in V, B-V	Reference
0.6m NAO	11	≤0.01; ≤0.01	Markova & Tomov (1998)
Zsoldos	10	not reported	private communication
CAMC	124	0.05;	Carlsberg 1985-1994
APT	220	0.006; 0.010	Genet et al. 1987

Table 4.2: Summary of the spectroscopic data of P Cygni used in the present thesis

Source	Time coverage	HJD 2440000+	region in Å	R=λ/Δλ,	N _{nights}
NAO (Bulgaria)	1981 - 1983	4 690–5 547	3500–4900	18 200	52
NAO (Bulgaria)	May–Sept. 90	8 017–8 137	3500–4900	18 200	9
			4900–6800	10 000	8
Landessternwarte, Germany	1990–1992	8 044–8 764	4050–6750	12 000	88
NAO	1993–1994	8 840–9 529	H _α	20 000	15
NAO	April–Oct. 98	10 915–11 095	H _α	15 200	7
TAO (Estonia)	1994–1997	9 512–10 264	H _α	16 000	30
RO (USA)	1994–1998	9 512–11 110	H _α	25 800	39
Taylor et al. 1991	1989–1990	7 668–8 159	H _α	193	20
Scuderi et al. 94	1988–1993	7 348–9 227	H _α	7 000	32
Pollmann 1999	1994–1999	9 600–11 300	H _α	2 000	128

graph (ASP-32) attached to 1.5-m telescope. The original data-sets were complemented with 88 more CCD spectra collected with a fiber-linked echelle spectrograph coupled to the 0.75m telescope at the Landessternwarte, Heidelberg (Stahl et al. 1994)). The distribution of the observations in time, the spectral resolving power, $R \equiv \lambda/\Delta\lambda$, and the number of the obtained spectra (one spectrum per night) are summarized in Table 4.2. More information about the original data and the data reduction can be found elsewhere (see, e.g., Markova & Kolka 1984; Markova et al. 2001a; Markova 2001)

4.2.2 H_α equivalent width measurements

Original data H_α equivalent widths (EW) were estimated through line flux integration within a carefully selected spectral window, same for all spectra. Since in P Cygni this line has strong and extended ($\pm 1500\text{km s}^{-1}$) emission wings, special care must be put to fix the limits of the integration window so that to cover these wings completely. However, in some cases (e.g., the Ritter observations) the spectral coverage turned out to be insufficient to include the true continuum on either side of H_α. In these cases then, *underestimated* EWs would be obtained which have been subsequently corrected for the undetected line flux (for more information see Markova et al. 2001b).

Another problem, concerning the H_α EW-determinations, are line blending effects which depend on time, on spectral resolution, and on the geographic location of the observatory (e.g., absorption from water vapour lines, absorption plus emission from the C II doublet and emission due to the N II forbidden lines). However, according to our estimates the total effect of blending does not seem to be significant: in the extreme case of the Ritter Observatory, which is located essentially at the sea level, the contribution of water absorption to the H_α equivalent width amounts to less than 2%. Thus, no correction for line blending was made. The accuracy of our individual EW-determination is mainly determined by the quality of the spectroscopic data, and is estimated to be better than 9%.

Literature data To complement our original sets of $H\alpha$ EWs, similar data from literature were also used. Information about these data is given in Table 4.2 while more detailed description can be found in the corresponding papers (Scuderi et al. 1994; Taylor et al. 1991; Pollmann 1999).

4.3 Emission line spectrum in the optical

The present day optical spectrum of P Cygni is notable with the great number of emission lines of various species and ions (Stahl et al. 1991, 1993; Markova 1994; Markova & Zamanov 1995). In some cases (e.g., H I, He I and low-excited Fe III and N II transitions), the emission is accompanied by blue-shifted absorption (the so-called P Cygni-type profiles), whilst in others – profiles of *pure* emission type have been observed. A detailed comparison with identification lists from earlier epochs (e.g., Beals 1950; de Groot 1969) has shown that more than 70 % of the *pure* emission lines in P Cygni's spectrum appear to be of recent origin (Markova & de Groot 1997). If not due to observational selection caused by the continuous improvement of the signal-to-noise ratio of photographic spectra during the last century, this finding might indicate the presence of a very long-term variation in the wind+photosphere properties of the star.

To get deeper inside into the nature and the origin of P Cygni's emission line spectrum, a detailed investigation of the properties of a large sample of permitted and forbidden emission lines was performed. In this section, main results derived throughout this project will be outlined and briefly discussed while a more detailed description can be found elsewhere (Markova & de Groot 1997; Friedjung et al. 2001; Muratorio et al 2002.)

4.3.1 Permitted lines

The permitted pure emission spectrum of P Cygni consists mainly of lines of Fe III, N II and Si II. Some line parameters, such as, e.g., the position of the peak intensity, V_e and the full width at half the maximum

Table 4.3: Permitted emission lines in P Cygni's optical spectrum. V_e and FWHM are respectively, the velocity of the emission peak and the full width at half maximum averaged over the number of the studied lines, N ; $e_{\text{exc(l)}}$ and $e_{\text{exc(up)}}$ denote the excitation energy of lower and upper levels, respectively.

line	N	V_e [in km s^{-1}]	FWHM [in \AA]	$e_{\text{exc(l)}}$ [in eV]	$e_{\text{exc(up)}}$ [in eV]
N II 1	1	-34	92	17.80	20.32
Fe III 113	7	-32	76	18.19	20.54
Fe III 114	2	-24	66	18.43	20.54
Fe III 115	2	-44	145	18.71	20.79
Fe III 117	2	-28	78	18.73	20.79
N II 28	3	-31	85	21.07	23.14
N II 31	1	-35	72	21.51	23.37
Fe III 118	2	-46	65	20.54	23.50
Fe III 119	2	-64	97	20.54	23.57
N II 36	3	-58	65	23.04	25.04
N II 41	1	-69	90	23.10	24.96
N II 45	1	-28	83	23.14	25.04
N II 46	3	-54	101	23.14	25.09
N II 57	1	-45	112	23.37	25.35
Si II 1	2	-35	79	6.83	10.03
Si II 2	2	-42	192	8.09	10.03
Si II 4	2	-51	196	10.02	12.09
Si II 5	2	-48	136	10.02	12.47

intensity (FWHM), averaged over the number of the measured lines, N , are summarized in Table 4.3.

Location of the line formation zones. Most of the permitted pure emission lines are symmetric with a sharp maximum, blue-shifted in respect to V_{sys} . The obvious similarity in the V_e - and FWHM-estimates of most Fe III and N II lines points to a possible formation of both in same wind layers. By averaging the FWHM-data, we located the formation zone of these lines below 90 km s^{-1} . The Si II emission lines, on the other hand, are considerably broader than the Fe III and N II indicating formation at outflow velocities of about 230 km s^{-1} . Concerning the few outliers (Fe III 115, N II 57 and Si III), from a closer inspection of the observed spectrum we found that an explanation of their peculiar behaviour in terms of influence of blends and/or rather strong photographic noise is possible in any of these cases. Assuming a β -type velocity law of the form given by Eq. 2.9 with $\beta=4$, $v_\infty=240 \text{ km s}^{-1}$, and $v(R_\star)=4 \times 10^{-4} v_\infty$, the Fe III/N II and Si II emitting regions were located at $r \leq 5R_\star$ and $r \leq 100R_\star$, respectively.

Excitation mechanism. All of the observed Fe III and N II transitions are from higher excited levels which seems overpopulated. At distances $r \leq 5R_\star$ where these lines probably form, the wind temperature and density are likely higher than 14000 K and $10 \times 10^{10} \text{ cm}^3$, respectively (Drew 1985). At these circumstances, fluorescence seems to be the most plausible mechanism to populate the Fe III and N II levels with energies between 23.14 and 23.57 eV , which produce the emission lines of Fe III 118, 119 and N II 28, 31.

In particular, we suggest that these levels could be pumped by two UV transitions in He I atoms at energies of 23.09 eV ($\lambda 537\text{\AA}$) and 23.74 eV ($\lambda 522\text{\AA}$). Similar mechanism to feed the upper levels of Fe III 115 and 117 was suggested by Wolf & Stahl (1985). Concerning the Fe III 113 and 114, the upper levels of these multiplets coincide with the lower levels of Fe III 118 and 119. Consequently, these levels might be populated via cascade transitions.

On the other hand, for N II levels with energies between 25.04 and 25.35 eV, dielectronic recombination seems to be more probable, although at the base of the wind the corresponding temperatures are more likely too low to make this mechanism effective.

Concerning the excitation mechanism of the Si II lines, two alternative possibilities exist: fluorescence – pumping of electrons by Lyman β and Lyman γ to levels 4^2D and 5^2S , respectively – and radiative recombination, both followed by cascade transitions. If these lines actually form at $r \sim 100 R_\star$ where the wind temperature and density are below, respectively, 10^4 K and $5 \times 10^6 \text{ cm}^{-3}$, the last possibility seems more probable.

The Self Absorption Curve (SAC) analysis is a semi-empirical method developed by Friedjung & Muratorio (1987) to analyze emission line spectra of complex atoms, and ions without assuming detailed models for the objects emitting these spectra.

The basic idea of this method is that *if* level populations inside the same spectroscopic term are proportional to the statistical weight of each level in the term, the points of a graph of $\log \frac{E\lambda^3}{gf}$ against $\log(gf\lambda)$ for lines of the same multiplet will define a curve, called a *self-absorption curve*¹. The exact shape of the curve will depend on the nature of the line-forming region, but if the lines are optically thin (i.e., at smaller values of $\log(gf\lambda)$), this curve will tend to resemble a horizontal straight line. On the other hand, if the lines are optically thick, the corresponding SAC will tend to a line with a slope of -1 at large values of $\log(gf\lambda)$. Another important feature is that curves originating from multiplets with same upper term will be shifted horizontally while curves from multiplets with same lower term will be shifted vertically. As long as the shapes of the curves are nearly the same, these shifts can be used to determine the relative values of the corresponding level populations.

The main requirement of the SAC method to be applied is to have a *large* number of emission lines of different multiplets of the same ion originating from nearly the same region of the stellar envelope. In P Cygni this requirement is fulfilled for the case of Fe III and N II ions: from 11 multiplets of Fe III and 7 multiplets of N II a total of 72 pure emission/P Cygni- type lines have been selected and subsequently analyzed by means of the SAC method.

¹This is because lines of one multiplet have the same upper and lower terms.

Table 4.4: Results from the SAC analysis.

multiplet	$e_{\text{exc(l)}}$ [in eV]	$e_{\text{exc(up)}}$ [in eV]	slope	rms	lines
Fe III 4	8.2	11.1	-0.40	0.20	4
Fe III 5	8.6	11.1	-0.16	0.20	8
Fe III 68	14.1	16.5	0.00	0.20	3
Fe III 113	18.2	20.6	-0.35	0.20	7
Fe III 114	18.4	20.6			2
Fe III 115	18.7	20.9			2
Fe III 117	18.7	20.9	-0.42	0.30	3
Fe III 118	20.5	23.6	-0.44	0.20	4
Fe III 119	20.5	23.6			2
Fe III 705	22.5	24.6			2
Fe III 756	23.6	25.7	-0.80	0.40	5
N II 3	18.5	20.7	-0.44	0.10	6
N II 5	18.5	21.2	-0.62	0.20	6
N II 19	20.7	23.1	-0.70	0.20	3
N II 20	20.7	23.1	-0.21	0.10	4
N II 28	21.2	23.2	-0.81	0.15	4
N II 36	23.1	25.1	-0.81	0.10	3
N II 46	23.1	25.1	-0.86	0.40	4

To construct the corresponding SACs, several parameters such as, e.g., the statistical weight of the upper level, g ; the oscillator strength, f , and the dereddened emission flux, F_λ of each line in the sample must be known. A brief description of the procedure we have followed to determine these parameters is given below, whilst more detailed information can be found in Friedjung et al. (2001) and in Muratorio et al (2002).

In our approach, the dereddened emission flux of a given line was determined from the corresponding *net* emission equivalent width using a continuum flux calculated from $B = 5.14$ and $V = 4.72$, and subsequently dereddened with $E(B - V) = 0.63$. To estimate the *net* emission, we took account of blending, correcting for the presence of superposed photospheric lines, and blue shifted absorption. In particular, to minimize blending effects, Gaussian fits to the profiles were made. The presence of photospheric absorption was corrected for using the predictions of model calculations as described by Israelian (1995). While blue-shifted absorption was present, only the flux in the red half of each emission profile was measured, this flux then being multiplied by 2.

Having the dereddened fluxes thus determined, for each multiplet the corresponding SAC was constructed, and its slope was measured by means of a linear least square fit to the data-points. The obtained results are listed in Table 4.4 where data for two groups of very highly excited Fe III lines, called “multiplet 705” and “multiplet 756”, are also provided.

From the small value of the root mean square (rms) deviations (Column 5 of Table 4.4), it is obvious that in all but two cases the corresponding points do lie near a curve. Interestingly, the slope of the curves was found to be large for more excited multiplets, thus indicating their lines are optically thick, even though

their blue shifted absorption is not detectable. Also, there are some hints of a slope increase for the most excited multiplets. In addition, the range of $\log(gf\lambda)$ -values hardly changes between the least and the most excited multiplets of N II, whilst for Fe III these values are considerably smaller for the low-excited compared to the high-excited multiplets.

While the optical thickness of the more excited Fe III and N II lines is quite surprising, the established increase of the SAC slope with increasing excitation is actually counter-intuitive because at same $\log(gf\lambda)$ more excited lines are expected to be optically thinner. The interpretation of these results is difficult, but some possibilities still exist. In particular, due to the small values of the rms deviations, a conspiracy of differential non-LTE effects appears unlikely as an explanation. However, note, that it is hard to rigorously test for such an effect as both the upper and lower levels of the observed Fe III and N II lines could in principle show deviations from LTE.

Another explanation, which could be suggested, will not work either, if the increase of curve slope at the same $\log(gf\lambda)$ for more excited multiplets is confirmed in future work. In particular, one might suppose that the more excited lines are only emitted from certain parts of a spherically symmetric wind. Then, the absence of blue-shifted absorption components for these lines might be explained by a large source function, so the emission in the lines per unit surface area would be larger than that of the photosphere. In that case extra emission instead of absorption would be present on the blue side of the more excited lines, resulting in a blue-shift of the mean radial velocity as was in fact observed by Markova & de Groot (1997). Such a blue-shift could be particularly important if part of the receding material was behind, and so occulted, by the photosphere, but the symmetry of the lines, noted by Markova & de Groot, would suggest that such occultation is small. In any case, if the wind has spherical symmetry, the less excited lines could not be optically thinner because these lines would also be emitted in the region of emission of the more excited lines, where they should not be optically thinner than those excited lines.

An alternative explanation is to assume that the wind of P Cygni is anisotropic. Optically thick excited lines with no blue-shifted absorption components would in that case be mainly formed in clouds, which either have large source function, or do not occult much of the photosphere. The optically thinner lower excitation lines with blue-shifted absorption could then be mainly formed in regions of the wind, covering the photosphere, with only small optically thicker contribution to their emission from the clouds. The physical reason for such a situation is however not immediately clear. Heating due to shock waves might occur in the clouds, producing extra ionization radiation, followed by more recombinations and cascades plus pumping to extremely excited levels. Such a situation might also be a way of explaining the presence of the most excited N II lines. Theoretical work is required to see whether this is a viable option.

From the outlined in this sub-section it follows that non-LTE effects and deviations from homogeneity

and spherical symmetry both seem to have place in the wind of P Cygni.

4.3.2 Forbidden lines

Stahl et al. (1991) were the first to note the presence of Fe II forbidden lines in the P Cygni optical spectrum. Soon after that the forbidden spectrum of the star was investigated in detail, and a large number of [Fe II], [Fe III], [N II], [Ti II] and [Ni II] lines were identified and subsequently analyzed (Stahl et al. 1993; Markova 1994; Markova & Zamanov 1995; Markova & de Groot 1997).

As a result, it was found that the [Fe II] lines show flat-topped profiles indicative of line formation in a region of constant expansion velocity. From the line width we estimated $V_{\text{exp}}=231\pm 3 \text{ km s}^{-1}$. Surprisingly, this value turned out to be a factor of two smaller than the wind terminal velocity, as determined from the blue edge of the UV metal absorption lines (e.g., Underhill 1979; Cassatella et al 1979).

Since v_{∞} originating from measurements of the blue edge of UV profiles might be overestimated (due to macro-turbulence, or presence of optical depth enhancements), we decided to re-determined this parameter, employing an alternative approach (Prinja et al. 1990) that makes use of observed parameters of Discrete Absorption Components, DACs (see Sect. 4.4.2). To this end we used data for DACs from Markova (1986b) and from Lamers et al (1985) and obtained a value of 236 km s^{-1} , in perfect agreement with V_{exp} from [Fe II] lines. This finding indicates (i) that the earlier estimates of v_{∞} , based on the blue edge of UV absorption lines, are likely overestimated, and (ii) that the [FeII] lines are formed at large distances from the stellar surface where the wind has already reached its terminal velocity. The latter possibility was suggested by Stahl et al. (1991) as well.

Another important result of our analysis is the identification of the [NII] red lines in addition to the yellow one already identified by Stahl et al. (1991). The observed properties of these three lines are quite similar suggesting they all form in same wind region with an outflow velocity of $\sim 200 \text{ km s}^{-1}$. With this in mind and taking into account the theoretical intensity of [N II] $\lambda 6584$ is about 3 times that of [N II] $\lambda 6548$, we estimated the [NII] ($\lambda 6548+\lambda 6584$)/[NII] $\lambda 5755$ ratio, and subsequently used it to put constrains on the electron density, n_e , and temperature, T_e , in the region of line formation. In particular, we derived [NII] ($\lambda 6548+\lambda 6584$)/[NII] $\lambda 5755 = 1.50$. According to Sobolev (1975), a flux ratio between 1 and 2 corresponds to n_e from 5×10^6 to $5 \times 10^7 \text{ cm}^{-3}$ and T_e from 5 700 to 10^4 K where the former value of T_{eff} refers to the high-density limit of Sobolev's formula.

As a next step we tried to constrain the [NII] forming region in space. In particular, adopting $\dot{M}=1.5 \times 10^{-5} M_{\odot}/\text{yr}$, $R_{\star}=76 R_{\odot}$ (Lamers 1989) and $v_{\infty} = 240 \text{ km/s}$, we estimated an electron density between 5×10^6 and $5 \times 10^7 \text{ cm}^{-3}$ at distances from 30 to 110 stellar radii². At these distances the linear ve-

²In these calculations the gas is assumed to be fully ionized hydrogen.

locity law of Waters & Wesselius (1986) gives $V=v_\infty$ implying a flat-topped profile with $HWZI=240$ km/s for an optically thin line formed there; this is contradicted by the observations. At the same distances the BC-velocity law with $\beta=4$ gives a velocity of 220 to 230 km/s (for $v_\infty=240$ km/s). The observed width of the [NII] profiles, however, is below these values. Obviously, a velocity law flatter than one with $\beta=4$, but yielding the same density structure, would give better results. Such a velocity law was obtained by Pauldrach & Puls (1990) in the framework of their best model. Its terminal velocity, however, is quite low (195 km/s) compared with our value of 240 km/s. Concerning the [Fe II] formation region, a combination of a BC-velocity law with stellar parameters as already adopted would locate this region at $r \geq 110R_\odot$ where $n_e \leq 5 \times 10^6 \text{ cm}^{-3}$.

Finally, let me point out that with $d=1.8$ kpc for P Cygni the [NII] emitting region as determined by us would have an angular radius smaller than 1.5 arcsec, in perfect agreement with Stahl (1989) who argued that beyond an angular radius of 1.5 arcsec no evidence for excess [NII] $\lambda 6584$ emission exists. Interestingly enough, Johnson et al. (1992) did not find any [NII] emission in their on-star spectrum. Differences in the slit position angles could possibly cause such a discrepancy. This points to a possible asymmetry in the emitting [NII] region close to the star.

4.4 Photometric and line-profile variability

4.4.1 Photometric variability

To learn more about the nature and the origin of spectroscopic variability parallel information about the photometric behaviour of the star is required.

To this end we investigated the light and colour curves of P Cygni over a period of 13.5 years, from March 1985 to October 1998. The distribution of the used data in time is shown in Figure 4.1 (left). The solid line (upper panel) connects points which represent the mean values of V , computed over time windows naturally defined by major seasonal gaps in the observations. The intention of this line is to guide the eye and to emphasize the presence of a slow component in the photometric behaviour of the star. The amplitude of this variation is about 0.1 mag on a time scale of about 7.3 years. Two cycles, both incomplete, seems to present, during which the star becomes redder in $B - V$ as it brightens and vice versa. Apart from the rapid and very strong variation between JD 2 448 538 and JD 2 448 567, the behaviour of the $U - B$ colour index tends to follow that of $B - V$.

In addition to this very long-term (VLT) variability in the stellar brightness, the observations furthermore revealed the existence of short-term (ST) variations with amplitudes between 0.1 to 0.2 mag, and a

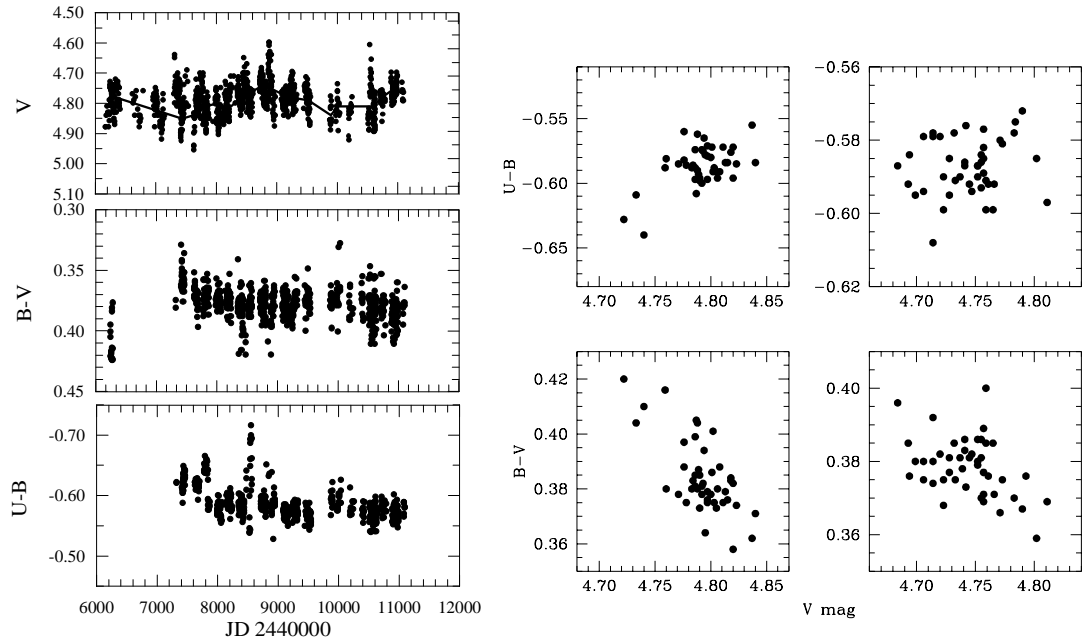


Figure 4.1: *Left*: Light and color curves of P Cygni. The presence of a very long-term (VLT) variability component is highlighted by a solid line. *Right*: Color behaviour of the short-term (ST) variations in the stellar brightness.

characteristic time-scale of 3 to 4 months. The colour behaviour of these variations, shown in the right-hand panels of Figure 4.1, is redder in $B - V$ and bluer in $U - B$ as the star brightens. Irrespective of the small amplitudes of the established colour variations, we are inclined to consider them real due to their systematic character.

4.4.2 Line-profile variability in the optical

Merrill (1913) was the first who reported variations in the visual spectrum of P Cygni. Since then a huge amount of studies have been implemented to investigate this issue. Nevertheless, even at the early eighth a consistent description of the P Cygni spectral variability was still missing (see, e.g., Markova 1986a).

Discrete Absorption Components

One of the most intriguing aspects of wind variability is the presence of narrow optical depth enhancements, called *Discrete Absorption Components* (DACs), superimposed at velocities close to v_∞ in the UV spectra of hot stars (see, e.g., Underhill 1975; Morton 1976; Lamers et al. 1982; Howarth & Prinja 1989). The features seem to be permanent: neither the velocity, nor their strength vary with time. Due to their ubiquity, DACs are thought to be a fundamental property of hot star winds. Therefore, it should be not a surprise that

a huge amount of papers devoted to this topic have been published during the last 20 years. Nevertheless, the nature and the origin of these features still remain a mystery.

So far, P Cygni is the only known LBV with DAC signature in its UV spectrum (Cassatella et al 1979; Lamers et al 1985). Interestingly, and most important, in earlier studies similar features have been detected in Balmer lines of this star as well (de Groot 1969; Lood et al. 1975). However, the dynamical properties of DACs in UV seemed to be different from those of DACs in Balmer lines – the former persist at almost same velocity for a long time, while the latter oscillate within a wide range of velocities, from ~ 100 to $\sim 250 \text{ km s}^{-1}$ – that might point out to different origin. Irrespective of this possibility, the presence of DACs in Balmer lines of P Cygni was a real opportunity to come nearer to a better understanding of this phenomenon because UV data can be obtained only from space whilst optical observations is easy to collect.

Guided by these prospectives, the long-term behaviour of Balmer lines in P Cygni was investigated with the primary goal to identify and follow the development of DACs, and to determine their properties as a function of time. This way valuable information about the nature of these features can be obtained which might eventually provide us with a clue to solve the puzzling issue of their origin. Below, main results of this investigation are summarized, and various possibilities to interpret the DAC phenomenon in P Cygni are briefly discussed. More detailed description can be found in Markova & Kolka (1984) and in Markova (1986a,b).

Dynamical properties. From the analysis of radial velocities, two types of DACs were identified: “high-velocity” components which persist at almost same position ($210 \leq V_r \leq 210 \text{ km s}^{-1}$) for a relatively long time, and “low-velocity” components which migrate from red to blue within the profile ($90 \leq V_r \leq 200 \text{ km s}^{-1}$). In these properties, our “high velocity” DACs obviously resemble those observed in UV, while the “low-velocity” ones are similar to the features observed by de Groot (1969) and by Lood et al. (1975) with one exception though: no clear evidence of decelerating components was found. In addition, the analysis of the corresponding FWHMs and equivalent widths showed that accelerating in velocity space the ‘low-velocity’ components become narrower and weaker. Interestingly, and in contrary to the situation established in UV, the “high-velocity” components also decrease in strength *vanishing* completely after some time. Based on these findings we concluded that “low-velocity” DACs in Balmer lines do not seem to oscillate, as suggested in earlier studies, but rather accelerate continuously becoming “high-velocity” components when they reach $V_r \geq 200 \text{ km s}^{-1}$.

Time scale Our analysis furthermore showed (i) that the appearance of DACs in Balmer lines is a recurrent phenomena with a characteristic time of about 200 days, and (ii) that independent of their individual

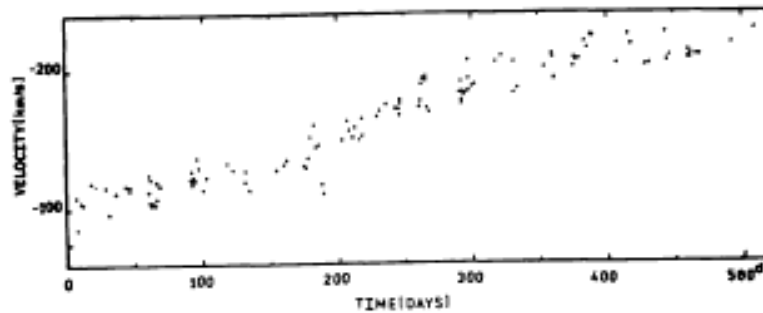


Figure 4.2: Composite velocity vs. time curve representing typical development of DACs in Balmer lines of P Cygni.

properties (e.g. acceleration, optical depth etc), the components develop in a similar way, i.e. they accelerated till the time they reach a given velocity different for various DAC events, but limited between 200 and 230 km s⁻¹. To test these findings on a larger statistical base, we constructed a composite velocity vs time curve using own radial velocity data, and incorporating similar data from de Groot (1969) and Kolka (1983). The total time coverage of these data is about 50 years. The obtained curve, shown in Figure 4.2, is obviously well-defined supporting our suggestion that the variability pattern of DACs in Balmer lines of P Cygni is relatively stable, with a cycle length of about 200 days.

Density and excitation Close inspection of all lines in the optical spectrum of the star indicated that clear line-splitting can be confidently and frequently detected not only in Balmer lines, but also in other lines of relatively *low* excitation such as, e.g., the K-line of Ca II, Mg II $\lambda 4481.14$ and He I lines of:

- the triplet series 2³P - n³D with $\lambda \leq 3819 \text{ \AA}$;
- the triplet series 2³P - n³S with $\lambda \leq 4713 \text{ \AA}$;
- the singlet series 2¹P - n¹D with $\lambda \leq 4387 \text{ \AA}$;

This result suggests that the excitation/ionization inside the region of DAC formation appears to be relatively low, lower than in the ambient wind.

Concerning the density, applying the Inglis Teller relation to the last visible Balmer line with and without line-splitting, we found this quantity to be typically one order of magnitude higher than in the ambient wind. At such densities the excitation /ionization of the plasma must be indeed lower inside than outside the structure.

Optical and UV DACs As already noted above, the behaviour of DACs in Balmer lines of the LBV P Cygni seems to be qualitatively different from that of DACs in UV spectra of hot stars, where these components tend to reside at same velocity with no variations in their optical depth for a long time. This result could be interpreted in terms of different origin of the both. However, such a concluding might be misleading for the correct way to proceed is to compare features observed *simultaneously* in one and the same star, but not in different stars³.

Luckily, it turned out that our optical data overlap, though in part, with similar data from UV (Lamers et al 1985). By means of a direct comparison, good correspondence in velocity and acceleration of Balmer and UV DACs was established for several observational epochs. (Note that in P Cygni DACs have been observed not only in Fe II, but also in Fe III lines in the UV. Note also that the dynamical properties of the Fe II and Fe III components are different. For more information see Lamers et al 1985 and Markova 1986b.) This finding has at least two major consequences: first, it suggests that DACs in optical and UV lines are signatures of same physical phenomenon, and second, that the "low-velocity" components in Balmer lines are more likely progenitors of the high-velocity stable components in the UV Fe II lines. Within a wind model with a velocity field as described by Eq. 1.9, this would mean that the DAC phenomenon is not related to only the outer layers of the wind, as previously thought, but appears to affect the inner parts of the wind as well.

Possible origin About 20 years ago, when the origin of DACs in UV was still an open issue, it was believed that these features originate and develop in the outer wind only. However, this picture is questioned by our results which in contrary suggest DACs more likely form in the inner parts of the wind and accelerate outwards. In addition, we also found suggestive evidence that inside the structures producing DACs the gas density is higher, and the excitation/ionization is lower than outside. Based on our observational findings, a scenario consisting of a sequence of outward moving, extended, dense shells was suggested to interpret the appearance and evolution of DACs in P Cygni (Markova 1986b). This scenario was supported by other investigations as well (e.g., Lamers et al 1985; Van Gent & Lamers 1986; Israelian et al. 1996).

Although many of the DAC properties can be easily explained in terms of the shell scenario, there is at least one feature that could not conform with the idea of outward moving dense shells: within a given DAC episode an increase in emission strength of the lines showing DACs should appear (due to the shell expansion), but has not been observed. To avoid this difficulty an alternative hypothesis could be suggested where DACs originate from material confined in discrete geometric units ("blobs", "puffs" or "spirals") situated just in front of the stellar disk. And although the presence of such structures is strongly

³And even then one could not be absolutely sure since these two type of DACs may form in different parts of the wind, and might therefore provide different insides into the same phenomenon.

supported by radio (Skinner et al. 1997), spectral (Barlow et al. 1994), interferometric (Vakili et al. 1997) and polarimetric (Taylor et al. 1991) observations, it is invincible difficult to reconcile the idea of randomly-distributed regions of excess density with the recurrent appearance of DACs.

Recently, a model consisting of co-rotating spirals rooted in the photosphere, the so-called Co-rotating Interacting Region (CIR) model, has been developed (Cranmer & Owocki 1996, see also Mullan 1984, 1986) and successfully applied to interpret DACs in UV spectra of O-type stars (Kaper et al. 1997; Kaper et al. 1999). A simple qualitative consideration however shows that the CIR scenario does not seem to be suitable for P Cygni. In particular,

- i) if DACs in P Cygni were due to spiral-shaped structures that co-rotate (or nearly co-rotate) with the star, their character should be strictly periodic (even over a limited time interval) with a length of the cycle (determined by the rotational period of the star and the number of co-rotating spirals) comparable to, or an integer fraction of, the rotational period.

However, our analysis shows that the DAC-induced variability is *not* periodic, but recurs on a time-scale that varies from about 150 to about 250 days with a mean value of 200 days. Also, it is a factor of 2 to 3 longer than the maximum rotational period of 96 days, as determined from the rotation velocity ($=40 \text{ km s}^{-1}$, Israelian 1995) and the radius ($=76 R_{\odot}$, Pauldrach & Puls 1990) of P Cygni. All this indicates that rotation does not seem to play a fundamental role in determining the recurrence of DACs in P Cygni.

- ii) if DACs in P Cygni were due to spiral-shaped structures rooted in the photosphere, it should be in principle possible to follow their development starting from the wind base up to the wind terminal velocity. However, no indication of any DACs with velocities lower than 90 km s^{-1} has been provided by the observations (Markova 1986b; Markova 2000; Israelian et al. 1996).

On the other hand, the life-time of a given component is very long, about a factor of 100 longer than the radial flow times of the wind⁴. This result implies that the structures producing DACs might not represent single mass-conserving features, but might rather arise from slowly evolving perturbations through which wind material flows. Since the phenomenon is stable over more than 50 years, these perturbations are more likely maintained by photospheric processes. The latter possibility seems to be supported by the fact that on several occasions the appearance of a new DAC was accompanied by an increase in the stellar brightness (Israelian et al. 1996). Thus, it seems rather likely that the physical source of the perturbation producing DACs is coupled with the stellar photosphere. However, so far no clear indication has been found that these perturbation also develop in the inner part of the wind.

⁴The characteristic radial flow time of P Cygni's wind is about 2.8 days

Other forms of LPV

Most lines in P Cygni's optical spectrum do not show clear line-splitting, but exhibit significant variations in their profiles on a variety of time-scales, and variability patterns. To obtain a detailed picture, we examined the temporal behavior of a large sample of lines of various ions and species (e.g. He I, O II, Si III, Si IV, N II etc), with the primary goal to classify different forms of LPV, to specify their properties, and to search for possible relationships between them. Brief description of the outcomes of this analysis is given below while more detailed information can be found elsewhere (e.g., Markova & Kolka 1985, 1988; Markova 1993a,b; Markova 2000; Markova 2001).

To detect and localized variations across the line profiles, a modified version of the Temporal Variance Spectrum (TVS) (Fullerton, Gies & Bolton 1996), firstly used by Prinja et al. (1996), was employed. As a result, in addition to the DAC-induced variability four different forms of LPV were identified: short-term (ST) variability in the troughs and lobes of lines of intermediate and high excitation; long-term (LT) variability in Balmer and He I lines of relatively high optical depth; very long-term (VLT) variability in the H_α EWs, and a red emission-wing variability.

Short-term variability To identify the physical ingredients of the established variability, the absorption troughs and emission lobes of the lines were measured (using a fitting procedure with Gaussians) for the size and position of the absorption core and/or emission peak, and for equivalent width. The obtained data, partly illustrated in Fig. 4.3, give clear evidence of radial velocity and line-strength variations in emission and absorption.

In particular, it was found that independent of their excitation and optical depth all lines behave in a similar way showing smooth fluctuations (i) in velocity of absorption cores and emission peaks; (ii) in maximum absorption and/or emission fluxes, F_{\max} (em/abs), and in absorption and/or emission EWs. The fluctuations appear around a mean level specific for each transition. Their amplitudes are usually small, but genuine since they exceed the accuracy of the individual determinations. The variations in emission and absorption fluxes do not correlate justifying they are not an artifact of inconsistent continuum placement. (Otherwise, a distinct anticorrelation must be observed.) Clear signature of ST variability are also seen in the total EWs of the lines (see the right-hand panel of Figure 4.5). Interestingly, and most importantly, even the high excitation lines, such as, e.g. Si IV lines whose effective level of formation is close to the wind base, vary in symphony with the strongest Balmer and He I transitions.

These results indicate that the ST variability can not be solely due to a redistribution of a fixed amount of line absorbers, but instead requires real alterations of the number of absorbers, either through changes in the ionization/excitation, or in the number density. And although changes in the excitation temperature

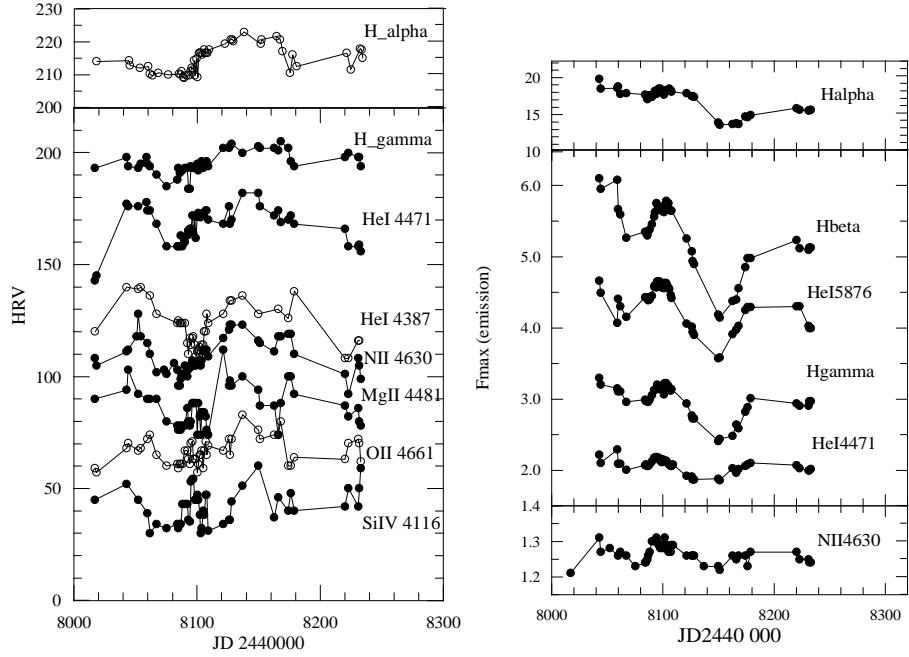


Figure 4.3: Variability patterns in velocity of the absorption cores (left panel) and in the maximum emission flux (right panel) of lines of various ions. All velocities are negative and taken respect to the Sun.

of the wind were in fact established – By means of a curve-of-growth analysis of 35 NII lines we found evidence of a 15% decrease in T_{exc} in parallel to the increase in velocity and strength of the lines during the ST variation, – we consider the latter interpretation more probable because lines of quite different excitation have been simultaneously affected. Thus, we suggest that the ST modulations in P Cygni’s optical spectrum more likely originate from time-dependent enhanced-density structures that operate in the inner layers of the wind, from about $14 R_{\star}$ (where the H_{α} line forms) down to its base.

A puzzling aspect of our results is that though qualitatively similar, the behaviour patterns of the ST modulations in velocity and in line strength are characterized by different time scales (~ 100 days in velocity and $\sim 50 \pm 10$ days in line strength). A comparison with results from Kolka (1989, 1991) showed that similar variations, but on a shorter time-scales (~ 50 days in velocity and ~ 30 days in line strength) have been detected in other observational epochs as well. These findings suggest (i) that the wind structure producing the ST modulation is likely caused by a photospheric process which is capable of reproducing itself on a different time-scale, and (ii) that irrespective of the difference in the corresponding time-scales, the modulations in velocity and line strength appear to be physically linked. Since these time-scales are similar, or/and smaller than the maximum rotational period of the star, stellar rotation might be an issue.

Long-term variability Stahl et al. (1994) have published radial-velocity and emission peak-intensity measurements of the strongest Balmer and He I lines in P Cygni’s optical spectrum. Based on these data,

the authors found evidence of a slow variation both in the velocity of the absorption cores, and in the intensity of the emission peaks of the lines (I shall call this variation long-term (LT) variation to distinguish it from the ST variation described above). Analyzing the Stahl et al. data we furthermore found that:

- i) the LT variation in velocity is anti-correlated with the LT variation in emission-peak intensity: when the size of the emission peak increases, the absorption core moves to longer wavelength;
- ii) the amplitude of the LT variation, both in velocity and in line intensity, decreases with decreasing line optical depth.

The latter result is illustrated in the right-hand panel of Fig. 4.3, where the limiting case of a line with and without LT variability is represented, respectively, by $H\alpha$ and N II $\lambda 4630$. Note that while all lines exhibit ST modulations in the size of their emission peaks, only the stronger Balmer and He I lines do show LT variability component. Note also that in the $H\alpha$ EW curve, the LT variability can be easily recognized as a sharp dip situated between JD 2 448 000 and JD 2 448 600 (see the right-hand panel of Figure 4.5). We are confident that this feature is real since it was independently recorded by different authors (Markova et al. 2001a; Taylor et al. 1991).

Thus, it seems likely that the LT spectral variability is located only in the relatively outer part of the wind ($V \leq 0.82 v_\infty$) with no obvious connection to the inner parts.

The red-emission-wing variability affects the high-velocity part of the P Cygni-type profiles, $+90 \leq V \leq +230/250 \text{ km s}^{-1}$. This variability seems to be caused by low-intensity bumps whose position varies with time. The properties of this phenomenon are still largely unknown. A similar phenomenon may have been observed by Kuss & Duemmler (1995) who suggested that the bumps are due to light echos from outward-moving dense shells that produce different DAC sequences.

Very long-term variability Finally, let me note that the analysis of the $H\alpha$ EWs provided convincing evidence of a very slow (time-scale of about 7 years or more) variability component with an amplitude of $\sim 20 \text{ \AA}$. In Sect. 4.5 I will describe and discuss this phenomenon in detail.

4.4.3 Comparison between photometric and spectroscopic variabilities

Self-consistent non-LTE calculations (Pauldrach & Puls 1990) have shown that the wind of P Cygni is highly unstable with respect to extremely small changes in the fundamental stellar parameters. Therefore, some relation between variations in the wind and in the photosphere might be expected to present in the star.

Guided by these prospects, several investigators tried to find observational evidence in support of such photospheric connection, but, in general, the results are contradictory. In particular, a possible relation between brightness variations and changes in line profiles, due to the recurrent appearance of DACs, was suggested by Israelian et al. (1996). Suggestive evidence for V-band variations being correlated with changes in the emission-flux of H_α were also reported by de Groot (1990) and by Percy et al. (1996).

On the other hand, Scuderi et al. (1994) noted that although the behaviour of the stellar parameters, as deduced from UBV photometry, do correlate with variations in the structure of the wind, the global mass-loss rate does not seem to react in symphony. Also, Stahl et al. (1994) argued that no clear evidence of a correlation between photometric variability and LPV could be found over the period covered by their observations. To investigate this issue further, we performed a detailed comparison of the available photometric and spectroscopic data of P Cygni.

ST variability Our analysis provided clear evidence of a close relationship between changes in V , $B - V$ and $U - B$, on the one hand, and the ST variability as traced by the H_α EWs, on the other: when the EW decreases, the star becomes brighter in V , redder in $B - V$ and bluer in $U - B$. This finding is fundamentally important since it strongly supports our hypothesis about the photospheric origin of the wind structure generating the ST variability. (For more detailed information the interested reader is referred to Markova et al. 2001a.)

If the ST wind modulations were indeed triggered by photospheric processes what could these be? Since on the HR-diagram, P Cygni falls within the predicted instability strip for strange-mode oscillations (Kiriakidis 1993), non-radial pulsations of strange-mode oscillations might be the cause for the ST variability of the star. On the other hand, Lamers et al (1998) argued that the microvariability of LBVs could be explained by means of NRPs of gravity-modes of low l . Thus, and at least at present, NRPs of either strange-mode or g-mode oscillations seem to be the most plausible candidates to explain the appearance of the ST variability of P Cygni.

Another important issue to be address is: *Are the ST modulations and DACs linked to each other?* There are at least two pieces of indirect evidence that suggest the modulations and the DACs are probably *not* linked to each other. First, the time-scales of the two phenomena are too different to suggest they might be physically coupled, and second, there are lines (e.g. the resonance lines of Na I and Ca II) that show DACs, but do not show modulations in velocity or strength of their troughs.

On the other hand, on two occasions in 1981 the appearance of a new DAC event was preceded by increase in velocity of high-excitation lines during the ST variations, suggesting possible relation between the two. However, in this case, some additional factor is needed to explain why structures of sufficient

strength to produce observable DACs do not occur during every cycle of the ST modulations.

LT variability Concerning the LT variability established in the lower members of the Balmer series (H_γ to H_α) and in the strongest He I transitions, no evidence of a counterpart in the photometric behaviour of the star was found. No clear evidence for a direct coupling between this variability and the VLT photometric variability was found either. The time-scales of the two phenomena differ too much to suggest they may be physically linked.

On the other hand, the maximum of the LT variation in H_α was found to occur very close to the maximum in the VLT photometric curve, and also, practically coincides with the strong and rapid increase of the brightness in the U-band. It is not clear at present whether these events are causally or physically linked.

The correspondence between the VLT variability in the spectral and photometric behaviour of P Cygni will be discussed in the next section.

4.5 P Cygni in a short SD phase

Recently, Van Gendered (2001) has published an extensive review of the 20th century scientific achievements on LBVs where 46 confirmed and candidate members of the class are listed. In addition, the author updated the criteria for membership in the LBV class from those given by Humphreys & Davidson (1994) introducing new terms, such as “S Dor (SD)-eruption” and “S Dor (SD)-phase”. The latter is described as *a brightness variation of up to 2.5 mag on a time scale of years to decades and even to centuries during which the star becomes redder when it brightens and vice versa*.

P Cygni is a notorious S Dor-type star. It has a high luminosity ($\log L/L_\odot = 5.86$; Pauldrach & Puls 1990), a high mass-loss rate ($\sim 2 \times 10^{-5} M_\odot \text{yr}^{-1}$; Scuderi et al. 1994, 1998; Markova et al. 2001a), an extended atmosphere and four visible ejecta containing processed material (Barlow et al. 1994; Meaburn et al. 1996; Skinner et al. 1997; Johnson et al. 1992). In addition, the star has undergone at least one SD-eruption (in 17th century). However, and surprisingly, no evidence of any SD-phases were reported to date.

4.5.1 Photometric evidences

The properties of the VLT photometric variation in P Cygni established by us appear to be quite similar to those of weak-active S Dor variables in a *short SD-phase* as described by van Genderen (2001). To investigate this issue further, we determined the basic parameters T_{eff} and R_\star of the star following a simple 3 step procedure. First, the observed $B - V$ colours were corrected for interstellar extinction with $E(B - V) =$

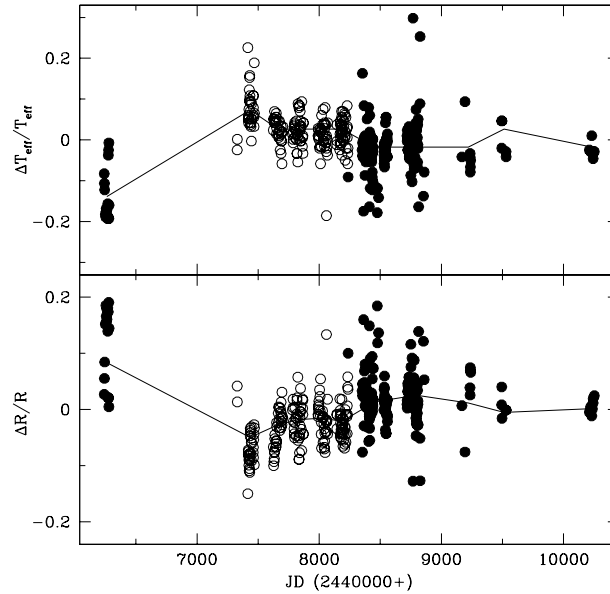


Figure 4.4: Relative variations in T_{eff} and R_{\star} as derived from the corresponding B-V data. The presence of a very long-term (about 7.3 year) variation in the star behaviour is highlighted by a solid line.

0.63 to derive the corresponding intrinsic colours $(B - V)_0$. Then, using the empirical relation between $(B - V)_0$ and T_{eff} for normal SGs (Schmidt-Kaler 1982), the temperature of the star was determined at any time for which photometric data are available. Finally, from the T_{eff} and the corresponding V magnitudes, the stellar radius was derived using again the empirical relations of Schmidt-Kaler (1982). Since the *absolute* values of T_{eff} and R_{\star} thus obtained were expected to be rather uncertain (due to the uncertainty in the used calibrations), the *relative* variations in these quantities, $\Delta T_{\text{eff}}/T_{\text{eff}}$ and $\Delta R_{\star}/R_{\star}$, can be only considered reliable. The accuracy of these estimates is 2% in T_{eff} and 4% in R_{\star} .

The temporal behaviour of $\Delta T_{\text{eff}}/T_{\text{eff}}$ and $\Delta R_{\star}/R_{\star}$ is illustrated in Figure 4.4 where in addition to our data (dots), similar data from Scuderi et al. (1994) (circles) are also used to increase the statistics. Solid lines connect points that represent mean values of variations in T_{eff} and R_{\star} , calculated over time windows naturally defined by seasonal gaps in the observations. Obviously, when the star brightens its temperature decreases (by $\sim 10\%$) while the radius increases (by $\sim 7\%$). In this behaviour P Cygni closely resembles other SD variable in a short SD-phase. Thus, we conclude that during the period covered by our observations *P Cygni has experienced a short SD phase* with a possible maximum in the fall of 1985, a minimum in the winter of 1988, a maximum in the summer of 1992, and a minimum in the winter of 1995.

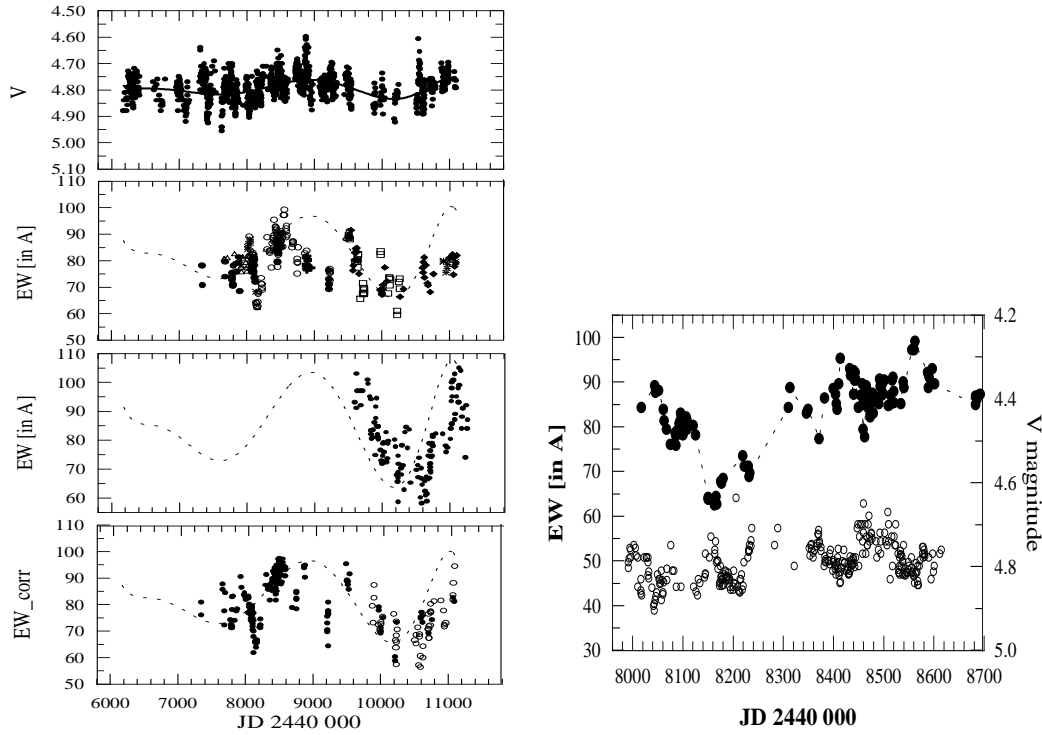


Figure 4.5: Comparison between V -band variations and changes in the $H\alpha$ equivalent width. *Left*: The presence of a VLT variability component is highlighted by a solid and dashed lines. *Right*: V -band data are represented by circles; $H\alpha$ EWs - by dots. For more information see text.

4.5.2 Spectroscopic evidences

To learn more about the nature of the VLT variability in P Cygni, the behaviour of the $H\alpha$ EW has been compared to that of the stellar brightness. The obtained results are shown in Figure 4.5 (left). In the top panel, the solid line traces out the VLT component in the V -band variability. In the three panels below, the same curve (scaled in an appropriate way to fit the relevant data) is represented by a dashed line. The purpose of these curves is to guide the eye and to make the comparison easier. From the two panels in the middle of the figure, it is apparent that, although some correspondence between the V -band variability through the short SD-phase and the VLT spectral variability does exist, the two phenomena do not seem to be strictly correlated.

However, given that the $H\alpha$ EWs are directly influenced by changes in the V -band trough the continuum normalization, this result might not be absolutely correct. To remove this effect, we proceeded as follows. For observations close enough in time to be considered simultaneous, we scaled the EWs to a constant continuum level chosen to correspond to $V_0 = 4.8$ mag. Thus, the measured EWs were multiplied/divided by a factor K , where $\log K = 0.4\Delta V$ and $\Delta V = V(t) - V_0$ correspondingly when P Cygni is brighter/fainter. Strictly speaking, differences in the continuum flux at $\lambda=6563 \text{ \AA}$ should be used, but in our case ΔV is

a good approximation since the colour indices of P Cygni do not vary greatly. The corrected EWs from all observers, W_{corr} , are shown in the bottom panel of Figure 4.5. Unfortunately, the lack of complete simultaneity between the spectroscopic and photometric observations has led to a noticeable reduction in the number of available EW estimates. Nevertheless, one can see that the pattern of the VLT variability of $H\alpha$ does not change significantly when the effect of the changing continuum is taken into account. In addition, it appears (if it is not an artefact of bad data sampling) that the corrected EW data follow more closely the pattern of the S Dor-variability. In summary, we conclude that the VLT variability established in $H\alpha$ is intrinsic to the wind (not the photosphere), and that this variability is more likely linked to the 7.3-year SD-phase.

4.5.3 $H\alpha$ variability due to changes in \dot{M}

Since the $H\alpha$ emission is directly related to wind density, the variations in this quantity can be due to changes in the mass-loss rate. A rough estimate of the *relative* variation in \dot{M} that could result in the variations observed in $H\alpha$ during the SD phase can be derived employing the scaling relation found by Puls et al. (1996, Eq. 43). This relation connects mass-loss rate, terminal wind velocity, stellar parameters and $H\alpha$ equivalent width, and in the optically thick limit can be approximated as:

$$\dot{M}(\text{thick}) \sim v_{\infty}^{3/4} R_{\star}^{3/2} [W_{\lambda}^{\prime\prime}]^{3/4} \quad (4.1)$$

where $W_{\lambda}^{\prime\prime} = W_{\lambda}^{\text{obs}} + W_{\lambda, \text{phot}}^{\text{red}}$. In fact this approximation was derived under the assumption of a β -velocity law with $\beta = 1$, but it is appropriate for P Cygni as well since the authors argued that at larger \dot{M} the value of β is not of importance. (Note that for P Cygni $\beta=4$ Pauldrach & Puls 1990.)

From the observations we derived $W_{\text{corr}}(\text{max})=95 \text{ \AA}$ and $W_{\text{corr}}(\text{min})=75 \text{ \AA}$. With these estimates, and neglecting the contribution of the photospheric absorption⁵, we then derived (under the additional assumption of constant stellar radius and wind terminal velocity):

$$\frac{\dot{M}(\text{max})}{\dot{M}(\text{min})} = 1.19. \quad (4.2)$$

And although this value might be a bit overestimated (v_{∞} is expected to vary in opposite to \dot{M} Markova et al. 2001a), we conclude the variability of $H\alpha$ EW during the SD phase can be associated with a 19% increase in \dot{M} .

⁵In P Cygni the contribution of the photospheric absorption to the total equivalent width of $H\alpha$ is less than 2%

4.5.4 Possible interpretation

Neither the mechanism causing the SD-phases, nor the region where this mechanism originates is known. Presently, two hypothesis exist. In the first one, the SD phase is assumed to be due to a drastic increase in \dot{M} leading to the formation of a pseudo-photosphere (the so-called atmospheric hypothesis). In the second one, an alternative sub-photospheric origin is suggested due, at least partly, to variations in the underlying stellar radius.

To check the first hypothesis, we followed de Koter et al (1996) and calculated the optical depth of the P Cygni wind, τ_v (at 5555 Å). The obtained value of 2.30 implies that the wind of this star is sufficiently optically thick to create a permanent pseudo-photosphere, and that relatively small variations in \dot{M} could cause 0.1 to 0.2 mag variations in the stellar brightness. This possibility received additional support by further computations which showed that a 19% increase in \dot{M} can in fact lead to a $\sim 7\%$ increase in the apparent stellar radius, in perfect agreement with estimates reported in previous sections. (For more information see Markova et al. 2001b.) These findings suggest that in P Cygni the SD phase could be interpreted as an atmospheric phenomenon.

However, note that in a case of a star like P Cygni, the interpretation of the SD variability as a pure atmospheric phenomenon is never straightforward. Indeed, if the wind is optically thick and if "small" photometric variations do exist, an alternative scenario where an increase/decrease in R_*/T_{eff} (due to some unknown reason) at constant luminosity result in an increase/decrease in \dot{M}/v_∞ , which in turn lead (because of the high wind opacity) to an increase/decrease in the apparent stellar radius/temperature is always possible. With this in mind, we conclude that the 7.3-year SD oscillation in P Cygni is more likely a mixture of an expanding radius/decreasing temperature and an expanding pseudo-photosphere.

4.6 Summary

The main outcomes of our long-term optical survey of P Cygni can be summarized as follows:

- **Emission line spectrum** Our observations suggest that the emission line spectrum of P Cygni was much richer and intensive in the early 90 than 60 years before. If not due to observational selection this finding might indicate the presence of a very long-term variation in the wind+photosphere properties of the star.

To address this issue, the parameters of a large sample of emission lines, permitted and forbidden, have been derived and used to localize the region of line formation, and to put constraints on the physical parameters of the gas inside these regions. In particular, we found that the optical [N II] lines are formed in

a wind region situated between 30 and 110 stellar radii which is likely asymmetric. In this region $5 \times 10^6 \leq n_e \leq 5 \times 10^7 \text{ cm}^{-3}$ and $5700 \leq T_e \leq 10^4 \text{ K}$. Concerning the [Fe II] lines, these lines more likely form at distances $r \geq 110 R_\odot$ where the density drops below $5 \times 10^6 \text{ cm}^{-3}$.

From the analysis of the permitted emission lines, on the other hand, a quite surprising behaviour was revealed: more excited lines without blue-shifted components appear to be optically *thicker* than less excited lines with P Cygni-type profiles. This finding cannot be interpreted in terms of the standard wind models, but might indicate deviations from spherical symmetry and homogeneity in P Cygni's wind.

• **Wind variability in the form of Discrete Absorption Components (DACs)** About 20 years ago, when the nature and the origin of DACs in the UV spectra of hot stars was an open issue, it was believed that these features originate and develop in the outer wind only. However, by means of a direct comparison of DACs observed in the UV and optical spectrum of P Cygni we unambiguously showed that this hypothesis is not correct, and that DACs in UV form in the inner parts of the wind and subsequently accelerate outwards. Based on a detailed analysis of the behaviour of these feature, we showed that their properties are to a large extent consistent with a scenario where DACs originate from large-scale, time-dependent, enhanced-density (low-excitation) perturbations, which develop in the intermediate and outer parts of the wind, $V \geq 0.41 V_{\text{inf}}$, but appear to be maintained by photospheric processes. The geometry of the perturbations cannot be constrained with confidence. They could be either spherically symmetric like shells, or curved, like kinks. The recurrence time-scale of the phenomenon does not appear to be directly related to the stellar rotation.

During the next 10 to 15 years, our hypothesis about the nature and the origin of DACs in hot star winds have received additional theoretical (the CIR model, Cranmer & Owocki 1996) and observational support (see, e.g., Kaper et al. 1996, 1997; Kaper et al. 1999 leading to the idea for “*a photospheric connection*”).

• **Short-term (ST) photospheric variability** By means of a detailed analysis of the photometric behaviour of the star over a period of 13.5 years, we found convincing evidence of permanent microvariability which we called ST variability. The properties of this phenomenon are similar to those of the so-called “100d-type microvariation” recognized in other LBVs (van Genderen 1997a,b), thus suggesting they both are due to same physical mechanism. NRPs of either strange-mode or gravity-mode oscillations might be equally responsible for this phenomenon.

• **ST wind variability** The detailed analysis of LPV in optical lines of P Cygni has provided first observational evidence for a direct coupling between wind and photospheric variability in hot stars. In

particular, we showed that the ST photometric variability has its counterpart in the behaviour of H_α and other optical lines, including those formed close to/at the base of the supersonic wind. Both the position and the strength of the lines are continuously changing where the time scale of the former tends to be a factor of two longer. The signature of the ST spectral variability can be easily recognized in other observational epochs, though on a different time scale. The properties of this variability, at least during our observational campaigns, suggest an interpretation in terms of extended, rotationally modulated, enhanced density wind structure generated by photospheric processes (e.g. NRPs), and developing in the inner (below $\sim 14R_\star$) part of the wind only. In this scenario, ST variations in velocity and line strength should originate from different region of the structure.

•**Short S Dor phase** Our analysis of the long-term photometric behaviour of P Cygni provided first observational evidence that the star has experienced a short SD phase. In particular, we established the presence of a cyclic 7.3-year oscillation in the stellar brightness, during which the stellar radius increases (by about 7 %), the temperature decreases (by about 10 %) as the star brightens. In addition, we also found that this very slow photometric variation is *positively* correlated with similar variations in the H_α emission strength. Interpreted in terms of variable mass-loss, the latter finding would require a 19 % variation in \dot{M} . In this behaviour P Cygni is similar to S Dor and R71, which experience a sequence of such variations, called SD-phases.

Concerning the origin of this variability, based on our results we suggest that in P Cygni the 7.3-year SD oscillation is more likely due to a mixture of an expanding radius/decreasing temperature and an expanding pseudo-photosphere.

Chapter 5

Clumping in O-star winds

In Chapter 1, Section 1.6.1 I have pointed out that notwithstanding its considerable successes (e.g., Vink et al. 2000; Kudritzki 2002; Puls et al. 2003), the *standard* radiation driven wind theory is certainly oversimplified. Stellar rotation (e.g., Owocki et al. 1996; Puls et al. 1999 and references therein), and the intrinsic instability of the line-driving mechanism (see below), produce non-spherical and inhomogeneous structure, observationally evident from, e.g., X-ray emission and line-profile variability (for summaries, see Kudritzki & Puls 2000 and Oskinova et al. 2004 regarding the present status of X-ray line emission).

Theoretical efforts to understand the nature and origin of these observational findings have generally focused on the line-driving mechanism itself; the first linear-stability analyses showed the line force to be inherently unstable (Owocki & Rybicki 1984 and references therein). Subsequent numerical simulations of the non-linear evolution of the line-driven flow instability (for a review, see Owocki 1994) have shown that the outer wind (typically, from $1.3 R_{\star}$ on) develops extensive structure, consisting of strong reverse shocks separating slower dense shells from high-speed rarefied regions. Only a very small fraction of material is accelerated to high speed, and then shocked; for most of the flow, the major effect is a compression into narrow, dense “clumps”, separated by large regions of much lower density.

The amount of clumping is conveniently quantified by the so-called clumping factor (Runacres & Owocki 2002, 2005)

$$f_{\text{cl}} = \frac{\langle \rho^2 \rangle}{\langle \rho \rangle^2} \geq 1, \quad (5.1)$$

which is a measure of the over-density inside the clumps compared to a smooth flow of identical average mass-loss rate. (Angle brackets denote (temporal) average quantities.) For the particular case of self-excited instabilities (e.g., without any photospheric disturbances such as pulsations or sound-waves), this clumping factor was predicted to be radially stratified: beginning with an unclumped wind in the lowermost part

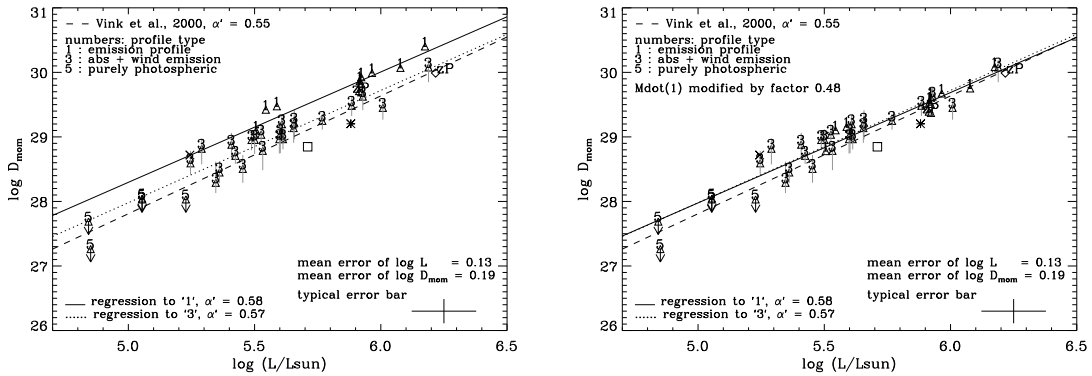


Figure 5.1: Left: WLR for Galactic O-type stars as derived in Section 2.1, but with regressions in dependence of profile type (fully drawn and dotted). Class 1 corresponds to objects with H_{α} in emission, class 3 to objects with H_{α} in absorption and class 5 to objects with an almost purely photospheric profile. Right: As on the left, but with \dot{M} of class 1 objects (H_{α} in emission) decreased by a factor of 0.48.

($f_{\text{cl}} = 1$), the clumping becomes significant ($f_{\text{cl}} \approx 4$) at wind speeds of a few hundreds of km s^{-1} , reaches a maximum ($f_{\text{cl}} \approx 15 \dots 20$), and thereafter decays, settling at a factor of roughly four again. In addition, it was furthermore found that mass-loss rate diagnostics that are linearly dependent on the density (e.g., resonance lines in the UV) are insensitive to clumping, whilst those sensitive to ρ^2 (e.g., recombination lines and free-free continua) will tend to overestimate \dot{M} of a clumped wind by a factor $f_{\text{cl}}^{0.5}$. For further details, see, e.g., Abbott et al. (1981) and Lamers & Waters (1984b).

Clumping in OB-star winds Although the potential effects of clumping were first discussed some time ago (e.g., Abbott et al. 1981; Lamers & Waters 1984b; Puls et al. 1993b), and have been accounted for in the diagnostics of Wolf-Rayet stars since pioneering work by Hillier (1991) and Schmutz (1995), this problem has been reconsidered by the “OB-star community” only recently, mostly because of improvements in the diagnostic tools, and particularly the inclusion of line-blocking /blanketing in NLTE atmospheric models.

Indeed, while earlier studies (e.g., Vink et al. 2000; Kudritzki 2002) found a rather good agreement between theoretically predicted and observed (unblanketed) wind momenta of O-stars, more recent investigations (e.g., Markova et al. 2004; Repolust et al. 2004) have shown that SGs lie above the theoretical WLR, whilst Gs and DWs fit perfectly. And although this discrepancy might in principle be explained by a different number of effective lines driving the wind,¹ an interpretation in terms of wind clumping seems to be also possible. In particular, Puls et al. (2003) have suggested that there might be no separation at all, but that for objects with H_{α} in emission (i.e., SGs) one observes the effects of clumping which mimics a higher mass-loss rate than actually present.

To investigate this possibility in more detail, in Figure 5.1 (left panel) the WLR of our “unified” sample

¹(The coefficient D_0 depends on this quantity via $D_0 \propto N_0^{1/\alpha'}$ (c.f. Kudritzki & Puls 2000, their Eq. 18).

of O-stars (from Section 2.1) was plotted as a function of profile type. Consequently, and apart from two outliers, a clear separation between objects with H_α in emission (marked as class 1) and those with H_α in absorption (marked as class 3) has been established with the former having systematically larger wind momenta than the last. Following the idea of Puls et al. (2003), we shifted the WLR of class 1 stars onto the WLR for class 3 stars and found that by reducing \dot{M} by a factor of 0.48 (corresponding to an effective clumping factor of 4.3, $\langle \rho^2 \rangle / \langle \rho \rangle^2 = 0.48^{-2}$) the differences in the corresponding WLRs vanish almost completely, and a unique relation, similar to that predicted by theory can be obtained (see right panel of Fig. 5.1)

The possibility to use the WLR as an indicator of wind clumping in O-star winds is very exciting, but needs to be proven independently, e.g., by comparing H_α , and radio mass-loss rates. In case both the suggested radial stratification of the clumping factor (Owocki et al. 2000), and the assumption made by Puls et al. were correct, one might expect larger H_α mass-loss rates for stars with stronger winds (H_α in emission), whereas the opposite, i.e., similar or even higher radio mass-loss rates, might be expected for stars with weaker winds (H_α in absorption).

With these perspectives a combined H_α , infrared (IR) and radio survey of a large sample of Galactic O-stars was initiated and realized by me in collaboration with colleagues from the University Observatory Munich, Germany; the Catania Astrophysical Obs. and the Bologna Radio Institute, Italy; The Sternberg Astronomical Institute, Russia and the University College London, UK. The main objective of the project was to determine the clumping properties of the stars, to constrain the radial stratification of the clumping factor, and to test how far the empirical results meet the predictions given by Runacres & Owocki (2002, 2005). In the following, I will describe and comment on the main outcomes of this analysis; more detailed information can be found elsewhere (Markova & Markov 2005; Puls et al. 2006, 2008a; Puls, Markova and Scuderi 2008b)

5.1 A combined H_α , IR and radio analysis

In the very beginning, let me note that investigations such as the one I'm going to describe here are not new. Indeed, a number of similar studies have been presented during the recent years, e.g., Leitherer et al. (1982); Abbott et al. (1984); Lamers & Leitherer (1993); Runacres & Blomme (1996); Blomme & Runacres (1997); Scuderi et al. (1998); Blomme et al. (2002, 2003). However, in comparison to these earlier works, our survey has at least three main advantages. First, the adopted stellar parameters are more reliable, since they have been derived by means of state-of-the-art, line-blanketed models. Secondly, we did not derive (different) mass-loss rates from the different wavelength domains based on a homogeneous wind model,

Table 5.1: Sample stars and stellar/reddening parameters as used in this study. Note that due to minor revisions with respect to reddening, the stellar radii and H_α mass-loss rates for most objects are (slightly) different from the original values (from “ref1” and “ref2”). v_∞ is in km s^{-1} ; \dot{M} - in $10^{-6} M_\odot/\text{yr}$; and distances are in kpc. “pt” denotes the H_α profile type (emission/absorption/intermediate). “ref1” refers to the “preferred” model chosen in Markova et al. (2004) (see text).

Star	T_{eff}	$\log g_{\text{eff}}$	R_\star	Y_{He}	v_∞	pt	\dot{M}	β	M_V	E(B-V)	R_V	dist	ref1	ref2
Cyg OB2#7	45800	3.93	15.0	0.21	3080	e	10.61	0.77	-5.98	1.77	3.00	1.71	2	5
HD190429A	39200	3.65	22.7	0.14	2400	e	16.19	0.95	-6.63	0.47	3.10	2.29	1	1-0
HD15570	38000	3.50	24.0	0.18	2600	e	17.32	1.05	-6.69	1.00	3.10	2.19	4	6
HD66811	39000	3.60	29.7	0.20	2250	e	16.67	0.90	-7.23	0.04	3.10	0.73	3	1-4
			18.6				8.26		-6.23	0.04	3.10	0.46	3	1-0
HD14947	37500	3.45	26.6	0.20	2350	e	16.97	0.95	-6.90	0.71	3.10	3.52	3	1-2
Cyg OB2#11	36500	3.62	23.6	0.10	2300	e	8.12	1.03	-6.67	1.76	3.15	1.71	2	5
Cyg OB2#8C	41800	3.73	15.6	0.13	2650	a	4.28	0.85	-5.94	1.62	3.00	1.71	2	5
Cyg OB2#8A	38200	3.56	27.0	0.14	2650	i	11.26	0.74	-6.99	1.63	3.00	1.71	2	5
HD210839	36000	3.55	23.3	0.10	2250	e	7.95	1.00	-6.61	0.49	3.10	1.08	3	1-2
HD192639	35000	3.45	18.5	0.20	2150	e	6.22	0.90	-6.07	0.61	3.10	1.82	3	1-0
HD34656	34700	3.50	25.5	0.12	2150	a	2.61	1.09	-6.79	0.31	3.40	3.20	1	1-6
HD24912	35000	3.50	24.2	0.15	2450	a	2.45	0.80	-6.70	0.33	3.10	0.85	3	1-2
HD203064	34500	3.50	12.4	0.10	2550	a	0.98	0.80	-5.23	0.23	3.10	0.79	3	6
HD36861	33600	3.56	14.4	0.10	2400	a	0.74	0.80	-5.52	0.08	5.00	0.50	1	1-1
HD207198	36000	3.50	11.6	0.15	2150	a	1.05	0.80	-5.15	0.58	2.56	0.83	3	1-1
HD37043	31400	3.50	17.9	0.12	2300	a	1.03	0.85	-5.92	0.04	5.00	0.50	1	1-1
HD30614	29000	3.00	20.7	0.10	1550	e	3.07	1.15	-6.00	0.25	3.10	0.79	3	1-2
Cyg OB2#10	29700	3.23	30.7	0.08	1650	i	2.74	1.05	-6.95	1.80	3.15	1.71	2	5
HD209975	32000	3.20	14.7	0.10	2050	a	1.11	0.80	-5.45	0.35	2.76	0.83	3	1-1

References: 1. Markova et al. (2004), 2. Mokiem et al. (2005), 3. Repolust et al. (2004), 4. Repolust et al. (2005), 5. Hanson (2003) (distance from Massey & Thompson (1991)), 6. Mais-Apellaniz et al. (2004).

but aimed at a unique solution by explicitly allowing for clumping as a function of radius. Thirdly, we used original more recent radio observations obtained with the Very Large Array (VLA), which, because of its gain in sensitivity, allowed us to measure the radio fluxes for stars with only moderate wind densities, which produce H_α in absorption. In this way, we were able to test the above hypothesis concerning the differences of H_α mass-loss rates from stars with H_α in emission and absorption. Lastly, our IR analysis does not depend on assumptions used in previous standard methods exploiting the IR excess (e.g., Lamers & Waters 1984a), since we have calibrated against results from line-blanketed NLTE models.

Stellar sample The stellar sample consists of 19 Galactic supergiants/giants, covering spectral types O3 to O9.5. These stars have been analyzed in the optical (Repolust et al. 2004; Mokiem et al. 2005; Markova et al. 2004) to derive their stellar parameters and, to a large part, (re-)observed by us with the VLA.

The stellar properties adopted in this study are presented in Table 5.1. Note that due to minor revisions with respect to reddening, the stellar radii and H_α mass-loss rates (rescaled by assuming $\dot{M}/R_\star^{1.5} = \text{const}$, e.g., Puls et al. 1996) for most objects are (slightly) different from the original sources (from ref1 and ref2). In Sect 5.1.3, I will discuss why these revisions were necessary, and how they have been obtained. Note also

that $\log g$, are “effective” values, i.e., without centrifugal correction, derived from H_γ or calibrations, and that \dot{M} - and β -estimates originate from optical diagnostics, i.e. H_α . Finally, note that for ζ Pup (HD 66811) two entries have been used based on different distances.

5.1.1 Variability of the diagnostics used

Stellar winds are known to be variable on different timescales and in all wavelength ranges in which they are observed. Thus, the use of non-simultaneous measurements, as in our analysis, can be an issue.

H_α variability Line profile variations in H_α of early-type stars have been observed for years. According to our results (see Sect. 3.5) the uncertainty in \dot{M} caused by these variations is constrained within $\pm 4\%$ of the corresponding mean value for stars with stronger winds, and to about $\pm 16\%$ for stars with weaker winds. These estimates are in remarkably good agreement with those from previous studies (Ebbets 1982; Scuderi et al. 1992), which report variations in \dot{M} of about 10 to 30%.

Variability of the IR and radio continua Assuming the corresponding emission to be thermal, the *timescales* of variability (due to variations of the local density or mass-loss rate²) can differ significantly in these two wavelength regimes: from hours (near-IR) to months and even years (radio domain). Consequently, whilst the IR emission would display short-term variability, variations in the radio would be averaged out if they occurred on timescales much shorter than the transit time.

Different considerations apply when the variability is of non-thermal origin. Then, only the radio emission is affected. The main observed characteristics are variability over timescales of up to months, and a power-law spectrum increasing with wavelength and with a variable spectral index (Biegging et al. 1989). In such a case, which is met at least by one of our objects, Cyg OB2#8A, the measured radio-flux(es) can still be used as an upper limit of the thermal free-free emission, by analyzing the lowermost flux measured at the shortest radio wavelength.

Regarding the *amplitude* of variability, no clear evidence of IR continuum variability has been reported up to now. (see also Sect. 5.1.2). With respect to radio emission, there are several pieces of evidence for variability, both in the observed fluxes and in the spectral index. In the case of non-thermal origin, variability is *always* present (e.g., Biegging et al. 1989). Of our targets, in addition to #8A, this might be a problem only for HD 190429A where no clear indication about the thermal origin of the observed emission are present (and for HD 34656 and HD 37043 for other reasons).

Among thermal emitters, on the other hand, the situation is less clear (see e.g., Biegging et al. 1989;

²Note that variations in the ionization can also induce temporal variability, e.g., Panagia (1991).

Scuderi et al. 1998; Blomme et al. 2002, 2003: while short-term variability could be ruled out, long-term variations of up to 50 to 70 percent may still present at least in some objects.

Variability issue and the outcomes of our analysis The major hypothesis underlying our investigation is that the clumping properties of a specific wind are controlled by small-scale structures. If related to any intrinsic wind property, the derived clumping properties should be (almost) independent of time, as long as the major wind characteristics remain largely constant. Accounting for the observational facts above, this assumption seems to be reasonable, and justifies our approach of using observational diagnostics from different epochs.

If we had analyzed only one object, the derived results might be considered as spurious, of course. However, due to the significant size of our sample, any global property (if present) should become visible. Let me already mention here that our findings, on average, indicate rather similar behaviour for similar objects, and thus we are confident that these results remain largely unaffected by issues related to *strong* temporal variability.

5.1.2 Observations and data processing

H_α , radio, IR and mm observations

Concerning H_α , the same observational material as described in Chapter 3, Sect. 3.5 was used.

Radio observations Table 5.2 (left part) displays our original radio data together with similar data from other sources used to complement the sample. In particular, for 13 stars new radio observations have been carried out at the VLA in several sessions between February and April 2004, for a total of about 36 hours. For four of them, additional VLA data derived by Dr. Scuderi in different sessions between 1998 and 1999 were also used.

For the remaining stars, we used literature values, in particular from Scuderi et al. (1998), Bieging et al. (1989) and Lamers & Leitherer (1993). For ζ Pup, finally, we used the radio data obtained by Blomme et al. (2003). For those objects which have been observed both by us and by others, or where multiple observations have been obtained, we have added these values to our database. In almost all cases, the different values are consistent with each other.

IR observations In the right part of Table 5.2 we have summarized the used IR data, which are to a large part drawn from the literature. For a few objects, IRAS data for 12, 25, 60 and 100 μm are also available

Table 5.2: VLA radio fluxes (in μJy), with $1-\sigma$ errors in brackets. Data without superscripts are new observations, whilst data with superscripts correspond to either (a) unpublished measurements by Scuderi et al. or literature values: (b) Scuderi et al. (1998); (c) Bieging et al. (1989); (d) 3.6 cm observations from Lamers & Leitherer (1993); (e) Blomme et al. (2003, including 20 cm data for ζ Pup, at $760 \pm 90 \mu\text{Jy}$). Also indicated are the IR to mm fluxes and the sources from which they have been drawn (see foot of table). Data denoted by “own” refer to our own observations) for more details see Sect. 5.1.2).

Star	4.86 GHz (6 cm)	8.46 GHz (3.6 cm)	14.94 GHz (2 cm)	43.34 GHz (0.7 cm)	IR- and mm- bands used	references (IR and mm)
Cyg OB2#7	<112	<100			<i>HKLMN</i>	1,14
Cyg OB2#8A	<540 ^a 1000(200) ^c 800(100) ^c 700(100) ^c 400(100) ^c	920(70) ^a	500(200) ^c		<i>JHKLMNQ</i>	1,5,14,19,20
Cyg OB2#8C	<200 ^c				<i>HKLMN</i>	14
Cyg OB2#10	134(29)	155(26)	300(100)		<i>JHKLMN</i>	5,14,19
Cyg OB2#11	182(33)	228(28)	<400		<i>JHKLMN</i>	5,14
HD 14947	<110 < 90 ^a	<135 90(30) ^a 120(30) ^a 110(30) ^b	<700		<i>JHKLMN</i>	2,5,15,own
HD 15570	100(40) ^a	220(40) ^a 125(25) ^d			<i>JHKLMNQ</i> , 1.35 mm	1,5,8,11,15, 18,SCUBA
HD 24912	<200	<120	<390	<840	<i>JHKLMN,IRAS</i>	3,5,7,16
HD 30614	230(50) ^b	440(40) ^b	650(100) ^b		<i>JHKLMN</i>	5,7,own
HD 34656	<132	119(24)	<510		<i>JHKL</i>	17,own
HD 36861	<112	<90	<1000		<i>JHKLMN</i>	2,5,7
HD 37043	203(38)	<90 46(15) ^d	<330		<i>JHKLMN</i>	4,5,16,21,22
HD 66811	1640(70) ^e 1490(110) ^c	2380(90) ^e	2900(300) ^c		<i>JHKLM,IRAS</i> , 0.85 mm,1.3 mm	6,9,10,12,13, 22,23,24
HD 190429A	250(37)	199(36) 280(30) ^b	<420	<540	<i>JHKLM</i>	5,20,own
HD 192639		<90 ^a			<i>JHKLM</i>	5,15,own
HD 203064	114(27)	126(20)	<330		<i>JHKLM,IRAS</i>	3,5,own
HD 207198	105(25)	101(21)	249(82)		<i>JHKLM,IRAS</i>	3,own
HD 209975	165(36)	184(28)	422(120)		<i>JHKLM,IRAS</i>	3,own
HD 210839	238(34)	428(26)	465(120)	790(190)	<i>JHKLMNQ</i> , IRAS,1.35 mm	1,2,3,5,14, 15,own,SCUBA

References for IR and mm data: 1. Abbott et al. (1984), 2. Barlow & Cohen (1977), 3. Beichman et al. (1988), 4. Breger et al. (1981), 5. Castor & Simon (1983), 6. Dachs & Wamsteker (1982), 7. Gehrz et al. (1974), 8. Guetter & Vrba (1989), 9. Johnson & Borgman (1963), 10. Johnson (1964), 11. Johnson et al. (1966a), 12. Johnson et al. (1966b), 13. Lamers et al. (1984), 14. Leitherer et al. (1982), 15. Leitherer & Wolf (1984), 16. Ney et al. (1973), 17. Polcaro et al. (1990), 18. Sagar & Yu (1990), 19. Sneden et al. (1978), 20. Tapia (1981), 21. The et al. (1986), 22. Whittet & van Breda (1980), 23. Leitherer & Robert (1991), 24. Blomme et al. (2003).

(Beichman et al. 1988), unfortunately mostly as upper limits for $\lambda \geq 25 \mu\text{m}$. For ζ Pup (HD 66811), however, actual values are present at all but the last wavelength ($100 \mu\text{m}$); see Lamers et al. (1984).

For nine objects (denoted by “own” in the “references” column of Table 5.2), new *JHKLM* fluxes have been obtained at the 1.25 m telescope of the Crimean Station of the Sternberg Astronomical Institute (Russia). Appropriate stars from the Johnson catalog (Johnson et al. 1966b) were selected and used as photometric standards. Where necessary, the *HLM* magnitudes of the standards have been estimated from their spectral types using relations from Koorneef (1983).

Mm observations For three objects, we were also able to use 1.3/1.35 mm fluxes, acquired either with the Swedish ESO Submillimeter Telescope (SEST) at La Silla (ζ Pup; see Leitherer & Robert 1991), or with the Submillimetre Common User Bolometer Array (SCUBA; Holland et al. 1999) at the James Clerk Maxwell Telescope (HD 15570 and HD 210839). Additional 0.85 mm SCUBA data have been taken from the literature (Blomme et al. 2003), for ζ Pup.

Detailed information about the original radio, IR and mm observations and the corresponding data reduction procedures can be found in Puls et al. (2006).

Absolute flux calibration

To convert the observed IR magnitudes into *meaningful* (i.e., *internally consistent*) physical units, an adequate absolute flux calibration has to be performed. For such a purpose, at least three different methods can be applied: (i) calibration by means of the solar absolute flux, using analogous stars; (ii) direct comparison of the observed Vega flux with a blackbody and (iii) extrapolation of the visual absolute flux calibration of Vega, using suitable model atmospheres. Although the first two methods are more precise, the latter one provides the opportunity to interpolate in wavelength, allowing the derivation of different sets of IR-band Vega fluxes for various photometric systems. Thus, such an approach is advantageous in the case encountered here (observational datasets obtained in different photometric systems), and we have elected to follow this strategy.

Atmospheric model for Vega. To this end, we used the latest Kurucz models³ to derive a set of absolute IR fluxes for Vega in a given photometric system, by convolving the model flux distribution (normalized to the Vega absolute flux at a specific wavelength; see below) with the corresponding filter transmission functions. In particular, we used a model with $T_{\text{eff}} = 9550 \text{ K}$, $\log g = 3.95$, $[M/H] = -0.5$ and $v_{\text{mic}} = 2.0 \text{ km s}^{-1}$ (Castelli & Kurucz 1994). In order to account for the possibility that the metallicity of Vega might

³from <http://kurucz.harvard.edu/stars/vega>

differ from that adopted by us, an alternative model with $[M/H] = -1.0$ (cf. Garcia-Gil et al. 2005) was used to check for the influence of a different metallicity on the derived calibration. At least for the Johnson photometric system, the differences in the corresponding fluxes turned out to lie always below 1%.

Visual flux calibration. The most commonly used visual flux calibration for Vega is based on the compilation by Hayes (1985). However, this has been questioned by Megessier (1995), who recommends a value being 0.6% larger than the value provided by Hayes (3540 Jy), and equals 3560 Jy (i.e., $3.46 \cdot 10^{-9}$ erg cm⁻² s⁻¹ Å⁻¹) at $\lambda = 5556$ Å. This value has been used when normalizing the Kurucz model fluxes to the monochromatic flux at $\lambda = 5556$ Å. Since the standard error of the Megessier calibration is about one percent, this error is also inherent in our absolute flux distribution.

Vega V-band magnitude. The available V-band magnitudes of Vega range from 0.026 (Bohlin & Gilliland 2004) to 0.035 (Colina & Bohlin 1994), while in the present investigation we adopt $V = 0.03$ mag in agreement with Johnson et al. (1966b). With this value, the monochromatic flux for a Vega-like star at the effective wavelength of the V filter is $F_{5500}(m_V = 0.0) = 3693$ Jy.

Filter transmission functions. To calculate the absolute fluxes of Vega in a given photometric system, one has to know the corresponding filter transmission functions, for each band of this system. In those cases where such functions were explicitly available we used them, while for the rest (including our own IR data) we used trapezoidal transmission curves based on the published effective wavelength and FWHM of the filters.⁴

Vega IR magnitudes. To convert stellar magnitudes into absolute fluxes using Vega as a standard, the magnitudes of Vega in the different filters for the various photometric system have to be known. In our case, these data have been taken from the corresponding literature, and the errors inherent to these measurements are usually very small.

For a detailed discussion about the accuracy of our absolute flux calibration the interested reader is referred to Puls et al. (2008).

5.1.3 De-reddening and stellar radii

To compare the observed with the theoretical fluxes, one has to de-redden the observed fluxes and to derive a consistent stellar radius for a given distance d (or vice versa). In our case this has been done in two step

⁴For more detailed information about the shape of the filter transmission functions used to convert the literature data, see Runacres & Blomme (1996, their Table 3).

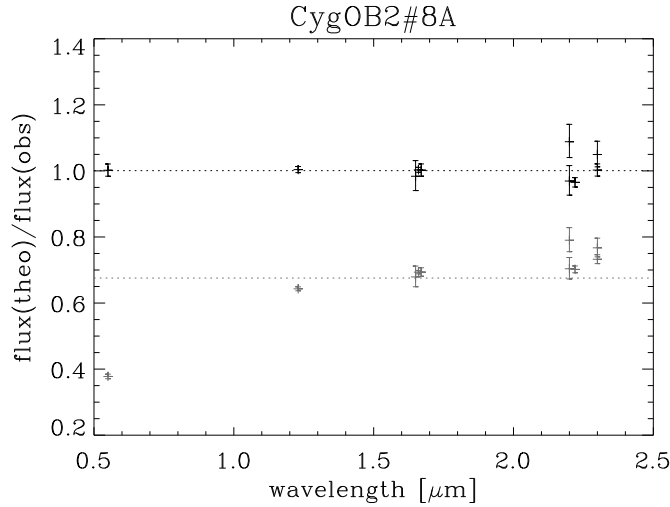


Figure 5.2: De-reddening procedure for the example of Cyg OB2#8A. Displayed is the ratio of distance-diluted, theoretical fluxes and de-reddened, observed $VJHK$ fluxes, corresponding to our final solution for $E(B-V) = 1.63$, $R_V = 3.0$ and $R_\star = 27 R_\odot$, as a function of wavelength. Another solution with $E(B-V) = 1.9$, $R_V = 3.0$ and $R_\star = 24 R_\odot$ (lower signs) is also shown for comparison. Obviously, in the latter case the extinction is too large (the ratio is much smaller at shorter than at larger wavelengths) and the assumed radius is too small (the dotted line is well below unity).

procedure, using our own (simplified) model (see Sect. 5.1.4) to synthesize theoretical $VJHK$ fluxes.⁵

In particular, by comparing the observed IR fluxes with the theoretical predictions, we derived “empirical” values for the color excess $E(B-V)$ and/or the extinction ratio R_V , by requiring the ratio between de-reddened observed and distance-diluted theoretical fluxes to be constant within the V - to K -bands. For this purpose, we adopted the reddening law provided by Cardelli et al. (1989). Visual fluxes were calculated using V -magnitudes from Markova et al. (2004) or from Mais-Apellaniz et al. (2004).

In a second step, we adapted the stellar radius (for a given distance) in such a way that the *mean* ratio becomes unity. This procedure ensures the correct *ratio* between radius and distance, i.e., angular diameter, which is the only quantity which can be specified from a comparison between synthetic and observed fluxes. Fig. 5.2 gives an impression of this procedure, for the example of Cyg OB2#8A.

One problem inherent to our approach is that the derivation of reddening parameters and R_\star requires an a priori knowledge of \dot{M} (and clumping properties). Since a precise knowledge of the “real” wind density and the near-photospheric clumping properties is not possible at this stage, only an iteration cycle exploiting the results of our following mass-loss/clumping analysis could solve the problem “exactly”.

To avoid such a cycle, we followed a simplified approach, where to calculate the theoretical fluxes for objects with H_α in absorption we used the actual, Q' -scaled, H_α mass-loss rates, whereas for objects with H_α in emission the corresponding value reduced by a factor of 0.48 were used instead. This approach is

⁵Only near-IR fluxes were used to ensure that the flux excess due to the wind remains low, i.e., rather unaffected by clumping.

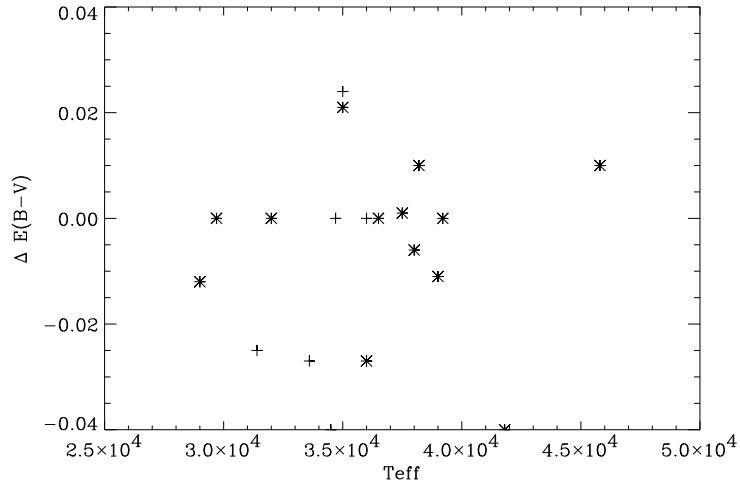


Figure 5.3: Differences between *derived* color excess, $E(B-V)$, and corresponding literature value, as a function of T_{eff} . Asterisks denote supergiants, and crosses bright giants and giants, respectively. The mean deviation for supergiants is -0.004 ± 0.016 mag, and for l.c. II/III stars -0.01 ± 0.023 mag.

based on the hypothesis that the lowermost wind is unclumped, and that the previously derived H_α mass-loss rates for objects with H_α in emission are contaminated by clumping, with average clumping factors of the order of $\left(\frac{1}{0.48}\right)^2$ as derived in the beginning of this section. From the almost perfect agreement of the theoretical V -to- K fluxes with the observations for our final, clumped models, this assumption seems to be fairly justified.

Fig 5.3 summarizes the results of our de-reddening procedure, by comparing the *derived* values of $E(B-V)$ for our complete sample with the corresponding “optical” values, $(B-V) - (B-V)_0$, as a function of T_{eff} (with $(B-V)$ given by the references in Table 5.1, entry “ref 2”, and the intrinsic colors as discussed above).

From this figure, we find no obvious trend of the difference in $E(B-V)$ as a function of T_{eff} (the average differences being almost exactly zero for supergiants and -0.01 mag for the remaining objects), which is also true if we plot this quantity as a function of M_V (not shown). The majority of these differences are less than 0.02 mag, which seems to be a reasonable value when accounting for the inaccuracy in the observed $(B-V)$ colors, the uncertainties in the intrinsic ones, the errors resulting from our flux calibration and the typical errors on the theoretical fluxes (cf. Sect. 5.1.4). Comments on individual objects one can find in Puls et al. (2006).

5.1.4 Simulations

In this section, I will describe our approach for calculating the various energy distributions required for our analysis, and our approximate treatment of wind clumping, which is based upon the assumption of *small-*

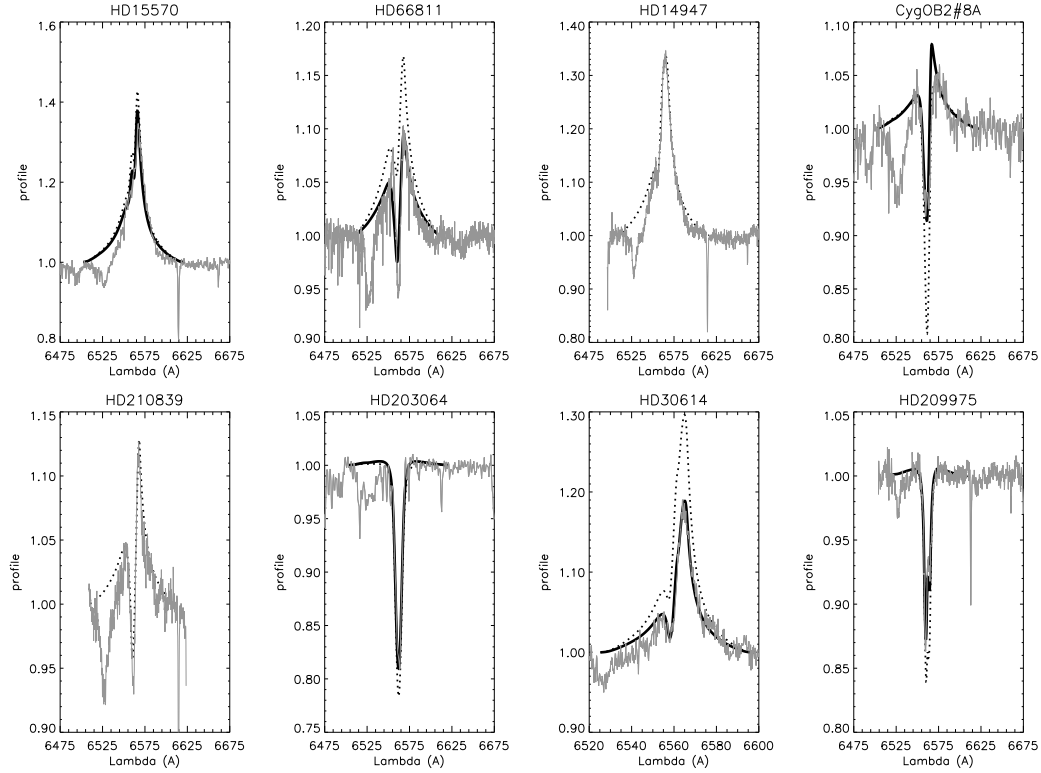


Figure 5.4: Consistency check for H_α profiles: results of our approximate H_α line synthesis, for some representative cases from Table 5 of Puls et al. (2006). Dotted: H_α line profiles with parameters \dot{M} (in) and β (in) as derived from a complete NLTE analysis (cf. Table 5.1); bold: corresponding profiles with $\dot{M} = \dot{M}_1$ or $\beta = \beta_2$ (see Table 5 of Puls et al. (2008)).

scale inhomogeneities. Since this treatment consists of a simple manipulation of our homogeneous models, I will start with a description of these.

Because of the large number of parameters to be varied (\dot{M} , β , clumping factors), and accounting for the rather large sample size, an “exact” treatment by means of NLTE atmospheres is (almost) prohibitive. Thus, we follow our previous philosophy of using *approximate* methods, which are calibrated by means of our available NLTE model grids (Puls et al. 2005), to provide reliable results.

H_α

Synthetic H_α profiles have been calculated using the approximate approach described in detail in Sect. 2.1. Except for the inclusion of clumping, no further modifications have been applied.

On the other hand, for most of our sample stars we have quoted (and used, within our de-reddening procedure) wind parameters from a complete NLTE analysis, which do not rely exclusively on H_α , but also on He II 4686 and other diagnostics. Furthermore, the observed H_α profiles used here are different to those in the corresponding sources, because of the variability of H_α (cf. Sect. 5.1.1). Thus, we have to check

how far the values from the complete analysis (denoted by \dot{M} (in) and β (in)) might deviate from solutions resulting from our simplified method, used in combination with our different H_α data, to obtain consistent initial numbers for the following investigations and to re-check the reliability of our approach.⁶ To this end, we have re-determined mass-loss rates and velocity exponents, using our observational material, the stellar parameters from Table 5.1 and the approximate H_α line synthesis as outlined above.

The obtained results, listed in Table 5 of Puls et al. (2006), indicate that in most of the cases small or negligible modifications of \dot{M} have been required to reproduce our H_α observations, mostly by keeping the nominal velocity exponent. The average ratio between modified and input mass-loss rates was 1.07 ± 0.22 . Typical examples to illustrate this finding are shown in Fig. 5.4. Thus, we conclude that our simplified routine delivers reliable numbers and thus can be used in our further approach to derive constraints on the clumping factors.

Infrared fluxes

For the calculation of the infrared fluxes, we closely followed the approximations as outlined by Lamers & Waters (1984a), with Gaunt factors from Waters & Lamers (1984). The major difference concerns the fact that the radiative transfer is solved by means of the ‘‘Rybicki algorithm’’ (Rybicki 1971), to account for electron scattering in a convenient way. A further modification regards the photospheric input fluxes which were chosen in such a way as to assure that the emergent fluxes, on average, comply with the results from our detailed NLTE model grids.

After some experiments, it turned out that the best choice for the various parameters is the following:

The velocity law is specified by

$$v(r) = v_\infty(1 - b/r)^\beta, \quad b = 1 - (v_{\min}/v_\infty)^{1/\beta}, \quad (5.2)$$

where r is calculated in units of R_\star , and the minimum velocity, v_{\min} , is set to 10 km s^{-1} .

Electron temperature. All Gaunt factors are calculated at a temperature of $0.9 T_{\text{eff}}$, and the electron temperature is calculated using Lucy’s temperature law for spherical atmospheres (Lucy 1971, his Eq. 12, and using grey opacities), with an optical depth scale accounting for electron scattering only, and a temperature cut-off at $0.5 T_{\text{eff}}$.

⁶Concerning those (four) objects with wind parameters taken from Markova et al. (2004), we have convinced ourselves that the corresponding fits could be reproduced.

Ionization equilibrium. Hydrogen is assumed to be (almost) completely ionized, helium as singly ionized outside the recombination radius ⁷ and the CNO metals as either two or three times ionized. An extensive and detailed discussion about the influence of the helium ionization balance can be found in Puls et al. (2006) while here I shall only note that in O-star winds helium is singly ionized in the *radio* emitting region (for $\lambda > 2$ cm), but with respect to the mid- and far-IR emitting region, this statement is no longer justified and needs to be additionally investigated.

Photospheric input fluxes For $\lambda < 1 \mu\text{m}$, we used Kurucz fluxes, whereas for higher wavelengths we used Planck functions with $T_{\text{rad}} = 0.87 T_{\text{eff}}$ for $1 \mu\text{m} \leq \lambda \leq 2 \mu\text{m}$, $T_{\text{rad}} = 0.85 T_{\text{eff}}$ for $2 \mu\text{m} \leq \lambda \leq 5 \mu\text{m}$ and $T_{\text{rad}} = 0.9 T_{\text{eff}}$ elsewhere. To verify this approach, we have compared the fluxes resulting from this simplified model with those from our NLTE model grid as calculated by FASTWIND, for the wavelength bands *V* to *Q* and found the corresponding mean ratio to be of the order of 0.99...1.01 (different for different wavelengths), with a typical standard deviation for each wavelength band below 5%.

Radio fluxes

Radio fluxes are calculated in analogy to the IR fluxes (with identical parameters, but neglecting electron scattering) using a numerical integration, with $R_{\text{max}} = 10,000 R_{\star}$, instead of the analytical expression provided by Panagia & Felli (1975) and Wright & Barlow (1975). (Of course, we have checked that for constant clumping factors and large wind densities, the analytical results are recovered by our approach.) Unless explicitly stated otherwise, helium is adopted to be singly ionized in our radio simulations.⁸ In the following figures, the radio range is indicated to start at $400 \mu\text{m} = 0.4 \text{ mm}$ (end of IR treatment at $200 \mu\text{m}$), but this serves only as a guideline, since at these wavelengths helium might still not be completely recombined.

Inclusion of wind clumping

To account for the influence of wind clumping, we follow the approach as described by Abbott et al. (1981). Modified by one additional assumption (see below), this approach has been implemented into NLTE model atmospheres already by Schmutz (1995), and is presently also used by the alternative NLTE code CMFGEN. In the following, I will recapitulate the method and give some important caveats.

As I have noted in the beginning of this section, the term “clumping factor”, as defined from the *temporal* averages in Eq. 5.1, has been introduced by Owocki, Castor and Rybicki (1988) To allow for

⁷The radius at which the ionization fraction of He becomes larger than the fraction of He II when proceeding from outside to inside

⁸Concerning the influence of the adopted He ionization on derived mass-loss rates, see also Schmutz & Hamann 1986.

a translation to stationary model atmospheres, one usually assumes that the wind plasma is made up of two components, namely dense clumps and rarefied inter-clump material. The volume filling factor, f , is then defined as the fractional volume of the *dense* gas, and one can define appropriate *spatial* averages for densities and density-squares (cf. Abbott et al. 1981),

$$\langle \rho \rangle = \frac{1}{\Delta V} \int [f\rho^+ + (1-f)\rho^-] dV \quad (5.3)$$

$$\langle \rho^2 \rangle = \frac{1}{\Delta V} \int [f(\rho^+)^2 + (1-f)(\rho^-)^2] dV, \quad (5.4)$$

where ρ^+ and ρ^- denote the overdense and rarefied material, respectively. Here, and in the following, I have suppressed any spatial dependence, both of these quantities and of f . The actual mass-loss rate (still assumed to be spatially constant) is then defined from the mean density,

$$\dot{M} = 4\pi r^2 \langle \rho \rangle v, \quad (5.5)$$

and *any* disturbance of the velocity field (e.g., influencing the line-transfer escape probabilities; see Puls et al. 1993a) is neglected.

The modification introduced by Schmutz (1995) relates to the results from all hydrodynamical simulations collected so far, namely that the inter-clump medium becomes almost void *after the instability is fully grown*, i.e. outside a certain radius. In this case then, $\rho^- \rightarrow 0$, and we find, assuming sufficiently small length scales,

$$\langle \rho \rangle = \frac{1}{\Delta V} \int [f\rho^+] dV = f\rho^+ \quad (5.6)$$

$$\langle \rho^2 \rangle = \frac{1}{\Delta V} \int [f(\rho^+)^2] dV = f(\rho^+)^2 = \frac{\langle \rho \rangle^2}{f}. \quad (5.7)$$

Comparing with Eq. 5.1 and identifying temporal with spatial averages, we obtain

$$f_{\text{cl}} = \frac{1}{f} \quad \text{and} \quad \rho^+ = \frac{\langle \rho \rangle}{f} = f_{\text{cl}} \langle \rho \rangle, \quad (5.8)$$

i.e., the clumping factor describes the overdensity of the clumps, if the inter-clump densities are negligible.

Concerning model atmospheres and (N)LTE treatment, this averaging process has the following consequences:

- Since, according to our model, matter is present only inside the clumps, the actual (over-)density

entering the rate equations is $\rho^+ = f_{\text{cl}} \langle \rho \rangle$ (where the latter quantity is defined by Eq. 5.5). Since both ion and electron densities become larger, the recombination rates grow, and the ionization balance changes. As a simple example, under LTE conditions (Saha equation), and for hot stars, one would find an increased fraction of neutral hydrogen *inside the clumps*, being larger by a factor of f_{cl}^2 compared to an unclumped model of the same mass-loss rate. Further, more realistic, examples for important ions have been given by Bouret et al. (2005) and by Najarro et al. (2008).

- The overall effect of this increase in density, however, is somewhat compensated for by the “holes” in the wind plasma. For processes which are linearly dependent on the density (e.g., resonance lines of major ions), the optical depth is similar in clumped and unclumped models, provided that the scales of the clump/inter-clump matter are significantly smaller than the domain of integration. For ρ^2 -dependent processes, on the other hand, the optical depth is proportional to the integral over $\langle \rho^2 \rangle = f_{\text{cl}} \langle \rho \rangle^2 \approx f_{\text{cl}}(\rho^{\text{uncl}})^2$, i.e., the optical depths are larger by just the clumping factor. Consequently, mass-loss rates derived from such diagnostics become lower by the square root of this factor, compared to an analysis performed by means of unclumped models.

Now with respect to our models, the inclusion of clumping effects in the spirit as described above (i.e., optically thin clumps and void inter-clump matter⁹) becomes very simple. In particular, since all opacities entering the calculations (bound-free, free-free and the H_α line opacity) are dependent on ρ^2 , they are multiplied with a pre-described clumping factor, whereas the corresponding source functions remain free from such a manipulation, which is also true for the electron scattering component, being proportional to ρ . In addition, to obtain constraints on the radial stratification of the clumping factor, we have defined five different regions of the stellar wind with corresponding *average* clumping factors, denoted by

region	1	2	3	4	5
r/R_\star	$1 \dots r_{\text{in}}$	$r_{\text{in}} \dots r_{\text{mid}}$	$r_{\text{mid}} \dots r_{\text{out}}$	$r_{\text{out}} \dots r_{\text{far}}$	$> r_{\text{far}}$
f_{cl}	1	$f_{\text{cl}}^{\text{in}}$	$f_{\text{cl}}^{\text{mid}}$	$f_{\text{cl}}^{\text{out}}$	$f_{\text{cl}}^{\text{far}}$

The first region with fixed clumping factor, $f_{\text{cl}} = 1$, has been designed mainly to allow for a lower, unclumped wind region, in accordance with theoretical predictions. Also, by choosing $r_{\text{in}} = 1$ we are alternatively able to simulate a wind where the medium is clumped from the wind base on.

Typical values for r_{in} , r_{mid} , r_{out} and r_{far} are 1.05, 2, 15 and 50, respectively. For not too thin winds, this corresponds to the major formation zones of H_α (region 1 and 2), the mid-/far-IR (region 3), the mm range (region 4) and the radio-flux (region 5). Note that for a number of test cases we have used different borders, and sometimes combined region 4 and 5 into one outer region. All clumping factors derived in

⁹For a critical discussion on the assumptions involved in our models see Puls et al. (2006).

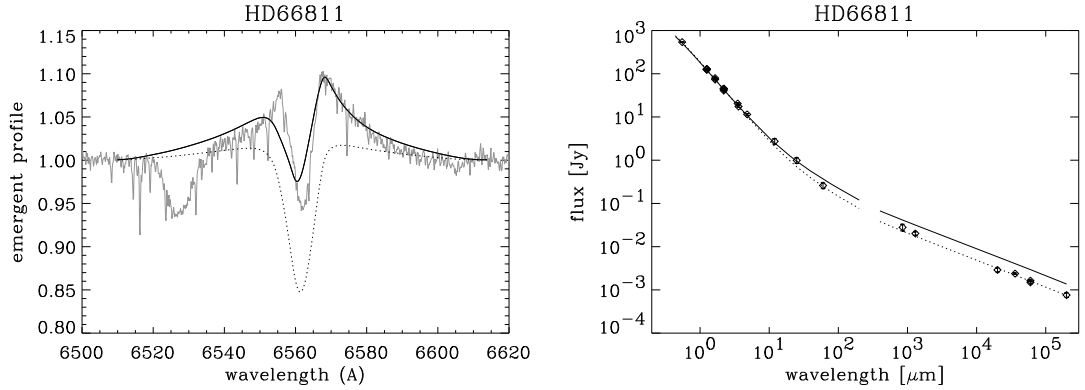


Figure 5.5: Homogeneous models for ζ Pup which either fit H_α ($\dot{M} = 13.5 \cdot 10^{-6} M_\odot/\text{yr}$, solid) or the radio range ($\dot{M} = 8.5 \cdot 10^{-6} M_\odot/\text{yr}$, dotted). A simultaneous fit cannot be achieved. (Regarding the “gap” between 0.2 and 0.4 mm in the theoretical predictions, see Sect. 5.1.4).

the following are average values regarding the different regions, which admittedly are rather extended. In almost all cases, however, with such a low number of regions consistent fits could be obtained, with rather tight constraints on the *global* behaviour of the clumping factor.

As a final comment, I like to stress that since (except for electron scattering) all diagnostics used in this investigation have the same dependence on the clumping properties, we are not able to derive *absolute* values for the clumping factors, but only *relative* numbers. Note at first that in the case $r_{\text{in}} = 1$ all results derived for $f_{\text{cl}}(r)$ could be multiplied with an arbitrary factor, if in parallel the mass-loss rate were reduced by the square root of this value, without any loss in fit quality. The only *physical* constraint is the requirement that the minimum value (regarding all five regions) of the derived clumping factor must not be lower than unity. The corresponding mass-loss rate is then the *largest possible* one.

If, on the other side, $r_{\text{in}} \neq 1$, this scaling property is no longer exactly preserved, because of the presence of an unclumped region not affected by such a scaling. Since particularly the innermost core of H_α , but also the optical/near-IR fluxes (cf. Sect 5.1.3), are formed in this region, they consequently deviate from this scaling. As it turned out from the analysis performed in the next section, these deviations remain fairly small, so that, unfortunately, the derivation of *absolute* values for f_{cl} and \dot{M} will require the use of different diagnostics.

5.1.5 Two prototypical test cases: ζ Pup and HD 209975

In this section, I will describe how our procedure to obtain constraints on the clumping factor works using ζ Pup (HD 24912) as a representative for a high-density wind (H_α in emission), and HD 209975 as a representative for a moderate-density wind (H_α in absorption).

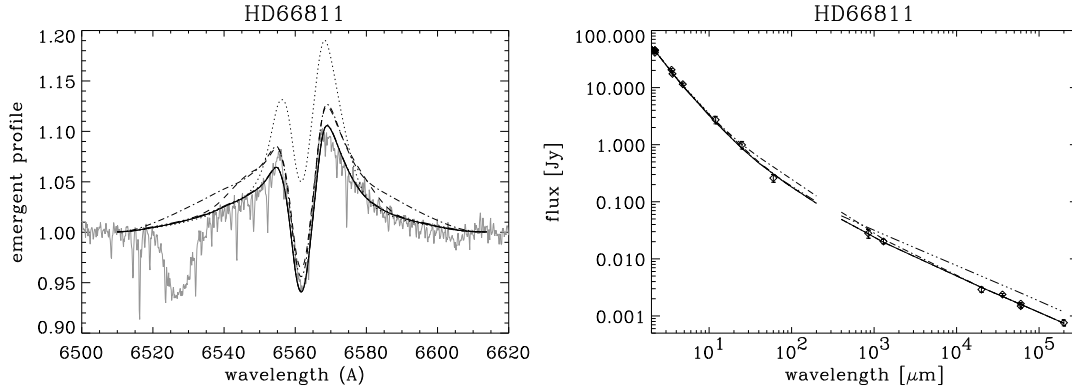


Figure 5.6: Clumped models for ζ Pup compared to H_α (left) and the IR/radio continuum (right). The best-fitting model is displayed in bold. Other curves represent variation of the clumping factor in individual regions, by a factor of two; dotted: $f_{cl}(1.12 \dots 1.5 R_\star)$ $5.5 \rightarrow 11$; dashed: $f_{cl}(1.5 \dots 2 R_\star)$ $3.1 \rightarrow 6.2$; dashed-dotted: $f_{cl}(2 \dots 15 R_\star)$ $2 \rightarrow 4$; dashed-dotted-dotted: $f_{cl}(> 15 R_\star)$ $1 \rightarrow 2$. Note that H_α remains sensitive to *all* variations except for the last one. The mid-/far-IR, on the other hand, is sensitive “only” to variations in the range $2 \dots 15 R_\star$.

ζ Pup. In Fig. 5.5 the results of our simulations (without clumping) for H_α and the IR/radio range are compared to the observations. This figure immediately shows the dilemma typical for all our objects with H_α in emission: the best fit for H_α requires a mass-loss rate typically twice as large as for the radio domain, if homogeneous models are used. The far-IR fluxes are also closer to the low- \dot{M} solution than to the H_α -fitting one.

Fig. 5.6, on the other hand, displays our best solution for a *clumped* model which consistently reproduces H_α and the complete IR/radio band in parallel. In the spirit as outlined above, the mass-loss rate has been chosen from the region with lowest clumping, which in this case is the radio domain. By setting f_{cl}^{far} to unity then, the adopted mass-loss rate is the *largest possible* one and corresponds to the “homogeneous” radio mass-loss rate, $\dot{M} = 8.5 \cdot 10^{-6} M_\odot/\text{yr}$ (cf. Fig. 5.5, right panel). In this case, the H_α -forming region displays a typical clumping factor of 5.5 (from $r = 1.12$ to 1.5) to 3.1 (from $r = 1.5$ to 2), and β has been adapted to 0.7 to provide a perfect H_α fit.

Fig. 5.6 furthermore displays the advantage of fitting H_α and the IR/radio range in parallel. Note that although the primary formation region of H_α is below $2 R_\star$, it also remains sensitive to variations of the clumping factors in the intermediate wind, $r \leq 15$, as can be seen from the reaction in the line wings if f_{cl} is doubled from 2 to 4 (dashed-dotted profile). Of course, a variation of the clumping factors in the inner regions (dotted and dashed) has even more impact. On the other hand, as displayed in the right panel of this figure, the IR/radio band reacts complementarily to variations beyond $r = 2$, although only from the mid-IR on ($\lambda \geq 10 \mu\text{m}$). Thus, a combined analysis is able to provide tight constraints on the largest possible mass-loss rate and to scan the complete stratification of $f_{cl}(r)$ (at least differentially, i.e., modulo a constant

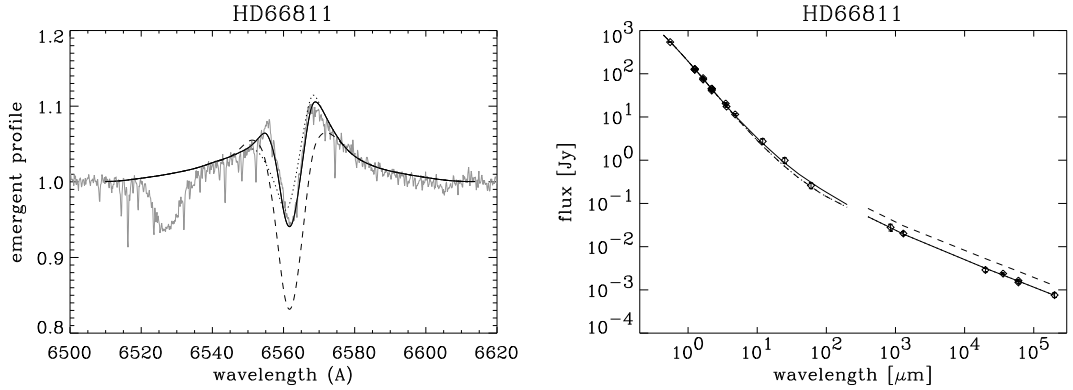


Figure 5.7: *Left*: Clumped models for ζ Pup: influence of a different onset of clumping on H_α . Solid: best-fitting model, $r_{\text{in}} = 1.12 R_\star$; dotted: $r_{\text{in}} = R_\star$, i.e., clumping starting at the wind base; dashed: $r_{\text{in}} = 1.3 R_\star$.

Right: Clumped models for ζ Pup in the IR/radio band: influence of helium ionization. Solid: best fitting model, with He III as the major ion for $v < v_{\text{rec}} = 0.86 (5.3 R_\star)$, and He II as the dominant ionization stage outside v_{rec} ; dashed-dotted: He II as the major ion everywhere; dashed: He III as the major ion in the radio emitting domain.

factor) if the far-IR is well observed. Concerning the possible degeneracy of clumping factors and β , we refer the reader to Sect. 5.1.7.

Another important issue to be discussed here is the sensitivity of the outcomes of our analysis on the assumed value of r_{in} and the helium ionization balance. The first effect is illustrated in the left panel of Fig. 5.7 where the change in H_α caused by a different onset of clumping is shown. If r_{in} were 1.3 (dashed profile), the central emission would be missing, whereas for $r_{\text{in}} = 1.0$ (dotted profile, corresponding to a model which is clumped from the wind base on), the absorption trough is not perfectly reproduced: the position of maximum depth is located at too high velocities, and the trough becomes too broad, resembling our best solution for the homogeneous model.

From the arguments given at the end of Sect. 5.1.4, it should be clear that the derived best solution is not unique, since an alternative model with *all* clumping factors multiplied by an arbitrary factor f , in parallel with a mass-loss rate reduced by a factor of $1/\sqrt{f}$, would result in an identical fit. If, on the other hand, the perfectly matched absorption trough for our model with $r_{\text{in}} = 1.12$ were actually due to a clumping-free lower wind base (and not coincidentally matched due to somewhat erroneous departure coefficients and/or the specific observational snapshot¹⁰), such a scaling would no longer work (because of the presence of an unclumped region), and our solution would become “almost” unique, at least regarding the clumping properties of the inner wind.

The “almost” refers to the fact that a different distribution of the individual regions, combined with

¹⁰Concerning the temporal variability of H_α in ζ Pup, see Reid & Howarth (1996) and references therein, Puls et al. (1993b) and Berghöfer et al. (1996). From these data-sets, a moderate variability of the absorption trough is visible indeed.

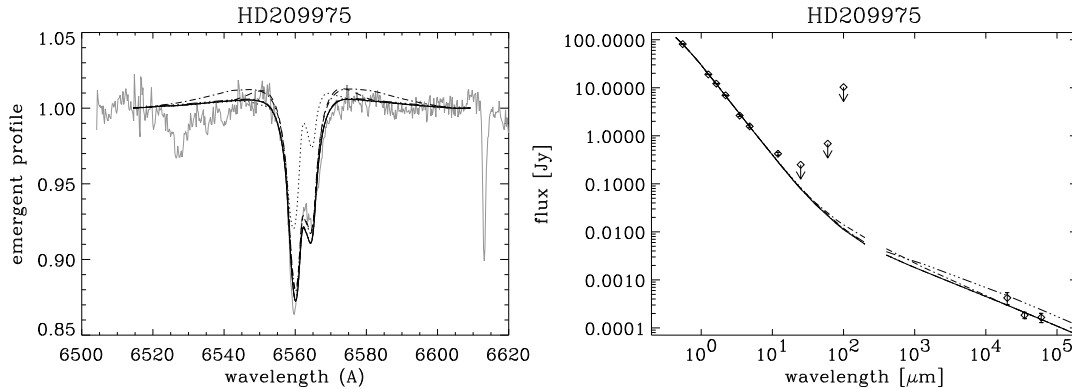


Figure 5.8: As Fig. 5.6, but for HD 209975. The best-fitting model (with *all* clumping factors at or close to unity) is displayed in bold. Other curves show the effects of varying, by a factor of 2, the clumping factors in individual regions alone. Dotted: $f_{cl}(1.05 \dots 1.5 R_\star) 1 \rightarrow 2$; dashed: $f_{cl}(1.5 \dots 2 R_\star) 1 \rightarrow 2$; dashed-dotted: $f_{cl}(2 \dots 15 R_\star) 1 \rightarrow 2$; dashed-dotted-dotted: $f_{cl>(> 15 R_\star) 1.3 \rightarrow 2.6$. Again, H_α remains sensitive to variations below $r = 15 R_\star$ (but see text), whereas the far-IR (not constrained by observations) is mostly sensitive to variations in the range $2 \dots 15 R_\star$. Note that the dashed solution is also consistent with the observations.

somewhat different clumping factors, gives fits of similar quality. The 2nd entry of Table 6 of Puls et al. is such an example. In this case, we have combined the region between $r = 1.12$ to 2 into one region, whereas we have split the outer region, beyond $r = 15$, into two regions, with a border at $r = 50$. To fit H_α (with a slightly worse quality than displayed in Fig. 5.6), the innermost clumping factors had to be reduced (from 5.5 and 3.1 to an average factor of 5.0), whereas, by adapting the clumping factors in the middle and outer part, the fit quality at $60 \mu\text{m}$ becomes perfect and the quality at $0.85/1.3 \text{ mm}$ remains preserved. Note, however, that the overall stratification of the clumping factors is rather similar.

Concerning the effect of helium ionization balance, the right panel of Fig. 5.7 displays the possible error if the helium ionization were different to that assumed here (cf. Sects. 5.1.4 and 5.1.4.). If helium were singly ionized throughout the complete wind (instead of recombining only at $v_{\text{rec}} = 0.86$), the synthetic 10 and $20 \mu\text{m}$ fluxes in particular would become too low; compensating for this effect by increasing clumping factors is not possible, because H_α would then no longer be fit. If, on the other hand, helium were to remain doubly ionized in the outermost region also, the radio/mm (and the far-IR fluxes) would become larger than observed; in this case, a reasonable fit is still possible, by lowering the mass-loss rate and increasing the inner clumping factors (with a factor roughly corresponding to $(\dot{M}_{\text{old}}/\dot{M}_{\text{new}})^2$). The parameters for such a model (which fits both H_α and the entire IR–radio range) is given in Table 6 (3rd entry) of Puls et al. (2006). The rather large difference in the resulting (maximum) mass-loss rate (factor 0.7) and clumping factors is due to the fact that our model of ζ Pup has a helium content which is twice solar, $Y_{\text{He}} = 0.2$. For solar helium abundance, as is typical for most of the other objects of our sample, the corresponding factor

would be 0.85, as outlined in Sect. 5.1.4. Note again, however, that it is rather improbable that helium is still doubly ionized in the radio-forming region. From the consistency of the mm and radio fluxes, it is also clear then that the Helium ionization must be similar in the mm and the radio forming region, in agreement with our predictions for v_{rec} .

HD 209975. Fig. 5.8 displays the results of our combined fit procedure for this star, which has a moderate wind density and H_α in absorption. Again, we have indicated the resulting profiles/fluxes when the derived clumping factors are varied by a factor of two in specific regions, to check for their sensitivity. Most interestingly, *this object can be fitted with almost constant clumping factors throughout the wind*, in stark contrast to the above example. Indeed, with slightly different \dot{M} and β , an almost equally perfect fit is possible with all clumping factors being unity. If at all, the (homogenous) radio mass-loss rate is somewhat higher than the mass-loss rate derived from H_α , so that in this case $f_{\text{cl}}^{\text{in}}$ is set to unity.

Note that a moderate clumping factor of 2 for $1.5 < r < 2$ is still consistent with the data, and that due to missing far-IR information (the indicated data denote upper limits derived by IRAS), the clumping in the intermediate wind remains somewhat unconstrained. After some experimentation, it turned out that the data are also consistent with a moderately clumped wind ($f_{\text{cl}} = 10$) in the region $10 < r < 50$, or a weakly clumped wind ($f_{\text{cl}} = 2$) in the region $3 < r < 50$. Only for the outermost wind ($r > 50$), do the clumping properties *have* to be similar to the inner wind conditions.

Since the innermost wind has the lowest clumping, no statement concerning its onset is possible within our approach. Thus, any scaled solution (f_{cl} multiplied with f , \dot{M} reduced by $1/\sqrt{f}$) provides an equally perfect fit and cannot be excluded. In summary, the inner and outer wind of this object have similar clumping properties, whereas far-IR observations are required to constrain the intermediate region.

5.1.6 Clumping properties of the complete sample

Before discussing the results of our analysis for the complete sample, let me point out some general findings, and remind the reader that the derived clumping factors are independent of any uncertainty concerning radius and distance, since all our diagnostics (H_α /radio/IR) scale in an identical way with respect to these quantities.

The core of H_α as a tracer of wind clumping below $r \approx 2R_\star$. Our simulations show that the strength of the core of H_α , whether in emission or in absorption, is quite sensitive to the value of the clumping factor in the inner part of the wind, and thus can be used to determine this parameter out to distances of about $r \approx 2$. If one relies on the value of β as derived by means of unclumped models, the corresponding (average)

clumping factors are very precise, with an accuracy of roughly 10% (but see Sect. 5.1.7). Note particularly that clumping factors f_{cl}^{in} of order 2 or larger *are still visible for objects with H_α in absorption* (Figure 9 of Puls et al. 2006, dotted profile).

Constraints on the clumping factor beyond $r \approx 2R_\star$. In addition to constraining the clumping properties in the lower wind, H_α can even serve as an indicator of wind clumping in layers beyond $r \approx 2$ (e.g, Fig. 5.6, left panel). *How much beyond?* The answer depends, of course, on the specific wind density.

For those objects with H_α in emission and missing far-IR/mm information, in Table 5.3, column 14, we have indicated the outermost radius, r'_{out} , to which H_α *alone* can provide information on the clumping factor, on the assumption that the region, $r'_{out} < r < r_{far}$, is “unclumped” (or, more precisely, has the same clumping properties as region 5). Indeed, for almost all objects, r'_{out} is of the order of $5 R_\star$, except for HD 14947 (No. 5) and HD 192639 (No. 8), where H_α provides information only out to $3 R_\star$. Thus, it is safe to conclude that H_α constrains the clumping factor up to distances of $r = 3. . . 5R_\star$ *if in emission*. Note, however, that in some cases, significant clumping in region 4 (from r_{out} to r_{far}) has an effect on H_α , which leads to an additional constraint on the clumping in this region. For objects with H_α in absorption, on the other hand, the intermediate region remains much less constrained (Fig. 9 in Puls et al., left panel), and I will comment below on the corresponding limits.

Table 5.3 summarizes the results of our simultaneous H_α /IR/radio analysis. The objects are ordered according to H_α profile type and spectral type where actual names can be found in Table 7 of Puls et al. For almost all objects, we have used identical boundaries, $r_{in} = 1.05$, $r_{mid} = 2.0$ and $r_{far} = 50$, to obtain comparable results. The default values for r_{out} (region 3) correspond to 15 (H_α in emission) and 10 (H_α in absorption or of intermediate type). Detailed comments regarding the individual objects are given in Puls et al. (2006), where all fits are displayed as well.

Overall, our simulations show that for stars with H_α in emission, a simultaneous fit of the observed radio fluxes and the shape and strength of H_α , requires clumping factors which are always higher in the H_α -forming region than in the radio-forming one. For stars with H_α in absorption, the situation seems to be different: in most cases, the required clumping factors are of similar order in the inner and outer regions. However, this preliminary impression is dependent on the actual value of β , a problem which will be discussed in our error analysis further below.

For all objects quoted with a definite mass-loss rate (and not only an upper limit), this value represents the *largest possible value* (for given R_\star), usually derived from adopting an outer, unclumped wind with $f_{cl}^{far} = 1$ or, for weaker winds, $f_{cl}^{out} = 1$. These mass-loss rates correspond to the “usual” radio mass-loss rate. (Except for HD 34656 (No. 13) where the maximum mass-loss rate have to be derived from H_α .)

Table 5.3: Clumping properties as derived from our combined H_α /IR/radio analysis. Stars are ordered according to H_α profile type (“pt”) and spectral type with actual names as given in Table 7 of Puls et al. Entries in bold mark objects with extremely well-constrained clumping parameters.

T_{eff} is in kK, and \dot{M}_{cl} - in units of $10^{-6}M_\odot/\text{yr}$. “ratio” gives the ratio of “clumped” mass-loss rate to optical results using unclumped models (cf. Table 5.1). β_{cl} is the velocity field exponent as derived or adopted here. v_{rec} and r_{rec} are the velocity (in units of v_∞) and radius where He recombines (see Sect. 5.1.4), and $r(\tau_2)$ is the radius where the radio continuum becomes optically thick¹² at 2 cm (r_{rec} and $r(\tau_2)$ in units of R_\star). Clumping factors and boundaries are defined as in Sect. 5.1.4. For all models, region 1 with $f_{\text{cl}} = 1$ (not tabulated) extends from $r = 1$ to $r_{\text{in}} = 1.05$, except for HD 66811 (No.4) where $r_{\text{in}} = 1.12$, and r_{far} (defining the border between region 4 and 5) has been set to $50 R_\star$ always. For objects with H_α in emission or of intermediate type, and missing far-IR/mm data, r'_{out} (with corresponding clumping factor) indicates the maximum radius to which H_α alone can provide constraints on the clumping, on the assumption that the outer wind is “unclumped” (see text). For objects with H_α in absorption, $f_{\text{max}}^{\text{mid}}$ gives the maximum possible clumping factor in region 3, which is still consistent with the data. $f_{\text{max}}^{\text{out}}$ is defined similar to $f_{\text{max}}^{\text{mid}}$, but for region 4.

Star	pt	T_{eff}	\dot{M}_{cl}	ratio	β_{opt}	β_{cl}	v_{rec}	r_{rec}	$r(\tau_2)$	region 2		region 3		region 4		reg. 5
										$f_{\text{cl}}^{\text{in}}$	r_{mid}	$f_{\text{cl}}^{\text{mid}}$	$f_{\text{cl}}^{\text{mid}}(r'_{\text{out}})$	$f_{\text{cl}}^{\text{out}}$	$f_{\text{max}}^{\text{out}}$	$f_{\text{cl}}^{\text{far}}$
1	e	45.8	$\leq 4.0^{\text{a,b}}$	0.38	0.77	0.90	1.00	inf	29.7	5.0	2.0	4-6.	7.0(5)	1.0	10.0	1.0
2	e	39.2	9.5	0.59	0.95	0.95	0.85	6.2	49.6	3.0	2.0	3.0	3.5(5)	1.0	2.0	1.0
			7.5	0.46						5.0	2.0	5.0	5.8(5)	1.0	2.0	1.0
3	e	38.0	6.5	0.38	1.05	1.05	0.84	6.3	45.0	5.5	2.0	4-6		13.0	20.0	1.0
4	e	39.0	8.5	0.51	0.90	0.70	0.86	5.3	36.1	5.0	2.0	1.5		1.4	1.8	1.0
			4.2	0.51	0.90	0.70	0.86	5.0	36.5	5.0	2.0	1.5		1.4	1.8	1.0
5	e	37.5	10.0	0.59	0.95	0.95	0.81	5.0	37.9	3.1	2.0	2.5	4.0(3)	1.0	5.0	1.0
6	e	36.5	5.0	0.62	1.03	1.10	0.81	5.6	30.7	3.0	2.0	5.0	6.0(5)	1.0	15.0	1.0
7	e	36.0	3.0	0.38	1.00	1.00	0.83	5.9	24.7	6.5	4.0	10.0		1.0	8.0	1.0
8	e	35.0	$\leq 3.0^{\text{a}}$	0.48	0.90	1.14	0.82	6.3	27.7	3.5	2.0	3.5	6.0(3)	1.0	10.0	1.0
9	e	29.0	1.5	0.49	1.15	1.15	0.16	1.2	25.7	2.6	2.0	3.0	3.5(5)	1.0	4.0	1.0
10	i	38.2	$\leq 8.0^{\text{c}}$	0.71	0.74	0.74	0.84	4.7	33.6	2.5	2.0	1-2	2.5(3)	1.0	10.0	1.0
11	i	29.7	2.74	1.00	1.05	1.05	0.17	1.2	23.2	1.4	2.0	1.8	2.0(3)	1.0	4.0	1.0
12	a	41.8	$\leq 3.5^{\text{d}}$	0.82	0.85	1.00	0.94	17.3	33.0	1.0	2.0	1.0	$f_{\text{max}}^{\text{mid}}$	1.0	5.0	1.0
13	a	34.7	3.0	1.15	1.09	1.00	0.60	2.5	28.2	1.0	2.0	1.0	-	1.0	8.0	6.0
14	a	35.0	$\leq 2.3^{\text{a}}$	0.94	0.80	0.90	0.85	6.1	16.4	2.1	2.0	5.0	7.0	1.0	2.0	1.0
			$\leq 1.2^{\text{a}}$	0.49						8.0	2.0	20.0	25.0	1.0	3.0	1.0
15	a	34.5	1.1	1.12	0.80	0.90	0.57	2.2	23.3	1.0	2.0	1.0	2.0	1.0	8.0	1.0
16	a	33.6	$\leq 0.4^{\text{a}}$	0.54	0.80	0.90	0.51	1.9	10.2	2.0	2.0	1.0	20.0	1.0	2.0	1.0
17	a	36.0	1.0	0.95	0.80	0.90	0.82	5.2	22.5	1.0	2.0	1.0	2.0	1.0	15.0	1.0
18	a	31.4	0.8	0.78	0.85	0.90	0.29	1.3	14.4	1.0	2.0	1.0	4.0	1.0	2.0	1.0
			0.25	0.24						12.0	1.3	1.0	20.0	1.0	10.0	1.0
19	a	32.0	1.2	1.08	0.80	0.90	0.42	1.6	27.1	1.0	2.0	1.0	1.5	1.0	10.0	1.3

^{a)} only upper limits of radio fluxes available; \dot{M} maximum radio mass-loss rate.

^{b)} He assumed to be recombined in radio region.

^{c)} upper limit, since non-thermal radio emitter; \dot{M} from 2 cm flux.

^{d)} \dot{M} from H_α , since radio fluxes (upper limits only) give larger value.

For six objects, on the other hand, the maximum mass-loss rate could not be uniquely constrained, and the quoted limits correspond to the largest value consistent with the data. In five of these cases (denoted by superscripts “a”), all radio fluxes are upper limits only whilst for Cyg OB2#8A (No. 10, a non-thermal emitter) the adopted maximum mass-loss rate relies on the 2 cm which gives the lowest (radio) \dot{M} within the available data set (see Sect. 5.1.1). In addition to these objects, three more stars (HD 190429A (No. 2), HD 34656 (No. 13), and HD 37043 (No. 18, SB2!)) have somewhat peculiar radio fluxes, and might also be non-thermal emitters.

Mostly because of these peculiarities, we have given two possible solutions for HD 190429A (No. 2), HD 37043 (No. 18) and also HD 24912 (No. 14) in Table 5.3, comprising a minimum and maximum solution with respect to the (relative) clumping properties. For the latter two, the 2nd entries are the more plausible ones, whereas for HD 190429A both solutions have similar problems (though the difference is not as large as for the other two stars).

Indicated by their number appearing in bold face, the remaining objects have well-constrained clumping properties, i.e., the derived results are robust *if β is not too different from the values derived or adopted here*

The latter quantity has been specified as follows. For objects with H_α in emission and of intermediate type, we have used the values from our unclumped analyses (see Tables 5.1, present study, and Table 5 of Puls et al. 2006) wherever possible, i.e., if satisfactory fits could be achieved. This turned out to be true in almost all cases, with the notable exception of ζ Pup, where our clumped analysis favours a much lower value ($\beta_{cl} = 0.70$) than previously found. For most objects with H_α in absorption (except Cyg OB2#8C, No. 1 and HD 34656, No. 13), because of missing constraints we used the “standard” value (from hydrodynamical models) of $\beta = 0.9$, to obtain at least consistent results. Further consequences of this uncertainty are discussed in the next section.

For those stars where H_α is of P-Cygni shape, or displays a well-refilled absorption trough, conclusive limits could be derived regarding the maximum value of r_{in} , i.e., the maximum extent of a potentially unclumped region. In all cases, this region lies below $1.2 R_\star$.

In addition to the derived clumping factors which represent the best-fitting solution, we also provide maximum values for f_{cl}^{mid} and f_{cl}^{out} which are still consistent with our data, and can be restricted further only by additional far-IR and sub-mm observations. For the first 11 objects in Table 5.3, f_{cl}^{mid} could be constrained from the wings of H_α , either for the entirety of region 3 or, if indicated, at least out to r'_{out} . For the other objects, the wind density is too low to induce significant reactions in either H_α , or the IR when the clumping properties in region 3 are changed, such that more definite statements are not possible.

5.1.7 Errors in the derived clumping factors

In the following, I will concentrate on the errors introduced into the derived clumping factors; errors in the mass-loss and modified wind-momentum rates are dominated by errors in the angular diameter and radius, but do not affect the major outcome of our investigation.

Let me first mention that during our detailed fits we found no *systematic* problem concerning an under-estimation of the N - and Q -band fluxes, so that at least our absolute flux calibration seems to be appropriate (see Sect. 5.1.2). On the contrary, for some objects (Q -band: HD 15570; N -band: Cyg OB2#11, #10 and HD 207198), these fluxes lie above our predictions for the best-fitting model. To investigate this point in more detail, however, additional fluxes in the mid- and far-IR are required.

Errors introduced by uncertainties in the radio continuum Changing $f_{\text{cl}}^{\text{in}}$ and $f_{\text{cl}}^{\text{mid}}$ by identical factors and adapting \dot{M} accordingly, until the observed radio fluxes could no longer be matched, we found that the clumping factors in the regions traced by H_α (i.e., below $r = 3 \dots 5$) are accurate (on an absolute scale) to within 20 to 50%, whereas the *ratio* of the clumping factors in the various regions remains preserved. Extreme cases regarding this uncertainty in the radio fluxes are HD 190429A, HD 14947 and Cyg OB2#11 (cf. Table 8 (3rd column) of Puls et al.)

The degeneracy of β and clumping factors in the inner wind. As noted in the previous section, the strength of the core of H_α is highly sensitive to the value of the clumping factor in the inner part of the wind, below $r \approx 2R_\star$. But it is also sensitive to the value of the velocity exponent, β , and in a similar way: larger values of both β and clumping factors lead to more emission in the line core, giving rise to an unfortunate degeneracy.

This degeneracy requires an investigation into the question of how far any uncertainty in β will propagate into the errors of f_{cl} . To this end, we have varied β and determined the appropriate values of $f_{\text{cl}}^{\text{in}}$ and $f_{\text{cl}}^{\text{mid}}$ such that the quality of our H_α fit remained preserved. For profiles with H_α in emission and of intermediate type, the minimum and maximum values of β were taken from those solutions which were still compliant with the observed profile shape. For objects with H_α in absorption, we used reasonable limits, at $\beta = 0.7$ and $\beta = 1.1$, respectively. Larger values could usually be excluded from the profile shape, whereas in certain cases a lower value (though being larger than the physical limit, $\beta \geq 0.5$) might still be possible. This procedure is somewhat similar to our approach to resolving the alternative β vs. \dot{M} degeneracy in homogeneous winds, when \dot{M} is derived from H_α alone.

The results of this investigation are summarized in Table 8 of Puls et al.. As expected, for stars with H_α in emission, the uncertainty in β is not dramatic. This uncertainty leads to an average uncertainty in $f_{\text{cl}}^{\text{in}}$ of about $\pm 30\%$, whereas for objects with H_α in absorption, much larger uncertainties are possible (factors of

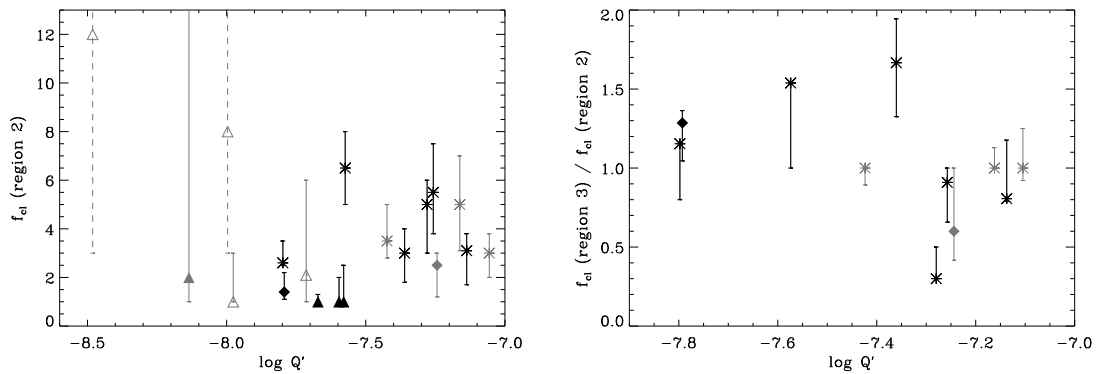


Figure 5.9: *Left*: Clumping factors, $f_{\text{cl}}^{\text{in}}$ (region 2), for our sample, as a function of the distance-invariant quantity, $\log Q'$. Asterisks: objects with $\text{H}\alpha$ in emission; diamonds: objects with intermediate $\text{H}\alpha$ profile type; triangles: objects with $\text{H}\alpha$ in absorption. Black colors: objects with definite maximum mass-loss rates (corresponding to bold-face entries in Table 5.3). Grey colors: objects with upper limits for \dot{M} and corresponding lower limits for $f_{\text{cl}}^{\text{in}}$. Maximum values of $f_{\text{cl}}^{\text{in}}$ correspond to minimum values of β_{cl} , and vice versa for the minimum values. The open triangles with solid error bars display the high- \dot{M} –weak-clumping solution for HD 24912 and HD 37043, and the open triangles with dashed error bars the alternative low- \dot{M} –strong-clumping solution for these objects.

Right: As left, but for the ratio $f_{\text{cl}}^{\text{mid}}/f_{\text{cl}}^{\text{in}}$, and objects with $\text{H}\alpha$ in emission or of intermediate profile type only. The star with the lowest ratio (0.3) is ζ Pup. For the three objects with a given interval for $f_{\text{cl}}^{\text{mid}}$ (Cyg OB2#7, HD 15570 and Cyg OB2#8A, see Table 5.3), we have used the mean value regarding this interval.

between 2 and 7), if β were 0.7 instead of 0.9.

An interesting outcome of this analysis furthermore shows that *if* low-density winds ($\text{H}\alpha$ in absorption) were to have a velocity field exponent larger than the standard one (e.g., 1.1 instead of 0.9), the differences to the objects with $\text{H}\alpha$ in emission would become even more pronounced: in this case, the outer region would be even more clumped than the inner one. Only if β were close to its lower limit, would the clumping properties of some of the thin winds become similar to those of high-density winds.

Concerning the resulting uncertainties for $f_{\text{cl}}^{\text{mid}}$ (region 3), the situation for $\text{H}\alpha$ emission type objects is similar as for $f_{\text{cl}}^{\text{in}}$. The average minima and maxima lie $\sim \pm 20\%$ below and above the best-fitting value of β . For the objects with weaker winds, on the other hand, $f_{\text{cl}}^{\text{mid}}$ still remains unconstrained, and in all cases the upper limits as already quoted in Table 5.3 remain valid.

5.1.8 Clumping properties as a function of wind density

Fig. 5.9 (left panel) displays the derived clumping factors for region 2 (i.e., the first clumped region) as a function of $\log Q' = \log \dot{M}/R_{\star}^{1.5}$, i.e., a quantity which is closely related to the mean wind density, but is additionally distance invariant. Remember that in the present context \dot{M} is the largest possible mass-loss rate, and that most of the derived factors refer to outermost clumping factors set to unity. In other words,

they have to be regarded as a measurement of the clumping properties of the inner wind *relative to the outermost one*.

The most important conclusions which can be drawn from this figure are the following. For thinner winds with $\log Q' \leq -7.5$ (objects with H_α in absorption or of intermediate type plus α Cam), *the inner wind seems to be clumped by a similar degree as the outermost one*, at least if we discard the alternative low- \dot{M} -strong-clumping solutions for HD 24912 (No. 14) and HD 37043 (No. 18) (open triangles with dashed error bars). Note that if the latter solutions were the actual ones (and we have indicated that this is rather possible), then both stars are behaving completely different to the other absorption-type stars.

On the other hand, for stronger winds (almost all stars with emission profiles, plus Cyg OB2#8A), *the inner wind seems to be more strongly clumped than the outermost one*, with an average ratio of 4.1 ± 1.4 . Of course, for this class of objects there is also the possibility that we encounter moderately ($f_{\text{cl}}^{\text{in}} \approx 3$) and stronger ($f_{\text{cl}}^{\text{in}} \approx 5$) clumped lower wind regions, or that the degree of clumping decreases again towards the largest wind densities. However, due to the restricted number of objects, the influence of temporal variations (Sect. 5.1.1) and the error introduced by the uncertainty of the continuum flux level, such statements cannot be verified at the present time.

Fig. 5.9 (right panel) displays the ratio of clumping factors in the intermediate and inner part of the wind, for objects with H_α in emission or of intermediate type. Obviously, in most cases, the clumping properties in both regions are either similar, or the (average) clumping factors increase moderately from region 2 towards region 3, at most by a factor of 2. For objects with H_α in absorption, on the other hand, at least upper limits for the clumping factors in region 3, $f_{\text{max}}^{\text{mid}}$, could be derived. For three well-constrained objects, HD 203064 (No. 15), HD 207198 (No. 17) and HD 209975 (No. 19), these upper limits lie between 1.5 and 2, i.e., they might be twice as large as the corresponding values for $f_{\text{cl}}^{\text{in}}$, but are still rather low. For the remaining stars, the maximum values for $f_{\text{cl}}^{\text{mid}}$ lie in between 4 and 25, but only for HD 24912 is a large value actually *needed*, if the observed emission humps are to be interpreted in terms of clumping and β were of order 0.9 or larger (see above).

Concerning the clumping properties in region 4 ($15 \leq r \leq 50$), finally, definite statements are only possible for those 3 stars observed in the mm region, namely ζ Pup (No. 4), HD 15570 (No. 3) and HD 210839 (No. 7). The first of these objects, ζ Pup, displays the only notable exception concerning the ratio of $f_{\text{cl}}^{\text{mid}}$ and $f_{\text{cl}}^{\text{in}}$, namely that region 3 is much less clumped than region 2. In other words, maximum clumping must be close to $2 R_\star$, or even lower. For this star, the *derived* clumping factor for region 4 (extending from 15 to $50 R_\star$) is even lower than for region 3: at most, $f_{\text{cl}}^{\text{out}} \leq 1.8$.

For HD 15570, (No. 3) on the other hand, regions 2 and 3 are similarly clumped, and the derived clumping factor might increase even further towards region 4, with $f_{\text{cl}}^{\text{out}}$ being 5 to 20 times larger than

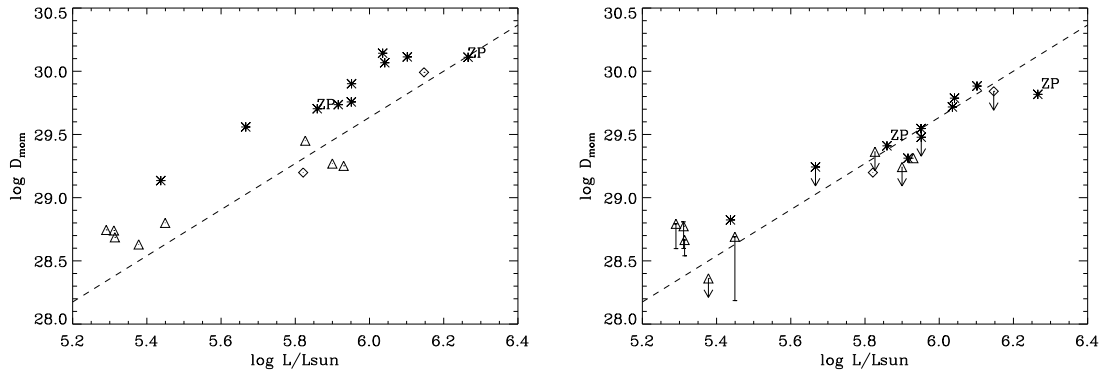


Figure 5.10: Wind-momentum–luminosity relation for our sample. Modified wind-momentum rate. *Left*: mass-loss rates derived from H_α , using *homogeneous* models. *Right*: largest possible mass-loss rates. Upper limits indicate those cases where radio fluxes are upper limits and/or non-thermal emission cannot be excluded. Asterisks: objects with H_α in emission; diamonds: objects with intermediate profile type; triangles: objects with H_α in absorption. Dashed line indicates theoretical prediction by Vink et al. (2000).

the average clumping in the radio-emitting region. For this object, the mm measurements from SCUBA are extremely valuable, though the rather large error bars leave the situation not as clear as desirable.

For λ Cep (HD 210839, No.7), finally, the intermediate region is more heavily clumped than the inner one, whereas region 4 could be constrained (again via SCUBA observations) to display clumping factors between 1 and 8.

In summary, at least one of these three objects is rather weakly clumped in region 4. Although the same might be true for the other two stars (accounting for the lowest possible fluxes), a significantly clumped outer region is more probable.

5.1.9 Wind-momentum–luminosity relation

Before discussing some further implications of our findings, let me consider the wind-momentum–luminosity relation for our stellar sample, accounting for the results I have outlined above. Fig. 5.10 displays two such relations, in comparison with the theoretical predictions by Vink et al. (2000). The left panel shows the results using H_α mass-loss rates derived by unclumped models, updated for a re-determined stellar radius. As already noted in the beginning of this chapter, objects with H_α in absorption and of intermediate type are perfectly consistent with the predictions (except for a few objects at $\log L/L_\odot < 5.35$), whereas objects with H_α in emission populate a strip parallel to, but above, the predictions. Only the large-distance solution for ζ Pup lies *on* the relation, whereas the low-distance solution displays the same discrepancy as the other stars (both solutions indicated by “ZP”).

In the right panel, our new results, with mass-loss rates from Table 5.3 are displayed. These mass-loss

rates are the largest possible ones, and are essentially the radio mass-loss rates if the winds were unclumped in the radio-forming regime. Except for this assumption, the largest errors present in this figure are due to errors in the distance estimate. What is obvious from this plot, however, is that the agreement between observations and theoretical predictions has significantly improved. Almost all objects now lie very close to the theoretical relation, *independent of profile type*.

The reason, of course, is that the newly derived (radio) mass-loss rates for emission-profile objects are smaller than the H_α mass-loss rates (see Table 5.3, column “ratio”), by an average factor of 0.49 ± 0.10 . Most interestingly, this is almost exactly the same factor which has been claimed in Markova et al. (2004) (0.48, drawn from a much larger sample), and which has been used a priori in our de-reddening procedure (see Sect. 5.1.3). A factor of the same order (0.42) has also been found by Fullerton et al. (2006), for a sample comprising objects similar to those considered here. For objects with H_α in absorption and of intermediate type, H_α and radio mass-loss rates agree well, and they remain at their “old” position. Note that for the only absorption-type object in the sample of Fullerton et al. with H_α and radio data available in parallel (HD 149757), a comparable agreement was found, supporting our results.

Whereas the “new” WLR agrees extremely well with the theoretical predictions for objects with $\log L/L_\odot > 5.35$, the three best-defined absorption-type stars at the lower luminosity end of our sample (HD 203064, HD 207198 and HD 209975) lie too high, by a factor of ≈ 2.5 . To unify these objects with the others by clumping arguments *alone* would require that they have to be much more clumped in the radio regime (on an absolute level).

Of course, one might argue that this problem is not related to (unknown) physics, but to wrong distances and radii. Though this might be possible given the mean errors in modified wind-momentum rate (0.13 dex) and luminosity (0.19 dex) derived for Galactic objects (Markova et al. 2004), it is more plausible to invoke physical reasons, since we have to explain an identical problem for three different stars (with different T_{eff}) at identical positions in the diagram.

Again, I stress that all displayed positions rely on the derived, *largest possible* mass-loss rates. If the radio regime were clumped, downward corrections become necessary. In this case, however, the displayed agreement would be pure coincidence.

5.2 Summary

An extensive and detailed discussion on the major implications of the results outlined in this chapter can be found in Puls et al. (2006), while in the following I will only summarize the main outcomes.

In this investigation, we have performed a simultaneous analysis of H_α , IR, mm (if present) and radio

data to constrain the radial stratification of the clumping factor in a sample of 19 O-type supergiants/giants, with dense and moderate winds (H_α in emission and absorption). All analysis tools used involve certain approximations, but we have ensured that the derived results comply with state-of-the-art NLTE model atmospheres, by comparing and calibrating to a large grid of such models. Clumping has been included in the conventional approach, by manipulating all ρ^2 -dependent opacities and assuming the inter-clump matter to be void. Caveats to this assumption and other problems inherent to this approach, namely the neglect of disturbances of the velocity field due to the clumps, and the assumption of small length scales, related to the problem of porosity, are given in Puls et al. (2006).

Instead of adapting the clumping-factor at *each* radial grid point (which is possible only if using optimization methods, requiring a well-sampled observed wavelength grid), we have introduced 5 different regions, with constant clumping factors inside each region. Because all our diagnostics depends on ρ^2 (except for the small contribution by electron scattering), the most severe restriction within our approach is given by the fact that we cannot derive absolute clumping factors, but only factors normalized to a certain minimum. Since in all but one case (HD 34656) this minimum was found to be located in region 5 (or, in other words, since in all those cases the radio mass-loss rate is the lowest), our normalization refers to the radio regime, and the corresponding (radio) mass-loss rate as derived here is the largest possible one. Other solutions are possible as well, with all clumping factors multiplied by a constant factor, f , and a mass-loss rate reduced by \sqrt{f} .

Our analysis is based on H_α line profiles, near-/mid-/far-IR fluxes taken from our own observations and the literature (de-reddened as detailed in Sect. 5.1.3), mm fluxes observed by SCUBA/SEST (own and literature data), and radio data taken from our own VLA observations and the literature. We have discussed the issue of non-simultaneous observations: based on present-day observational facts, the H_α , IR and radio variability of thermal emitters is low enough so as not to pose any problems for our study, at least if the derived results are considered in a statistical sense. Within our sample, there is only one confirmed non-thermal emitter (Cyg OB2#8A), and three more objects display somewhat peculiar radio fluxes (HD 190429A, HD 34656, see above, and HD 37043). These objects might be non-thermal emitters as well, but this has to be confirmed by future observations. In any case, the derived mass-loss rates (from the minimum radio flux) can be considered as an upper limit.

As it turns out, the core of H_α provides very useful diagnostics for the clumping properties in the inner wind ($r \leq 2R_\star$), and, if in emission, the wings can be used to constrain the clumping inside the first five stellar radii, with an additional check provided by IR data. If mm fluxes were available, the outer wind ($15R_\star \leq r \leq 50R_\star$) could be constrained as well. Only the region between $5R_\star \leq r \leq 15R_\star$ remains “terra incognita” in most cases, due to missing far-IR fluxes.

For ten stars in our sample (six with H_α in emission, one of intermediate type and three with H_α in absorption), the derived clumping factors are robust and lie within well-constrained error bars. For six stars (including Cyg OB2#8A), only upper limits for the radio mass-loss rate are available, and the derived clumping factors have to be considered as lower limits. Obvious differences to the best-constrained objects were not found though, except for HD 24912, which behaves atypically. The three remaining objects constitute HD 34656, which is the only object in our sample with an H_α mass-loss rate lower than the radio mass-loss rate (and as such has been discarded from our further analysis), HD 37043, which exhibits similar problems to HD 24912 (but has a better-constrained radio mass-loss rate), and HD 190429A, which displays a certain degree of radio-variability. Taking the various results together, I can summarize our findings as follows:

- for almost all objects (except for 3 stars with H_α in absorption and $\log L < 5.35 L_\odot$), the derived (radio) mass-loss rates are in very good agreement with the predicted wind-momentum–luminosity relation (Vink et al. 2000), in contrast to previous results relying on unclumped H_α data alone. If ζ Pup is located at the “close” distance, then it behaves as the rest. If, on the other hand, it is located further away, its (radio) wind-momentum rate would lie considerably below the predictions.
- the mean ratio of radio mass-loss rates to unclumped H_α mass-loss rates for stars with H_α in emission is 0.49 ± 0.10 . This is almost exactly the same factor as found in Markova et al. (2004), by shifting the *observed* WLR (using unclumped models) for these objects onto the *predicted* one. It also agrees well with recent findings from Fullerton et al. (2006).
- the average, normalized clumping factor in the innermost region ($r \leq 2R_\star$) of stars with H_α in emission is $\sim 4.1 \pm 1.4$.
- thinner winds with H_α in absorption have lower normalized clumping factors in this region. For all three stars with robust constraints, these factors are similar to those in the radio region, at least if the velocity exponent is not too different from the hydrodynamical prediction, $\beta \approx 0.9$. Factors of the order of $f_{\text{cl}}^{\text{in}} \geq 2$ can be excluded, due to the sensitive reaction of H_α .
- for all objects where H_α is of P Cygni shape, or displays a well-refilled absorption trough, the maximum extent of a potentially unclumped region can be limited to lie inside $r \leq 1.2R_\star$.
- in most cases, the clumping factors in the inner and adjacent region ($2R_\star \leq r \leq 5 \dots 15R_\star$) are comparable or increase moderately from inside to outside. Only for ζ Pup, does our analysis restrict the maximum clumping at $r \leq 2R_\star$.

- the presence of clumping introduces a new degeneracy in the results, namely between the velocity field exponent, β , and the clumping factors. If β is lower than assumed or derived from the fits, the clumping factors are larger, and vice versa. Extreme deviations of β from values obtained from an unclumped analysis can be excluded though. Interestingly, a perfect fit for ζ Pup requires $\beta = 0.7$, contrasted with $\beta = 0.9$ from unclumped diagnostics (Repolust et al. 2004).
- two of the three stars with mm-observations (HD 15570 and HD 210839) indicate a certain probability that the outer region 4 ($15R_{\star} \leq r \leq 50R_{\star}$) is considerably more clumped than the radio domain (but remember the rather large error bars on the mm data), whereas the third star, ζ Pup (with negligible observational errors), displays similar clumping properties in both regions.
- Our results differ from hydrodynamical predictions (incorporating the intrinsic, self-excited line-driven instability, Runacres & Owocki 2002, 2005) at least in one respect: the latter imply a larger radio than H_{α} mass-loss rate (or, alternatively, lower clumping in the inner than the outer wind), which is definitely not true for our sample.

The major implications of the above outlined findings can be stated within three different assumptions concerning the clumping properties of the outermost regions:

1) The radio region is not, or only weakly, clumped. In this case, our “old” hypothesis (concerning a shift of mass-loss rates for objects with H_{α} in emission, due to clumping) would be confirmed, but there would be a physical difference between denser and thinner winds, in the sense that thinner winds would be less clumped than thicker winds in the inner region. This difference might then be related to different excitation mechanisms of structure formation. If assumption (1) were true, the theoretical WLR would be perfectly matched. On the other hand, the absolute numbers for clumping factors and mass-loss rates would be in severe contrast to results from other investigations that have used alternative diagnostics, not directly affected by clumping (e.g., the P ν resonance lines).

2) The radio region is strongly clumped, but the outermost clumping factors are independent of wind density. In this case, a unification with results from other diagnostics is possible, and the present mass-loss rates would have to be significantly revised, with serious implications for the evolution of, and feedback from, massive stars. Again, weaker winds would be less clumped in the inner region, and the theoretical WLR would no longer be matched. One of the most robust predictions from radiation-driven wind theory, namely that the modified wind-momentum rate should depend almost exclusively on luminosity (and not on mass or gravity), would still be consistent with our data, even if there were an offset between

the theoretical and observed WLR.

3) The radio region is strongly clumped, but the degree of clumping is different for different wind densities. This case is also consistent with present data, but would again imply, in addition to different offsets between the theoretical and observed WLR, that the observed WLR is dependent on a second parameter. Obviously, the implications of all three assumptions pose their individual problems, and would have different consequences regarding the urgent question about the “true” mass-loss rates of massive stars.

At these circumstances the real question now concerns the absolute value of the clumping factors. The only way to clarify this issue is the inclusion of processes which do not depend on ρ^2 . One such diagnostic is P_v (Massa et al. 2003; Fullerton et al. 2004, 2006) which under favourable circumstances scales $\propto \rho$ alone. The major problem here arises from the uncertainties regarding the ionization fraction of this ion, which might be additionally contaminated by the UV-tail of the X-ray emission. Assuming that P_v is a major ion between O4 and O7, Fullerton et al. (2006) derived a median reduction in \dot{M} (compared to homogenous H _{α} and radio diagnostics) by a factor of 20, where thin winds seemed to be more affected than thicker ones. Note that this would imply clumping factors of the order of 100 in the radio regime!

Detailed NLTE investigations accounting for clumping, on the other hand, are only in their infancy, and again, the inclusion of X-ray effects is a difficult task. The only object within our sample which can be compared with such an investigation is HD 190429A, analyzed by Bouret et al. (2005). In their conclusions, the authors quote a reduction of a factor of three in \dot{M} , compared to a homogeneous mass-loss rate of $6 \cdot 10^{-6} M_{\odot}/\text{yr}$ derived from the far-UV, exploiting ρ - and ρ^2 -dependent processes in parallel, and accounting for a consistent ionization equilibrium. Though the implied clumping factor would be not too different from “our” value, on an absolute scale there are much larger differences. Comparing their final mass-loss rate ($1.8 \cdot 10^{-6} M_{\odot}/\text{yr}$, with $R_{\star} = 19.5 R_{\odot}$ and $v_{\infty} \approx 2300 \text{ km s}^{-1}$) with our radio mass-loss rate ($7.5 \dots 9.5 \cdot 10^{-6} M_{\odot}/\text{yr}$, with $R_{\star} = 22.7 R_{\odot}$ and $v_{\infty} = 2400 \text{ km s}^{-1}$), this would suggest a strongly clumped radio regime, with $f_{\text{cl}}^{\text{far}} \approx 10 \dots 16$, at least if there have been no major changes in the average wind properties between their UV and our radio observations. Additionally, Bouret et al. (2005) point to the fact that the predictions by Lenorzer et al. (2004) concerning Br _{α} indicate that the outer winds “would be less affected by clumping”, compared to the regions they could access. Thus far, the situation remains unclear.

Notably, the other object investigated by Bouret et al. (2005) is an object with H _{α} in absorption, and for this object they find a reduction in \dot{M} by a factor of 7 (again with respect to UV observations alone). This result would agree with our statement from above that thin winds are expected to be more strongly structured than thick winds, at least if the latter are not externally triggered by photospheric disturbances.

Accounting for these findings and other investigations with similar results (e.g., Hillier et al. 2003;

Bouret et al. 2003), there seems to be increasing evidence that the agreement between the theoretical and observed WLR (which, if real, would imply a smooth wind in the radio regime) is indeed just coincidence, and that the radio regime must be strongly clumped, maybe even more strongly than presently described by hydrodynamics.

Aside from the major implications such a reduction of mass-loss rates would have, e.g., regarding stellar evolution in the upper HRD and feedback from massive stars, such a result would also lead to the following problem: since the present theoretical WLR originates from consistent calculations of the radiative line force, lower wind momenta would imply that too much radiative pressure is available. A reduction of this quantity, however, is rather difficult.

Finally, let me note that a significant down-scaling of mass-loss rates would unfortunately also affect stellar parameters (again!). For the ρ^2 -dependent results derived here, such scaling is easily possible, without modifying any result. *Photospheric* lines, on the other hand, might be differently affected by a strongly clumped, but weaker wind, since they do not always scale with Q , but depend on other combinations of \dot{M} , R_\star and v_∞ as well.

Chapter 6

Theory and observations

In this chapter, empirical results derived throughout our long-term extensive survey of Galactic OB-star winds will be confronted to theoretical predictions. In Sect. 6.1 to 6.4, I will examine in how far the predictions of Vink et al. (1999, 2000), obtained via a Monte Carlo technics, are followed by the observations. We chose to compare to these predictions because they seem to be superior to those originating from the improved CAK approach (Vink 2006). In Sect. 6.5, on the other hand, results derived via our combined H_α , IR and radio investigations will be compared to predictions of Runacres & Owocki (2002) about the radial stratification of the clumping factor in O-star winds. This way successes, but also failures, of the corresponding theories will be revealed, which might be used as guidelines for further developments and improvements of both the theory and the observations.

6.1 Monte Carlo predictions

In Chapter 1, Sect. 1.3, I have pointed out that the radiation driven wind theory is the most promising attempt to account for the effects of stellar wind in hot massive stars. In addition, I have also mentioned that within the *standard* theory, two basic approaches to predict wind properties exist: hydrodynamical methods based on the improve CAK theory (e.g., Pauldrach et al 1990; Kudritzki 2002; Pauldrach et al 2004), and methods based on Monte Carlo radiative transfer techniques (e.g., Vink et al. 1999, 2000, 2001). The major difference between these two approaches is that in the later case the effects of *multiple scattering* can be taken into account. Here I will open a bracket to say that due to the velocity gradient, a photon scattered in a given spectral line has no chance to be scattered again in that same line anywhere in the wind, and will therefore effectively escape, unless it is not scattered in *another* spectral line of lower frequency¹. The

¹Remind that for each point in an accelerating wind the surrounding is receding.

absorption of photons in different spectral lines is called *multiple scattering*.

The best theoretical reason to believe that *multiple scattering* is important, is the considerable line overlap seen in the UV spectra of hot stars which offers photons the possibility to multiply scatter. Concerning the observational evidence, the most striking example is the so-called “momentum problem” in WR stars, where the wind momentum efficiency, η , ($= \frac{\dot{M}v_\infty}{L_\star/c}$), was found to exceed unity. Note that in the *single scattering limit*, every photon transfers its momentum just once to the wind material, and thus the wind momentum $\dot{M}v_\infty$ must be equal to the radiative momentum L_\star/c , i.e., $\eta = 1$ (see, e.g., Vink et al. 1999 and references therein).

Using a Monte Carlo technique in which *multiple scatterings* are properly taken into account, Vink et al. (2000) have calculated a grid of wind models covering a wide range of stellar parameters throughout the upper part of the Hertzsprung-Russell diagram. In these models the photosphere and the wind are treated in a unified manner; the level populations of the iron-group elements are calculated within the nebular approximations, and the mass-loss follow from a global energy arguments.

Based on this model grid, the authors obtain two analytical expressions to calculate mass-loss rates of OB stars:

$$\begin{aligned} \log \dot{M} = & -6.697 + 2.194 \log(L_\star/10^5) - 1.313 \log(M_\star/30) \\ & - 1.226 \log \frac{v_\infty/v_{\text{esc}}}{2.0} + 0.933 \log(T_{\text{eff}}/40000) \\ & - 10.92 [\log(T_{\text{eff}}/40000)]^2 \end{aligned} \quad (6.1)$$

for stars with T_{eff} between 50 and 27.5 kK and $v_\infty/v_{\text{esc}} = 2.6$, and

$$\begin{aligned} \log \dot{M} = & -6.688 + 2.210 \log(L_\star/10^5) - 1.339 \log(M_\star/30) \\ & - 1.601 \log \frac{v_\infty/v_{\text{esc}}}{2.0} + 1.07 \log(T_{\text{eff}}/20000) \end{aligned} \quad (6.2)$$

for stars with T_{eff} between 15 and 22.5 kK and $v_\infty/v_{\text{esc}} = 1.3$. In both expressions \dot{M} is in $M_\odot \text{ yr}^{-1}$; L_\star and M_\star are in solar units, and T_{eff} is in Kelvin. Note also that the dependence of \dot{M} on the velocity exponent β (see Eq. 1.9) has been found to be significantly smaller than that on the other parameters, and thus this dependence is omitted from Eqs. 6.1 and 6.2.

By means of their model grid, Vink et al. (2000) have also derived the “theoretical” WLR for the two ranges of T_{eff} at either side of the bi-stability jump as follows:

$$\Pi^{\text{theory}} = -12.12 + 1.826 \log(L/L_\odot) \quad (6.3)$$

for $T_{\text{eff}} \geq 27\,500$ K, and

$$\Pi^{\text{theory}} = -12.28 + 1.914 \log(L/L_{\odot}) \quad (6.4)$$

for $12\,500 \leq T_{\text{eff}} \leq 22\,500$ K. Note that the predicted wind momenta for hotter stars ($T_{\text{eff}} \geq 27.5$ kK) are significantly lower than those for cooler ($T_{\text{eff}} \leq 22.5$ kK) ones. Note also that the slopes of the two relations are somewhat different resulting in different values of α' (Remind that $\alpha' = \alpha - \delta$), namely :

$$\alpha' = \frac{1}{1.826} = 0.548, \quad T_{\text{eff}} \geq 27500 \quad (6.5)$$

$$\alpha' = \frac{1}{1.914} = 0.522, \quad 12\,500 \leq T_{\text{eff}} \leq 22\,500 \quad (6.6)$$

These findings are particularly important because they indicate that one cannot expect a universal WLR over the complete spectral range of OB-stars, nor does one expect a constant value of α' (Vink et al. 1999, see also Puls et al. 2000).

Contrary to earlier comparisons where systematic discrepancies have been reported (see Lamers & Leitherer 1993; Puls et al. 1996), Vink et al. (2000) find good correspondence between their predictions and observational mass-loss (from radio and H_{α}) and wind momentum rates for a large sample of O stars. This finding has been interpreted as an indication that in these stars “multiple-scattering” is important while effects due e.g., to magnetic fields, clumping, and stellar rotation are likely not significant (however see Sect. 6.3).

6.2 The bi-stability jump

The solutions of the hydrodynamical equations for stationary, spherically symmetric line-driven winds (Eqs. 1.7 and 1.8) with radiative line acceleration as outlined in Sect 1.4.1 predict the terminal flow velocity to be proportional to the escape velocity:

$$v_{\infty} \propto \frac{\alpha}{1 - \alpha} v_{\text{esc}} \quad (6.7)$$

$$v_{\text{esc}} = \sqrt{2GM_{\text{eff}}/R_{\star}} \quad (6.8)$$

where M_{eff} is the effective mass, i.e. the mass corrected for the radiative force due to electron scattering and G is the gravitational constant. Note that the value of v_{∞} depends on α , the power law exponent of the line strength distribution function (see Eq. 1.3), in sense that a steep line-strength distribution function (small α , many weaker lines) will produce a slow wind, whereas a flatter function (large α , more stronger lines) will lead to a faster wind. Note also that the $v_{\infty}/v_{\text{esc}}$ ratio was predicted to depend on T_{eff} as well.

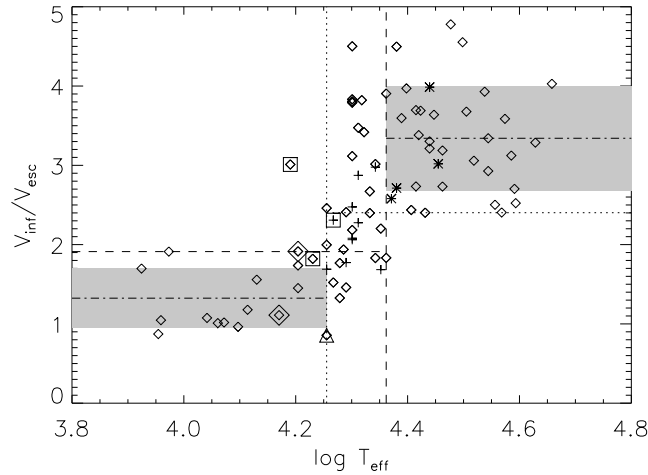


Figure 6.1: The $v_{\infty}/v_{\text{esc}}$ ratio as a function of $\log T_{\text{eff}}$ (from Markova & Puls 2008). Diamonds represent a combined sample of Galactic SGs of O- (from Repolust et al. 2005; Markova et al. 2004; Herrero et al. 2002) and B-types (from Sec. 2.2 and from Crowther et al. 2006; Urbaneja 2004; Lefever et al. 2007). Asterisks/plus-signs refer to the early/mid B supergiants from the sample by Kudritzki et al. (1999). Large diamonds correspond to the potentially misclassified B5-objects HD 191 243 and HD 108 659. The triangle denotes the hypergiant HD 152 236 and the three squares - the various positions of HD 53 138 as derived by Crowther et al. (2006), Lefever et al. (2007) and Kudritzki et al. (1999) (references ordered by increasing T_{eff}). Individual errors extend from 33% to 43%. See text.

The existence of a correlation between v_{∞} , on the one hand, and T_{eff} and v_{esc} , on the other, was for the first time demonstrated empirically by Abbot et al. (1978, 1982). These earlier findings have been confirmed by more recent investigations (e.g., Howarth & Prinja 1989; Prinja et al. 1990; Lamers et al. 1995; Haser et al. 1995), which furthermore provide quantitative coefficients to describe the correlations on a solid statistical base. In particular, it was found that v_{∞} experiences a dramatic decrease from $\sim 2.6v_{\text{esc}}$, for supergiants earlier than B1, to $\sim 1.3v_{\text{esc}}$, for those later than B1.

The presence of a jump in v_{∞} , called a *bi-stability jump*, is theoretically explained as due to changes in ionizations: winds of hotter stars are mainly driven by high ionization lines of C, N, O, etc in the Lyman continuum, whereas those of cooler stars, with T_{eff} between 20 and 10 kK, are mainly driven by a large number of metal lines in the Lyman and the Balmer continuum (Pauldrach & Puls 1990; Vink et al. 1999, 2001). Another jump, caused by similar reasons, is predicted to appear at 10 kK, but these predictions have not been observationally proven yet.

Interestingly, more recent observations (Crowther et al. 2006, see also Evans et al. 2004) have questioned the presence of a “jump” in v_{∞} at spectral type B1, and argued in favor of a gradual decrease in $v_{\infty}/v_{\text{esc}}$, from ~ 3.4 above 24 kK to ~ 1.9 below 20 kK. In the following, I will comment on our new findings regarding this problem.

First, let me define the “position” of the jump by means of the data from the OBA-supergiant sample as defined in Sect 2.2.5 (excluding the “uncertain” object HD 198478). As illustrated in Figure 6.1, two temperature regimes, with considerably different values of v_∞/v_{esc} , can be identified, connected by a transition zone. In the high temperature regime ($T_{\text{eff}} > 23$ kK), our sample provides $v_\infty/v_{\text{esc}} \approx 3.3 \pm 0.7$, whereas in the low temperature one ($T_{\text{eff}} < 18$ kK), we find $v_\infty/v_{\text{esc}} \approx 1.3 \pm 0.4$. (Warning: The latter estimate has to be considered cautiously, due to the large uncertainties at the lower end where $v_\infty = v_{\text{esc}}$ has been adopted for few stars due to missing diagnostics.) Note that the individual errors for v_∞/v_{esc} are fairly similar, of the order of 33% (for $\Delta M_V = 0.3$, $\Delta \log g = 0.15$ and $\Delta v_\infty/v_\infty = 0.25$) to 43% (in the most pessimistic case $\Delta M_V = 1.0$), similar to the corresponding Fig. 8 by Crowther et al..

In the *transition zone*, on the other hand, a variety of ratios are present, thus supporting the findings of Crowther et al. (2006) and Evans et al. (2004). Obviously though, large ratios typical for the high temperature region are no longer present from the center of the transition region on, so we can define a “jump temperature” of $T_{\text{eff}} \approx 20,000$ K. Nevertheless, we have shifted the border of the high- temperature regime to $T_{\text{eff}} = 23$ kK, since at least low ratios are present until then (note the dashed vertical and horizontal lines in Fig. 6.1). The low temperature border has been defined analogously, as the coolest location with ratios > 2 (dotted lines).

By comparing our (rather conservative) numbers with those from the publications as cited above, we find a satisfactory agreement, both with respect to the borders of the transition zone as well as with the average ratios of v_∞/v_{esc} . In particular, our high temperature value is almost identical to that derived by Crowther et al. (2006); Kudritzki & Puls 2000 provide an average ratio of 2.65 for $T_{\text{eff}} > 21$ kK), whereas in the low temperature regime we are consistent with the latter investigation (Kudritzki & Puls: 1.4). The somewhat larger value found by Crowther et al. results from missing latest spectral subtypes.

6.3 The Wind-momentum Luminosity Relationship

As outlined in Section 1.4.2, the radiation-driven wind theory (CAK approach) predicts that the mass-loss rates should obey the following scaling law:

$$\dot{M} \propto (kL)^{\frac{1}{\alpha'}} (M_{\text{eff}}/D')^{1-\frac{1}{\alpha'}} \quad (6.9)$$

where $\alpha' = \alpha - \delta$, and D' is a parameter related to the chemical composition. (Note that in this expression, the dependence of \dot{M} on D' is explicitly given while in Eq. 1.11, this dependence has been omitted.) This relation can in principle be used to compare observed and predicted mass-loss rates, but due to the strong

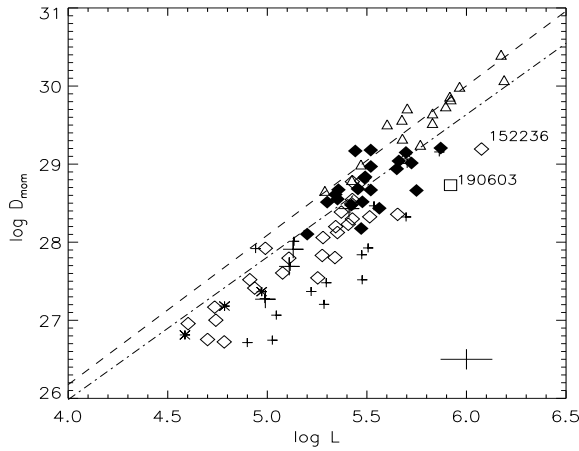


Figure 6.2: WLR for Galactic O (triangles) and B (diamonds and asterisks) SGs (from Markova & Puls (2008)). Filled diamonds indicate B-type objects with $T_{\text{eff}} \geq 21\,000$ K, asterisks such with $T_{\text{eff}} \leq 12\,500$ K and open diamonds B-types with temperatures in between $12\,500$ and $21\,000$ K. Overplotted are the early/mid B (small plus-signs) and A-SGs (large plus-signs) data derived by Kudritzki et al. (1999) and the theoretical predictions from Vink et al. (2000) for Galactic SGs with $27\,500 \leq T_{\text{eff}} \leq 50\,000$ (dashed-dotted) and with $12\,500 \leq T_{\text{eff}} \leq 22\,500$ (dashed)

Error bars provided in the lower-right corner represent the typical errors in $\log L/L_{\odot}$ and $\log D_{\text{mom}}$ for data from our sample.

dependence of \dot{M} on M_{\star} – of the order of $-1.5 \dots -0.5$ for typical values of $\alpha = 0.5 \dots 0.7$ and $\delta = 0.02 \dots 0.1$, and $D' = \text{const}$ – such approach would be very problematic (because of the high uncertainty of M_{\star} for single stars).

Luckily, it turned out that the strong dependence of \dot{M} on effective mass can be removed *if* a quantity, called “a modified wind momentum rate”, D_{mom} , instead of \dot{M} , is to be considered (Kudritzki et al. 1995). Then, assuming $\alpha' \sim 2/3$, and taking the logarithm, the following relation, known as the Wind-momentum Luminosity Relationship (WLR) is predicted to hold:

$$\log D_{\text{mom}} = \log(\dot{M} v_{\infty} R_{\star}^{\frac{1}{2}}) = x \log(kLD') + f(M, \Gamma, R_{\star}, \alpha, \delta) \quad (6.10)$$

where $x = \frac{1}{\alpha'}$, and f is an only mildly varying function of stellar and force-multiplier parameters.

Thus, for a given chemical composition ($D' = \text{const}$), a strict correlation of $\log D_{\text{mom}}$ with $\log L$ is expected, where the slope of this relation is predicted to yield an average value of $\alpha' = 2/3$, at least if the flux-weighted number of driving lines is not too different for different spectral types (Puls et al. 2000).

On the other hand, using the Monte Carlo approach in which *multiple scattering* is properly taken into account, Vink et al. (2000) predicted two, instead of one unique, relations for stars at either side of the bi-stability jump (see Eqs. 6.3 and 6.4) with somewhat smaller values of α' (see Eqs. 6.5 and 6.6). The vertical offset between these relations is explained by *a factor of five increase* in \dot{M} at the bi-stability jump (more

lines from lower iron ionization stages available to accelerate the wind), which is only partly compensated by the drop in v_∞ . Note that the size of the jump in \dot{M} is determined requiring a drop in v_∞ by a factor of two, as extracted from earlier observations (Lamers et al. 1995).

For solar metallicity, the presence of a strict correlation between D_{mom} and L has been *observationally* confirmed using data originating from *unblanketed* model analysis: by Puls et al. (1996); Herrero et al. (2000, 2002), for O-stars ; by Kudritzki et al. (1999), for BA-supergiants, and by Kudritzki et al. (1997), for Central Stars of Planetary Nebular (CSPN). However, the empirical results suggest that the coefficients of the WLR vary as a function of spectral type. In particular, Kudritzki et al. (1999) were the first to point out that the offset in the corresponding WLR of OBA-supergiants depend on spectral type, being strongest for O-types, decreasing from B0-B1 to B1.5-B3 and *increasing* again towards A-types. In addition, the slope of the observed WLR was found to vary as a function of spectral type: α decreases systematically with decreasing effective temperatures. The later result is consistent with calculations from line-statistics which predict smaller values of α for A SGs (~ 0.45) than for O-stars (~ 0.6 to 0.7) (see Puls et al. 2000).

While some of these earlier findings (theoretical and observational) have been confirmed by recent studies, utilizing *blanketed* model analysis, others have not (Repolust et al. 2004; Markova et al. 2004; Crowther et al. 2006; Markova & Puls 2008). In particular, the results of our analysis illustrated in Figure 6.2 show that the observed behaviour of Galactic OBA supergiants does not follow the predictions of Vink et al. (2000). Instead, the majority of O-SGs (triangles – actually those with H_α in emission, see below) follow the low-temperature predictions (dashed line), while most of the early B0-B1.5 subtypes (filled diamonds) are consistent with the high-temperature predictions (dashed-dotted), and later subtypes (from B2 on, open diamonds) lie below (!), by about 0.3 dex. Only few early B-types are located in between both predictions or close to the low-temperature one.

These results imply that the predicted strong increase in \dot{M} of a factor of 5 at the bi-stability jump is most probably *not* the case for a statistically representative sample of “normal” B-SGs, but more definite statements become difficult for two reasons. First, both the independent ($\log L$) and the dependent ($\log D_{\text{mom}}$) variables depend on R_\star (remember, the fit quantity is not \dot{M} , but Q , see Sect. 2.1.3), which is problematic for Galactic objects. Second, the wind-momentum rate is a function of L , but not of T_{eff} alone, such that a division of different regimes becomes difficult. To avoid these problems, let me firstly recapitulate the derivation of the WLR, to see the differences compared to our alternative approach formulated below.

As noted above (see also Eqs. 1.10 and 1.11), the theory predicts that:

$$\dot{M} \propto (kL)^{\frac{1}{\alpha'}} (M_\star(1-\Gamma))^{1-\frac{1}{\alpha'}} \quad (6.11)$$

$$v_\infty = C_\infty v_{\text{esc}}, \quad v_{\text{esc}} \propto (M_\star(1-\Gamma))^{\frac{1}{2}} \quad (6.12)$$

where α' is the difference between the line force multipliers $\alpha - \delta$ (corresponding to the slope of the line-strength distribution function and the ionization parameter; for details, see Puls et al. 2000), k - the force-multiplier parameter proportional to the effective number of driving lines and Γ - the (distance independent!) Eddington parameter.

Multiplying Eq. 6.11 with v_∞ and $(R_\star/R_\odot)^{1/2}$, and taking into account Eq. 6.12, we obtain the following expressions for the (modified) wind-momentum rate:

$$D_{\text{mom}} = \dot{M} v_\infty (R_\star/R_\odot)^{1/2} \propto C_\infty (kL)^{1/\alpha'} (M_\star(1-\Gamma))^{-\varepsilon} \quad (6.13)$$

$$\varepsilon = \frac{1}{\alpha'} - \frac{3}{2} \quad (6.14)$$

$$\log D_{\text{mom}} \approx \frac{1}{\alpha'} \log L + D_0 \quad (6.15)$$

$$D_0 = \frac{1}{\alpha'} \log k + \log C_\infty + \text{const} \quad (6.16)$$

where we have explicitly included here those quantities which are dependent on spectral type (and metallicity). Remember that this derivation assumes the winds to be unclumped, and that ε is small, which is true at least for O-supergiants (Puls et al. 2000).

Investigating various possibilities, it turned out that the (predicted) scaling relation for a quantity defined similarly as the optical-depth invariant is particularly advantageous:

$$Q' =: \frac{\dot{M} g_{\text{eff}}}{R_\star^{3/2} v_\infty} \propto \frac{k^{1/\alpha'}}{C_\infty} T_{\text{eff}}^{4/\alpha'} g_{\text{eff}}^{-\varepsilon}, \quad g_{\text{eff}} \propto \frac{M_\star(1-\Gamma)}{R_\star^2} \quad (6.17)$$

$$\log Q' \approx \frac{4}{\alpha'} \log T_{\text{eff}} + D'_0 \quad (6.18)$$

$$D'_0 = \frac{1}{\alpha'} \log k - \log C_\infty + \text{const}' \quad (6.19)$$

This relation for the *distance independent* quantity Q' becomes a function of $\log T_{\text{eff}}$ and D'_0 alone if α' were exactly $2/3$, i.e., under the same circumstances as the WLR. Obviously, this relation has all the features we are interested in, and we will investigate the temperature behaviour of \dot{M} by plotting $\log Q'$ vs. $\log T_{\text{eff}}$. We believe that the factor v_∞/g_{eff} is a monotonic function on both sides of and through the transition zone, as is also the case for g_{eff} itself. Thus, the $\log Q' - \log T_{\text{eff}}$ relation should react only on differences in the effective number of driving lines, and on the different ratio v_∞/v_{esc} on both sides of the transition region.

Fig. 6.3 displays our final result. At first glance, there is almost no difference between the relation on both sides of the “jump”, whereas inside the transition zone there is a large scatter, even if not accounting

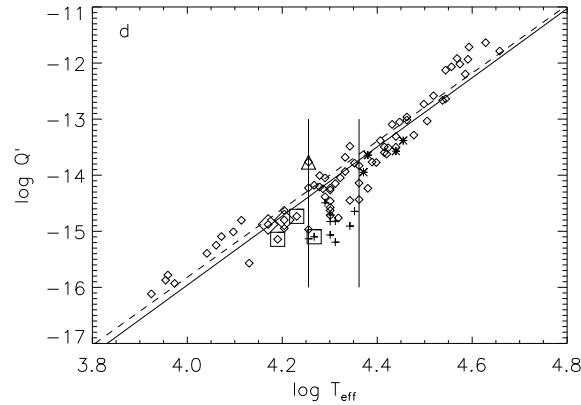


Figure 6.3: Modified optical depth invariant, $\log Q'$ (Eq. 6.17, as a function of $\log T_{\text{eff}}$. Symbols as in Fig. 6.1, with vertical bars indicating the “transition” region between 18 and 23 kK. Note that the mid B-type supergiants from the Kudritzki et al. sample (plus-signs) deviate from the trend displayed by the other objects. Regression for the complete sample (excluding HD 53 138, HD 152 236 and the Kudritzki et al. B-supergiants) overplotted in solid; dashed regression similar, but additionally excluding the objects in the transition region (see text).

for the (questionable) mid-B star data from Kudritzki et al. (1999).

Initially, we calculated the average slope of this relation by linear regression, and then the corresponding slope by additionally excluding the objects inside the transition region (dashed). Both regressions give similar results, interpreted in terms of α' with values of 0.65 and 0.66 (!), respectively², and with standard errors regarding $\log Q'$ of ± 0.33 and ± 0.28 dex.

If the relations indeed were identical on both sides of the jump, we would also have to conclude that the offset, D'_0 , is identical on both sides of the transition region. In this case, the decrease in v_∞/v_{esc} within the transition zone has to be more or less exactly balanced by the *same* amount of a decrease in $k^{\frac{1}{\alpha'}}$, i.e., both \dot{M} and v_∞ are decreasing in parallel, in complete contradiction to the prediction by Vink et al.

A closer inspection of Fig. 6.3 (in combination with the corresponding WLR of Fig. 6.2) implies an alternative interpretation. At the hottest (high luminosity) end, we find the typical division of supergiants with H_α in emission and absorption, where the former display an offset of a factor 2...3 above the mean relation, a fact which has been interpreted to be related to wind-clumping previously.

Proceeding towards lower temperatures, the Q' relation becomes well defined between roughly 31kK and the hot side of the transition zone (in contrast to the WLR, which shows more scatter, presumably due to uncertain R_\star). Inside the transition zone and also in the WLR around $\log L/L_\odot \approx 5.45$, a large scatter is present, followed by an apparent steep decrease in $\log Q'$ and wind-momentum rate, where the former is located just at the “jump temperature” of 20 kK. Note that the mid-B type objects of the Kudritzki et al.

²slope of regression should correspond to $4/\alpha'$, if the relations were unique.

sample are located just in this region. From then on, Q' appears to remain almost constant until 14 kK, whereas the WLR is rather flat between $5.1 < \log L/L_\odot < 5.4$, in agreement with the findings by Benaglia et al. (2007, their Fig. 8). At the lowest temperatures/luminosities, both Q' and the WLR decrease again, with a similar slope as in the hot star domain. This offers a possibility of a discontinuous behaviour, but, again, in contradiction to what is predicted.

We now quantify the behaviour of the mass-loss rate in the low temperature region (compared to the high temperature one), in a more conservative manner than estimated above, by using both the $\log Q'$ relation and the WLR. Accounting for the fact that the corresponding slopes are rather similar on both sides of the transition zone, we define a difference of offsets,

$$\Delta D_0 \approx \frac{1}{\alpha'} \Delta \log k + \Delta \log C_\infty \quad (6.20)$$

$$\Delta D'_0 \approx \frac{1}{\alpha'} \Delta \log k - \Delta \log C_\infty, \quad (6.21)$$

evaluated with respect to “low” minus “high”. From the WLR, we have $\Delta D_0 < 0$, whereas the Q' relation implies $\Delta D'_0 \geq 0$, to be cautious. Thus, the change in $\frac{1}{\alpha'} \Delta \log k$ (which expresses the difference in $\log \dot{M}$ on both sides of the jump, cf. Eq. 6.11) is constrained by

$$\Delta \log C_\infty \leq \frac{1}{\alpha'} \Delta \log k < -\Delta \log C_\infty. \quad (6.22)$$

To be cautious again, we note that $\Delta \log C_\infty$ should lie in the range $\log(1.9/2.4) \dots \log(1.3/3.3) = -0.1 \dots -0.4$, accounting for the worst and the average situation (cf. Fig. 6.1).

Thus, the scaling factors of mass-loss rates on both sides of the jump (cool vs. hot) differ by

$$0.4 \dots 0.8 \leq k^{\frac{1}{\alpha'}} < 1.25 \dots 2.5 \quad (6.23)$$

i.e., \dot{M} either decreases in parallel with v_∞/v_{esc} or increases *marginally*.

Thus, in addition to the well-known factor of two discrepancies for dense O-SG winds, the most notable disagreement (discarding local effects within the transition zone for the moment) is found in the low T_{eff} /low L B-SG domain, confirming the analysis by Crowther et al. (2006). The predictions by Vink et al. clearly require the decrease in v_∞ to be *overcompensated* by an increase in \dot{M} throughout the complete mid/late B-star regime, whereas our analysis has shown that this is not the case. At best, \dot{M} increases by the same amount as v_∞ decreases, though a reduction of \dot{M} seems to be more likely, accounting for the fact that the upper limit in Eq. 6.23 is a rather conservative estimate.

Since the calculation of *absolute* mass-loss rates and wind-momenta is a difficult task and depends on a number of uncertainties (see below), let me firstly consider the possibility that at least the predictions regarding the *relative* change in \dot{M} (from hot to cool objects) are correct, and that clumping affects this prediction only marginally.

In this case, the most simple explanation for the detected discrepancy is that cooler objects are less clumped than hotter ones. Since Vink et al. predict an increase in \dot{M} of a factor of five, this would imply that the clumping factors for hotter objects are larger by factors of 4 (most optimistic case) to 156 (worst case) compared to those of cooler ones.³ Given our present knowledge (see Fullerton et al. 2006, Puls et al. 2006 and references therein), this is not impossible, but raises the question about the physical origin of such a difference. This hypothesis would also imply that *all* B-SG mass-loss rates are overpredicted, though to a lesser extent for cooler subtypes.

In the alternative, and maybe more reasonable scenario that the clumping properties of OBA supergiants were not too different, we would have to conclude that at least the low temperature predictions suffer from unknown defects. Note, however, that a potential “failure” of these predictions does not invalidate the radiation driven wind theory itself. The actual mass-loss rates depend on the effective number of driving lines, and, at least in principle, this number should *decrease* towards lower T_{eff} , due to an increasing mismatch between the position of these lines and the flux maximum (e.g., Puls et al. 2000). In Vink’s models, it increases instead because Fe III has many more lines than Fe IV, and because these lines are distributed over a significant spectral range. The absolute number of these lines and their strengths, however, depend on details of the available data (not forgetting the elemental abundances, Krticka & Kubat 2007), a consistent description of the ionization/excitation equilibrium and also on other, complicating effects (e.g., the diffuse radiation field diminishing the line acceleration in the lower wind, Owocki & Puls 1999, and the potential influence of microturbulence, Lucy 2007), which makes quantitative predictions fairly ambiguous. Moreover, if the winds were clumped, this would influence the hydrodynamical simulations, due to a modified ionization structure.

That there is an effect which is most probably related to the principal bi-stability mechanism (Pauldrach & Puls 1990) remains undisputed, and is evident from the more or less sudden decrease in $v_{\infty}/v_{\text{esc}}$. Additionally, there is a large probability that at least inside the transition zone a “local” increase of (\dot{M}/v_{∞}) is present, which would partly support the arguments by Vink et al., though not on a global scale. Furthermore, the scatter of Q' (and wind-momentum rate) turned out to be *much* larger in the transition region than somewhere else. This might be explained by the fact that hydrogen begins to recombine in the wind just in this region, whereas the degree of recombination depends on a multitude of parameters, thus leading to the

³from Eq. 6.23 with ratios of $(5/2.5)^2$ and $(5/0.4)^2$

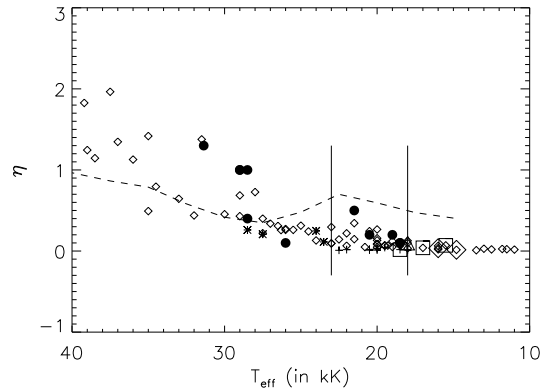


Figure 6.4: Wind-efficiency, η , as a function of T_{eff} , for our combined sample (symbols as in Fig. 6.1) and objects as analyzed by Benaglia et al. (2007) (filled dots, mass-loss rates from radio excess). Eight objects in common have been discarded from the *latter* sample. Overplotted (dashed) are their theoretical predictions, based on the models by Vink et al. (2000).

observed variety of mass-loss rates and terminal velocities. Finally, note that at least the observed hypergiant seems to be consistent with the bi-stability scenario, which, after all, has been originally “invented” for these kind of objects.

6.4 Wind efficiency

Recently Benaglia et al. (2007) have reported evidence of the possible presence of a local maximum in the wind efficiency, $\eta = \dot{M} v_{\infty} / (L/c)$, around 21 000 K, which would be at least in *qualitative* agreement with theoretical predictions of Vink et al. (1999, 2000). In Figure 6.4, we compare the wind-efficiencies as derived for our combined OB sample (from H_{α}) to corresponding data from their radio measurements (filled dots). The dashed line displays the theoretical predictions by Vink et al. (2000).

There are eight stars in common with our sample for which we display the H_{α} results only, not to artificially increase the statistics. At least for five of those, all of spectral type B0 to B2, a direct comparison of the H_{α} and radio results is possible, since same values of T_{eff} , R_{\star} and v_{∞} have been used to derive the corresponding wind efficiencies. In all but one of these stars ⁴, radio and optical mass-loss rates agree within 0.2 dex, which is comparable to the typical uncertainty of the optical data. Translated to potential wind-clumping, this would mean that the outer and inner wind-regions were affected by similar clumping factors, in analogy to the findings for *thin* O-star winds (Puls et al. 2006). From Fig. 6.4 now, several issues are apparent:

⁴HD 41 117, with \dot{M} from H_{α} being 0.37 dex lower than from the radio excess.

- i) As for the wind-momenta and mass-loss rates, also the wind-efficiencies of OB-supergiants do not behave as predicted, at least globally.⁵ Instead, they follow a different trend (for $\alpha' = 2/3$, one expects $\eta \propto T_{\text{eff}}^2 (R_{\star}^{0.5} k^{1.5} C_{\infty})$, i.e., a parabola with spectral type dependent offset), where, as we have already seen, the offset at the cool side of the jump is much lower than in the simulations by Vink et al. Actually, this is true for almost the complete B-SGs domain (between 27 and 10 kK).
- ii) Similar as in the *observed* wind-momentum luminosity diagram (Fig. 6.2), some of the O-supergiants do follow the predictions, while others show wind-efficiencies which are larger by up to a factor of two. Note that this result is supported by *both* H_{α} *and* radio diagnostics. If this discrepancy were interpreted in terms of small-scale clumping, we would have to conclude that the winds of these objects are moderately clumped, even at large distances from the stellar surface.
- iii) Within the transition zone, a large scatter towards higher values of η is observed, which, if not due to systematic errors in the adopted parameters, indeed might indicate the presence of a local maximum, thus supporting the findings of Benaglia et al. (2007). From a careful investigation of the distribution of stellar radii, terminal velocities and mass-loss rates, we believe that this local bump does not seem to be strongly biased by such uncertainties, but is instead due to a real increase in \dot{M} .

6.5 Wind clumping. Stratification of the clumping factor

One of the major results outlined in Sect. 5 is that in weaker winds, the clumping factor is the same in the inner and outermost regions, whereas for stronger winds clumping in the inner wind is a factor of 3 to 6 larger than in the outer one. This finding is in some contrast to hydrodynamical simulations, at least regarding *self-excited* structure formation. Indeed, if there was any dependence on wind density predicted at all, thin winds should be more strongly clumped than thick winds, because of the missing stabilization due to the continuum, which induces a more heavily structured wind in the lower part (Owocki & Puls 1999), and because of the relative importance of the (transonic) velocity curvature terms, leading to gradient terms in the source functions and modification of the line acceleration (Puls et al. 1998).

Concerning the radial stratification of the clumping factor, for the best constrained object, ζ Pup, where a direct comparison is possible, the derived stratification is found to be in strong contrast to the predictions (see Figure 6.5): while theory suggests the maximum f_{cl} -value to appear in the intermediate wind (10-20 R_{\star}), the observations indicate it has been reached already in the innermost part, below $2R_{\star}$.

⁵In contrast to Q' , η is not completely radius-independent, but includes a dependence $\propto R_{\star}^{-0.5}$, both if \dot{M} is measured by H_{α} and by the radio excess.

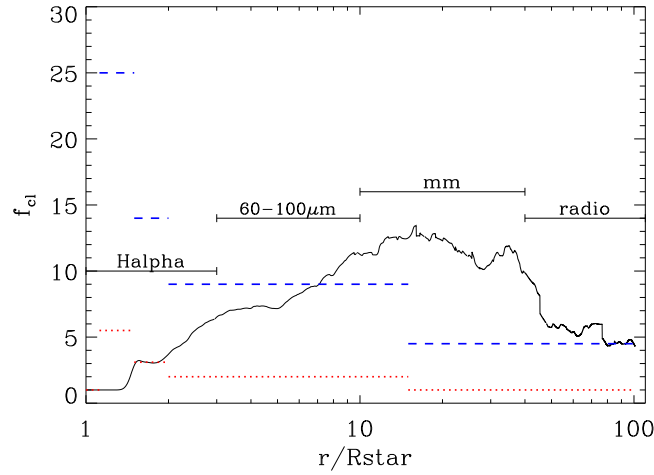


Figure 6.5: Theoretical predictions for the clumping factor (solid: from Runacres & Owocki 2002) compared to “observed” results from ζ Pup. The red (dotted) solution correspond to an unclumped outer wind, whereas the blue (dashed) solution (with an assumed $f_{cl}=4.5$ in the radio-emitting region) gives the same fit quality, when the mass-loss rate is reduced by a factor of $1/\sqrt{4.5}$. See text.

To get more quantitative inside into this issue, we decided to obtain appropriate spatial averages of the predicted clumping factor to be compared to the values derived for the 5 regions as introduced in Sect 5.1.4. The most decisive quantity regarding radiative transfer is the optical depth, being proportional to the spatial integral over $f_{cl}(r) \rho(r)^2$ (assuming the source function to be unaffected by clumping), so that a meaningful comparison requires the predicted clumping factors, $f_{cl}(r)$, to be averaged over ρ^2 inside the regions considered.⁶ To this end, we have used the results displayed in the various figures provided by Runacres & Owocki.

The predictions of Runacres & Owocki (2002) and the corresponding averages are summarized in Table 6.1. Before commenting on these data I feel it necessary to note that similar to the results from our simulations, the predicted radial stratification of the clumping factor (Runacres & Owocki 2002, 2005) also depends on a number of assumptions, the most important of which are:

- 1-D hydrodynamical treatment. First results from a 2-D approach (Dessart & Owocki 2003) might indicate somewhat lower (factor of 2) clumping factors than those resulting from a 1-D treatment.
- line-driven instability due to self-excited perturbations. Unfortunately, externally triggered perturbations, such as sound waves and photospheric turbulence (see Feldmeier et al. 1997), and photospheric pulsations, have not been examined with regard to this quantity.
- the use of a line-strength cut-off, κ_{max} , which is typically three dex below the actual value (Owocki,

⁶By adopting this approach, we discard certain details, such as the fact that H_α reacts to averages over constant velocity surfaces (and not along the radial direction), as well as optical depth effects.

Castor and Rybicki 1988). While in the inner and outermost parts of the wind f_{cl} seems to remain rather insensitive to the value of κ_{max} , in the outer one (around $50R_*$) it can increase if more realistic values are used (Runacres & Owocki 2002).

Due to these assumptions as well as to the fact that for our comparison we are going to use spatial averages instead of individual data, all numbers listed in Table 6.1 might be considered in qualitative sense. Another important issue to be noted is that to be consistent with the results from our combined H_α , IR and radio analysis a discrimination between absolute theoretical numbers and numbers referring to the average clumping factor in region 5 have to be made.

Table 6.1: Clumping factors as predicted by hydrodynamical simulations from Runacres & Owocki (2002), for the different regions as introduced in Sect 5. $\langle f_{cl} \rangle_1$ is a straight average, $\langle f_{cl} \rangle_2$ - an average weighted with ρ^2 (see text). Note that these numbers are only approximate ones, since they have been derived from figures and not from tables.

region	f_{cl}	$\langle f_{cl} \rangle_1$	$\langle f_{cl} \rangle_2$
1	1	1	1
2	1...4	2.5	≥ 2.1
3	4...13	8.5	≥ 4.7
4 ^a	13...5	9	≤ 11.6
5 ^a	5...4	4.5	≤ 4.7
4 ^b	13...20	16	≥ 14
5 ^b	20...4	12	≤ 15

^a κ_{max} from Owocki, Castor and Rybicki (1988); ^b κ_{max} larger by a factor of 10.

Regarding the data listed in Table 6.1, the first thing to be noted is that in the theoretical computations, the unclumped region 1 typically extends to $1.3 R_*$ which is fairly consistent with the *derived* maximum extent of such a potentially unclumped domain ($r_{in} \leq 1.1 \dots 1.2 R_*$, see Sect. 5.2). Also, for region 2, we find *average* values $\langle f_{cl} \rangle_2 \sim 2..3$ (lower than in region 5!), for region 3 values around 4...5, and for region 4 values around 11, which again might be even larger for large κ_{max} . Note that for different wind densities and wavelengths, the calculated averages for regions 3 and 4 might be higher and lower, respectively, than the indicated ones, depending on the radial position at which $\tau = 1$ is reached. Finally, the predicted maximum is located at the border between regions 3 and 4 (around $15 R_*$), but might be shifted towards larger radii for larger κ_{max} .

Compared to our results from Table 5.3, these predictions are significantly different, at least *if* the average clumping factor in the radio domain (region 5) is of the order of 4 or larger. In this case, all H_α mass-loss rates should be lower than the radio mass-loss rates, which is definitely not true. Thus, either the clumping factors in region 2 are predicted as too low, or those in region 5 as too large!

Disregarding this problem, the average clumping factor should increase monotonically from region 2 to 4 according to theory, and at least *some* of our emission type objects (e.g., HD 15570) are compatible with

this result (though for others $f_{\text{cl}}^{\text{out}}$ is of the same order or even lower than $f_{\text{cl}}^{\text{mid}}$, see Table 5.3). Only concerning the differential behaviour of region 2 to region 3, do *most* objects behave as predicted. As outlined already above, the notable exception to this rule is ζ Pup, where the complete run of $f_{\text{cl}}(r)$ and the position of its maximum definitely deviate from the predictions (and from the other objects investigated). Such a deviation was already found by Puls et al. (1993b), who tried to simulate the observed H_α profile and IR continuum for ζ Pup, based on hydrodynamical models from S. Owocki. Though they were quite successful in fitting H_α with a mass-loss rate just a factor of 2 lower than when using homogeneous models (and consistent with present estimates), the IR continuum was too strong at this \dot{M} , indicating lower clumping factors than predicted in region 3.

6.6 Summary

Regarding a comparison with theoretical models, the major conclusions to be drawn from the previous sections are as follows.

- **The Wind-momentum Luminosity Relation** The observed WLR of Galactic OB-stars is in strong contradiction to theoretical predictions from Vink et al. (2000). While the majority of O-type stars show larger wind momenta, B-SGs lie systematically below the predicted values. Also the wind-efficiencies of OB-supergiants do not behave as predicted, at least globally.
- **The bi-stability jump** That there is a certain effect separating hotter winds from cooler ones remains undisputed, and is also supported by our results. However, and in contrast with the predictions of Vink et al. (1999), our analysis indicates a gradual decrease instead of a jump in v_∞ in the bi-stability (“transition”) region, which is located at lower temperatures than predicted: 18 to 23 kK against 22.5 to 27 kK. This finding is in fair accordance with recent results by Evans et al. (2004) and by Crowther et al. (2006).

Concerning the behaviour of \dot{M} , by means of a *newly* defined, distance independent quantity $Q' = \dot{M}/R_\star^{1.5} g_{\text{eff}}/v_\infty$, we have shown that whilst within the transition zone a large scatter is present, Q' remains a well defined function with low scatter in the hot and cool temperature region outside this zone. Combining the behaviour of Q' and the modified wind-momentum rate, the change in \dot{M} over the bi-stability jump (from hot to cool) was constrained to lie within the factors 0.4 to 2.5, to be conservative. Thus, \dot{M} either decreases in parallel with v_∞/v_{esc} (more probable), or, at most, the decrease in v_∞ is just balanced by a corresponding increase in \dot{M} (less probable). This finding contradicts the predictions by Vink et al. that the decrease in v_∞ should be *over-compensated* by an increase in \dot{M} , i.e., that the wind-momenta should increase over the jump. Considering potential clumping effects, we have argued that such effects will not change our basic result, unless hotter objects turn out to be substantially more strongly clumped than cooler ones. In any

case, at least in the low temperature region present theoretical predictions for \dot{M} are too large!

- **Radial stratification of the clumping factor** Compared to theoretical predictions, the derived clumping properties of O-stars differ at least in two respects: first, thinner winds are not more clumped than thicker ones, as predicted by theory and second, the clumping factor in the inner wind is definitely not lower than in the outer wind.

Concluding remarks and future perspectives

In view of the important role of hot star winds in so many areas of astrophysics, it should be not a surprise that this topic is in the focus of attention for more than 30 years. While developments in the past decade have significantly improved our understanding of OB stars and their winds, a number of completely new, puzzling phenomena have been discovered, which clearly indicate that our knowledge about the nature of these object is still not as complete as we would like it to be. In particular, and if the outcome of our investigations is to be concerned, the most prominent challenges we are faced with at present are the wind clumping, the bi-stability jump, and the weak wind problem.

Wind clumping In this thesis compelling evidence about the clumped nature of O-star winds of solar metallicity have been presented. These results imply that the currently accepted mass-loss rates of these stars derived by means of ρ^2 -diagnostics may need to be revised downwards by a factor of $\sqrt{f_{cl}}$. The absolute value of the clumping factor however is still a subject of debates: the derived estimates range from about 5 (from H_α , see, e.g., Markova et al. 2004; Repolust et al. 2004) to about 100 (from UV diagnostics, e.g., Bouret et al. 2003; Fullerton et al. 2006).

In addition, we found that the empirical radial stratification of the clumping factor is not compatible with that predicted by the line-driven instability mechanism (either self-excited or triggered), showing stronger clumping in the inner than in the outer winds (Puls et al. 2006), while the opposite behaviour is predicted (Runacres & Owocki 2002, 2005). Also, our results suggest that the clumping factor depend on wind density, where weaker winds seem to be less clumped than stronger ones, in full contradiction with what might be expected from theory.

The lack of consistency between observed and predicted wind properties of O-stars might point out to some problems in our understanding of the physical cause of the clumping, but may also indicate that the presently accepted treatment of wind clumping (know as the *micro-clumping* approach) is rather simplified, i.e. that effects, such as, e.g., the feedback of clumping on the ionization and excitation of the gas; the velocity dispersion of the clump ensemble and inside individual clumps; the radial stratification of clumping and its properties and the spatial dementions of the clumps that have been so far neglected, are important and must therefore be consistently implemented in our future analysis.

While first steps to clarify these puzzling issues have been recently undertaken, further observational and theoretical investigations need to be foreseen to quantify these effects properly, and to find out whether one of them dominates, or several effects are required to resolve the mass loss discrepancy in O stars. (For an extensive review on this issue the interested reader is referred to Hamann et al. 2008).

Another important question to be answered is: *Do the clumping properties depend on metallicity ?*

Since in agreement with theoretical predictions (Vink et al. 2001), the global wind properties, \dot{M} and v_∞ , of O-stars are found to depend on the metal content (see, e.g., Mokiem et al. 2007b) such a question is more than legitimate. Direct evidence about wind inhomogeneities in low metallicity environment has been recently reported by Marchenko (2008). In addition, the wind momenta of O-stars in the Magellanic Clouds were found to be systematically larger than those predicted by Vink et al. (2001). Interpreted in terms of wind clumping, these results imply a clumping factor, that is somewhat lower than that derived for MW stars (de Koter et al. 2008). Due to the large uncertainties however this result cannot be considered conclusive and has to be additionally investigated.

The weak wind problem Our studies revealed that the wind momenta of Galactic B supergiants are significantly lower than the predicted ones. Similar situation has been established for low luminosity ($\log L/L_\odot \leq 5.3$) O-stars as well (see, e.g., Herrero et al. 2002; Bouret et al. 2003; Martins et al. 2004). This discrepancy has become popular as the “weak-wind problem”.

Various possibilities to explain this discrepant behaviour have been suggested (e.g., errors in the spectral analyses; missing physics and/or invalid assumptions in the wind predictions; different nature of the stars showing the weak wind problem, etc.), but due to the lack of reliable \dot{M} - estimates in this regime – Note that at $\dot{M} \sim 10^{-7}$ - $10^{-8} M_\odot$, H_α is not a reliable mass loss diagnostic, cf. Puls et al. (1996), – it does not seem possible, at least at present, to make any judgment which of these possibilities has the potential to account for the weak wind problem. In these circumstances, the use of UV and/or IR lines as mass-loss diagnostics would be particularly advantageous, since it might help to solve the problem by eliminating one potential cause, i.e., that of errors in the spectroscopic analysis. missing physics and/or invalid assumptions in the wind predictions; different nature of the stars showing the weak wind problem, etc. (For a detailed review on this issue the interested reader is referred to Kudritzki & Puls 2000 and Puls, Vink & Najarro 2008).

The bi-stability jump Due to changes in the ionization equilibrium of iron around spectral type B1, the overall properties of v_∞ and \dot{M} are predicted to change drastically (Vink et al. 1999). Although clear evidence about a certain effect, which divides hotter from cooler winds have been found, the predicted dramatic increase in \dot{M} at the bi-stability jump has not been empirically confirmed (Markova & Puls 2008 and references therein). Changes in the ionization equilibrium in the lower wind due to the presence of X-rays, with a subsequent effect on the efficiency of the radiative force, might cause such discrepancy, but further work is necessary to investigate this possibility in more details.

To conclude, let me point out that another important issue that challenges the present day hot star

wind research is the dependence of wind properties on metallicity. Both the improved CAK (see e.g., Kudritzki 2002), and the Monte Carlo (Vink et al. 2001) models predict \dot{M} should scale with Z as $\dot{M} \sim Z^m$, with $m = 0.5$ to 0.7 (Kudritzki 2002) and $m = 0.85$. This dependence has been basically confirmed by observations (e.g., Massey et al. 2004, 2005; Mokuem et al. 2006, 2007a,b), but problems still exist requiring further investigation to be foreseen.

Main results and achievements

The main results and achievements underlying this thesis can be summarized as follows:

1. The approximate method, originally developed by Puls et al. (1996), was additionally worked out to account for the effects of metal line-blocking/blanketing. By means of a comparative analysis it was shown that this approach can yield reliable results consistent with those from the complete model analysis. Therefore can be used to derived wind properties of a large sample of O-stars for which only H_α observations are available.
2. Using the NLTE, unified model atmosphere code FASTWIND, we determined the stellar and wind properties of a sample of Galactic B-supergiants with spectral types ranging from B0 to B9. Based on our T_{eff} - estimates and incorporating similar data from other investigations, the *blanketed* temperature scale for these stars was obtained. According to our results, the earlier (unblanketed) estimates of T_{eff} of B-supergiants need to be revised downward by 10 to 20%, the latter value being appropriate for stars with stronger winds. Calibrations such as the one derived by us are widely used to provide temperature estimates in cases where high-quality spectroscopy of stars are not available, but their spectral types are known. Also, they serve as a valuable tool to investigate the sensivity of T_{eff} on effects caused by different metallicity, or different strength of stellar winds.
3. Using the implementation of the Fourier transform technique, as developed by Simon-Diaz & Herrero (2007), we investigated the individual contributions of stellar rotation and “macro-turbulence” in the spectra of Galactic B-supergiants. Our results show that in this temperature regime a significant part (up to 50 %) of the measured line width can be attributed to macro-turbulence. Since rotation is a key parameter for stellar evolution calculation, this finding is particularly important.
4. It is a well-known fact that a non-zero micro-turbulent velocity, v_{mic} , can significantly improve the agreement between synthetical profiles and observations. Since v_{mic} affects the strength of Helium and metal lines, the derived T_{eff} and $\log g$ (but also abundances) might also be affected. Based on our model grids calculated by FASTWIND, we showed that for B-SGs of solar metallicity the effect of v_{mic} on T_{eff} is negligible, as long as the Si lines from the two major ions are used to determine it. In addition, we also showed that for these stars v_{mic} depends on T_{eff} with values ranging from about 15 to 20 km s⁻¹ at spectral type B0 to ~ 7 km s⁻¹ (at B9).
5. Compared to the predictions of Vink et al. (1999), the *blanketed* wind properties of Galactic OB-supergiants around the bi-stability jump were found to be somewhat discrepant. In particular,

- i) in fair accordance with recent results, our findings indicate a gradual decrease instead of a jump in v_∞ over the bi-stability region, where the limits of this region are located at lower T_{eff} than those predicted.
- ii) Introducing a distance-independent quantity Q' related to wind-strength, we showed that this quantity is a well defined, monotonically increasing function of T_{eff} *outside* the bi-stability region. *Inside* and from hot to cool, \dot{M} changes by a factor in between 0.4 and 2.5, which is much smaller than the predicted factor of 5. Thus, the decrease in v_∞ over the bi-stability region is *not* over-compensated by an increase of \dot{M} , as frequently argued⁷.

6 Including an *elaborate* error treatment ⁸, we studied the properties of the Wind-momentum Luminosity Relation for the *largest* sample of Galactic OB-stars gathered so far. Surprisingly and in full contradiction to theoretical predictions, the majority of our O-stars turned out to follow the low-temperature ($12\,500 \leq T_{\text{eff}} \leq 22\,500$ K) predictions; most of the early B0-B1.5 subtypes are consistent with the high-temperature ($T_{\text{eff}} \geq 27\,599$ K) predictions whilst the later subtypes (from B2 on) lie below (!), by about 0.3 dex. For O-stars the “observed” discrepancy can be interpreted as an indication of wind clumping with an effective clumping factor of 4.3. For B-SGs, however, this issue is still a mystery.

- 7. For the first time the consequences of “fine tuning” some of the direct and indirect parameters entering the WLR (e.g., the effects of wind variability and different values of stellar reddening and distances) have been studied. In particular, we found that the effect of such “fine tuning” on the corresponding mass-loss rates and wind momenta is rather insignificant, increasing only the local scatter without affecting the main concept of the Wind Momentum Luminosity Relationship.
- 8. To investigate line-profile variability for a large sample of O-supergiants in an objective and statistically rigorous manner, the Temporal Variance Spectrum analysis, developed for the case of photospheric absorption lines, was significantly modified to account for the effects of wind emission. Using this approach we showed that in O-supergiants the H_α variability is mostly dominated by processes in the wind, taking place between zero and $0.3 v_\infty$ (i.e., below $\sim 1.5 R_\star$). By means of line-profile simulations we furthermore showed that for stars with *intermediate* wind densities the properties of the H_α variability can be explained by simple models, consisting of coherent/broken shells (blobs) uniformly distributed over the wind volume, with an intrinsic scatter in the maximum density contrast

⁷provided that wind-clumping properties on both sides of this region do not differ substantially.

⁸To our knowledge, this investigation together with that of Repolust et al. (2004) are the first to account for errors in both directions. We consider this approach as essential, since the errors in $\log L$ are of the same order as those in $\log D_{\text{mom}}$, and they *are* correlated indeed

of about a factor of two. For stars at lower and higher wind densities, on the other hand, we found certain inconsistencies between the observations and our predictions, which might be explained with the presence of coherent large-scale structures (e.g., CIRs), partly confined in a volume close to the star.

9. Using time-series spectroscopy of the O9.5 supergiant α Cam from epochs spread over ~ 4 years, we found clear evidence that the wind of this star is not smooth but perturbed, starting from its base up to velocities of $\sim 500 \text{ km s}^{-1}$. In some occasions, the observed variations can be explained by short-term, low-amplitude recurrent variation in \dot{M} , which give rise to the formation of outward accelerating, consecutive shells or/and blobs. In others, a model involving two rotationally-modulated wind perturbations, which are not symmetric about the center of the star seems more appropriate. In addition, we also found clear evidence of occasional photospheric variability, which likely betrays prograde low-order non-radial pulsational. These findings identify α Cam as one of the most promising targets to investigate the origin of large scale wind structure in the light of the “photospheric connection”.
10. We have performed a quantitative analysis of time-variable phenomena in the photospheric, near-star, and outflow regions of the late-B supergiants HD 199 478. The analysis was based on photometric and optical spectroscopic datasets secured between 1999 and 2000. The obtained results indicate that the photometric variability of this star is consistent with a possible origin in terms of g -mode oscillations. Regarding the wind variability, from the behaviour of H_α we found clear evidence of strong deviations from spherical symmetry and homogeneity, originating more likely from the influence of a weak dipole magnetic field rather than from non-radial pulsations.
11. Extensive monitoring campaigns of several late-B supergiants, indicate that their H_α profiles exhibit quite similar peculiarities, consisting of a double-peaked emission with V/R variations, and occasional episodes of strong absorption indicating simultaneous mass infall and outflows. Using the NLTE line-blanketed code FASTWIND, we determined the stellar and wind properties of these stars, and showed that at the cooler temperature edge of B-supergiants ($T_{\text{eff}} \sim 11$ to 13kK) there are objects whose wind properties, as traced by H_α , are inconsistent with the predictions of the smooth, spherically symmetric wind approximation. This discordance is still not fully understood, but it may highlight the role of a non-spherical, disk-like, geometry, which may result from magnetically-driven equatorial compression of the gas. The proximity of the second bi-stability jump as predicted by theory might also be an issue.
12. Due to its extremely strong wind, the LBV P Cygni is an excellent target to study wind structures and variability. As a result of a long-term photometric and spectroscopic survey, we found convincing

evidence that the wind of this star is inhomogeneous and highly variable demonstrating different variability patterns on various time scales, from months to years and decades. In particular,

- i) we provided first observational evidence that Discrete Absorption Components seen in UV resonance lines presumably originate from large-scale, time-dependent, enhanced-density (low excitation) perturbations, which develop in the intermediate and outer part of the wind ($V \geq 0.41V_{\text{inf}}$), but appear to be maintained by photospheric processes. The geometry of the structures can be either spherically symmetric or curved, like kink. The recurrence of the DACs does not appear to be directly related to the stellar rotation.
 - ii) We discovered the presence of systematic microvariations in the stellar brightness with properties similar to the so-called “100d-type microvariation” recognized in other LBVs. Non-radial pulsations of either strange-mode or gravity-mode oscillations might be equally responsible for this phenomenon.
 - iii) We provided first observational evidence for a direct coupling between wind and photospheric variability in hot star. In particular, we showed that the microvariability has its counterpart in the spectral behaviour of P Cygni. The properties of this spectral variability, at least during our observational campaigns, suggest an interpretation in terms of extended, rotationally modulated, enhanced density wind structure generated by photospheric processes (e.g, NRPs), and developing in the inner (below $\sim 14R_{\star}$) part of the wind only. This finding is particularly important since it is a clearly indication that although the “photospheric connection” has not been so far discussed in relation to LBVs, it may be quite relevant to P Cygni.
 - iv) Using various methods and approaches, we studied the properties of a large sample of emission lines (permitted and forbidden) in the optical spectrum of P Cygni. In many cases the obtained results could not be interpreted in terms of the standard wind models, but require deviations from spherical symmetry and homogeneity to present in the wind.
13. P Cygni is usually considered as a notorious S Dor(SD)-type star although no indications for any SD-phases were reported till recently. Analysing an extended set of photometric and spectroscopic data covering a period of more than 13 years, we provided convincing evidence of a 7.3-year photometric oscillation, during which the behaviour of the star is such that when it brightens, the temperature decreases and the radius and mass-loss rate both increase. In this behaviour P Cygni is similar to S Dor and R71, which experience a sequence of such events, called short SD-phases. The reason for such behaviour might be at least twofold: drastic increase in \dot{M} , leading to the formation of a pseudo-photosphere, or a sub-photospheric perturbation, due at least partly, to variations in the underlying

stellar radius or T_{eff} . By means of simple calculations, we showed that the observed 7.3-year SD phase in P Cygni is more likely due to a mixture of an expanding radius/decreasing temperature and an expanding pseudo-photosphere.

14. To address the clumping issue and in particular the theoretically predicted radial stratification of the clumping factor, we analyzed a large sample of Galactic O-stars by combining our own and archival data for H_α , IR, mm and radio fluxes, and using approximate methods, calibrated to more sophisticated models. Because (almost) all our diagnostics depend on the square of wind density, we could not derive absolute clumping factors, but only factors normalized to a certain minimum. Since in all but one case the radio mass-loss rate were found to be the lowest ones, our normalization refers to the radio regime. With this in mind, the main results of our analysis can be summarized as follows:

- i) For almost all objects, the derived (radio) mass-loss rates are in very good agreement with the predicted wind-momentum–luminosity relation (Vink et al. 2000), in contrast to previous results relying on unclumped H_α data alone.
- ii) For all objects where H_α is of P Cygni shape, or displays a well-refilled absorption trough, the maximum extent of a potentially unclumped region can be limited to lie inside $r \leq 1.2R_\star$.
- iii) Our most important result concerns a (physical) difference between denser and thinner winds: for denser winds, the innermost region is more strongly clumped than the outermost one (with a normalized clumping factor of 4.1 ± 1.4), whereas thinner winds have similar clumping properties in the inner and outer regions.
- iv) In most cases, the clumping factors in the inner and adjacent region ($2R_\star \leq r \leq 5 \dots 15R_\star$) are comparable or increase moderately from inside to outside.
- v) In two of the three stars with mm-observations there is a certain probability that the outer region with $15R_\star \leq r \leq 50R_\star$) is considerably more clumped than the radio domain in agreement with what have been predicted by theory.
- vi) Our results differ from hydrodynamical predictions at least in one respect: the latter imply lower clumping in the inner than the outer wind, which is definitely not true for our sample.

Finally let me note that the presence of clumping introduces a new degeneracy in the results, namely between the velocity field exponent, β , and the clumping factors. If β is lower than assumed or derived from the fits, the clumping factors are larger, and vice versa.

List of publications

A. Refereed International Journals

1. Markova, N., Kolka, I. "Balmer lines in the spectrum of P Cygni. Dilemma of the interpretation of variability", 1984, *Afz*, 20, 465
2. Markova, N., Kolka, I. "The multicomponent structure of P Cygni spectral lines", 1985, *Afz*, 23, 539
3. Markova, N. "Some regularities in the variation of the Balmer line profiles in the P Cyg spectrum", 1986a, *Ap&SS* 123, 5
4. Markova, N. "The ejection of shells in the stellar wind of P Cyg: the most plausible explanation of the Balmer-line radial velocity variations", 1986b, *A&A* 162, L3
5. Markova, N., Kolka, I. "Radial velocity variations of certain OII, SiIII and NII lines - a confirmation of the shell ejection in the P Cygni stellar wind", 1988, *Ap&SS*, 141, 45
6. Markova, N. "Morphology and variability of helium line profiles in the P Cygni spectrum", 1993a, *Ap&SS* 201, 61
7. Markova, N. "A possible cause for the variations in the 'underlying' absorption-line profiles in the spectrum of P Cygni", 1993b, *A&A* 273, 555
8. Markova, N. "How did the spectrum of P Cygni look in 1985? Spectral atlas with complete line identifications in the wavelength range from 3550 to 4800Å", 1994, *A&AS* 108, 561
9. Markova, N., Zamanov, R. "P Cygni-spectral atlas with complete line identifications in the wavelength range from 4800 to 6760Å", 1995, *A&ASS* 114, 499
10. Markova, N., de Groot, M. "An analysis of emission lines in the spectrum of P Cygni", 1997, *A&A* 326, 1111
11. Markova, N., Tomov, N. "UBV photometry of P Cygni obtained in 1995, 1996 and 1997", 1998, *IBVS* 4641
12. Markova, N. "New aspects of line profile variability in P Cygni's wind", 2000, *A&AS*, 144, 391
13. Markova, N., Valchev, T. "Spectral variability of luminous early type stars. I. Peculiar supergiant HD199478", 2000, *A&A* 363, 995

14. Markova, N., Scuderi, S., de Groot, et al. "Simultaneous H α and photometric variability in P Cygni", 2001a, A&A, 366, 935
15. Markova, N., Morrison, N., Kolka, I., et al. "P Cygni in a short SD phase. Spectral and photometric evidences", 2001b, A&A, 376, 898
16. Muratorio, G., Markova, N., Friedjung, M., Israelian, G. " Properties of the P Cygni wind found using the SAC method ", 2002, A&A 390, 213
17. Markova, N. "Spectral variability of luminous early type stars. II. Supergiant Alpha Cam", 2002, A&A 385, 479
18. Markova, N., Puls, J., Repolust, T., et al. Bright OB stars in the Galaxy. I. Mass-loss and wind momentum rates of O-type stars: A pure H α analysis accounting for line-blanketing, 2004, A&A 413, 693
19. Markova, N., Puls, J., Scuderi, S., et al. Bright OB stars in the Galaxy. II Wind variability in O supergiants as traced by H alpha, 2005, A&A 440, 1133
20. Prinja, R. K., Markova, N., Scuderi, S., Markov, H. The superimposed photospheric and stellar wind variability of the O-type supergiant Alpha Camelopardalis, 2006, A&A 457, 987
21. Puls, J., Markova, N., Scuderi, S., et al. Bright OB stars in the Galaxy. III. Constraints on the radial stratification of the clumping factor in hot star winds from a combined H alpha, IR and radio analysis, 2006, A&A 454, 625
22. Markova, N., Puls, J. Bright OB stars in the Galaxy. IV. Stellar and wind parameters of B supergiants, 2008, A&A 478, 823
23. Markova, N., Prinja, R., Markov, H. et al. "Wind structure of late B supergiants. Multi-line analysis of near surface and wind structures in HD199478 (B8Iae), 2008, A&A 487, 211
24. Percy, J., Palaniappan, R., Seneviratne, R., Adelman, S., Markova, N. Photometric variability of the B8Iae Supergiant variable HD199478 (HR8020), 2008, PASP 120, 311

B. National and international meetings

1. Markova, N., Morrison, N., Kolka, I., et al. "Long-term spectral and photometric variability of P Cygni", 2000, ASPC 204, 11 (full text)

2. Markova, N. "New results on spectral and photometric variability of P Cygni", 2001, ASPCS 233, 113 (full text)
3. Friedjung, M., Muratorio, G., Markova, N., Israelian, G. "A study of the wind of P Cygni applying the self-absorption curve method", 2001, ASPC 233, 113 (full text)
4. Markova, N., Markov, H. Mass-loss and wind momentum rates of hot luminous stars. The effects of wind clumping and variability in Galactic O-type stars, Proceeding of the 2nd Bulgarian Astronomical Conference: *South-East European Astronomy and Space Research - Present and Future Perspectives*, 2005, ARBI, 20, 230 (full text)
5. Puls, J., Markova, N., Najarro, F. et al. "Clumping in O-star winds" 2007, Proceeding of an international workshop: *Clumping in hot star winds*, (eds.) W-R Hamann, A. Feldmeier, L. Oskinova, p. 35 (full text)
6. Puls, J., Markova, N., Scuderi, S., "Stellar winds from massive stars - What are the REAL mass-loss rates?", 2008, ASPC 388,101 (full text)
7. Markova, N., Markov, H. Wind structure in late B Supergiants, Proceeding of the 3rd National Conference of the Bulgarian Astronomical Society, 2008, BAJ, Vol. 10, p. 23 (full text)
8. Austin, M. G., Markova, N., Prinja, R. et al. Unusual variability and High Velocity Absorption in peculiar SG HD199478, 2008, in Proceeding of IAU Symp 250: *Massive stars as cosmic engines*, (in press) (poster paper)

Bibliography

Abbott, D. C. 1982, ApJ 259, 282

Abbott, D. C., Lucy, L. B. 1985 ApJ 288, 679

Abbott, D. C., Biegging, J. H., Churchwell, E. et al. 1980, ApJ 238, 196

Abbott, D. C., Biegging, J. H., Churchwell, E. et al. 1981, ApJ 250, 645

Abbott, D. C., Telesco, C. M., Wolff, S. C. 1984, ApJ 279, 225

Abbott, D. C., Garmany, C. D., Hansen, C. J. et al. 1986, PASP 98, 29

Abt, H. A., Levato, H., Grosso, M. 2002, ApJ 573, 359

Aerts, C., De Cat, P., Peeters, E. et al. 1999, A&A 343, 872

Asplund, M., Grevesse, N., Sauval, A. J. 2005, in ASP Conf. Ser. 336: *Cosmic Abundances as Records of Stellar Evolution and Nucleosynthesis*, eds. T. G. Barnes & F. N. Bash, p. 25

Azzopardi, M., Vigneau, J. 1975, A&AS 19, 271

Auer, L. H., Mihalas, D., 1972, ApJS 24, 193

Austin, M. G., **Markova, N.**, Prinja, R. et al. 2008, in Proceeding of IAU Symp 250: *Massive stars as cosmic engines*, (in press)

Barbier-Brossat, M., Figon, P. 2000, A&AS 142, 217

Barlow, M. J., Cohen, M. 1977, ApJ 213, 737

Barlow, M. J., Drew, J. E., Meaburn, J., et al. 1994, MNRAS 268, L29

Beals, C.S. 1950, Publ. Dominion Astroph. Obs., Vol. 9, No. 1

- Beichman, C. A., Neugebauer, G., Habing, H. J., et al. 1988, Infrared Astronomical Satellite (IRAS).
Catalog and Atlases. NASA Reference Publication 1190
- Benaglia, P., Vink, J. S., Marti, J., et al. 2007, A&A 467, 1265
- Berghöfer, T. W., Baade, D., Schmitt, J.H.M.M., et al. 1996, A&A 306, 899
- Biegging, J. H., Abbott, D. C., Chuchwell, E. B. 1989, ApJ 342, 883
- Bjorkman, J. E., Cassinelli, J. P. 1993, ApJ 409, 429
- Blomme, R., Runacres, M. C. 1997, A&A 323, 886
- Blomme, R., Prinja, R. K., Runacres, M. C., et al. 2002, A&A 382, 921
- Blomme, R., Van den Steene, G. C., Prinja, R. K., et al. 2003, A&A 408, 715
- Bloom, J. S., Kulkarni, S. L., Djorgovski, S. G. et al. 1999, Nature 401, 453
- Bohlin, R. C., Gilliland, R. L. 2004, AJ 127, 350
- Bouret, J-C., Lanz, T., Hillier, D. J., et al. 2003, ApJ 595, 1182
- Bouret, J-C., Lanz, T., Hillier, D. J. 2005, A&A 438, 301
- Breger, M., Gehrz, R.D., Hackwell, J. A. 1981, ApJ 248, 963
- Bresolin, F., Kudritzki, R-P., Mendez, R. H. et al. 2001, ApJ 548, L159
- Bresolin, F., Gieren, W., Kudritzki, R-P. et al. 2002, ApJ, 567, 277
- Bromm, Kudritzki & Loeb 2001, ApJ 552, 464
- Broom, Coppi & Larson 2002, ApJ 564, 23
- Burki, G. 1978, A&A, 65, 357
- Bychkov, V. D., Bychkova, L. V., Madej, J. 2003, A&A 407, 631
- Cardelli, J. A. 1988, ApJ 335, 177
- Cardelli, J. A., Clayton, G. C., Mathis, J. S. 1989, ApJ 345, 245
- Cassatella, A., Beeckmans, F., Benvenuti, D., et al. 1979, A&A 79, 223
- Cassinelli, J. P., Macgregor, K. B. 2000, in ASP Conf. Ser. 214: *The Be phenomenon in early-type stars*, p.

- Cassinelli, J. P., Olson, G. L., Stalio, R. 1978, ApJ 220, 573
- Castelli, F., Kurucz, R. L. 1994, A&A 281, 817
- Castor, J. I., Simon, T. 1983, ApJ 265, 304
- Castor, J. L., Abbott, D. C., Klein, R. 1975, ApJ 195, 157 (CAK)
- Clayton, G. C., Cardelli, J. A. 1988, AJ 96, 695
- Colina, L., Bohlin, R. C. 1994, AJ 108, 1931
- Conti, P. S., Frost, S. A. 1977, ApJ 212, 728
- Conti, P.S., Ebets, D. 1977, ApJ, 213, 438
- Conti, P. S., Leep, E. M., Lorre, J. J. 1977, ApJ 214, 759
- Cranmer, S. and Owocki, S. 1996, ApJ 462, 469
- Crowther, P. 2004, EAS 13, 1
- Crowther, P., Hillier, D. J., Evans, C. J., et al. 2002, ApJ 579, 774
- Crowther, P. A., Lennon, D. J., Walborn, N. R. 2006, A&A 446, 279
- Cruz-Gonzalez, C., Recillaz-Cruz, E., Costero, R., et al. 1974, RMxAA 1, 211
- Dachs, J., Wamsteker, W. 1982, A&A 107, 240
- Denizman, L., Hack, M. 1988, A&AS 75, 79
- Dessart, L., Owocki, S.P. 2003, A&A 406, L1
- Drew, J. E., 1985, MNRAS 217, 867
- Dufton, P. L., Ryans, R. S. I., Simon-Diaz, S., et al. 2006, A&A 451, 603
- Ebbets, D. 1982, ApJSS 48, 399
- Evans, C. J., Lennon, D. J., Trundle, C., et al. 2004, ApJ 607, 451
- Fan, X., Whitee, R., Davis, M. et al. 2000, AJ 120, 1579
- Feldmeier, A., Puls, J., Pauldrach, A.W.A. 1997, A&A 322, 878
- Felli, M., Habing, H. J., Israel, F. P. 1977, A&A 59, 43

- Figer, D. F., Najjarro, F., Morris, M. et al. 1998 ApJ 506, 384
- Fitzgerald, M. P. 1970, A&A 4, 234
- Fitzpatrick, E. L., Garmany, C. D. 1990, ApJ 363, 119
- Friend, D. B., Castor, J. L. 1983 ApJ 272, 259
- Friedjung, M., Muratorio, G. 1987, A&A 188, 100
- Friedjung, M., Muratorio, G., **Markova, N.**, Israelian, G. 2001, ASPC 233, 113
- Fullerton, A. W., Gies D. R., Bolton C. T. 1996, ApJSS 103, 475
- Fullerton, A. W., Massa, D. L., Prinja, R. K. 2004, AAS 205, 5305
- Fullerton, A. W., Massa, D., Prinja, R. K. 2006, ApJ 637, 1025
- Gabler, R., Gabler, A., Kudritzki, R-P. et al. 1989, A&A 226, 162
- Galama, T. J., Briggs, M. S., Wijers, R.A.M.J. et al. 1998, Nature 398, 394
- Galama, T. J., Tanvir, N., Vreeswijk, P. M. et al. 2000, ApJ 536,185
- Garcia-Gil, A., Garcia Lopez., R. J., Allende Pietro, C., et al. 2005, ApJ 623, 460
- Garcia, M., Bianchi, L. 2004, ApJ 606, 497
- Garmany, C. D., Stencel, R. E. 1992, AAS 94, 211
- van Genderen, A. M. 2001, A&A 366, 508
- van Genderen, A. M., Sterken, C., de Groot, M. 1997a, A&A 318, 81
- van Genderen, A. M., de Groot, M., Sterken, C. 1997b, A&AS 124, 517
- Van Gent, Lamers H.J.G.L.M., 1986, A&A 158, 335
- Gehrz, R. D., Hackwell, J. A., Jones, T. W. 1974, ApJ 191, 675
- Gies, D. R. 1987, ApJS 64, 545
- Gies, D. F., Lambert, D. L. 1992, ApJ 387, 673
- Glatzel, W., Kiriakidis, M., Chemigovskij, S. et al. 1999, MNRAS, 303, 116
- Gräfener, G., Hamann, W-R. 2005, A&A 432, 633

- Gray, D. F. 1973, ApJ 184, 461
- Gray, D. F. 1975, ApJ 202, 148
- Grevesse, N., Sauval, A. J. 1998, SSRv 85, 161
- Groenewegen, M.A.T., Lamers, H.J.G.L.M. 1989, A&AS 79, 359
- Groenewegen, M.A.T., Lamers, H.J.G.M.L., Pauldrach, A.W.A. 1989, A&A 221, 78
- de Groot, M. 1969, Bull. astr. Insts Neth. 20, 225
- de Groot, M. 1990, in: *Properties of Hot Luminous Stars*, ed. C. D. Garmany, San Francisco, ASP Conf. Ser., 7, 165
- de Groot, M., Sterken, C., van Genderen, A.M. 2001a, in: *P Cygni 2000: 400 years of progress*, eds. M. de Groot & C. Sterken, ASP Conf. Ser. 233, p. 59
- de Groot, M., Sterken, C., van Genderen, A.M. 2001b, A&A 376, 224
- Guetter, H. H., Vrba, F. J. 1989, AJ 98, 611
- Haislip, J. B., Nysewander, M. C., Reichart, D. E. et al. 2006 Nature 440 (7081): 181-183
- Hamann, W-R. 1980, A&A 84, 342
- Hamann, W.R., Oskinova, L.M., Feldmeier, A. in: *Clumping in hot star winds: Proceeding of an international workshop held in Potsdam, Germany*, (eds.) W-R Hamann, A. Feldmeier, L. Oskinova, p. 75
- Hanson, M. M. 2003, ApJ 597, 957
- Hanson, M. M., Luhman, K. L., Rieke, G. H. 2002, ApJS, 138, 35
- Harries, T. J. 2000, MNRAS, 315, 722
- Haser, S. M. 1995, PhD thesis, University of Munich
- Haser, S. M., Lennon, D. J., Kudritzki, R-P. et al. 1995, A&A 295, 136
- Hauschildt, P. H. & Baron, E. 1999, J. Comp. Appl. Math., 109, 41
- Hayes, D. S. 1985, in: Proc. of IAU Symposium No. 111: *Calibration of Fundamental Stellar Quantities*, eds. D.S. Hayes, L.E. Pasinetti, A.G. Davis Philip (Reidel:Dordrecht), p. 225
- Heger, A., Woosley, S. E., Baraffe, I. 2005, ASPC 332, 339

- Henrichs, H. F. 2001, ASP Conf. Ser. 248, 393
- Herrero, A., Puls, J., Villamariz, M. R. 2000, A&A
- Herrero, A., Puls, J., Najarro, F. 2002, A&A 396, 946
- Herrero, A., Kudritzki, R-P., Vilchez, J. M., et al. 1992, A&A 261, 209
- Hillier, D. J. 1991, A&A 247,455
- Hillier, D. J., Miller, D. L. 1998,ApJ, 496, 407
- Hillier, D. J., Kudritzki, R-P., Pauldrach, A. W. et al. 1993, A&A, 276, 117
- Hillier, D. J., Crowther, P., Najarro, P. et al. 1998, A&A 340, 438
- Hillier, D. J., Lanz, T., Heap, S. R., et al. 2003, ApJ, 588, 1039
- Hiltner, W. A. 1956, ApJS 2, 389
- Hiltner, W. A., Iriarte, B. 1955, ApJ, 122, 185
- Hirschi, R., Meynet, G., Maeder, A. 2004, A&A 425, 649
- Hirschi, R., Meynet, G., Maeder, A. 2005a, ASPC 342, 131
- Hirschi, R., Meynet, G., Maeder, A. 2005b, A&A 443, 581
- Holland, W. S., Robson, E. I., Gear, W. K., et al. 1999, MNRAS 303, 659
- Howarth, I., Prinja, R. 1989, ApJS 69, 527
- Howarth, I. D., Seibert, K. W., Hussain, G.A.J. et al. 1997, MNRAS 284, 265
- Hummer, D. G., Rybicki, G. B. 1985, ApJ 293, 258
- Humphreys, R. 1978, ApJS 38, 309
- Humphreys, R., McElroy, D. B. 1984, ApJ 284, 565
- Humphreys, R., Davidson, K. 1994, PASP, 106, 1025
- Hurbig, S., Szeifert, T., North, P. 2005, ASPC 337, 236
- Hurbig, S., Briquet, M., Scholler, M. et al. 2007, ASPC 361, 434
- de Jager, C., Lamers, H.J.G.L.M., Macchetto, F. et al. 1979, A&A 79, L28

- Jarrett, T. H., Polletta, M., Fournon, I.P et al. 2006, AJ 131, 261
- Jenness T., Lightfoot J. F., 2000, Starlink User Note 216, Starlink Project, CLRC
- de Jong, J.A., Henrichs, H.F., Schrijvers, C. et al., 1999, A&A 345, 172
- Johnson, M. C. 1925, MNRAS 85, 813
- Johnson, H. L. 1964, Comm. Lunar and Planet. Lab. 3, 79
- Johnson, H. L., Borgman, J. 1963, BAN 17, 115
- Johnson, H. L., Mendoza, V., Eugenio, E. 1966a, AnAp 29, 525
- Johnson, H. L., Mitchell, R. I., Iriarte, B., et al. 1966b, Comm. Lunar and Planet. Lab. 4, 99
- Johnson, D.R.H., Barlow, M. J., Drew, J. E. et al. 1992, MNRAS 255, 261
- Israelian G., 1995, A&A 300, 834
- Israelian, G., de Groot, M. 1999, SSRv 90,
- Israelian, G., de Groot, M., Parker, J.W. 1996, MNRAS 937, 280
- Israelian, G. Chentsov, E. & Musaev, E. 1997, MNRAS 290, 521
- Israelian, G., Herrero, A., Musaev, F., et al. 2000, MNRAS 316, 407.
- Izzard, R.G., Ramier-Ruiz. E., Tout, Ch. A. 2004, MNRAS 348, 1215
- Kaper, L., Henrichs H. F., Nichols J. S. et al. 1996, A&AS 116, 237
- Kaper, L., Henrichs H. F., Fullerton A. W. et al. 1997, A&A 327, 281
- Kaper, L., Henrichs, H. F., Nichols, J. S. et al. 1999, A&A 344, 231
- Kaufer, A., Stahl, O., Wolf, B. et al. 1996a, A&A 305, 887
- Kaufer, A., Stahl, O., Wolf, B. et al. 1996b, A&A 314, 599
- Kaufer, A., Stahl, O., Wolf, B. et al. 1997, A&A 320, 237
- Kendall, T.R., de Wit, W.J., Yun, J.L. 2003, A&A 408, 313
- Kiriakidis M., Pricke K.J., Glatzer W., 1993, MNRAS 264, 50
- Kolka, I. 1983, Eesti NSV Tead. Acad.Toim.Fuus. Matem., 32, 51

- Kolka, I. 1989, in Proceedings of IAU Coll 113, eds K. Davidson, A.F.G. Moffat, H.J.G.L.M. Lamers (Kluwer, Dordrecht and Boston), p. 265
- Kolka, I. Workshop on *The atmosphere of early type stars*, eds, U. Herber, C.S. Jeffery, 1992, Lect. Notes Phys 401, 125 (Springer, Berlin)
- Koorneef, J. 1983, A&ASS 51, 489
- de Koter, A., Lamers, H.J.G.L.M., Schmutz, W. 1996, A&A 306, 501
- de Koter, A., Vink, J.S., Muijres, L. *Clumping in hot star winds*: Proceeding of an international workshop held in Potsdam, Germany, (eds.) W-R Hamann, A. Feldmeier, L. Oskinova, p. 47
- Krticka, J., Kubat, J. 2007, A&A 464, L17
- Kudritzki, R.P. 1979, LIACo, 22, 295
- Kudritzki, R-P. 1980, A&A, 85, 174
- Kudritzki, R-P. 1998, in VIII Canary Islands Winter School of Astrophysics on *Stellar Astrophysics for the Local Group*, eds. A. Aparicio, A. Herrero, & F. Sanchez (Cambridge: Cambridge Univ. Press), 149
- Kudritzki, R-P. 1999, in Proc. IAU Coll. No. 169, eds. B. Wolf, O. Stahl & A.W. Fullerton, Springer Verlag, p. 405
- Kudritzki, R-P. 2002, ApJ 577, 389
- Kudritzki, R-P., Puls, J. 2000, ARA&A 38, 613
- Kudritzki, R-P., Urbaneja, M. A. 2006, STSci Symposium, May 2006, arXiv:astro-ph/0607460)
- Kudritzki, R-P., Lennon, D.J., Puls, J. 1995, in the ESO Workshop: *Science with the Very Large Telescope*, eds. Walsh, J.R., Danziger I.J. (Berlin:Springer-Verlag), 246
- Kudritzki, R-P., Bresolin, F., Przybilla, N. 2003, ApJL 582, L83
- Kudritzki, R-P., Pauldrach, A., Puls, J. et al. 1989, A&A 219, 205
- Kudritzki, R-P., Mendez, R. H., Puls, J. et al. 1997, Proc. IAS Symp 180, p. 64
- Kudritzki, R-P., Springmann, U., Puls, J et al. 1998, ASP Conf. Series 131, 299
- Kudritzki, R-P., Puls, J., Lennon, D.J. et al. 1999, A&A 350, 970
- Kunth, D., Mas-Hesse, J.M., Terlevich, R. et al. 1998, A&A, 334, 11

- Kuss C., Duemmler R., 1995, *Astron. Gess., Abst. Ser.*, No. 9, 136
- Langer, N., Hamann, W.R., Lennon M., et al. 1994, *A&A*, 290, 819.
- Lamers, H.J.G.L.M. 1986, in: *Luminous stars and associations in galaxies*; Proceedings of the Symposium, Porto-Kheli, Greece, May 26-31, 1985 (A87-16301 04-90). Dordrecht, D. Reidel Publishing Co., p. 157
- Lamers, H.J.G.L.M. in: IAU Coll No. 113, eds., K. Davidson, A.F.J. Moffat H.J.G.L.M. Lamers, p. 135
- Lamers, H.J.G.L.M., Cassinelli, J.P., in: *Introduction to stellar winds* (Cambridge University Press, 1999)
- Lamers, H.J.G.L.M., Leitherer, C. 1993, *A&A* 412, 771
- Lamers, H.J.G.L.M. & Morton, D.C. 1976, *ApJ Suppl.* 32, 715
- Lamers, H.J.G.L.M., Waters, L.B.F.M. 1984a, *A&A* 136, 37
- Lamers, H.J.G.L.M., Waters, L.B.F.M. 1984b, *A&A* 138, 25
- Lamers, H.J.G.L.M., Gadier, R., Snow, T.P. 1982 *Apj* 258, 186
- Lamers, H.J.G.L.M., de Groot, M., Cassatella, A. 1983 *A&A* 128, 299L
- Lamers, H.J.G.L.M., Waters, L.B.F.M., Wesselius, P.R. 1984, *A&A* 134, L17
- Lamers, H.J.G.L.M., Korevaar, P., Cassatella, A. 1985, *A&A* 149, 29
- Lamers, H.J.G.L.M., Cerruti-Sola, M., Perinotto, M. 1987, *ApJ* 314, 726
- Lamers H.J.G.L.M., Snow, T.P., Lindholm, D.M. 1995, *ApJ* 455, 269
- Lamers H.J.G.L.M., Snow Th., de Jager C. , Langerwere A. 1988, *ApJ* ??,??
- Lamers H.J.G.L.M., Bastiaanse C., Aerts C., Spoon H.W.W, 1998, *A&A* 335, 605
- Lefever, K., Puls, J., Aerts, C. 2007, *A&A* 463, 1093
- Leitherer, C., Robert, C. 1991, *ApJ* 377, 629
- Leitherer, C., Wolf, B. 1984, *A&A* 132, 151
- Leitherer, C., Hefele, H., Stahl, O., et al. 1982, *A&A* 108, 102
- Leitherer, C., Chapman, J.M., Koribalski, B. 1995, *ApJ* 450, 289
- Leitherer, C., Leao, J.R.S., Heckman, T.M. et al. 2001, *ApJ* 550,724

- Lennon, D.J. 1997, A&A 317, 871
- Lennon, D.J., Dufton, P.L. & Fitzsimmons, A. 1992, A&AS, 94, 569
- Lennon, D.J., Dufton, P.L., Fitzsimmons, A. 1993, A&AS 97, 559
- Lenorzer, A., Mokiem, M.R., de Koter, A. et al. 2004, A&A, 422, 275
- Lood, L., Gallandsky, O., Yarygina, T. 1975, Publ. Tartu Astrofiz. Obs. 43, 250
- Lucy, L.B. 1971, ApJ 163, 95
- Lucy, L.B. 2007, A&A, in press, astro-ph 3650
- Lucy, L.B. & Solomon, P. 1970, ApJ 159, 879
- MacFadyen, A. I., Woosley, S. I. 1999, ApJ 524, 262
- Maiz-Apellaniz, J., Walborn, N.R., Galue, H.A., et al. 2004, ApJS 151, 103
- Malhotra, S., Rhoads, J.E. 2002, ApJ 565, L71
- Marchenko, S. V., 2008, *Clumping in hot star winds*: Proceeding of an international workshop held in Potsdam, Germany, (eds.) W-R Hamann, A. Feldmeier, L. Oskinova, p. 29
- Markova, N. 1986a, Ap&SS 123, 5
- Markova, N. 1986b, A&A 162, L3
- Markova, N. 1993a, Ap&SS 201, 61
- Markova, N. 1993b, A&A 273, 555
- Markova, N. 1994, A&AS 108, 561
- Markova, N. 2000, A&AS, 144, 391
- Markova, N. 2001, ASPCS 233, 113
- Markova, N. 2002, A&A 385, 479
- Markova, N., de Groot, M. 1997, A&A 326, 1111
- Markova, N., Kolka, I. 1984, Afz, 20, 465
- Markova, N., Kolka, I. 1985, Afz, 23, 539

- Markova, N., Kolka, I. 1988, Ap&SS, 141, 45
- Markova, N., Markov, H. 2005, ARBI, 20, 230
- Markova, N., Markov, H. 2008, BAJ, Vol. 10
- Markova, N., Puls, J. 2008, A&A 478, 823
- Markova, N., Tomov, N. 1998, IBVS 4641
- Markova, N., Valchev, T. 2000, A&A 363, 995
- Markova, N., Zamanov, R. 1995, A&ASS 114, 499
- Markova, N., Morrison, N., Kolka, I., et al. 2000, ASPC 204, 11
- Markova, N., Scuderi, S., de Groot, et al. 2001a, A&A, 366, 935
- Markova, N., Morrison, N., Kolka, I., et al. 2001b, A&A, 376, 898
- Markova, N., Puls, J., Repolust, T., et al. 2004, A&A 413, 693
- Markova, N., Puls, J., Scuderi, S., et al. 2005, A&A 440, 1133
- Markova, N., Prinja, R., Markov, H. et al. 2008, A&A 487, 211
- Martins, F., Schaerer, D., Hillier, D.J. 2002, A&A, 382, 999
- Martins, F., Schaerer, D., Hillier, D.J., et al. 2004, A&A 420, 1087
- Martins, F., Schaerer, D., Hillier, D.J., et al. 2005, A&A 441, 735
- Massa, D., Fullerton, A.W., Sonneborn, G., et al. 2003, A&A 586, 996
- Massey, P., Thompson, A.B. 1991, AJ 101, 1408
- Massey, P., Bresolin, F., Kudritzki, R-P., et al. 2004, ApJ 608, 1001
- Massey, P., Puls, P., Pauldrach, A.W.A., et al. 2005, ApJ 627, 477
- Mathias, P., Aerts, C., Briquet, M. et al. 2001, A&A 379, 905
- McErlean, N. D., Lennon, D. J., Dufton, P. L. 1998, A&A 329, 613
- McErlean, N. D., Lennon, D. J., Dufton, P. L. 1999, A&A 349, 553
- Meaburn, J., Lopez, J. A., Barlow, M. J., & Drew J.E., 1996, MNRAS, 283, L69

- Megessier, C. 1995, A&A, 296, 771
- Merrill, R. W. 1913, Lick Obs. Bull 8, 24
- Meynet, G., Maeder, A. 2000, A&A 361,101
- Meynet, G., Maeder, A., Schaller, G et al. 1994, A&AS 103, 97
- Milne, E. A. 1924, MNRAS 84, 354
- Milne, E. A. 1926, MNRAS 86, 459
- Mokiem, M. R., de Koter, A., Puls, J., et al., 2005, A&A 411, 711
- Mokiem, M. R., de Koter, A., Evans, C.J., et al. 2006, A&A 456, 1131
- Mokiem, M. R., de Koter, A., Evans, C.J. et al. 2007, A&A 465, 1003
- Mokiem, M. R., de Koter, A., Vink, J.S. et al. 2007, A&A 473, 603
- Morton, D. C. 1976, ApJ 203, 386
- Mullan D. J., 1984, ApJ 283, 303
- Mullan D. J., 1986, A&A 165, 157
- Muratorio, G., Markova, N., Friedjung, M., Israelian, G. 2002, A&A 390, 213
- Najarro, F. Hillier, D. J. Stahl, O. 1997, A&A 326, 1117
- Najarro, F., Kudritzki, R. P., Cassinelli, J. P. et al. 1996, A&A, 306, 892
- Najarro, F., Kudritzki, R.P. , Hillier, D.J. et al. 1998, ASP Conf. Series Vol. 131, ed. I. Howarth, p.57
- Najarro, P., Puls, J., Herrero, A. et al. 2008, In: Clumping in hot star winds , eds Hamann, W.R., Oskinova, L.M. Feldmeier, A., p. 43
- Nelan, E. P., Walborn, N. R., Wallace, D. J. et. al. 2004, AJ 128, 323
- Ney, E. P., Strecker, D. W., Gehrz, R. D. 1973, ApJ 180, 809
- Oey, M. S., Massey, P. 1995, ApJ 452, 210
- Oskinova, L. M., Feldmeier, A., Hamann, W-R. 2004, A&A 422, 675
- Owocki, S. P. 1994, in Proc. Isle-aux-Coudre Workshop; *Instability and Variability of Hot star Wind*, A&SS 221, 3

- Owocki, S. P., ud-Doula, A. 2003, ASP Conf. Ser. 305, 350
- Owocki, S. P., ud Doula, A. 2004, ApJ 600, 1004
- Owocki, S. P., Rybicki, G. B. 1984, ApJ 284, 337
- Owocki, S. P., Rybicki, G. B. 1985, ApJ 299, 265
- Owocki, S. P., Castor, J. I., Rybicki, G. B. 1988, ApJ 335, 914
- Owocki, S. P., Puls, J. 1996, ApJ, 462, 894
- Owocki, S. P., Puls, J. 1999, ApJ, 510, 355
- Owocki, S. P., Cranmer, S. R., Gayley, K. G. 1996, ApJ 472, L1150
- Owocki, S. P., Runacres, M. C., Cohen, D. H. 2000, in ASP Conf. Ser. 204, *Thermal and Ionization Aspects of Flows from Hot Stars: Observations and Theory*, eds. H.J.G.L.M. Lamers & A. Sapar, p. 183
- Owocki, S. P., Gayley, K. G., Shaviv, N. J. 2005, ApJ 616, 525
- Panagia, N. 1991, in: *The physics of star formation and early star evolution*, eds. C. J. Lada & N. D. Kylafis, Kluwer Academic Publishers, p. 565
- Panagia, N., Felli, M. 1975, A&A 39, 1
- Parker, E. N. 1958, ApJ, 128, 664
- Parker, E. N. 1960, ApJ 132, 821
- Pauldrach, A., Puls, J. 1990, A&A 237, 409
- Pauldrach, A. W. A., Puls, J., Kudritzki, R. P. 1986, A&A, 164, 86
- Pauldrach, A. W. A., Kudritzki, R-P., Puls, J. et al. 1990, A&A 228, 125
- Pauldrach, A. W. A., Kudritzki, R-P., Puls, J. et al. 1994, A&A 283, 525
- Pauldrach, A. W. A., Hoffmann, T. L., Lennon, M. 2001, A&A, 375, 161
- Pauldrach, A. W. A., Hoffmann, T. L., Mendez, R. H. 2002, in Proc. IAU Symp. No. 209, eds. S.Kwok & M.Dopita, p. 177
- Pauldrach, A. W. A., Hoffmann, T. L., Mendez, R. H. 2004, A&A 419, 1111
- Penny, L. R. 1996, ApJ, 463, 737

- Pettini, M., Kellogg, M., Steidel, C. C. et al. 1998, ApJ, 508, 539
- Pettini, M., Steidel, C. C., Adelberger, K. L. et al. 2000, ApJ, 528, 96
- Petrenz, P., Puls, J. 1996, A&A 312, 195
- Percy, J., Attard, A., Szczesny, M. 1996, A&AS, 117, 255
- Percy, J., Palaniappan, R., Seneviratne, R., Adelman, S., **Markova, N.** 2008, PASP 120, 311
- Polcaro, V. F., Rossi, C., Giovannelli, F., et al. 1990, A&A 231, 354
- Pollmann, E. 1999, Be Star Newsletter 34, ??
- Press, W. H., Flannery, B. P., Teukolsky, S. A. et al. 1992, *Numerical Recipes: The Art of Scientific Computing* (2nd edition), Cambridge: Cambridge Univ. Press, p. 634
- Prinja, R. K. 1988, MNRAS, 231, 21
- Prinja, R. K., Howarth, I. D. 1986, ApJS 61, 357
- Prinja, R. K., Barlow, M. J., Howarth, I. D. 1990, ApJ 361, 607
- Prinja, R. K., Fullerton, A. W., Crowther, P. 1996, A&A 311, 264
- Prinja, R. K., Massa, D., Fullerton, A. W. 2002, A&A 388, 587
- Prinja, R. K., **Markova, N.**, Scuderi, S., Markov, H. 2006, A&A 457, 987
- Przybilla, F., Butler, K., Becker, S. R. et al. 2006, A&A, 445, 1099
- Przybilla, N., Bresolin, F., Butler, K. et al. 2007, in: *Massive stars: Fundamental parameters and Circumstellar interaction*, Rev. Mex. AC 33, 169
- Puls, J. 1987, A&A 184, 227
- Puls, J. 2008, in: *Massive stars as Cosmic Engines*, IAU Symp No. 250 eds. F. Bresolin, P. Crowther & J. Puls, in press
- Puls, J., Petrenz, P., Owocki, S. 1999, LNP 523, 131
- Puls, J., Owocki, S. P., Fullerton, A. W. 1993a, A&A 279, 457
- Puls, J., Pauldrach, A. W. A., Kudritzki, R-P., et al. 1993b, in: *Reviews in Modern Astronomy* 6, Springer, Heidelberg, p. 271

- Puls, J., Kudritzki, R.P., Herrero, A., et al. 1996, A&A 305, 171
- Puls, J., Springmann, U., Owocki, S.P. 1998, in: *Cyclical Variability in Stellar Winds*, Proc. ESO Workshop, eds. L. Kaper & A.W. Fullerton, Springer, Berlin, New York, p. 389
- Puls, J., Springmann, U., Lennon, M. 2000, A&AS 141, 23
- Puls, J., Vink, J., Najarro, F, 2008, A&ARv , 16, 209
- Puls, J., Repolust, T., Hoffmann, T., et al. 2002, in Proc. IAU Symp. No. 212, eds. K.A. van der Hucht, A. Herrero & C. Esteban, ASP Conf. Ser, p. 61
- Puls, J., Urbaneja, M.A., Venero, R. et al. 2005, A&A 435, 669
- Puls, J., **Markova, N.**, Scuderi, S., et al. 2006, A&A 454, 625
- Puls, J., Vink, J., Najarro, F., 2008, A&ARv 16, 209
- Puls, J., **Markova, N.**, Najarro, F. et al. 2007, *Clumping in hot star winds: Proceeding of an international workshop held in Potsdam, Germany*, (eds.) W-R Hamann, A. Feldmeier, L. Oskinova, p. 35
- Puls, J., **Markova, N.**, Scuderi, S. ,2008, ASPC 388,101
- Rauw, G. , Morrison, N. D., Vreux, J-M. et al. 2001, A&A 366, 585
- Reid, A. H. N., Howarth, I. D. 1996, A&A 311, 616
- Renzini, A., Voli, M. 1981, A&A 94, 175
- Repolust, T., Puls, J., Herrero, A. 2004, A&A 415, 349
- Repolust, T., Puls, J., Hanson, M. et al. 2005, A&A, 440, 261
- Rhoads, J. E., Malhotra, S. 2001, ApJ, 563, L5
- Roberts, D. H., Lehar, J., Dreher, J. W. 1987, AJ, 93, 968
- Rolleston, W. R. J., Smartt, S. J., Dufton, P. L., et al. 2000, A&A, 363, 537
- Rosenhald, J. D 1970, ApJ 159, 107
- Rosendhal, J. F. 1973, ApJ 186, 909
- Ryans, R. S. I., Dufton, P. L., Rolleston, W. R. J., et al. 2002, MNRAS 336, 577
- Rybicki, G. B. 1971, JQRST, 11, 589

- Runacres, M. C., Blomme, R. 1996, A&A 309, 544
- Runacres, M. C., Owocki, S. P. 2002, A&A 381, 1015
- Runacres, M. C., Owocki, S. P. 2005, A&A 429, 323
- Sahu, M., Blaauw, A. 1993, in: ASP Conf. Ser. 35, *Massive Stars: Their Lives in the Interstellar Medium*, eds. J.P. Cassinelli & E.B. Churchwell, p. 278
- Sagar, R., Yu, Q.Z. 1990, ApJ 353, 174
- Santolaya-Rey, A. E., Puls, J., Herrero, A. 1997, A&A 323, 488
- Schaller, G., Schaerer, Z. D., Meynet, G., et al. 1992, A&AS, 96, 269
- Schmutz, H. 1995, in: Proc IAU Symp. 163, eds. K.A. van der Hucht & P. M. Williams, p. 127
- Schmutz, H., Hamann, W-R. 1986, A&A 166, L11
- Schmidt-Kaler, 1982, in: Landolt-Bornstein, New Series: A&A, Vol. 25, Berlin: Springer-Verlag
- Scuderi, S., Bonanno, G. , Di Benedetto, R. et al. 1992, ApJ 392, 201
- Scuderi, S., Bonanno, G., Spadaro, D., et al. 1994, ApJ, 437, 465.
- Scuderi, S., Panagia, N., Stanghellini, C. et al. 1998, A&A 332, 251
- Shapley, A. E., Steidel, S. C., Pettini, M. 2003, ApJ, 588, 65
- Schröder, S. E., Kaper, L., Lamers, H.J.G.L.M., et al., 2004, A&A 428, 149
- Shimada, M.R., Ito, M., Hirata, R. et al. 1994, in: *Pulsation, Rotation and Mass Loss in Early Type Stars*, eds. L. Balona et al. (Dordrecht: Kluwer), p. 487
- Severny, A. 1970, ApJ 159, L73
- Sim, S. 2004, MNRAS 349, 899
- Simon-Diaz, S., Herrero, A. 2007, A&A 468, 1063
- Simon-Diaz, S., Herrero, A., Esteban, C., et al. 2006, A&A 448, 351
- Skinner, C. J., Exter, K. M., Barlow, M. J., et al. 1997, MNRAS, 288, L7
- Smith, K. C., Howarth, I. D. 1998, MNRAS 299, 1146

- Snedden, C., Gehrz, R. D., Hackwell, J. A., et al. 1978, ApJ 223, 168
- Sobolev, V. 1957, Sov. A&A J. 1, 678
- Sobolev, V. 1960, *Moving envelopes of stars*, Cambridge: Harvard University Press
- Sobolev, V. 1975, *Theoretical Astrophysics*, Nauka, Moskow, p. 309
- Stahl, O. in: IAU Coll. 113, *Physics of Luminous Blue Variables*, eds., K. Davidson, A.F.J. Moffat, H.J.G.L.M. Lamers, p. 149
- Stal, O., Mandel, H., Szeifert, Th. et al., 1991, A&A 244, 467
- Stal, O., Mandel, H., Wolf, W. et al., 1991, A&AS 99, 167
- Stahl O., Wolf B., Gng Th., et al., 1994, A&AS 107, 1
- Stone, R. C. 1979, ApJ 232, 520
- Stothers, R. B., Chin, C.W. 1996, ApJ 468, 842
- Stothers, R. B. & Chin, C. W. 2000, ApJ, 540, 1041
- Tapia, M. 1981, MNRAS 197, 949
- Taylor, M., Nordsieck, R. E., Schulte-Ladbeck, R. E., et al. 1991, AJ, 102, 1197
- The P. S., Wesselius, P. R., Janssen, I.M.H.H. 1986, A&AS 66, 63
- Tovmassian, H. M., Hovhannessian, R. Kh., Epremian, R. A., ????
- Trundle, C., Lennon, D. J. 2005, A&A, 434, 677
- Trundle, C., Lennon, D. J., Puls, J., et al. 2004, A&A 417, 217
- Underhill, A. B., 1975, ApJ 199, 691
- Underhill, A. B., 1995, ApJS 100, 433
- Vacca, W. D., Garmany, C. D., Shull, J. M. 1996, ApJ 460, 914
- Vakili F., Mourard D., Bonneau F., et al. 1997, A&A 323, 183
- Venn K. A. 1995, ApJS 99, 659
- Villamariz, M. R., Herrero, A. 2000, A&A 357, 597

- Vink, J. S. 2000, PhD thesys
- Vink, J. 2006, in ASPCS 353: *Stellar evolution at low metallicity: Massloss, Explosions, Cosmology*, Lamers, HJGLM, Langer, N., Nugis, T., Annuk, K. (eds), p. 113
- Vink, J. S., de Koter, A., Lamers, H.J.G.L.M. 1999, A&A 350, 181
- Vink, J. S., de Koter, A., Lamers, H.J.G.L.M. 2000, A&A 362, 295
- Vink, J. S., de Koter, A., Lamers, H.J.G.L.M. 2001, A&A 369, 574
- ud-Doula, A., Owocki, S. P., Townsend, R. H. D. 2008, MNRAS 385, 97
- Underhill, A.B., 1979, ApJ 234, 528
- Urbaneja, M. A. 2004, PhD Thesis, University of La Laguna, Spain
- Urbaneja, M. A., Herrero, A., Bresolin, F. et al. 2005, ApJ, 622, 862
- Yoon, S-C., Langer, N. , 2005, A&A 443, 643
- Waelkens, C., Aerts, C., Kestens, E. et al. 1998, A&A 330, 215
- Walborn, N. R. 1971, ApJS 23, 257
- Walborn, N. R. 1972, AJ 77, 312
- Walborn, N. R. 1973, AJ 78, 1067
- Wheeler, J. C., Sneden, Ch., Turan, J. W. 1989, ARA&A 27, 279
- Wright, A. E., Barlow, M. J. 1975, MNRAS 170, 41
- Waters, L.B.F.M., Lamers, H.J.G.L.M., 1984, A&AS 57, 327
- Wegner, W. 1994, MNRAS 270, 229
- Whittet, D. C. B., van Breda, I. G., 1980, MNRAS 192, 467
- Wolf, B., Stahl, O. 1985, A&A 148, 412
- Waters, L.B.F.M., Wesselius, P. R. 1986, A&A 155, 104
- de Zeeuw, P. T., Hoogerwerf, R., de Bruijne, J.H.J. et al. 1999, AJ 117, 354
- Zeinalov, S. K., Musaev, F. A. 1986, Sov. Astron. Lett., 12, 125
- natbib